WILEY-VCH

Elena Y. Vedmedenko

# Competing Interactions and Pattern Formation in Nanoworld

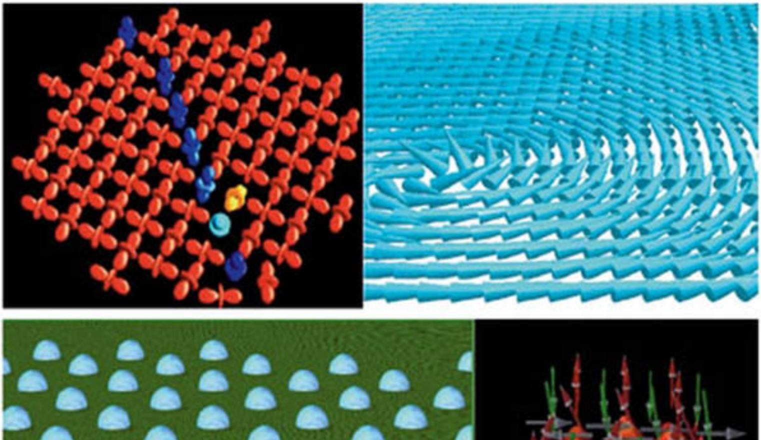

*Elena Y. Vedmedenko*

# Competing Interactions and Patterns in Nanoworld

WILEY-VCH Verlag GmbH & Co. KGaA

*Elena Y. Vedmedenko*

# Competing Interactions and Patterns in Nanoworld

## 1807–2007 Knowledge for Generations

Each generation has its unique needs and aspirations. When Charles Wiley first opened his small printing shop in lower Manhattan in 1807, it was a generation of boundless potential searching for an identity. And we were there, helping to define a new American literary tradition. Over half a century later, in the midst of the Second Industrial Revolution, it was a generation focused on building the future. Once again, we were there, supplying the critical scientific, technical, and engineering knowledge that helped frame the world. Throughout the 20th Century, and into the new millennium, nations began to reach out beyond their own borders and a new international community was born. Wiley was there, expanding its operations around the world to enable a global exchange of ideas, opinions, and know-how.

For 200 years, Wiley has been an integral part of each generation's journey, enabling the flow of information and understanding necessary to meet their needs and fulfill their aspirations. Today, bold new technologies are changing the way we live and learn. Wiley will be there, providing you the must-have knowledge you need to imagine new worlds, new possibilities, and new opportunities.

Generations come and go, but you can always count on Wiley to provide you the knowledge you need, when and where you need it!

William J. Pesce

*William J. Pesce*
President and Chief Executive Officer

Peter Booth Wiley

*Peter Booth Wiley*
Chairman of the Board

*Elena Y. Vedmedenko*

# Competing Interactions and Patterns in Nanoworld

WILEY-VCH Verlag GmbH & Co. KGaA

**The Author**
***Dr. Elena Y. Vedmedenko***
Institute for Applied Physics
University of Hamburg
Jungiusstr. 11
20355 Hamburg
Germany
vedmedenko@physnet.uni-hamburg.de

**Cover**
*Top left:* Theoretically predicted phase domain wall in a quadrupolar system on a square lattice (see Chapter 2).
*Bottom left:* Schematic representation of the hexagonal ordering in a two-dimensional electron Wigner crystal at He surface (see Chapter 2).
*Top right:* Theoretically predicted vortex excitations in a magnetostatically coupled array of ferromagnetic nanoparticles on a triangular lattice (see Chapter 3).
*Bottom right:* Collage of experimental spin-polarized scanning tunnelling microscopy image of a phase domain wall in the antiferromagnetic Fe monolayer on W(001) and theoretically calculated magnetic structure of the domain wall (see Chapter 4).

**Library of Congress Card No.:** applied for

**British Library Cataloguing-in-Publication Data**
A catalogue record for this book is available from the British Library.

**Bibliographic information published by the Deutsche Nationalbibliothek**
The Deutsche Nationalbibliothek lists this publication in the Deutsche Nationalbibliografie; detailed bibliographic data are available in the Internet at http://dnb.d-nb.de.

**Typesetting** K+V Fotosatz GmbH, Beerfelden
**Printing** betz-druck GmbH, Darmstadt
**Bookbinding** Litges & Dopf GmbH, Heppenheim
**Wiley Bicentennial Logo** Richard J. Pacifico

Printed in the Federal Republic of Germany
Printed on acid-free paper

**ISBN** 978-3-527-40484-1

# Contents

4.1 Two Short- or Mid-Range Interactions

# Preface

During my academic lifetime I have been in contact with several different scientific communities, including informatics, medical physics, and the physics of soft matter or magnetism. Each of these branches of science has long had a fascination with patterns, whether data ordering, memory patterns, coat patterns of animals, arrangements of molecules or spin configurations. The reason for the inexhaustible interest in the patterning on all length scales is three-fold: (i) it is recognizable and just beautiful; (ii) it is often unpredictable – that is, it contains a mystery; and (iii) any ordered structure is an encrypted message concerning the reasons for its formation. Thus, all the ingredients of a "good detective story" are at hand!

There are many exciting interpretations of this story in the literature. Most often, a tale begins with a description of a system in which a pattern has been observed, after which the mystery is lifted – at least partially – by a description of the microscopic properties of the system. Sometimes, this leads to a situation when one and the same pattern is known under diverse conditions, whilst all captivating names in different communities. Consequently, papers using different names are not cited, and phenomena are reinvented. Examples are the "micro-vortex structure", "spin ice", and "$\pi/4 \pm n\pi/2$ configuration" – three notions all of which describe a ground state of a dipolar system on a square lattice in different systems. In a rarer and more general interpretation, the analysis is started with the depiction of a pattern, which is then characterized on the basis of an order parameter. The order parameter is an abstract construction and often is not directly related to the properties of a system. This may lead to a misinterpretation of the hidden message – that is, the physical or chemical grounds for pattern formation. For example, the organization of stripes is traditionally related to the competition between attractive- and repulsive interactions. However, a stripe pattern with the same order parameter can appear in a system with two repulsive couplings, or even for a single dipolar interaction in the presence of anisotropy. Thus, in order to decrypt the puzzles posed to us by Nature, an additional generalization by the type of interactions involved would be very helpful.

This idea appeared very clearly to me following the plenary lecture given by Professor J. Kirschner at the Annual Meeting of the German Physical Society in Dresden, March 2003. Professor Kirschner has demonstrated an experimental model made from small magnets which were free to rotate on different lattices. The geometry of magnets and the model as whole has been adapted to represent pure dipolar systems. Both, the lecture and the model have attracted the vivid interest of researchers from a number of different fields. As the person responsible for construction of the model, I was confronted with diverse questions from the meeting participants with regard to interactions, lattice geometry, or the correspondence of the model to real physical systems.

This book is a systematic reply to a variety of questions addressed to me in Dresden. It is intended to serve as an introduction, for students and researchers alike, into the patterns arising in nanosystems caused by competing interactions. These interactions are classified into four main groups: (i) self-competing interactions; (ii) competition between a short- and a long-range interaction; (iii) competition between interactions on a similar length scale; and (iv) competition between interactions and anisotropy. Each class is further divided into subclasses corresponding to the localized and delocalized particles. For each subclass, concrete sets of interactions, corresponding patterns and microscopic details of systems where they appear are presented. Chapter 1 provides an introduction to modulated phases and models for their description, whilst in Chapter 6 several new advances in visualization of dynamical patterning are introduced.

The book can be read from cover to cover in order to explore the principles of self-organization and diversity of systems. However, it can be used as well in "cookbook" style – with a certain amount of cross-referencing – to obtain the recipe for structuring a particular set of interactions, lattice structure, and localization. For example, if the reader wishes to know which type of pattern appears in a spin system localized on a hexagonal lattice with antiferromagnetic first/second/third nearest-neighbor and ferromagnetic first/second/third nearest-neighbor interactions, he or she has simply to consult Chapter 4, which details the competition on a similar length scale for magnetic systems. Moreover, if the reader is interested in patterns arising in systems of moving charges or dipoles (e.g., electron gas or colloidal suspensions), he or she is referred to Chapters 2 or 3, depending on whether the short-range coupling between the particles exists.

This book is written at a fairly introductory level, for graduate or even undergraduate students, for researchers entering the field, and for professionals who are not practicing specialists in subjects such as statistical mechanics. Specialized terms are explained in the Insets, and patterns are visualized in many figures. My main aim was to write a readable text which can be understood without consulting numerous references, though for specialists in the field a vast body of literature is provided at the end of each chapter. I have also included a number of problems (with solutions provided!) at the end of each chapter for the reader to work through if he or she wishes. These problems can also be used by lecturers of applied mathematics, physics, or biology courses. Some of the problems are purely analytic, whereas others ask the reader to create a short program.

I would like to thank the editors, Michael Bär and Heike Höpcke at Wiley-VCH Verlag, not only for proposing the production of the book, but also for their help. I am grateful to many colleagues and friends for fruitful discussions and suggestions, including Roland Wiesendanger, Jürgen Kirschner, Hans Peter Oepen, Kirsten von Bergmann, Andre Kubetzka, Matthias Bode, Oswald Pietzsch, Jean-Claude Lévy, Abdel Ghazali, Kai Bongs, Mykhaylo Kurik, and Stefan Heinze. I thank Nikolai Mikuszeit for the help with programming on “Mathematica” and discussions. I also sincerely thank my family for their great patience and support during the production of this book.

Hamburg, October 2006 *Elena Y. Vedmedenko*

# 1
# Introduction

What distinguishes order from disorder? Some would argue that we experience structure as ordered only when the visual (aural) stimuli reveal patterns. If so:

- What are the physical reasons for the pattern formation?
- To what extent do the patterns observed in the world at large resemble those in the atomic world?
- What happens on the nanometer scale, in two- or even one-dimensional systems?
- Can the nanoscale patterns always be recognizable?
- What if the complexity of the patterns exceeds our powers of cognition?

In exploring these issues, I will first introduce experimental data on nano- and mesoscopic patterns, and then present the earliest theoretical models of pattern formation. We will then move on to investigate in detail the relationships between the patterns and the interactions within a material that operate on different length scales or in opposing/cooperating manners.

## 1.1
## How the Story Began

*Self-organization* describes the evolution process of complex structures where ordered systems emerge spontaneously, driven internally by variations of the system itself. One can say that self-organized systems have order for free, as they do not require help from the outside to order themselves. Although the self-organization phenomena – for example, the formation of snowflakes or the stripes of zebras or tigers – were known empirically as early as Antiquity, it was only during the twentieth century that studies on that subject become more or less systematic. The very first publications on self-organization on the micrometer scale appeared in the surface chemistry due largely to the studies of I. Langmuir and, after the turning point in surface physics, when the first low-energy electron diffraction (LEED) experiments were conducted by C. J. Davisson and L. Germer in 1927. Nevertheless, rather few experimental investigations were carried out until the 1970s, this presumably being due both to the technological complexity of the measurements and the lack of an adequate theory. During the past 20 years, however, new – apparently fundamental – patterns and superstructures on the nanometer scale have been discovered at an alarming rate. This advance was sparked in particular by the development of electron-, scanning tunneling, atomic force, friction force and magnetic force microscopies. However, despite several very good reviews [1, 2], editorial collections of articles [3, 4] and books [5–9], self-organization is still not considered to be a science in its own tight. The reason for this is that there is a very wide spectrum of scientific directions, each with their own Lexis and goals, where the ordered superstructures appear. Thus, systematization of the patterns and reasons for their formation are necessary. As a first step in this direction, Section 1.1 provides a brief review of the earliest known micrometer/nanometer scale patterns, namely modulated structures and magnetic domains. Subsequently, in Section 1.2, the answer is provided to the first question listed above, namely “What are the physical reasons for pattern formation?”

### 1.1.1

### Structure Periodicity and Modulated Phases

One is aware that many materials have an ordered structure and, indeed, the symmetry of the crystalline lattice, for example, is generally well known from X-ray experiments. These structures are very often periodic, with an ideal crystal being constructed by the infinite repetition of identical structural units in space. The philosophy of the life, however, is that all situations – the best and the worse – have their limits. All materials have surfaces, the physical properties of which differ from those of the bulk material due to the different atomic surroundings. It is said that a surface atom has a reduced (compared to the bulk material) coordination number that is nothing other than the number of nearest-neighbor atoms. But the question here is: “What type of structure should the surface atoms admit?”

During the 1920s this simple question gave rise to the new scientific directions of surface physics and chemistry. The answer was soon found, namely that as the surface atoms lost their neighbors in layers above, the surfaces are under tensile stress; that is, the surface atoms would prefer to be closer to their neighbors in the surface layer. This phenomenon, which exists in both liquid and solid materials, is known as *surface tension.* It determines the equilibrium shape of a body that is a minimum state of its surface tension. In a drop of liquid, the surface tension is isotropic, and hence the drop’s equilibrium shape is a sphere. When this drop is placed on top of a substrate the shape will usually change. In the case of a solid crystal, the answer to this question is not trivial because the surface tension is highly anisotropic. With some limitations, the surface tension of a solid or a liquid body can be calculated theoretically [10].

The existence of surface tension leads to a number of interesting structural phenomena [13]. One of these is the formation of surface domains with different atomic structure, while another is the formation of surface dislocations. In contrast to the bulk dislocations, which are linear defects inside a crystal lattice governing the plastic behavior of a material, the surface dislocations are concentrated mainly in the region beneath the topmost atomic layer (see Fig. 1.1 a). Many close-

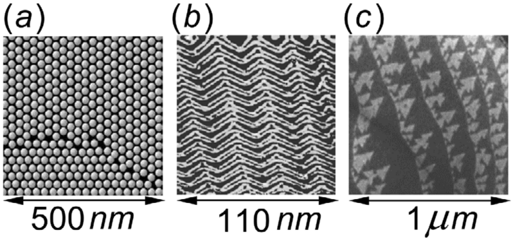

**Fig. 1.1** (a) Schematic representation of a surface dislocation. (b) Scanning tunneling microscopy (STM) image of the Au(111) reconstruction; adapted from [11]. (c) Low-energy electron microscopy (LEEM) image of the reconstruction that occurs on Si(111) surface; adapted from [12].

packed metal systems show patterns of surface dislocations, which form in order to relieve the strain between an overlayer and a bulk crystal. Indeed, the well-known herringbone reconstruction of a clean gold (111) surface [11] [see Inset 1.1 and Fig. 1.1 b] is a striking example of such a dislocation pattern, formed because the lower coordinated surface gold atoms have a closer equilibrium spacing than normally coordinated bulk gold atoms. The "herringbone" pattern of Figure 1.2 b is comprised of "double stripes", the orientation of which changes periodically. Each double stripe consists of a wide face-centered cubic (*fcc*) domain and a narrower hexagonal close-packed (*hcp*) domain, separated by domain walls where atoms sit near the bridge sites. Atoms at bridge sites are pushed out of the surface plane, and thus show up as light regions on scanning tunneling microscopy (STM) images. Hence, the stripe contains two partial misfit dislocations. To form the herringbone out of the double stripe, the stripes must bend at the "elbows". There are additional point dislocations at pointed elbows.

Another prominent example of the surface reconstruction give the reorientation of the surface atoms that occur on Si(111) surface below a temperature of 860 °C [14]. Figure 1.1 c illustrates a low-energy electron microscopy (LEEM) image of that type of reconstruction. The contrast between light and dark regions illustrates the sharp division between ordered (light) and disordered (dark) phases. Both patterns are periodic and can be usefully described in terms of larger than atomic basic structural units or modules. There exist many other complex systems which

**Inset 1.1** Crystallographic directions

Cutting and polishing a single crystal defines a certain surface. The orientation of the surface (the arrow in Fig. 1.2) with respect to the crystallographic structure is usually given by a number in brackets (Miller indices) [15]. For the gold crystal of Figure 1.1 a it was the "(111)"-surface. In this drawing, the *desired* direction of the cut is symbolized by the blue line. The *actual* cut always has a slight error (green dashed line). This results in a surface with monoatomic steps. The surfaces with a miscut are also called *vicinal surfaces.*

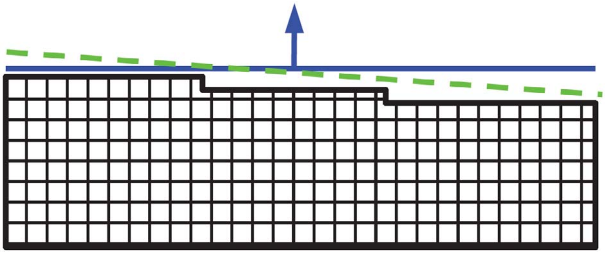

**Fig. 1.2** Single crystal with a miscut resulting in monoatomic steps. The blue arrow denotes the orientation of the ideal surface with respect to the crystallographic structure (see Inset 1.1).

may be also systematized in terms of periodic series of stacking variants of the simple subunits; these structures are often denoted as "arrays".

An important example of periodic surface structures gives thin epitaxial films and nanoscale self-assembly on solid surfaces. Epitaxial films are usually obtained by depositing of a material on top of a single crystal (substrate) on which it can be investigated. Material deposited on top of the substrate may cover it, thus forming a smooth film or so-called "islands". Whether a smooth film or islands are formed depends critically on the properties of the substrate, the deposited material, and the temperature. Remember "water on glass": if the glass is slightly dirty, the water forms a film on it; however, on fresh cleaned glass the formation of drops is favored. The islands themselves also often represent single crystals, and have an ordered superstructure. Figure 1.3 provides an example of ordered metallic epitaxially grown nanoarrays in three different systems. However, in the area of the organic and the molecular epitaxy, very successful self-assembly techniques have been also elaborated [16, 17]. Of course, there are many other nano-, meso- and macroscopic systems where the self-organized arrays can be identified. However, the aim of this section is not to provide a complete review of the modulated structures, but rather to determine how they should be described.

As could be seen, the self-organized surface structures possess certain periodicity. The periodicity has at least two length scales – that of the atomic lattice inside of the islands or domains, and that of an array. Such structures, which consist of a perfectly periodic crystal, but with an additional periodic modulation of some order parameter, are denoted as *modulated structures*. An important question is, "How the periodicity of the order parameter is related to the periodicity of the underlying bulk crystal?" If atoms or molecules are weakly bonded to a surface, the structure they adopt – even periodic – may be almost completely independent of the lattice structure of the substrate. The periodicity is then dictated almost solely by the interparticle interactions. If the adsorbed particles have a strong bonding to the surface, they may be arranged with the same lattice structure as the substrate. Often however, because of lattice mismatch or tensile strain, the overlayer has a lattice structure, which differs from

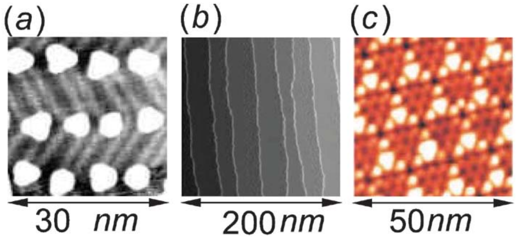

**Fig. 1.3** (a) Flat *Co* dots on the herringbone reconstructed Au(111) surface, that are obtained in the subatomic-monolayer regime; reprinted with permission from [18]. (b) STM image of the *Fe* nanowires on the W(110) surface; reprinted with permission from [19]. (c) STM image of the In/Ag alloy cluster array fabricated on Si(111)-(7×7) surface; reprinted with permission from [20].

that of substrate. If the lattice vectors of the top layer are *rationally related* to the substrate lattice vectors, such a structure is denoted as a "commensurate". In the case of an *irrational relation* between the overlayer and the substrate lattice vectors, one says that an "incommensurate" structure is formed. Many surface layers – for example herringbone reconstruction and epitaxially grown systems – adopt incommensurate structures, and consequently the questions arise:

- Are the modulated structures – and particularly incommensurate configurations – thermodynamically stable, or are these some disturbed, metastable states?
- What is the physical mechanism underlying the formation of modulated phases?

These questions will be answered in Section 1.2.1.

### 1.1.2
### Ferromagnetic and Ferroelectric Domains

Materials whose atoms carry strong magnetic/electric moments are called *ferromagnets* and *ferroelectrics*, respectively. Many different substances demonstrate ferromagnetic and/or ferroelectric properties. For example, iron, nickel, cobalt and some of the rare earth metals (e.g., gadolinium, dysprosium) exhibit ferromagnetism, with iron (ferric) being the most common and most dramatic example. Samarium and neodymium in alloys with cobalt are used to fabricate very strong rare-earth magnets. Among the different ferroelectrics, oxides showing a perovskite or a related structure are of particular importance.

Ferromagnetic/ferroelectric materials possess their properties not only because their atoms carry a magnetic/electric moment, but also because the material is composed of small regions known as magnetic/ferroelectric domains. The concept of domains was first introduced by Weiss, in his famous study [21].

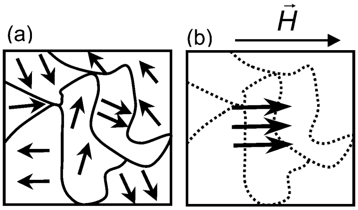

**Fig. 1.4** (a) Weiss domains, the total magnetization of the sample is zero. (b) The domains are aligned under the action of the external magnetic field *H*; the total magnetization has a finite value.

In each domain, all of the atomic dipoles are coupled together in a preferential direction (see Fig. 1.4). This alignment develops during solidification of a crystal from the molten state, during an epitaxial growth, or during the ordering of a liquid mixture. Ferromagnetic materials are said to be characterized by "spontaneous" magnetization as they obtain saturation magnetization in each of the domains without an external magnetic field being applied. Even though the domains are magnetically saturated, the bulk material may not show any signs of magnetism because the domains are randomly oriented relative to each other (Fig. 1.4 a). Ferromagnetic materials become magnetized when the magnetic domains are aligned (Fig. 1.4 b); this can be done by placing the material in a strong external magnetic field, or by passing electrical current through the material. The more domains that are aligned, the stronger the magnetic field in the material. When all of the domains are aligned, the material is said to be saturated, and no additional amount of external magnetization force will cause an increase in its internal level of magnetization. At the start of the 20th century the domains were introduced only as an abstract construction to explain:
- that below the critical temperature, the total magnetization of a magnet is not the same as its saturation magnetization;
- that a permanent magnet can be made from a ferromagnetic material by applying a magnetic field;
- the hysteresis and necessity for a coercive field to remove any net magnetization;
- the zero average magnetization and non-zero local magnetization of a ferromagnet [22].

Despite this very useful phenomenological theory of magnetic domains, the mechanism of the domain formation remained obscure until the 1930s.

In the seminal report by Landau and Lifshitz in 1935 [24], the domains were proposed to originate from the minimization of the magnetostatic energy stemming from the dipolar interaction. Since then, a wide variety of two-, three- and even one-dimensional physical-chemical systems, which display domain patterns in equilibrium [2], has been found. Among these are ferroelectrics [25], liquid crystals [26], block-copolymers [26], ferrofluids [27], Langmuir layers [28], superconductors [29], and other related systems. The domains can have peri-

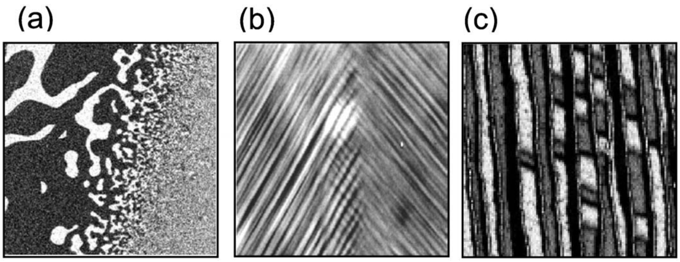

**Fig. 1.5** (a) Scanning electron microscope with polarization analysis (SEMPA) images of magnetic domain structures in a wedge-shaped Co/Au(111) film; reprinted with permission from [31]. Dark and light regions represent areas of antiparallel magnetization. The smallest domain size is 300 nm. (b) Typical fragment of a domain pattern in electrically poled along the [001] direction ferroelectic $Pb(Mg_{1/3}Nb_{2/3})O_{3-x}PbTiO_2$ crystal observed in a polarizing microscope; adapted from [23]. The typical domain size is 20 μm. (c) STM image of the magnetic domains (dark and light gray areas) and domain walls (black lines) in Fe/W(110) nanowires; reprinted with permission from [19]. The typical domain size is 20 nm.

odic, random or incommensurate superstructure. Nowadays, nanometer-sized magnetic [19, 30, 31] and ferroelectric [23] domains, which cannot be expected from the original theoretical concepts, have been discovered (Fig. 1.5). The explanation of the origin of those domain nanopatterns requires new theoretical concepts, which will be addressed in Section 1.2.2.

## 1.2
## First Theoretical Approaches for Competing Interactions

### 1.2.1
### Frenkel–Kontorova Model

One of the earliest theories of a system with competing length scales is known as the Frenkel–Kontorova (FK) model. This was introduced more than half a century ago [32, 33] in the theory of dislocations in solids to describe the sim-

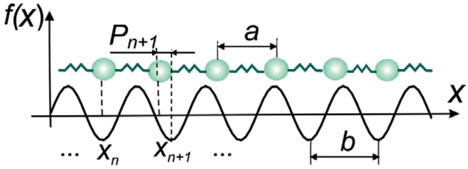

**Fig. 1.6** Schematic representation of the Frenkel–Kontorova model. The balls represent surface atoms bonded with neighboring atoms by the interatomic interactions (Hook's springs of natural length *a*) and with the substrate through the potential *V* (solid black line) of periodicity *b*.

plest situation when the surface atomic layer is assumed to contain a dislocation (see Fig. 1.1). Subsequently, this model has been used extensively for the modeling of nonlinear dynamical processes in a variety of condensed matter [34, 35] and biophysical [36] systems. As the FK model captures the essential physics of many different problems, it is broadly used in present-day research investigations into metal surfaces [37, 38], atomic friction [39, 40], biological [41, 42] and quantum [43] systems.

The surface layer in the FK approach is modeled by a chain of balls (atoms) connected by harmonic Hook's springs of natural length $a$ and stiffness $k$. The bottom solid is assumed to be rigid, so that it can be treated as a fixed periodic substrate potential $V$ (Fig. 1.6) – that is, the surface/interface part of a crystal can be sheared with respect to the bulk material.

**Inset 1.2** Solitons

The word "soliton" was first used to describe nonlinear waves interacting as particles [44]. In fact, the term soliton almost became "solitRon", as an abbreviation for the "solitary wave", but at the time a company was trading with the identical name, and hence the 'r' had to be removed. The history of studying solitons began in August 1834, when the Scottish engineer John Scott Russell observed a large solitary wave in the Union Canal near Edinburgh. In the days of Russell there were many debates concerning the very existence of that type of solitary wave, but today many complex dynamic systems throughout science are known to possess soliton solutions: from hydrodynamics to nonlinear optics; from plasmas to shock waves; from tornados to the Great Red Spot of Jupiter; from the elementary particles of matter to the elementary excitations.

The physics of the model is determined by competition between the elastic energy, which favors incommensurate (see Section 1.1.1) separation between atoms, and the tendency for the atoms to sit at the bottom of potential wells, leading to a commensurate structure. The competition can lead to an interesting situation when the surface atoms are neither ordered (as at the top of Fig. 1.1 a) nor disordered (as beans spilled upon a table), but rather form a nontrivial pattern of assembled atoms. The exciting question here is what this pattern should look like, and how it depends on the parameters of the FK model.

The periodic force of the substrate has the form (Fig. 1.6) $f(x) = V_0 \sin\left(\frac{2\pi x}{b}\right)$, $V_0$=const. The elongation of the string from its natural length $a$ is $x_n - x_{n-1} - a$ and, consequently, the Hook's force between two neighboring atoms (Fig. 1.6) is $f_H(x) = -k(x_n - x_{n-1} - a) = -k(x_{n+1} - x_n - a)$.

The potential energy corresponding to a conservative force $F(x)$ is known to be $U(x) = -\int_{x_0}^{x} F(x)dx + U(x_0)$. As $f(x)$ and $f_H(x)$ are not path-dependent they are conservative. Hence, if $U(x_0) = 1$, the energy of a configuration $U(x)$ or, in other words, the Hamiltonian of the whole systems can be written as

$$H = \sum_n \left[ \frac{1}{2} k (x_{n+1} - x_n - a)^2 + V(1 - \cos(2\pi x_n / b)) \right] \tag{1.1}$$

with $V = V_0 \cdot 2\pi/b$ the amplitude of the potential. It is helpful to introduce a phase $P_n$, which measures the position of the atoms relative to the minima of the potential (Fig. 1.6). $P_n$ can be either positive or negative. Then, the atomic coordinate is defined by:

$$x_n = nb + bP_n/2\pi\,, \tag{1.2}$$

$$\cos(2\pi x_n/b) = \cos(2\pi n + P_n) = \cos P_n \tag{1.3}$$

and the elongation of a string between $n$ and $n$–1 balls becomes

$$x_n - x_{n-1} - a = P_n - P_{n-1} - 2\pi \cdot (a - b)/b\,. \tag{1.4}$$

The expression $d = 2\pi \cdot (a - b)/b$ measures the misfit between two competing length scales $a$ and $b$; $P_n - P_{n-1}$ gives the mismatch between the equilibrium positions of the atoms and the periodicity of the cosine potential (i.e., it represents the heart of the problem).

For a strong interatomic potential $k \gg 1$ in Eq. (1.1) the displacement of atoms from the corresponding potential minima is a smooth function of the coordinate and can be treated in continuum limit

$$P_n - P_{n-1} = dP/dn\,. \tag{1.5}$$

With (1.5) the equation (1.1) transforms to

$$H = \int \left\{ \left( \frac{dP}{dn} - d \right)^2 /2 + V(1 - \cos P) \right\} dn\,. \tag{1.6}$$

Minimization of the energy $H$ is equivalent to finding a solution of

$$\partial^2 P/\partial n^2 = V \sin P\,, \tag{1.7}$$

which is the one-dimensional sine-Gordon equation, a special case of the time-dependent sine-Gordon equation $\frac{\partial^2 P}{\partial t^2} + \frac{\partial^2 P}{\partial n^2} = V \sin P$ with $t$ – the time.

**Inset 1.3** Numerical approximation of the sine-Gordon equation

$$\frac{\partial^2 u}{\partial t^2} - \frac{\partial^2 u}{\partial x^2} + \sin(u(x,t)) = 0$$ using difference equations

1) Defining of the coordinate-time rectangle (see sketch below);
2) $u_{ij} = u(x_i, t_j)$ ;

3) $\dfrac{\partial^2 u(x,t)}{\partial t^2} = \dfrac{u_{i,j+1} - 2u_{i,j} + u_{i,j-1}}{\Delta t^2}$

4) $\dfrac{\partial^2 u(x,t)}{\partial x^2} = \dfrac{u_{i+1,j} - 2u_{i,j} + u_{i-1,j}}{\Delta x^2}$

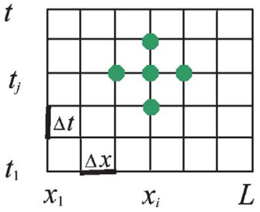

5) $r = \dfrac{\Delta t}{\Delta x}$
initial position function $u_{i,1} = f(x_i)$
1st derive velocity function $u^t_{i,1} = g(x_i)$

6) $u_{i,2} = f(x_i)(1 - r^2) + g(x_i)\Delta t + \dfrac{r^2}{2}(f(x_{i+1}) + f(x_{i-1})) - \sin(f(x_i))$

$$u_{i,j+1} = f(x_i)(2 - 2r^2) + g(x_i)\Delta t + r^2(u_{i+1,j} + u_{i-1,j}) - \sin(u_{i,j})\Delta t^2$$

For further details see [45].

Solutions of that equation are known from mathematics and physics of nonlinear phenomena [46]. The simplest are the “kink” (the black curve at the top of Fig. 1.7) and the “anti-kink” (the black curve at the bottom of Fig. 1.7) solitons (see Inset 1.2). A kink is a solution whose boundary value at the left infinity is 0 ($-\pi$), and at the right infinity is $2\pi$ ($+\pi$); the boundary values of an anti-kink are 0 ($+\pi$) and $-2\pi$ ($-\pi$), respectively (black curves in Fig. 1.7). Physically, this means that the atomic displacement from the position of a potential well $P_n$ is 0 or $2\pi$ at the boundary – that is, the atoms are placed in the wells. These are all light-blue atoms in Figure 1.7. Inside of the kink (anti-kink), the displacements $P_n$ are different as from both 0 and $2\pi$; these are the dark-blue atoms in Figure 1.7. In our case, the kink describes a vacancy in the chain (as in Fig. 1.7, top), while the anti-kink corresponds to excess particles (as in Fig. 1.7, bottom). Thus, the kink-solutions model two simplest types of dislocations.

For a weak interatomic potential $k<1$ (see Eq. (1.1)) the kink becomes very narrow and, therefore, essentially discrete. As a matter of fact, only very few atoms lying near the center of the kink (anti-kink) have different from 0 or $2\pi$ displacements $P_n$. In that case, Eq. (1.1) must be solved discretely. To do so, one rewrites the elongation of a string (see Eq. (1.4)) as

$$x_{n+1} - x_n - a = x_{n+1} - x_n - (x_n - x_{n-1}) = x_{n+1} - 2 \cdot x_n + x_{n-1} \tag{1.8}$$

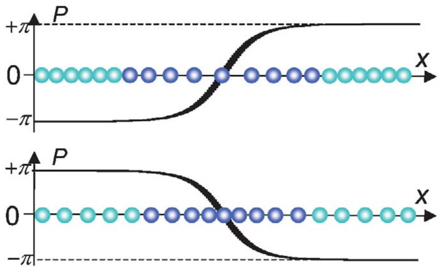

**Fig. 1.7** Schematic representation of the "kink" (top of the figure) and "antikink" (bottom of the figure). While the balls show real space displacements of the atoms, the black curves correspond to the function $P_i=f(x)$, where $P_i$ is displacement of the $i$-th atom.

and Eq. (1.1) as

$$H = \sum_n \left[ \frac{1}{2} k (x_{n+1} - 2 \cdot x_n + x_{n-1})^2 + V(1 - \cos(2\pi x_n / b)) \right] . \tag{1.9}$$

The right-hand part of Eq. (1.8) is nothing else than the central difference approximation to the second-order derivative, and can be solved numerically (see Inset 1.3 and Exercise 1). The FK problem in the discrete case is more complicated than the previous one, as it may have unstable solutions [45]. For different boundary conditions and different parameters of the model, more complicated solutions than a simple kink exist. These are sequences of kinks or anti-kinks – that is, the lattice of domain and domain walls is formed (Exercise 1). As the kinks-series is similar to stairs, it had become a rather colorful name: the "devil's staircase" (see Exercise 1). Besides this unusual name, this result leads to a very important conclusion – that the perfect crystal ordering is not always the most stable! Over a certain range of temperatures, pressures, etc., crystals or crystal surfaces can spontaneously exhibit a periodic modulation which is not always a rational combination of the natural periods of the crystal. Examples of such a configuration are shown in Figures 1.1 b, 1.6 and 1.7.

### 1.2.2
### Theoretical Models of the Magnetic/Ferroelectric Domains

The term "domains" can be used in different contexts. In Section 1.1.1, this notation was used to describe those regions of a crystal with different atomic structures. In the context of the present section, however, a crystalline structure is the same everywhere, while the orientation of spontaneous polarization in different domains is different. Although the complete mechanism of the formation of magnetic/ferroelectric domains is rather complex, the main principles can be understood on the basis of phenomenological conception of the exchange and the dipolar energy. Therefore, although in the next section I will provide a basic notion of these energies, they will be described in more detail in the following chapters.

#### 1.2.2.1 **Phenomenology of the Dipolar Interaction**

In the first approximation, a magnet or a ferroelectric can be successfully treated as an ensemble of atomic magnetic or electric moments (dipoles). Each dipole can be modeled as a pair of magnetic/electric charges of equal magnitude but opposite polarity, or as an arrow representing the direction of a moment. The moments are known to align themselves in an external magnetic or electric field (just as a compass needle in the magnetic field of the Earth). As every moment itself is a source of a field (Fig. 1.8), it can be aligned in the field of any other dipole and vice versa – that is, the moments interact. The space distribution of the field produced by a dipole is nonlinear. The strength of magnetic or electric field is a vector quantity; it has both magnitude and direction, and is also rather weak. The strength of a dipolar interaction between two dipoles is of order of few degrees Kelvin. The magnitude of the dipole field decreases with distance as $1/r^3$, while its direction depends on the relative positions and orientations of atomic moments (Fig. 1.8). As a crystal consists of milliards of atoms, each atomic dipole experiences the action of milliards of fields with different direction and amplitude coming from all other dipoles (see Fig. 1.8). The total field acting on a moment can be determined as a vector superposition of all atomic fields. Because of the long-range character and position-dependence of the field distribution, a low-energy configuration of a pure dipolar ensemble is fairly difficult to predict. Some of the striking features of the dipolar coupling, however, can be derived even on the basis of school-level physics.

It is widely known that opposite charges attract whilst unlike charges repel each other, or that two bar magnets are attracted the North to the South pole. Why is this? Two separate magnets have two South and two North poles – together, four uncompensated poles. But two coupled bar magnets have only one South and one North pole – the other two poles are compensated. Hence, by means of attraction, the so-called surface charges – that is, the charges on an open surface – are minimized. The surface charge minimization leads to the de-

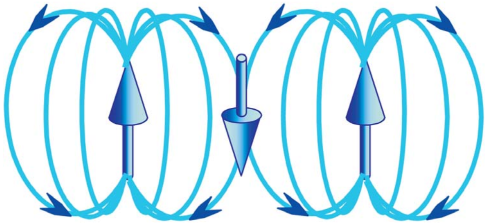

**Fig. 1.8** An energetically favorable orientation of a dipole in the field of two other dipoles.

crease of the magnetic/electric field and, hence, to a decrease in the total energy. Thus, one of the main features of dipolar interaction is that this coupling attempts by all means to avoid free poles. This feature, which is referred to as the "pole avoidance principle" [47], is very important when explaining domain formation.

#### 1.2.2.2 **Phenomenology of the Exchange and Exchange-Like Interactions**

As the dipolar interaction is rather weak it cannot serve as a reason for spontaneous magnetization or polarization at room temperature. Hence, aside from the dipolar coupling, there should exist another, much stronger coupling, and for a magnet this is the quantum mechanical exchange interaction. Without going into details, the exchange coupling between two neighboring magnetic ions will force the individual moments into either parallel (ferromagnetic) or antiparallel (antiferromagnetic) alignment with their neighbors. Such coupling is very strong (of the order of $10\ldots10^3$ K), but is of short range – that is, it decreases rapidly as the ions (atoms) are separated. The direct exchange interaction in its simplest form can be described by the Heisenberg Hamiltonian [48]:

$$H_{\mathrm{ex}} = -2J \sum_{\langle i,j \rangle} \mathbf{S}_i \cdot \mathbf{S}_j$$

where $J$ is the exchange coupling constant which is non-zero only for nearest neighbor spins $S$. For a ferromagnet, $J$ is positive, that is $H_{\mathrm{ex}}$ has its minimum for parallel spins; however, for an antiferromagnet $J$ is negative and $H_{\mathrm{ex}}$ has its minimum for antiparallel spins.

A ferroelectric crystal is a crystal which exhibits an electric dipole moment even in the absence of an external electric field. The spontaneous ferroelectric polarization arises due to distortion of the primitive crystal cell inducing the displacement of positive and negative ions with respect to each other. The charge displacement leads to the formation of strong molecular dipoles oriented along certain crystallographic directions. If it is possible to reorient the spontaneous polarization of a material between crystallographically equivalent states (so-called "variants") by an external electric field; then, in analogy to ferromagnets, one speaks about ferroelectrics. In ferroelectrics, nearest neighboring moments prefer to be collinear, as a non-collinear configuration requires changes in the geometry of neighboring crystalline cells that would produce a huge strain in the crystal. Thus, elastic strain energy in ferroelectrics acts similarly to ferromagnetic exchange [25, 49, 50]. As in the case of magnetism, the electric dipoles may also orient themselves in an antiparallel fashion, in which case the associated dipoles create an antiferromagnetic order. Two types of the ferroelectric order are shown schematically in Figure 1.9.

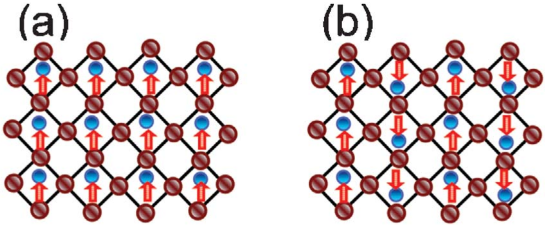

**Fig. 1.9** Schematic diagram of (a) a ferroelectric and (b) an antiferroelectric with perovskite structure. The brown circles represent the sublattice with positive charges; the blue dots are negative ions. The red arrows show the direction of electric polarization of a cell. The polarization arises due to the displacement of negative charges from the center of an atomic cell.

#### 1.2.2.3 **Mechanism of the Domain Formation**

It was highlighted in Section 1.2.2.1 that the dipolar interaction is very weak compared to the exchange coupling or strain. However, the exchange interaction is quite short-ranged, whereas the dipolar interaction is not. As a result, the total dipolar energy becomes significant when enormous numbers of dipoles are involved, and can compete with the stronger exchange coupling. In particular, a uniformly magnetized configuration such as that in Figure 1.4 b or Figure 1.9 a is highly uneconomical in terms of dipolar energy as it has fully uncompensated surfaces. The poles at the surface can be avoided and, thus, the dipolar energy substantially reduced by dividing the specimen into uniformly magnetized domains, the magnetization vectors of which point in opposite or widely different directions. Such a subdivision is paid for in exchange energy, since near the boundary of two domains the neighboring moments will have a rather large mutual angle. However, the region where non-collinearity occurs is very narrow because of the short range of the exchange interaction. In contrast, the gain in dipolar energy of every dipole drops when the domains are formed. Therefore, provided that the domains are not too small compared to the boundary between them (the so-called domain wall), domain formation will be favored. Thus, a lowering of the dipolar energy of the whole sample will compensate for the rise in exchange energy in the domain walls.

There are many different types of domains and domain walls. In the simplest case, the magnetization in domains have antiparallel orientation, and consequently the moments in the two domains always lie in equivalent crystallographic directions. Such domains are separated by the so-called 180° domain walls, which occur in virtually all materials and are distinct from all other non-180° walls in that they are not affected by stress [51]. The 180° walls can be also of different type, depending on the manner in which the magnetization rotates between two stable orientations. A comprehensive description of magnetic walls for beginners is provided by Jiles [52], while a more in-depth study is provided by Hubert and Schäfer [53]. In many cases, the so-called Bloch wall – where

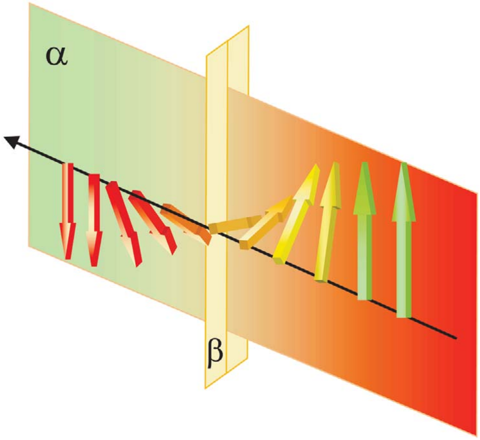

**Fig. 1.10** Schematic representation of a Bloch domain wall.

magnetic moments rotate in the plane perpendicular to that of the stable magnetization in domains (Fig. 1.10) – has a lowest possible energy. The period of magnetization rotation in that simple case is $2\pi$ and is, usually, a multiple of a lattice constant (Fig. 1.10); that is, it has a commensurate structure. In some more complicated cases, however, so-called helical or "spin-wave"-like magnetic structures can occur [54]. In such structures the domains pass smoothly one into another, and the magnetization rotates in a helicoidal form along certain crystallographic directions. One can visualize a helical structure as an infinite sequence of Bloch walls. For such a structure, the period of rotation of the magnetization is not necessarily a rational multiple of the lattice constant as the beginning of a period can lie in-between two atomic sites.

Thus, in addition to atomic incommensurability, incommensurate magnetic structures can also appear.

## 1.3
## Summary

Now, we are able to answer the question that was posed in Section 1.1 concerning the *physical reasons for the pattern formation*. The self-organization of subunits of different nature – whether atomic or magnetic/electric – into ordered patterns is due to the competing interactions. The competition between different energies often leads to the spontaneous formation of modulated structures, the period of which is not always a rational combination of the natural periods of the crystal. For certain range competing energies, incommensurate phases appear.

## 1.4
## Exercises

1. Check numerically that Eq. (1.10) really gives a “devil staircase” of kinks or anti-kinks in a one-dimensional system.

*Solution*

Listed below (see Fig. 1.11), Mathematica Notebook permits us to solve numerically a one-dimensional (no time-dependence) sine-Gordon equation (Eq. 1.7). In this simple example, Neumann-like boundary conditions are used. The first two values $u_0$, $u_1$ of the function $u$ are fixed, while the next $n$ values are calculated using difference equations method (see Inset 1.3).

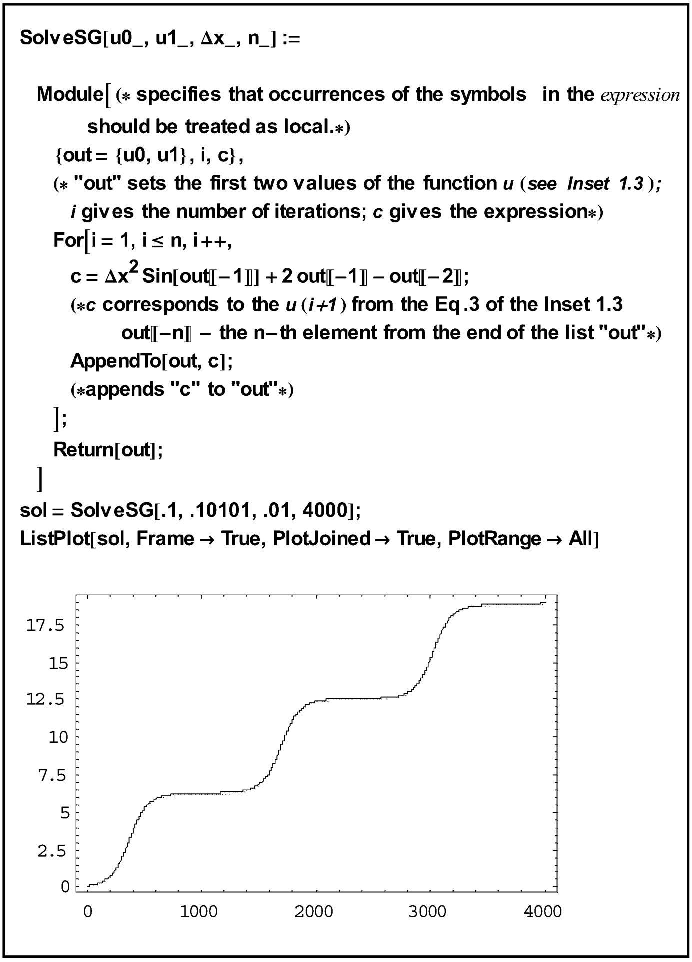

```
SolveSG[u0_, u1_, Δx_, n_] :=

  Module[(* specifies that occurrences of the symbols  in the expression
        should be treated as local.*)
   {out = {u0, u1}, i, c},
   (* "out" sets the first two values of the function u (see Inset 1.3);
     i gives the number of iterations; c gives the expression*)
   For[i = 1, i ≤ n, i++,
     c = Δx^2 Sin[out[[-1]]] + 2 out[[-1]] - out[[-2]];
     (*c corresponds to the u(i+1) from the Eq.3 of the Inset 1.3
           out[[-n]] - the n-th element from the end of the list "out"*)
     AppendTo[out, c];
     (*appends "c" to "out"*)
   ];
   Return[out];
  ]
sol = SolveSG[.1, .10101, .01, 4000];
ListPlot[sol, Frame → True, PlotJoined → True, PlotRange → All]
```

Fig. 1.11 The Mathematica Notebook.

2. Decreases or increases the number of domains/domain walls with increasing strength of the dipolar interaction relative to the strength of the exchange coupling?

*Solution*
The number of domains increases as with decreasing exchange interaction the energy losses due to the formation of domain walls become smaller.

3. The paradigm of a periodic function is the trigonometric function sin($x$), which is periodic with period $2\pi$, i.e., $\sin(x + 2\pi) = \sin(x)$. Consider the sum of two sine functions

$$f(x) = \sin(x) + \sin(cx) = 2\sin\left(\frac{1+c}{2}x\right)\cos\left(\frac{1-c}{2}x\right)$$

where $c$ is some fixed number. Is the function $f(x)$ always periodic? For which $c$ the function $f(x)$ is aperiodic?

*Solution*
The periodicity depends on the values of $c$. If $c$ is a rational number, $c = m/n$ with coprime integers $m$ and $n$ then the periods $2\pi$ (for sin($x$)) and $2\pi c = 2/n$ (for sin($cx$)) are commensurate, and the function is periodic with period as $2\pi n$ as $\sin[c(x + 2\pi n)] = \sin(cx + 2\pi m) = \sin(cx)$. However, if $c$ is irrational, e.g., $c = \sqrt{2}$, the two frequencies are incommensurate, and $f(x)$ is aperiodic. Still, $f(x)$ retains much of its regularity – after all, it is simply the sum of two sine functions. It shows a so-called superstructure. Several examples of such superstructures have been provided in Sections 1.1.1 and 1.2.1. Another comprehensible example of the incommensurable structures is provided in [55].

## References

1 C. Bowman, A.C. Newell, *Rev. Mod. Phys.* **1998**, *70*, 289.
2 M. Seul, D. Andelman, *Science* **1995**, *267*, 476.
3 R. LeSar, A. Bishop, R. Heffner (Eds.) *Competing Interactions and Microstructures: Statics and Dynamics,* Springer Proceedings in Physics, Vol. 27, Springer, **1988**.
4 H.T. Diep (Ed.) *Magnetic Systems with Competing Interactions*, World Scientific Pub. Co., Singapore, **1994**.
5 D. Tompson, *On Growth and Form*, Cambridge University Press, Cambridge, **1961**.
6 S.A. Kauffmann, *The Origins of Order: Self-Organization and selection in Evolution*, Oxford University Press, Oxford, **1993**.
7 S. Camazine, J.-L. Deneubourg, N.R. Franks, J. Sneyd, G. Theraulaz, E. Bonabeau, *Self-Organization in Biological Systems*, Princeton University Press, Princeton, **2001**.
8 P. Ball, *The Self-made Tapestry: Pattern formation in Nature*, Oxford University Press, Oxford, **1998**.
9 P. Ball, *Designing the Molecular World*, Princeton University Press, Princeton, **1994**.

10 L. D. Landau, E. M. Lifshitz, *Statistical Physics*, Chapter 15, Pergamon, London, **1958**.

11 S. Rousset, V. Repain, G. Baudot, Y. Garreau, J. Lecoeur, *J. Phys.: Condens. Matter* **2003**, *15*, S3363.

12 W. Telieps, E. Bauer, *Ber. Bunsenges. Chem. Phys.* **1986**, *90*, 197.

13 H. Lüth, *Surfaces and Interfaces of Solid Materials*, 3rd edn., Springer, Berlin, **1995**.

14 W. Telieps, E. Bauer, *Surface Science* **1988**, *200*, 512.

15 C. Kittel, *Introduction to Solid State Physics*, 2nd edn., John Wiley & Sons, New York, **1956**.

16 G. P. Lopinski, D. D. M. Wayner, R. A. Wolkow, *Nature* **2000**, *406*, 48.

17 M. Eremtchenko, J. A. Schaefer, F. S. Tautz, *Nature* **2003**, *425*, 602.

18 O. Fruchart, M. Klaua, J. Barthel, J. Kirschner, *Phys. Rev. Lett.* **1999**, *83*, 2769.

19 M. Bode, O. Pietzsch, A. Kubetzka, S. Heinze, R. Wiesendanger, *Phys. Rev. Lett.* **2001**, *86*, 2142.

20 J.-L. Li, J.-F. Jia, X.-J. Liang, X. Liu, J.-Z. Wang, Q.-K. Xue, Z.-Q. Li, J. S. Tse, Z. Zhang, S. B. Zhang, *Phys. Rev. Lett.* **2002,** *88*, 66101.

21 P. Weiss, *J. de Physique et le Radium* **1907**, *6*, 661.

22 C. L. Dennis, R. P. Borges, L. D. Buda, U. Ebels, J. F. Gregg, M. Hehn, E. Jougulet, K. Ounadjela, I. Petej, I. L. Prejbeanu, M. J. Thornton, *J. Phys.: Condens. Matter* **2002**, *14*, R1175.

23 A. A. Bokov, Z. G. Ye, *J. Appl. Phys.* **2004**, *95*, 6347.

24 L. D. Landau, E. M. Lifshitz, *J. Phys. USSR* **1935**, *8*, 153.

25 D. Richter, S. Trolier-McKinstry, Ferroelectrics. In: *Nanoelectronics and Information Technology*, Waser, R. (Ed.), Wiley-VCH, Weinheim, **2003**.

26 E. N. Thomas, T. Witten, *Physics Today* **1990**, *21*, 21.

27 R. E. Rosenzweig, *Ferrohydrodynamics*, Cambridge University Press, Cambridge, **1985**.

28 P. Muller, F. Gallet, *J. Phys. Chem.* **1991**, *95*, 3257.

29 L. D. Landau, *J. Phys. USSR* **1943**, *7*, 99.

30 O. Pietzsch, A. Kubetzka, M. Bode, R. Wiesendanger, *Science* **2001**, *292*, 2053.

31 M. Speckmann, H. P. Oepen, H. Ibach, *Phys. Rev. Lett.* **1995**, *75*, 2035.

32 J. Frenkel, T. Kontorova, *Z. Sowjetunion* **1938**, *13*, 1.

33 F. C. Frank, J. H. van der Merwe, *Proc. R. Soc. Ser. A* **1948**, *198*, 205.

34 S. Aubry, in: *Solitons in Condensed Matter Physics*, A. R. Bishop, T. Schneider (Eds.), Springer, Berlin, **1978**, p. 264.

35 M. Peyrard, M. D. Kruskal, *Physica D* **1984**, *14*, 88.

36 For a review see, e.g., L. V. Yakushevich, *Physica D* **1994**, *79*, 77.

37 R. Pushpa, S. Narasimhan, *Pure Appl. Chem.* **2002**, *74*, 1663.

38 J. C. Hamilton, R. Stumpf, K. Bromann, M. Giovanni, K. Kern, H. Brune, *Phys. Rev. Lett.* **1999**, *82*, 4488.

39 M. O. Robbins, M. H. Müser, Computer simulations of friction, lubrication and wear. In: *Handbook of Micro/Nano Tribology*, B. Bhushan (Ed.), CRC Press, Boca Raton, FL, **2001**, pp. 717–765.

40 L. Consoli, H. J. F. Knops, A. Fasolino, *Phys. Rev. Lett.* **2000**, *85*, 302.

41 I. M. Kuli, H. Schiessel, *Phys. Rev. Lett.* **2003**, *91*, 148103.

42 S. L. Shumway, J. P. Sethna, *Phys. Rev. Lett.* **1991**, *67*, 995.

43 B. Hu, B. Li, *Europhys. Lett.* **1999**, *46*, 655.

44 N. J. Zabusky, M. D. Kruskal, *Phys. Rev. Lett.* **1965**, *15*, 240.

45 S. J. Farlow, *Partial Differential Equations for Scientists and Engineers*, Wiley-VCH, Weinheim, **1982**.

46 I. N. Bronstein, K. A. Semendjajew, *Taschenbuch der Mathematik*, B. G. Teubner Verlagsgesellschaft, Stuttgart and Nauka, Moskau, **1991**.

47 W. F. Brown, Magnetostatic principles in ferromagnetism. In: *Selected Topics in Solid State Physics*, Vol. 1, E. P. Wohlfarth (Ed.), North-Holland Publishing Company, Amsterdam, **1962**.

48 N. W. Ashcroft, N. D. Mermin, *Solid State Physics*, Holt-Saunders International Editions, New York, **1976**.

49 R. J. Elliot, in: *Structural Phase Transitions and Soft Modes*, E. J. Samuelson, E. Andersen, J. Feder (Eds.), Universitetsforlaget, Oslo, **1971**, p. 235.

**50** R. B. Stinchcomb, *J. Phys. C* **1973**, *6*, 2459, 2484, 2507.

**51** S. Chikazumi, *Physics of Magnetism*, Wiley, New York, p. 192.

**52** D. Jiles, *Introduction to Magnetism and Magnetic Materials*, Chapman & Hall, London, **1991**.

**53** A. Hubert, R. Schäfer, *Magnetic Domains: The analysis of magnetic microstructure*, Springer, Berlin, **2000**.

**54** E. Y. Vedmedenko, H. P. Oepen, A. Ghazali, J. C. Lèvy, J. Kirschner, *Phys. Rev. Lett.* **2000**, *84*, 5884.

**55** U. Grimm, M. Scheffer, Incommensurate crystals and quasicrystals. In: *Encyclopedia of Physical Science and Technology*, R. Meyers (Ed.), Elsevier Science Ltd, New York, **2001**.

# 2
# Self-Competition: or How to Choose the Best from the Worst

As has been demonstrated in Chapter 1, one possible reason for the self-organization of subunits into ordered patterns is due to competing interactions. Two striking examples of such structures – dislocation arrays and magnetic domains – were described in Sections 1.1 and 1.2. In both cases ordered patterns were seen to arise from the competition between two or more *different* couplings. Sometimes, however – as strange it may seem – *identical* subunits coupled via *one single interaction* can also compete with each other and form due to this competition non-trivial, ordered configurations. The reason for the self-competition is what is often called a "frustration effect".

## 2.1
## Frustration: The World is not Perfect

The word "frustration" is familiar to everyone – even to those who are unconcerned with physics! In a common sense, frustration means a general mood of listlessness – "because anyhow everything runs wrong". Frustration is a natural part of all problem-solving, whether it be physics problems, relational problems, or mechanical problems. In physics, the term "frustration" was first introduced in 1977 by Toulouse [1], and has a very similar meaning: it is the inability to satisfy fully all interactions. The challenge is to optimize the situation by making a compromise. Frustration occurs in many physical, chemical and biological systems owing to a variety of microscopic mechanisms:

- competing long-range interactions;
- geometry of the lattice; and
- competition between random ferro- and antiferromagnetic exchange interactions.

In this chapter I will concentrate on the most frequently addressed form in the literature, namely geometric frustration.

The phenomenon of geometric frustration is simple and fundamental. It can be applied to different interactions, and is present in a variety of physical systems such as magnets, liquid crystals, protein structures, or Josephson junction arrays [2]. One very simple example of local geometrical frustration is the ar-

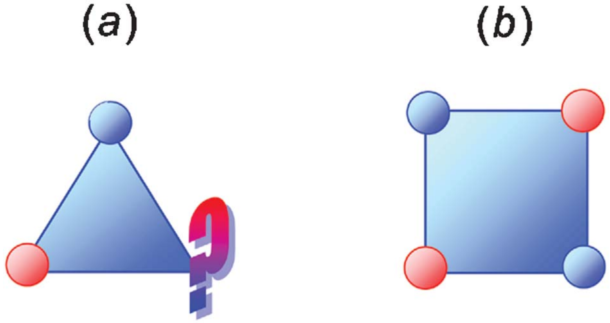

**Fig. 2.1** Triangle (a) and square (b) building blocks of two-dimensional crystals. The red and blue balls represent atoms or magnetic moments of different sort coupled by antiferromagnetic-like, short-range interactions. The interactions favor opposite alignment of neighboring units. This is not possible on a triangle (a), but it can be easily achieved on a square (b).

rangement of three identical units on an equilateral triangle (Fig. 2.1 a). The units are constrained to have one of two opposite properties (black/white, up/down, on/off, etc.), and the energy of the interaction between any two units is minimized if the two nearest neighbors on the triangle have different states. All three elements, however, can by no means have different states, and two out of three units will necessarily have the same property (Fig. 2.1 a). Hence, the energy of the system cannot be entirely minimized. There exist six possible configurations of equal energy with, for example, two units up and one down, or vice versa. Hence, the system is seen to be hesitating between those six configurations or, in other words, it is *frustrated*. If four such elements were to be placed on a square, all nearest neighbors could be in opposite states (Fig. 2.1 b), whereupon such a configuration is said to be *unfrustrated*. Almost all geometrically frustrated systems can be easily mapped onto an array of magnetic moments with the antiferromagnetic coupling (see Section 1.2.2.2), requiring an antiparallel alignment of neighboring spins. Therefore, the following description of the frustration effects will be based mainly on models with antiferromagnetic interactions.

## 2.2
## Why is an Understanding of Frustration Phenomena Important for Nanosystems?

Today, the physical properties of bulk materials are quite well understood. The game rules are clear and concise: bcc Fe is a prototypical ferromagnet, while bcc Cr is a prototypical antiferromagnet. In order to alter the properties of a material one needs either to change a structure (e.g., transform a bcc into an fcc crystal [3, 4]), or a chemical composition (e.g., to create an alloy). However, artificially constructed bulk material modifications are often highly unstable, or do not satisfy all of the requirements.

If the size or dimensions of a sample are reduced, then all cards are mixed. For example, the bcc Fe on W(110) is still ferromagnetic, whereas the same bcc Fe on W(001) becomes a very stable, collinear antiferromagnet [5]. Slight change in the lattice structure or a surface orientation in nanosystems may change the type of interactions or number of atoms involved in the interaction [30], and hence frustration effects can be expected in otherwise unfrustrated cases. As will be shown in the following sections, frustration may lead to unstable spin glass behavior and to stable ordering. Modern data storage relies on the coding of information into magnetic configurations in a storage medium; thus, in addition to a fundamental interest in an understanding of the order due to frustration, these magnetic structures may also be used in practical applications.

Another important aspect of modern technology is the production of metallic or molecular arrays consisting of nanoparticles. If an array is relatively densely packed, then the particles interact magnetostatically or electrostatically. These long-range order interactions are naturally frustrating and, hence, may influence the self-organization of the whole ensemble of particles. The frustration effects in antiferromagnetic and magnetostatic/electrostatic systems will be reviewed in the following sections.

## 2.3
## Ising, XY, and Heisenberg Statistical Models

All three models have a long history and have been extensively studied during the past 30 years. The oldest and simplest model is the Ising; this, without doubt, is the most famous and best understood among models of statistical mechanics. Although the model was first proposed in 1920 by Lenz as a toy model of ferromagnetism, five years later, Lenz's student Ernst Ising published a solution of the one-dimensional model as a part of his doctoral dissertation. Ising considered a linear chain composed of small magnets that were able to take an up or down orientation, such that the orientation of each magnet influenced the orientations of those magnets bordering it. Almost 20 years later the concept was expanded on two-dimensional lattices of upward/downward-oriented magnetic moments or spins, with each moment influencing the behavior of its nearest neighbors. For magnetic systems this short-range interaction is simply the strong ferro- or antiferromagnetic exchange coupling described in Section 1.2.2.2. However, instead of orientation, each site can have any two values as 1/0 or +/–, whilst neighboring sites have an energetic preference to have the same or opposite values. Hence, a particular case of the Ising model is described in the example of Figure 2.1. Mathematically, the Ising model is normally described by one of the following Hamiltonians:

$$H = \sum_{\langle i,j \rangle} J_i S_i S_j \quad \text{or} \quad H = \sum_{i=1}^{N} J_i S_i S_{i+1} \,, \tag{2.1}$$

where $J$ is the nearest-neighbor ferro- (negative $J$) or antiferromagnetic (positive $J$) coupling constant. The notation $\langle i,j \rangle$ in the first Hamiltonian means that the sum is restricted to the nearest neighbors only. $S$ denotes "Ising spin" variables, which can take values $S_i \in \{1,-1\}$. For example, a vector Ising spin can point either into the $+z$ or the $-z$ direction. Both interpretations of Eq. (2.1) are identical, though the second one is more appropriate for the introduction of periodic boundary conditions, that is: $S_{N+1} = S_1$.

The "Heisenberg" model was introduced into the literature by Werner Heisenberg in 1928 [6]. The intention was to capture some of the important aspects of the quantum mechanical many-body problems in condensed matter, specifically on a spatial lattice. Heisenberg proposed the following Hamiltonian:

$$H = \sum_{\langle i,j \rangle} J_i \overline{S}_i \cdot \overline{S}_j \,, \tag{2.2}$$

where $i$ and $j$ are sites in a lattice, $\overline{S}$ is a spin operator for site $i$, and the notation $\langle i, j \rangle$ is identical to that of the Ising case. Hence, in contrast to the classical Ising functional this Hamiltonian is an operator in the Hilbert space of lattice states and not just a simple classical variable. The motivation for this model is that the wave functions for the valence electrons are localized on lattice sites and have significant overlap only with their neighbors. The coupling constant $J$ is then interpreted as an exchange integral. In many cases, however, the spin operator $\overline{S}$ can be interpreted as a classical, three-dimensional vector $(S_x, S_y, S_z)$ and $\overline{S}_i \cdot \overline{S}_j$ is then a simple scalar product of two vectors.

The XY-model or the so-called "planar rotator" is a lattice system with spins having a two-dimensional (2D) planar degree of freedom at each lattice site. In the simplest case the Hamiltonian of 2D XY model may be written by

$$H = \sum_{\langle i,j \rangle} J_i \overline{S}_i \cdot \overline{S}_j = \sum_{\langle i,j \rangle} J_i \cos(\varphi_i - \varphi_j) \,, \tag{2.3}$$

where $\varphi_i$ is an azimuthal angle associated with each vector moment on a lattice.

Thus, all three models contain a sum of the products of two variables, vector spins or operators belonging to the nearest-neighboring lattice sites. With this in mind one may generalize the exchange Hamiltonian by

$$H = \sum_{\langle i,j \rangle} J_i \overline{S}_i \cdot \overline{S}_j = \sum_{\langle i,j \rangle} J_i (\alpha (S_i^x S_j^x + S_i^y S_j^y) + \beta (S_i^z S_j^z)) \,, \tag{2.4}$$

where $S^x, S^y, S^z$ are projections of either an operator $\overline{S}$ for a quantum system or of a vector $\vec{S}$ for a classical system. The case of $\alpha = 0\, \beta = 1$ corresponds then to the Ising model, $\alpha = 1\, \beta = 0$ to the XY model, and $\alpha = \beta = 1$ to the Heisenberg model.

The main difference between the three models is the different number of available states. Indeed, an Ising spin attached to a lattice site can have only two states ($W_i^{\text{Ising}} = 2$) – either "up" or "down". An XY-rotator of a unit length can have any orientation in the plane of rotation. Hence, number of available states (orientations) of such a spin increases comparably to the Ising case and is proportional to the angular coordinate $\varphi$ and to the density of states $\rho(\varphi)$, i.e., $W_i^{XY} = \int_0^{2\pi} \rho(\varphi) d\varphi$. A three-dimensional Heisenberg vector of a unit length can have any orientation in 3D physical space. Thus, the number of available states for such a spin increases further. It is proportional to the surface element of a unit sphere and to the density of states $\rho(\varphi, \theta)$, i.e., $W_i^{\text{Heisenberg}} = \int_{\varphi=0}^{2\pi} \int_{\theta=0}^{\pi} \sin\theta \rho(\varphi, \theta) d\varphi d\theta$. Following Boltzmann theory, the entropy of a system is defined as $S = k_B \ln W$, where $k_B = 1.38 \cdot 10^{-23}$ J/K is Boltzmann's constant. Hence, the configurational entropy of a Heisenberg system is much higher than that of an Ising or a XY system.

*Entropy* is also used to indicate disorganization or disorder. J. Willard Gibbs, the 19th century American theoretical physicist, called this "mixedupness". The American Heritage Dictionary gives, as the second definition of entropy, "… a measure of disorder or randomness in a closed system". In other words, a higher entropy corresponds to a higher disorder. The Heisenberg system possesses the highest entropy among the three models, but on the other hand the antiferromagnetic interaction between neighboring spins in all three models requires one and the same thing – antiparallel alignment of the magnetic moments. Thus, it seems that for the same strength of $J$ a Heisenberg system should be more disordered than an Ising one:

- Is this true?
- How does the increasing configurational entropy change ordering in an otherwise identical system?
- What is the role of geometric frustration in the ordering?

## 2.4
## Order-Disorder Phenomena

In order to answer the questions posed at the end of Section 2.3 we must first investigate the so-called "ground state" configurations of the three models with identical interactions on an identical crystallographic lattice. We must then compare the type of ordering and the degree of geometric frustration in all three cases. Therefore in the following section I will introduce the notions of phase transition and ground state, and demonstrate how the frustration can be measured. Following this, the frustrated self-organized systems on different lattices will be described and compared with experimental nanosystems.

### 2.4.1
### Phase Transitions and their Characterization

Although it is not really the intent of this book to discuss critical phenomena in detail, there are certain points about phase transitions which must be recognized in order to understand the ordering at nanoscale. In physics, a phase transition is a transformation of a thermodynamic system from one phase to another. The distinguishing characteristic of a phase transition is an abrupt change in one or more physical properties, and with a small change in a thermodynamic variable such as temperature. The phase transitions of water are matters of everyday experience: water turns into vapor, vapor into ice, and ice into water. Another example is the superconductivity which arises in certain metals when cooled below a certain temperature. In magnetic materials, phase transitions appear between the ferromagnetic/antiferromagnetic and paramagnetic phases. All of these transitions occur at a *critical temperature, $T_c$*. For ferromagnets this critical temperature is called the Curie point, whereas for antiferromagnets it is the Néel point. At temperatures below the Curie point, the magnetic moments are partially aligned within magnetic domains in ferromagnetic materials (see Section 1.2.2.3). However, as $T_c$ is approached, thermal fluctuations increasingly destroy this alignment, until the net magnetization becomes zero – that is, the material becomes purely paramagnetic. Hence, at sufficiently high temperatures many systems will *disorder*, because the disordered state has a greater configurational entropy, and, therefore, a lower Gibbs energy at high temperatures:

$$G \equiv E + PV - TS\,, \tag{2.5}$$

where $G$ is the Gibbs energy, $E$ is the mean energy of a system, $P$ and $V$ are constraints, for example the pressure and the volume, and $T$ and $S$ are the temperature and entropy, respectively. Thus, unless very rare counter-trends occur [7], the usual situation is that $E$ drives ordering at low $T$, while the $TS$ term favors disorder at high $T$.

The ordering process associated with a phase transition is characterized, aside from a transition temperature $T_c$, by a long-range *order parameter $\eta$*, which is a normalized parameter that indicates the degree of order of a system. An order parameter of 0 indicates disorder; the absolute value in the ordered state is 1.

$$\begin{aligned} &T > T_c \rightarrow 1 \geq \eta \geq 0\,, \\ &T \geq T_c \rightarrow \eta = 0\,. \end{aligned} \tag{2.6}$$

One can measure $\eta$ via various physical properties or some abstract variables. For example, for a ferroelectric crystal such as $PbTiO_3$ the order parameter is numerically equal to the normalized polarization, whereas for an Ising ferromagnet it is the normalized magnetic moment. For a two-component alloy, AB, one can measure $\eta$ from the difference in occupation between two crystallographic sites $\alpha$ and $\beta$: $\eta = \frac{x_B^\beta - x_A^\beta}{x_B^\beta + x_A^\beta}$, where $x_A^\beta$ is the concentration of component $A$ on site $\beta$ [7]. All of these

$\eta$ are physical quantities. The XY model's order parameter, on the other hand, may be complex as two-dimensional vectors may be represented by complex numbers. Although the order parameter is measured via physical properties, it is always a thermodynamic function on a par with temperature and pressure, such that:

$$G = G(T, P, \eta)\,. \tag{2.7}$$

Therefore, $\eta$ and $T_c$ are essential components of a quantitative theory of phase transitions. Theories of order-disorder can be divided into phenomenological expansions of $G$ (Landau theory) and solutions of the Ising, XY, Heisenberg or other related models. Landau theory is a *mean-field* analytical approach in which $G$ is expanded as a Taylor series in the order parameter. In addition to mean-field methods, numerical solutions can be obtained via Monte-Carlo methods [8], which are more computationally intensive but always yield correct phase diagrams and critical exponents for a given model Hamiltonian.

Other important quantities for the characterization of a phase transition are *correlation length* $\xi$, *specific heat* $c$, and *susceptibility* $\chi$.

In order to characterize whether and what kind of phase transition appears in a system, $\eta$, $\xi$, $c$ and $\chi$ as a function of temperature must be analyzed. The first-order phase transitions are those during which a system adsorbs or releases a fixed amount of energy (latent heat), for example water evaporation. First-order phase transitions exhibit a discontinuity in a first derivative of the free energy with a thermodynamic variable. The second-order phase transitions have no associated latent heat; rather, they have a discontinuity in a second derivative of the free energy. The major part of ordering phenomena in which we are interested, including ferromagnetism, superfluidity and Bose–Einstein condensation, show phase transition of the second order. In the case of a ferromagnet magnetization, which is the order parameter and at the same time the first derivative

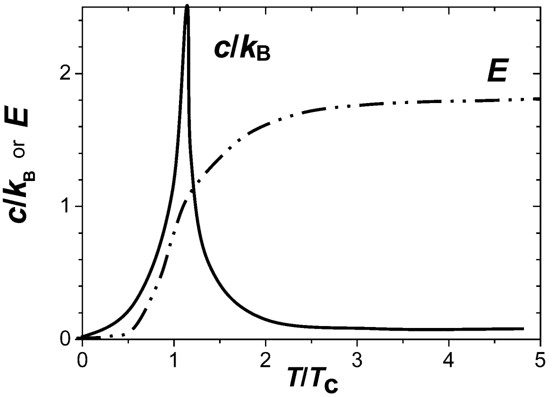

**Fig. 2.2** Schematic view of the internal energy $E$ (dashed curve) and specific heat $c$ (solid curve) of the Ising ferromagnetic model.

of the free energy with the field $\eta = M \propto dE/dH$, increases continuously from zero as the temperature is lowered below $T_c$. The magnetic susceptibility, the second derivative of the free energy with the field $\chi \propto d^2E/dH^2 = dM/dH$, changes discontinuously (see Fig. 2.2); $\xi$, $c$ also diverge at the critical temperature.

Interestingly, whether a system demonstrates a phase transition or not depends on its dimension. It had been proven that a one-dimensional Ising model with short-ranged interactions never exhibits phase transition at finite temperature [9]. In 1965, Mermin and Wagner [10] demonstrated conclusively that models with short-range interactions and rotationally symmetric order-parameters – among them the Heisenberg and XY models – are incapable of displaying long-range order at dimensions $d \le 2$ at finite temperature. The physical reason for this is that the energy of an interface between two domains of $n$ mutually aligned spins decreases with the dimension $d$, and when $d$ is diminished to its lower critical limit, the entropy increase associated with increasing the number of such domains outweighs the energetic cost of extra interfaces, no matter how low the temperature is. In other words, beyond some critical dimension the thermal fluctuations destroy the long-range order in *an infinite sample* as a mean-square deviation of the spins from their equilibrium positions increases logarithmically with the size of the system. In *a finite sample*, however, the long-range order can be obtained even at $d \le 2$ and finite temperature.

### 2.4.2
### Order Below $T_c$

At 0 K, thermal fluctuations and entropy are out of play. Nevertheless, the ordering of a *quantum-mechanical* system can be destroyed by quantum fluctuations even at zero temperature. In what follows, however, mainly *classical* systems will be described. The state of a classical system is determined completely by the energy and the geometry of the system. At zero temperature, the long-range static order can be established even in two- or one-dimensional systems with pure short-range interactions. Ordered zero temperature configurations are termed the *ground states* of a system. The calculation of 0 K or low-temperature phase diagrams for different values of energetic or geometric parameters is one of the main tasks of modern physics.

### 2.4.3
### Measure of Frustration: Local Energy Parameter

The first quantitative characterization of geometrical frustration was introduced by Toulouse [1]. It has been formulated for an Ising system where exchange bonds $J_{ij} = \pm 1$ were randomly distributed on a discrete lattice. This is a model for a disordered magnet or any disordered two-level system. Toulouse introduced the function $\Phi = \prod_c J_{ij}$, which measures the frustration effect in a local region of a lattice, where $c$ indicates any closed contour along the bonds of a lattice with interaction $J_{ij} = +1$ or $-1$. If $\Phi = +1$, it is possible to orient the spins without frustration; if $\Phi = -1$, it is not. Unfortunately, this function cannot be simply generalized to other models and it is not suited to models without underlying lattices.

Frustration has an effect on both ground-state energy and entropy. The ground state energy per element (e.g., spin, $E_{id}$) increases up to a critical value $E_i$. For example, for an isolated triangular cell (see Fig. 2.1) a spin at every node (vertex) would have the energy of $E_{id} = 2J \cdot S_i \cdot S_j = 2 \cdot (+1) \cdot (+1) \cdot (-1) = -2$. This is, however, not possible because of frustration, and only one out of three spins has $E_i = E_{id} = -2$. Two other spins have $E_i = \sum_{ij} J_{ij} S_i S_j = (+1) \cdot (+1) \cdot (+1) + (+1) \cdot (+1) - (-1) = 0$. The average energy per spin is $\langle E_i \rangle = -2/3$ instead of an ideal $-2$. Hence, the two spins with larger energy are frustrated whilst the spin with an ideal energy is not. Bearing this in mind, a *local* measure of frustration can be introduced

$$f_i = \frac{|E_{id}| - |E_i|}{|E_{id}|}, \tag{2.8}$$

which characterizes energy increase with respect to a relevant unfrustrated system. In the case of the triangle (Fig. 2.1), $f_1 = 0$, while $f_{2,3}$ has the maximal value of unity. Frustration of a whole system is then simply an average of local parameters $\langle f_i \rangle$; for our example, $\langle f_i \rangle = 2/3$. The advantage of the parameter $\langle f_i \rangle$ is that it can be applied to different models and any lattice [11–13].

As will be shown below, not all configurations in which local energies deviate from the local ground state energy are frustrated. In those cases, the parameter $\langle f_i \rangle$ determines the local energy instead of the frustration.

## 2.5
## Self-Competition of the Short-Range Interactions

Antiferromagnetic or antiferromagnetic-like systems are geometrically frustrated on lattices consisting of corner-sharing triangles or tetrahedra. These are a triangular and a kagome lattice in two dimensions, and pyrochlores in three dimensions. The kagome ordering is characteristic for $SrCr_{8-x}G_{a_{4+x}}O_{19}$ and jarosite family compounds [14, 18], 3 He on graphite, and some molecular magnets [15]. Both lattices can also be formed by an array of magnetic or ferroelectric molecules. The triangular symmetry is inherent to materials with *hcp*(0001), *fcc*(111) lattice structure, spinel, Laves phases, and pyrochlore crystals. Another class of frustrated symmetry represents quasicrystals. During recent years an evidence of antiferromagnetic interactions in many icosahedral rare-earth-based quasicrystals has been reported (for a review, see [21]). In the following section, the lowest energy states of an antiferromagnet on those lattices will be compared in the framework of different models.

### 2.5.1
### Ising Antiferromagnet on a Lattice

#### 2.5.1.1 Triangular Lattice

As shown in Figure 2.1, antiferromagnetism does not fit into the triangular pattern. Each triangle on a triangular lattice (Fig. 2.3 a) contains three interactions, the best of which can achieve two spins of one sign, and one spin of the other sign. Thus, the final arrangement contains at least one-third of the wrong interactions, and the ground state energy per spin satisfies

$$E_0 \geq -\frac{J \cdot nn}{3} \geq -2\,, \tag{2.9}$$

where the number of bonds with nearest neighboring spins on a triangular lattice is $nn = 6$. There are actually states in which the number of wrong interactions is just one-third with the energy minimum $E_0 = -2$. An example of such an arrangement is shown in Figure 2.3 (a).

However, whilst there exist only three variations of that configuration corresponding to three principal directions of the triangular lattice, there are many other ways to achieve this lowest energy state. The number of ground state con-

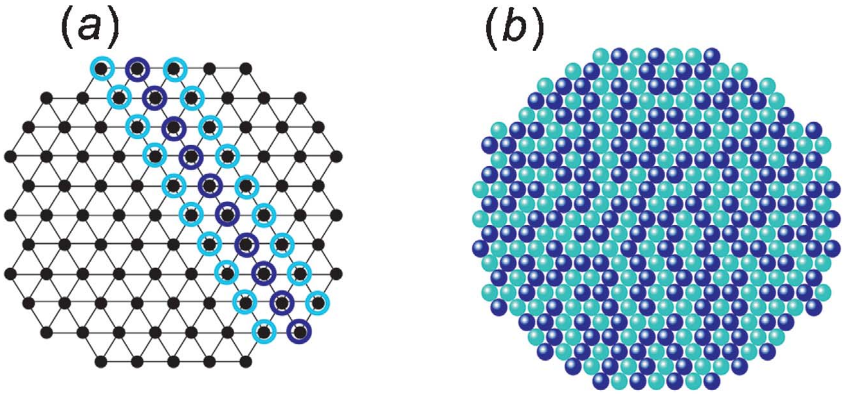

**Fig. 2.3** (a) One possible Ising antiferromagnetic ground state on a triangular lattice with low statistical weight. (b) Low-temperature Monte-Carlo configuration of an Ising antiferromagnet with high statistical weight on a triangular lattice. The different colors represent different orientations of spins.

**Table 2.1** Number of ground state configurations $W$ for triangular-shaped samples on a triangular lattice of $N$ sites.

| $N$ | 3 | 6 | 10 | 15 | 21 | 28 | 36 |
|---|---|---|---|---|---|---|---|
| $W$ | 6 | 26 | 160 | 1386 | 16814 | 284724 | 6693180 |

figurations increases drastically with the size of a lattice. The number of ground states $W$ as a function of the number of the lattice sites is provided in Table 2.1 [16]. It follows from the data in Table 2.1 that the statistical weight of the configuration in Figure 2.3 a for a triangular net of 36 sites $p_1 = \frac{3}{6693180} \to 0$ vanishes. At the same time, the statistical weight to find other arrangements is much higher (close to unity). Therefore, this particular configuration is unlikely ever to be realized because there are arrangements of much higher statistical weight. The idea about how those ground states should look like gives a low-temperature Monte-Carlo configuration (see Fig. 2.3 b). By exploring the configuration, one will never find an elemental triangle with all three spins being parallel. Absolutely all unit-triangles have the lowest possible energy – that is, two light and one dark spins, or vice versa. The energy density is also in good accordance with that of Eq. (2.9). However, as there exist thousands of possible combinations of such triangles, the whole structure of Figure 2.3 b is disordered. The average energy per site is $\langle E \rangle = -1.987$ and, hence, the local frustration is rather high

$$\langle f \rangle^{\text{triangular}} = \frac{6 - 1.987}{6} \approx 0.669\,. \tag{2.10}$$

As determined by Wannier [17], the entropy of an Ising system on a triangular lattice at absolute zero is finite, and equals

$$S^{\text{triangular}}(0) \propto \ln W \propto 0.3383 \tag{2.11}$$

with $W$ the number of possible ground states. The physical reason for the finite zero-point entropy of an Ising antiferromagnet on triangular lattice is the huge number of ground states without energy barriers between them.

#### 2.5.1.2 **Kagome Lattice**

Another celebrated triangular-based structure is the kagome lattice (kagome means a bamboo-basket (*kago*) woven pattern (*me*) in Japanese [18]). It is composed of interlaced triangles, the lattice points of which each have four neighboring points (Fig. 2.4 a). This lattice was first introduced by K. Husimi and I. Syôzi in 1951 [19], when such baskets were still in fashion, as a next link in the chain of reports about phase transitions on frustrated lattices. I. Syôzi demonstrated that, similar to a triangular lattice, a magnetic transition – that is, a singularity in the free energy and the specific heat $c$ – do not occur in the antiferromagnetic kagome structure. The ground state entropy is also finite and very high [20]: $S^{\text{kagome}}(0) \propto 0.5018$, and the ground state is disordered (see Fig. 2.4 b). The local frustration is $\langle f \rangle^{\text{kagome}} \approx 0.677$.

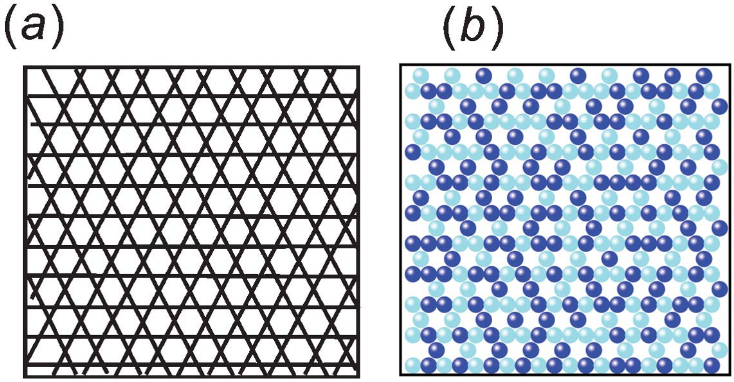

**Fig. 2.4** (a) A kagome pattern. (b) Low-temperature Monte-Carlo configuration of an Ising antiferromagnet on a kagome lattice. The different colors represent different orientations of spins.

### 2.5.1.3 Ising Antiferromagnet on Aperiodic Tilings

For almost 80 years scientists believed that the occurrence of sharp, pointed reflexes in the diffraction image are limited to usual, periodic crystals. Therefore, it was a shock for the physical community when, in 1984, materials showing perfect reflexes but fivefold incompatibility with any periodic lattice symmetry were discovered. These new substances were termed quasicrystals because of their aperiodic order.

Mathematically, the aperiodic but ordered structures were identified by the English mathematical physicist Roger Penrose who, in 1974, discovered a first aperiodic structure – the so-called Penrose tiling – which is formed from two tiles that can only fill the plane aperiodically. Subsequently, many other quasicrystalline configurations have been discovered, including the Amman–Beenker octagonal, the Tübinger triangle, Tie–Navett, Antipenrose, Shield, Chair, and many other tilings. In contrast to conventional crystals which consist of one single motif (triangle, square, etc.), aperiodic tilings are made from several units, with the tiles being arranged without gaps or overlaps according to matching rules. For example, the Penrose tiling consists of two rhombuses (Fig. 2.5 a), while the octagonal tiling is constructed from a square and a rhombus of equal edge lengths (Fig. 2.5 b).

The quasicrystals can be structurally ranked between periodic lattices and completely disordered media. The aperiodic tilings may be frustrated, as the rhombic tiles can be regarded as two triangles. In contrast to periodic structures with geometric frustration, however, in quasicrystals the number of nearest neighboring atoms varies widely from one point to another, as in disordered matter. The Penrose tiling (Fig. 2.6 c), for example, has atoms with coordination numbers changing from 3 to 7, while atoms of the octagonal tiling (Fig. 2.6 b) have from five to eight nearest neighbors. Hence, the energy per atom also varies. Unlike the disordered media, however, this variation exhibits a long-range orientational order –

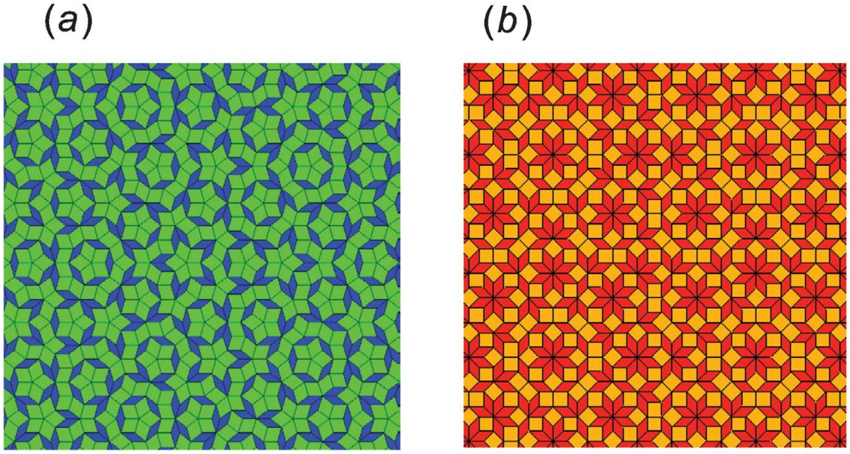

**Fig. 2.5** (a) A portion of a Penrose tiling. (b) A portion of an octagonal Amman-Beenker tiling. Courtesy of U. Grimm.

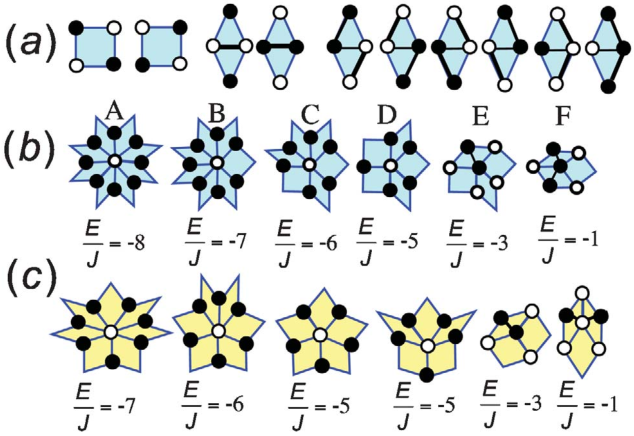

**Fig. 2.6** Configurations of a frustrated Ising antiferromagnet on octagonal and Penrose tilings. (a) Elementary tiles of an octagonal tiling. The bold lines denote frustrated bonds; the open and filled circles represent different spins. (b) Six local environments of the Ammann-Beenker (octagonal) tiling. (c) Six local environments of the Penrose (five-fold) tiling.

that is, any finite section of a quasicrystal is reproduced within a certain distance. Due to the specific atomic structure the quasicrystals pose a number of fundamental questions. One particularly intriguing problem is that of a long-range magnetic order due to unusual frustration effects [21–26].

In order to calculate the exchange energy of an atom in a quasicrystalline environment, the set of nearest neighbors that are coupled via the short-range in-

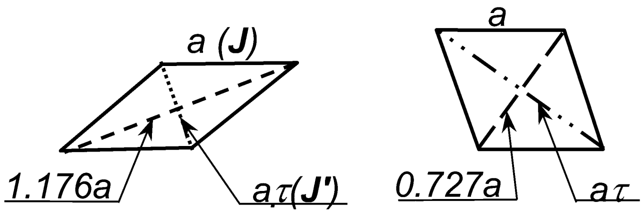

**Fig. 2.7** The original Penrose rhombic tiles with angles of 36° and 144° (left), and the other with angles of 72° and 108° (right). Five nearest-neighbor distances (the sides and diagonals of the rhombuses) and their lengths are given. $\tau$ is the golden mean. The two strongest exchange bonds according to two shortest nearest-neighbor distances are denoted as $J$ and $J'$.

teraction must be defined. In periodic crystals the exchange coupling between next nearest neighbors is usually enough to study the magnetic order in the first approximation. In quasicrystals, the situation is different since, as the pattern consists of two tiles with edges of equal length, this distance is usually taken as the nearest-neighbor distance. The shorter diagonal bonds are, usually, neglected in the calculations [26]. Such disregard is physically questionable as the exchange coupling increases exponentially with decreasing interatomic distance. In the following section the short diagonal of the rhombus and the sides of the motifs (see Fig. 2.7) will be considered as nearest neighbors.

The square tile of the octagonal structure is non-frustrated, as every pair of moments can be chosen to be antiparallel (Fig. 2.6 a). If we had not taken the short diagonals of the rhombic tiles into account, the same would have been true for the entire tiling, and there would be no frustration. Now, if we consider spins on short diagonals to be nearest neighbors, then the rhombic tiles are always frustrated. If the energy of one nearest-neighbor pair is minimized by having antiparallel spins, the third and fourth spins cannot be chosen to minimize the energy of both of its neighbors (Fig. 2.6 (a)). The magnetic moment will necessarily be parallel to one of the neighbors. For $J' < 2J$, two out of six possible configurations have less energy as they possess only one pair of parallel nearest neighbors per rhombus instead of two (Fig. 2.6 a). In this case the spins can have one of six possible energy values corresponding to different local environments (Fig. 2.6 b). For $J' > 2J$, the four configurations with two parallel bonds (Fig. 2.6 a) have the lowest energy as their weight is less than that of the strong diagonal coupling. The second case comprises much more different possibilities of energy distribution.

The calculation of the degree of frustrations according to Eq. (2.8) leads to the following results [27]. In the octagonal tiling, only the central spins of the vertices $F$ and $E$ are frustrated $f^{\text{octagonal}}(F) = 0.4$ and $f^{\text{octagonal}}(E) = 0.8$ for $J' < 2J$. The Monte-Carlo simulations confirm our reasoning based on the analysis of frustration [27]. Figure 2.8 illustrates graphically the frequency distribution of

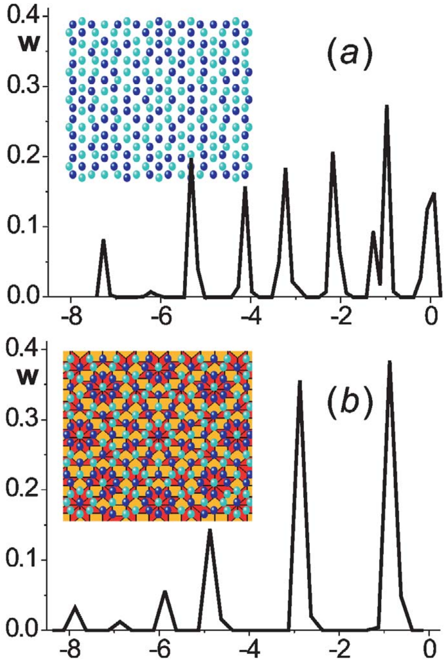

**Fig. 2.8** Frequency distribution of the energy per spin on the octagonal tiling for Ising spins. Top-views of portions of low-temperature Monte-Carlo configurations with underlying tilings are shown as insets. The light and dark circles represent different spins. (a) $J' > 2J$; (b) $J' < 2J$. Purely antiferromagnetic interaction at $kT = 0.01\,J$ is considered.

the exchange energy per atom for two cases and top-views of a portion of Ising configuration for $J' > 2J$ (Fig. 2.8 a) and $J' < 2J$ (Fig. 2.8 b). The energy distribution for $J' < 2J$ simply reproduces the frequency of six vertex configurations. The “up” and “down” configurations are perfectly ordered and coincide with the black-and-white model of Niizeki [28]. For large $J'$, eight possible energy values have been found, although the “up” and “down” subtilings are spatially disordered (see inset Fig. 2.8 a).

In the case of the ordered configuration with $J' < 2J$, only two global configurations exist. The first is that of Figure 2.8 b, and the second configuration is the reflection symmetric one (dark sites become light, and vice versa). Hence, the number of configurations per spin is $W = 2/N$, with $N$ as the number of spins and the ground state entropy as $S^{\mathrm{octagonal}}(0) \propto \ln W = 0$. The situation of the case $J' > 2$ is more complicated. From Figure 2.8 a it can be seen that the central spin of the vertex A (eight-fold stars) of the tiling has four light and four dark moments. Hence, we can reverse the central spin without changing the energy. The same is true for the vertices of type C (six-fold stars). A and C vertices occur with relative frequencies $\nu_A \approx 2.9\%$ and $\nu_C \approx 5.9\%$ [29]; this immediately yields a lower bond for zero temperature entropy

$$S^{\mathrm{octagonal}}(0) > 0.088 \ln 2 \approx 0.06\,. \tag{2.12}$$

### 2.5.2
### Heisenberg Antiferromagnet on a Lattice

#### 2.5.2.1 Triangular and Kagome Lattices

The frustration which disorders a triangular Ising antiferromagnet is somewhat relieved for the classical XY or Heisenberg systems, which order in the Néel state [30, 40]. The Néel configuration consists of sublattices for which average magnetization per site is not zero at low temperatures in three dimensions [31] and at 0 K in two dimensions [32]. The angle between magnetization vectors of the sublattices is 120°. An example of Néel structure on a triangular lattice is shown in Figure 2.9 a.

Both, classical [33, 34] and quantum [35, 36] theoretical studies of the Heisenberg antiferromagnet on a two-dimensional kagome lattice have concluded that there is no finite-temperature transition to a phase with long-range spin ordering. As the spin directions can be mapped onto the disordered hydrogen bonds of Pauling's cubic ice model, such systems have been called "spin ice" [37–39]. Although the whole spin configuration on a kagome lattice is disordered, the average angle between neighboring spins equals 120°. The six degenerate spin configurations for a single triangle of the kagome spin-ice model are shown in Figure 2.9 b. There are indications that although the ground state may be disordered, the fluctuations will tend to select coplanar spin arrangements at $T=0$ [35, 40, 41].

In contrast to the Ising frustrated system, where many comparable energy minima exist, the XY Néel configuration on a triangular lattice has a well-defined global minimum of energy and is ordered up to the global rotation. The 120° ordering of the XY kagome system is frustrated. However, because of the

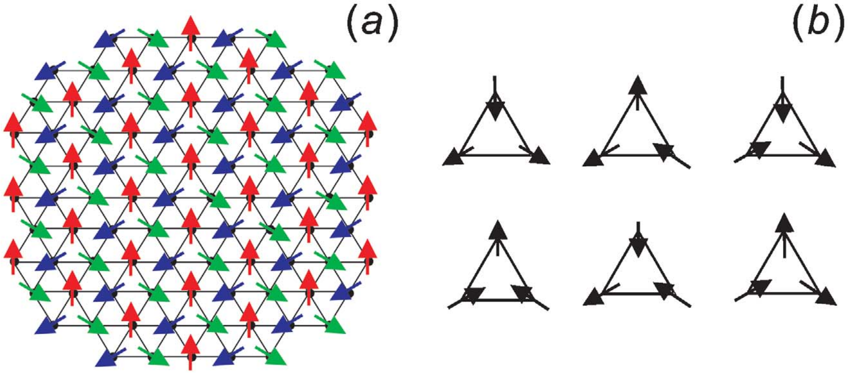

**Fig. 2.9** (a) Typical Néel spin configurations on a triangular lattice for XY spins. The colors define three sublattices. (b) The six degenerate spin configurations for a single triangle on the kagome lattice. Purely antiferromagnetic interaction with first nearest neighbors only is considered.

120° arrangement of magnetic moments, parameter $\langle f \rangle$ is identical for both lattices and lower than for the corresponding Ising systems

$$\langle f \rangle_{XY}^{\text{triangular}} = \frac{|-6-6\cdot\cos 120^\circ|}{6} = 0.5\,, \tag{2.13}$$

$$\langle f \rangle_{XY}^{\text{kagome}} = \frac{|-4-4\cdot\cos 120^\circ|}{4} = 0.5\,. \tag{2.14}$$

Thus, in contrast to what is usually expected, an increase in configurational entropy leads to a decrease in the total energy per magnetic moment – that is, to a more ordered magnetic structure. The residual entropy of kagome spin-ice has been found to be very close to that of the antiferromagnetic Ising kagome system $S_x^{\text{kagome}} = 0.4982(35)$ [39]. The Néel state on a triangular lattice in the XY model does not possess residual entropy.

Néel configurations obtained in the framework of the XY and the Heisenberg model on a triangular lattice are almost identical. In both cases, the three sublattice vectors define a plane (see Fig. 2.9). The only difference is that in the XY model this plane is given by definition, while the three-dimensional Heisenberg moments are free to choose any plane in space (see Fig. 2.10). Therefore, in the case of Heisenberg spins an even-ordered Néel state on a triangular lattice may lead to residual entropy. Indeed, if the orientation of one of three Néel sublattices is fixed, then two other subtilings may admit any orientation on a cone (as shown in Fig. 2.10). The total energy is independent of the azimuthal direction of a second and a third sublattice vectors, as all mutual angles remain at 120°. Thus, for such a classical system the second and third sublattices may freely rotate (precess) relative to a first one, even at zero temperature; that is, the number of available states $W$ may be rather large and the entropy finite. However, calculation of the entropy in systems with continuous symmetry is not simple, the main problem being difficulty in the definition of $W$, as a number of microscopic states depend on the size of a mesh in the azimuthal angle. For these

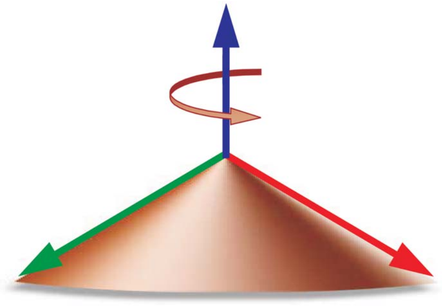

**Fig. 2.10** Possible mutual orientations of three Néel sublattices. Different sublattices are represented by vectors of different color.

types of problem other methods of defining entropy should be used; however, these are beyond the scope of this book and will not be discussed here.

#### 2.5.2.2 **Aperiodic Tilings**

One exciting question is whether minimization of the total energy and frustration in quasiperiodic tilings is also possible. Knowledge of an antiferromagnetic ordering in quasicrystals is especially important in view of the recent experiments described in Section 2.2. At first glance, the magnetic structure of low-temperature antiferromagnetic configurations on different tilings appears to be rather disordered for the XY-model, as for the Heisenberg model [42]. The analysis of local energies, however, reveals several characteristic energetic maxima in the frequency distribution [27, 42]. Figure 2.11 illustrates graphically the frequency distribution of the exchange energy per atom $\langle E \rangle$ for the Tübingen triangle, and Anti-Penrose, Penrose, and Tie–Navette tilings for the case of Heisenberg spins. The calculations have been performed for an exponentially decreasing exchange coupling $J_{ij} \propto e^{r_{ij}}$ and for a short-range exchange coupling $J_{ij} = \text{const} = 1$ for all $r_{ij} \leq 1$. The analysis of the local energies reveals several energetic maxima in the frequency distributions. The number of energy peaks for the same tiling is identical for both choices of exchange couplings. For different tilings, the number and width of the maxima are different, however. For planar XY magnetic moments the picture is quite similar, the only difference being the distinct positions of peaks in the local energy distribution.

The simple existence of the peaks means that there exist different sorts of magnetic moments having well-defined relative orientations with respect to their nearest neighbors. These relative orientations depend on the tiling and *not* on the choice of the exchange coupling $J_{ij}$. For $J_{ij} = 1$, however, it can be seen directly from the energy distributions of Figure 2.11, whether the magnetic ordering is either collinear or non-collinear. If all nearest neighbors are collinear (parallel or antiparallel), then the exchange energy per spin should have integral values that depend only on the number of neighboring moments. This is indeed the case for the Tie–Navette tiling (compare Fig. 2.11 d). For a non-collinear alignment of neighboring magnetic moments $\langle E \rangle$ should be non-integral, as the cosines of the angles between the moments are no longer zero or unity. This occurs for all other tilings considered here (compare Fig. 2.11 a–c). The average energy of non-collinear XY configurations is almost equal to that of a collinear Ising solution. In the case of the Heisenberg model, the minimal possible local energy peak increases from $-8\,J$ to approximately $-6\,J$ for $J' = J$ (see Fig. 2.7). The total average energy per spin, however, decreases by more than $0.3\,J$ and reaches the value of $\langle E \rangle = -2.85\,J$. Hence, the increase in configurational entropy leads to a non-collinear magnetic order, which in turn permits one to minimize the average local frustration and the total energy of the system.

Two questions remain: first, what is the range of the antiferromagnetic quasiperiodic order? And second, how does it appear? Three-dimensional representations of parts of the low-temperature quasiperiodic patterns observed for the

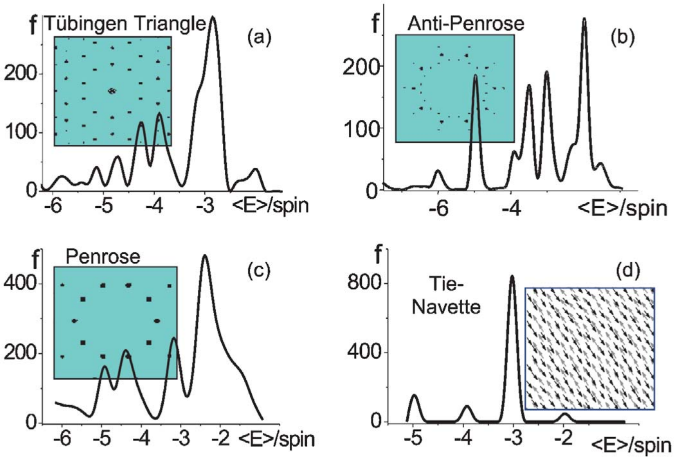

**Fig. 2.11** The frequency distribution of the energy per spin on the Tübingen triangle (a), Anti-Penrose (b), Penrose (c) and Tie-Navette (d) tilings for classical vector spins after the Monte-Carlo relaxation. A purely antiferromagnetic interaction $J$ at a temperature $kT = 0.01\,J$ is considered. The insets (a–c) provide calculated Bragg scattering of $S_y$ component of magnetization for subtilings composed of magnetic moments belonging to peaks with $-6 < \langle E \rangle < -4$. The scale goes from –6 to $6\,k_{x,y}^{Sy}/\pi$. The inset (d) provides a portion of the stable magnetic configuration on the Tie–Navette tiling, as described in the text. The dark and light gray arrows denote antiparallel magnetic moments.

Penrose and the octagonal tiling are shown in Figure 2.12. The corresponding configurations represent the characteristic Penrose and Amman–Beenker "stars", which are shown in Figure 2.12 as insets for clarity. On the Penrose tiling, the "star" pattern can easily be recognized in the magnetic structure, because the moments belonging to the perimeter of enclosed "stars" show perfectly antiparallel alignment. On the octagonal tiling, the situation is more complicated. The central magnetic moment is neither parallel nor antiparallel to the neighboring magnetic moments. Its eight nearest neighbors have different sets of mutual angles; thus, the moments forming the next ring have still another orientation with respect to their nearest neighbors. The non-collinear alignment of the neighboring moments indicates that $\langle f_i \rangle \neq 0$; that is, there is no possibility of aligning all neighbors in antiparallel fashion. Similar non-collinear antiferromagnetic configurations are formed in the Tübingen triangle and Anti-Penrose tilings. The subtilings of low energy $\langle E \rangle < -3$ are magnetically stable and ordered, while those of higher energy $\langle E \rangle > -3$ are disordered and frustrated. The disordering can be seen in the portion of the magnetic configuration of Figure 2.12 (bottom). The two front moments belonging to the subtiling of a large energy have angles which deviate considerably from those of the other moments in the ring, whereas the moments in the inner rings with lower energy have collinear orientations. With increasing temperature the magnetization of subtilings of large energy will fluctuate, while the magnetization of low-energy subtilings remains stable. Within the examples of tilings considered here, the Tie–

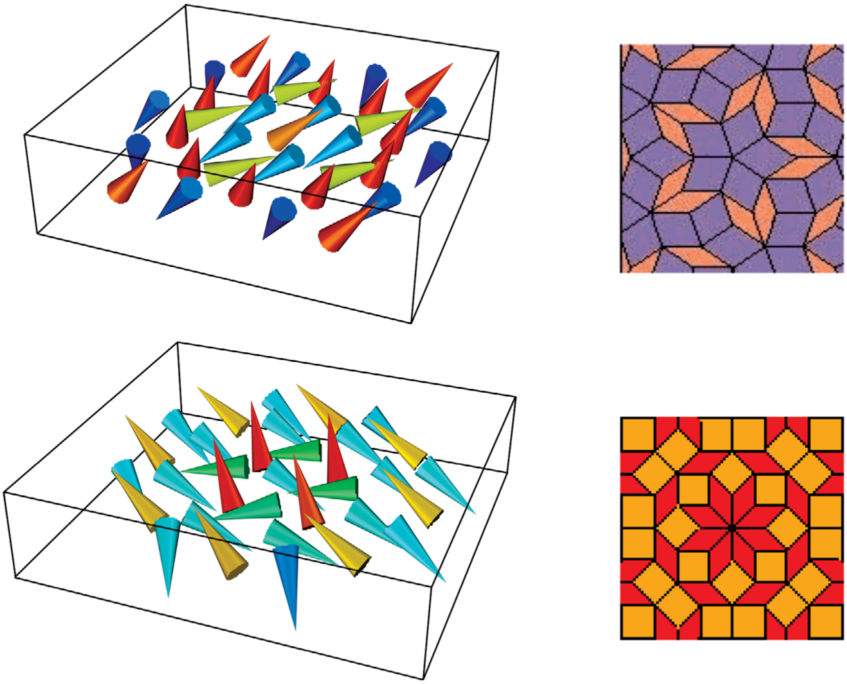

**Fig. 2.12** Perspective view of a portion of a Monte-Carlo configuration on the Penrose tiling (top) and octagonal tiling (bottom). Top views of the corresponding patches are shown at the right. The magnetic moments are represented as cones.

Navette tiling represents an exception, as the magnetic structure observed here consists of two antiferromagnetically aligned quasiperiodic sublattices (see Fig. 2.11 d). This means that every pair of nearest-neighbor moments can be aligned in antiparallel fashion – that is, the antiferromagnetic configuration is not frustrated.

The spatial arrangements of magnetic moments as a function of the exchange energies are illustrated in Figure 2.13, where each color represents a certain energy range corresponding to one of the peaks in the spectra of Figure 2.11. The magnetic moments form subtilings of different energies. In Figure 2.14, the subtilings for an octagonal tiling are resolved separately, with colors representing the X-projection of magnetization. The magnetic moments form eight subtilings of different energy $(E_1 \ldots E_8)$ which generally do not coincide with a specific vertex type (see Fig. 2.6). Splitting of the energy and frustration levels is described in detail in Figure 2.14. For example, the vertices B and C (see Fig. 2.6) belong to the same energy maxima $E_2$ but have different local frustration $f_B = 0.24$, $f_C = 0.11$ (Fig. 2.14). At the same time, the central spin of vertex D can have either energy $E_3$ or $E_4$ and, therefore, can have two different values of frus-

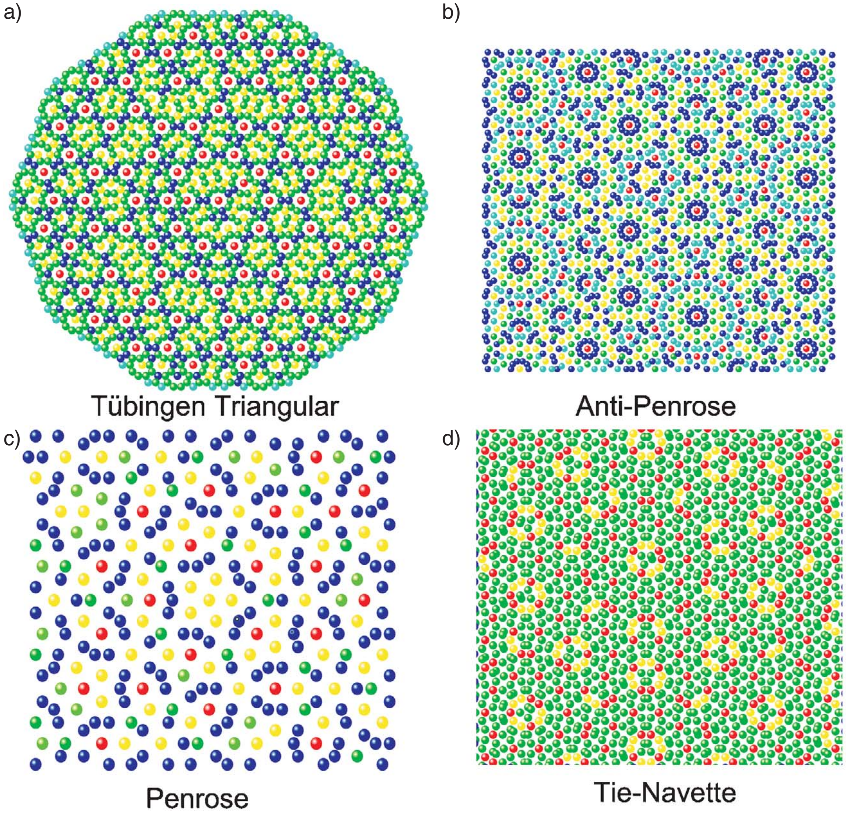

**Fig. 2.13** Energy maps for classical vector spins on Tübingen triangle (a), Anti-Penrose (b), Penrose (c) and Tie-Navette (d) tilings. The circles indicate the positions of magnetic moments. Different colors denote different energies corresponding to the peaks in Figure 2.11. Purely antiferromagnetic interaction with $J=1$ for all $r_{ij} \leq 1$ at $kT=0.01\,J$ is considered.

tration, $f_{D1} = 0.01$ and $f_{D2}=0.11$, depending on the local surroundings. Thus, every configuration of Figure 2.14 can enclose either a part of the atomic places belonging to one vertex type, or two different vertex types together. Nevertheless, all structures have a perfect general spatial ordering. Each subtiling can be separated into the energetically degenerate “right” and “left” parts, which also have a perfect quasiperiodic arrangement. However, not all right or left moments have identical orientation in space. The spatial quasiperiodic ten- or eight-fold symmetry of the ordered subtilings can be seen from the calculated magnetic Bragg scattering given in the insets to Figure 2.11. While the atomic ordering of the unstable subtilings can be seen in the Fourier space, their magnetic reflexes are extinct because of disorder.

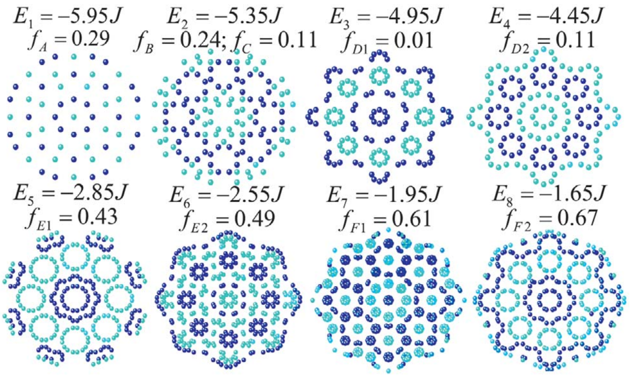

**Fig. 2.14** Spatial distribution of magnetic moments belonging to eight subtilings of a non-collinear configuration on an octagonal tiling. The light and dark circles represent positive and negative $X$ components of the magnetization. The in-plane components are not given for the sake of simplicity. Average values of the exchange energy $E$ and of the local frustration $f$ per spin are indicated.

Thus, the vector spin system on quasiperiodic tilings admits a three-dimensional non-collinear magnetic structure. The whole structure can be decomposed into subtilings of different energy which generally do not coincide with a specific vertex type. In contrast to an Ising system, all subtilings are frustrated. However, the total degree of frustration and the energy of the system is minimized compared to the non-collinear Ising case. The subtilings are degenerated with respect to the spin direction. The codirectional spins of every subtiling reveal quasiperiodic ordering with a wave vector which is specific for a given subtiling.

### 2.5.3
### Three-Dimensional Spin Structure on a Periodic Two-Dimensional Lattice: Itinerant Systems

As was shown in Section 2.5.2.1, short-range antiferromagnetic interactions may lead to non-collinear Néel ordering on periodic lattices with triangular symmetry. However, those non-collinear configurations are planar for two-dimensional geometry because the three sublattices of a Néel configuration always define a plane ($3\times120^\circ=360^\circ$). If the frustrated interactions are combined with structural aperiodicity, as in quasicrystals (see Section 2.5.2.2), the non-collinear structure may become three-dimensional. The question arises as to whether the same effect on a periodic lattice is also possible, and for which types of interaction.

The Heisenberg model describes a set of quantum mechanical or classical spins localized on a set of sites $i$, and interacting with neighboring sites $\langle i,j\rangle$ through inter-atomic exchange $H_{\text{int}}$ (see Section 2.3). This model is very successful for systems with a high degree of spin localization such as rare-earth magnets or transition-metal antiferromagnets (e.g., a monolayer of Fe/Cu(001)). In *itinerant* magnets, the electrons that are responsible for the formation of the magnetic state do participate in the formation of the Fermi surface and "hop" across the lattice. Monolayers of Cr and Mn deposited on a substrate with a triangular lattice are ideal candidates for physical realizations of frustrated 2D itinerant antiferromagnets [43].

One of the most adequate models describing exchange coupled itinerant systems is the Hubbard model [44]. The Hamiltonian of the Hubbard model, in addition to the interaction term, possesses a so-called hopping term $H = H_{\text{hop}} + H_{\text{int}}$. In spite of its apparent simplicity this model is very difficult to apply directly for studies on magnetic ordering, and to simplify the problem the *perturbation theory* is often used. This theory is a set of approximation schemes that describe a complicated system in terms of a simpler one. The perturbation expansion can be represented as a sum of expansion terms $H = H_1 + H_2 \ldots H_n$. Up to the second order, such a perturbation expansion reproduces the Heisenberg model with a Hamiltonian proportional to $\mathbf{S}_i \cdot \mathbf{S}_j$, but going beyond the second order yields more complicated spin interactions. In addition to terms which are proportional to $\mathbf{S}_i \cdot \mathbf{S}_j$ and may be incorporated into the Heisenberg term, the terms of different form appear. One is the four-spin exchange interaction:

$$H_{4-spin} = -\sum_{ijkl} K_{ijkl}[(\mathbf{S}_i\mathbf{S}_j)(\mathbf{S}_k\mathbf{S}_l) + (\mathbf{S}_j\mathbf{S}_k)(\mathbf{S}_l\mathbf{S}_i) - (\mathbf{S}_i\mathbf{S}_k)(\mathbf{S}_j\mathbf{S}_l)]\,. \tag{2.15}$$

The four-spin interaction arises from the hopping of electrons over four sites – that is, the process 1 → 2 → 3 → 4 → 1. On a triangular lattice the four sites involved form a minimal diamond (see Fig. 2.15). As Eq. (2.15) comprises scalar products of neighboring spins, it should be frustrated on a triangular lattice by analogy with the antiferromagnetic Heisenberg model. The resulting magnetic structure, however, should be different from that of the Néel ordering because of the hopping term.

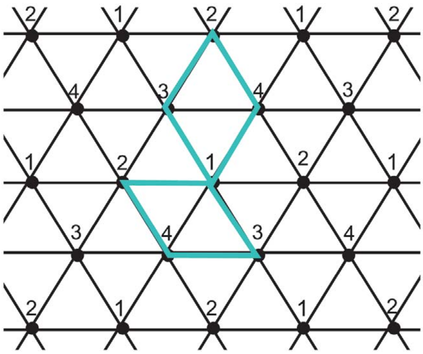

**Fig. 2.15** Example of minimal diamond clusters on a triangular lattice.

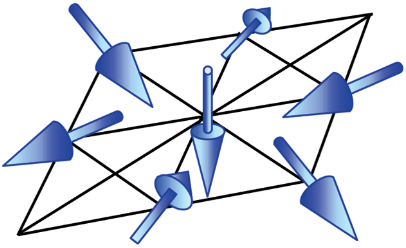

**Fig. 2.16** Three-dimensional spin structure on the two-dimensional triangular lattice formed due to the four-spin interaction term [45]. The structure is energetically degenerate with the row-wise antiferromagnetic state within a Heisenberg model. The relative angle between neighboring spins is the tetrahedron angle.

Recently, it was predicted that the four-spin interaction is a lowest-order correction to the Heisenberg model for a monolayer of Mn on Cu(111) substrate [45]. The magnetic ground state of this system has been predicted to be a three-dimensional non-collinear spin structure with four atoms per unit cell and four sublattices (see Fig. 2.16). This structure has been called the “3Q” state as it can be formed as a linear combination of the three row-wise antiferromagnetic (1Q) structures orthogonal in spin space. The 3Q state is frustrated because it is energetically degenerate with the row-wise antiferromagnetic structure [43].

Hence, frustration is not a privilege of a nearest-neighbor antiferromagnetic coupling on triangular-based or quasiperiodic geometries. Indeed, self-competition may appear even in collectivized itinerant systems.

### 2.5.4
### Frustration Squeezed Out

As we have seen in previous sections, frustrated systems have many faces. On the one hand, a frustrated system may be frozen at low temperatures in one of disordered configurations as, for example, an Ising antiferromagnet on a periodic or an aperiodic lattice (see Section 2.5.1). On the other hand, the spins may fluctuate between many degenerate configurations at temperatures much lower than the energy scale of the interactions, as for example a vector antiferromagnet on a triangular lattice (see Section 2.5.2 and Fig. 2.10). Such a cooperative phenomenon is denoted as “spin-liquid” behavior [46]. The spin-liquid phases result from an energy landscape that has a continuum of energetically equivalent states, with low or nonexistent barriers between them.

Experimentally, the spin-liquid phase is often found in so-called pyrochlores – compounds having a three-dimensional lattice structure formed by the core-sharing tetrahedra. One example is polycrystalline $Tb_2Ti_2O_7$, a pyrochlore antiferromagnet in which rare-earth $Tb^{3+}$ ions have strong magnetic moments. $Tb_2Ti_2O_7$ is a spin-liquid at low temperatures, with no evidence of long-range magnetic order. Recently, it was reported [47] that the application of pressure produces sharp peaks in the diffraction pattern below 2 K. Such long-range peaks mean that the application of pressure eliminates the frustration, and the system settles into one of allowed energy minima. This result would be less surprising if the pyrochlore lattice were to be deformed under the pressure, but in this particular case the pressure has been applied almost isotropically to the whole sample and the lattice was uniformly squeezed rather than distorted. The pyrochlore symmetry has been conserved. The reasons for this unusual ordering are not yet completely clarified, but experimental observations of these phases have suggested that weak energies – as for example dipole–dipole coupling or quantum-mechanical fluctuations – might be responsible for the unusual behavior in this temperature region. The quantum fluctuations are beyond the scope of this book, but the dipolar interactions will be discussed in the following section.

## 2.6
## Self-Competition of the Long-Range Interactions

The dipole–dipole interaction is described by the Hamiltonian

$$E_{dip} = D \sum_{i,j} \left( \frac{\mathbf{S}_i \cdot \mathbf{S}_j}{r_{ij}^3} - 3 \frac{(\mathbf{S}_i \cdot \mathbf{r}_{ij})(\mathbf{S}_j \cdot \mathbf{r}_{ij})}{r_{ij}^5} \right) , \tag{2.16}$$

where $D = \frac{\mu_0 \mu_g^2}{4\pi d^3}$ is the dipolar coupling parameter with $\mu_0$ the permeability of the vacuum, $\mu_g$ the magnetic moment of a particle, $d$ the interparticle distance, $\mathbf{S}$ the unit vector, and the relevant sum running over all spin pairs $i$ and $j$ defining the vector $\mathbf{r}_{ij}$.

Various problems in the theory of nanosystems have led to the consideration of interactions among dipoles. Whereas in atomic magnetic materials the exchange interaction usually dominates over dipolar interactions, the opposite occurs in many nanoscale particle or clustered magnetic systems, for which the interparticle interactions are mainly of dipolar origin. Long-range dipolar interactions are also at the heart of the explanation of many peculiar or anomalous phenomena observed in fine particles embedded in nonmagnetic matrix systems, molecular networks, colloids or rare-earth ions. This includes the 2D honeycomb magnets $ErX_3$, which show that dipolar interactions can be crucial in determining magnetic order at low temperatures. The long-range nature of dipolar interactions inevitably leads to frustration – a spin cannot simultaneously satisfy the conditions dictated by all of the interactions. Details of self-competition in dipolar systems will be provided in the following sections.

## 2.6.1
## Dipolar Interactions

### 2.6.1.1 Localized Ising Moments on a Periodic Lattice

In contrast to isotropic exchange coupling, dipolar interaction has an anisotropic character. This means that, even in a simple Ising case, the ground state depends on the spatial orientation of the magnetic moments. For example, if two Ising moments may have only up- or down-orientations with respect to a plane, the right part of Eq. (2.16) becomes zero as the cosine of 90° is zero. Therefore, the ground state configuration is an antiparallel alignment of the moments (Fig. 2.17 a) with energy per moment $E_{dip} = -1$ for $D = 1$ and $r_{ij} = 1$. For right- or left- orientations in the film plane, however, the ground state is head-to-tail configuration (Fig. 2.17 b) with $E_{dip} = -3$ as the right part of Eq. (2.15) is no longer zero.

Another important property of the dipolar coupling is its long range character. The dipolar interaction between vertical Ising spins corresponds to a long-range antiferromagnetic coupling. On a square lattice, the impact of the long-range contribution is not noticeable as the ground state of such a system is identical to that of usual Ising antiferromagnet – it is simply an unfrustrated checkerboard configuration. However, on triangular and kagome lattices the long-range part of the dipolar coupling favors the formation of long stripes consisting of parallel moments. Figure 2.18 a, b shows Monte-Carlo structures for vertical Ising moments on a triangular lattice for two temperatures [48]. At a local scale, an organization with parallel stripes of alternate spins occurs, while at larger sizes stripes become organized in chevrons and labyrinthine patterns, as observed previously in magnetic nanoarrays with uniaxial anisotropy [49] and magnetic liquids [50, 51]. The stripes always run along the three principal directions

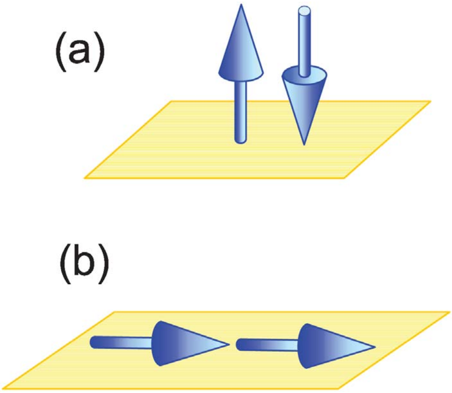

**Fig. 2.17** Ground dipolar states for two Ising moments which are oriented perpendicular (a) or parallel (b) to the film plane.

of an underlaying lattice. Hence, the configuration provides evidence of an effective in-plane anisotropy linked with the underlying discrete lattice. With increasing temperature, the zigzags and loops of the complex labyrinthine structure roughen and shorten. On a kagome lattice (see Fig. 2.18 c), the stripes are shorter, the labyrinthine pattern is not formed, and the whole configuration is frustrated.

The ground states for in-plane Ising systems on a triangular and a square lattice are shown in Figure 2.19. These are a single domain structure for a triangular geometry and antiparallel lines for a square lattice. The corresponding energies per spin on an infinite lattice are $E_{dip}^{\text{square}} = -2.5494$ for the configuration in Figure 2.19 a, and $E_{dip}^{\text{triangle}} = -2.7585$ for the configuration in Figure 2.19 b. The patterns of Figure 2.19 appear because of an inability to form the ideal configurations of Figure 2.17 for all pairs of spins – that is, because of geometric frustration.

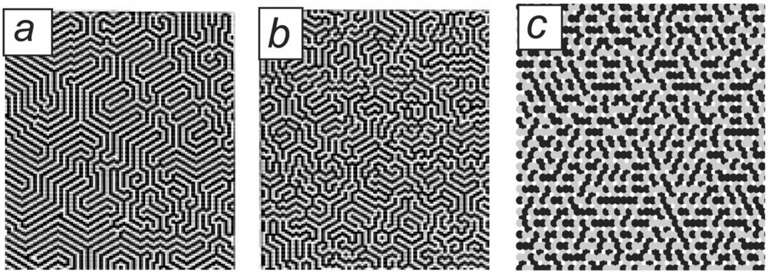

**Fig. 2.18** Pure dipolar coupling: portion of 200×200 vertical Ising spins on a triangular (a, b) and kagome (c) lattice with patterns of up (black) and down (light-gray) spin domains. (a, c) $kT/D = 0.05$; (b) $kT/D = 0.2$.

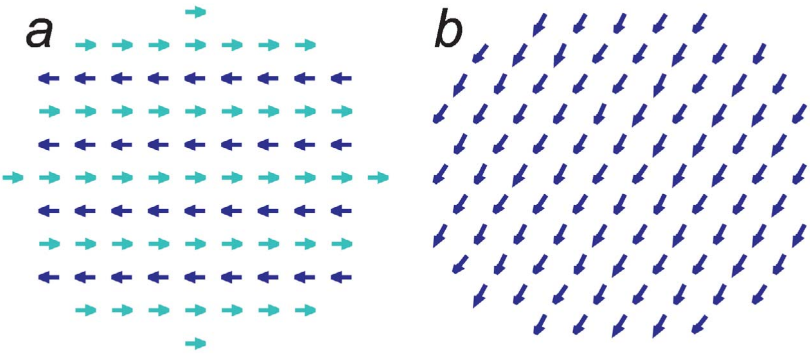

**Fig. 2.19** Zero temperature ground dipolar states for in-plane Ising moments on (a) a square and (b) a triangular lattice.

#### 2.6.1.2 **Localized Vector Moments on a Periodic Lattice**

As shown in the previous section, the in-plane configurations of magnetic/electric moments usually have a lower dipolar energy than an out-of-plane ordering. This becomes even more evident in systems consisting of vector moments that are free to choose any orientation in space. The pure dipolar systems on two-dimensional lattices often demonstrate an in-plane alignment of moments due to an anisotropy arising from the dipole–dipole interactions. In that case, the XY and Heisenberg models lead to very similar ground states.

Another striking feature of the dipolar interaction is that it decreases slowly as a function of the distance. As a consequence, the dipolar field $\mathbf{H}_{dip}(i) = \sum_{i,j}(\mathbf{S}_j/r_{ij}^3 - 3\mathbf{r}_{ij}(\mathbf{S}_j \cdot \mathbf{r}_{ij})/r_{ij}^5)$ experienced by a given moment $\mathbf{S}_i$ depends significantly on the moments located at the boundary of the sample, and this results in the so-called *shape anisotropy*. Shape anisotropy is usually calculated as a difference between the dipolar energy of a most unfavorable and that of a most favorable configuration.

It is well known that the ground state of a dipolar system on a square lattice is antiferromagnetic, just as the in-plane Ising configuration. However, several studies of this ground state have demonstrated that the situation is more subtle than one might initially suppose [52, 53]. The ground state of an infinite square lattice is highly degenerate, and defines a continuous manifold of spin configurations at $T=0$, although the dipolar coupling itself is not rotationally invariant. The same is true for a dipolar system on a honeycomb lattice – for zero temperature the spins lie in the film plane, but the ground state is continuously degenerate [54]. Examples of degenerated configurations are shown in Figure 2.20. The configurations in Figure 2.20 (a, b) have the same energy and are both ground states for a dipolar honeycomb lattice. The right configuration is obtained from the left one by rotation of the sublattice A (blue) by $\phi = +\pi/6$ and the sublattice B (red) by $\phi = \pi/6$ – that is, $\varphi(\mathbf{R}_A) \to \varphi(\mathbf{R}_A) + \phi$ and $\varphi(\mathbf{R}_B) \to \varphi(\mathbf{R}_B) - \phi$. The same transformation has been performed for a square lattice in Figure 2.20 c, d.

At finite temperatures, the situation for the square and the honeycomb symmetry is different. As has been shown by Monte-Carlo calculations and spin wave theory, a magnetic ordering and a critical temperature exist for dipole-coupled spins on a square lattice [53, 55], as the magnetic and temperature excitations are not continuously degenerate. In this case, a quartic shape anisotropy is present, the corresponding easy axes being the edges of the square lattice. In other words, the density of states – and thus the entropy – depends on the magnetic direction within the lattice. This phenomenon is an example of the *order-by-disorder* effect in frustrated magnets [55]. A typical configuration obtained by Monte-Carlo simulations for a finite square lattice at finite temperature is given in Figure 2.21 a. Lines of dipoles are observed at the edges which are formed due to the pole avoidance principle (see Section 1.2.2.1). The microvortex $\phi = 45^\circ$ configuration is formed in the center. Hence, the finite size and temperature remove the continuous degeneracy of the dipolar ground state on a square lattice. These Monte-Carlo data have been recently confirmed by an experimental model made of small magnets which are free to rotate in the XY-plane (see Fig. 2.21 c). A similar structure has

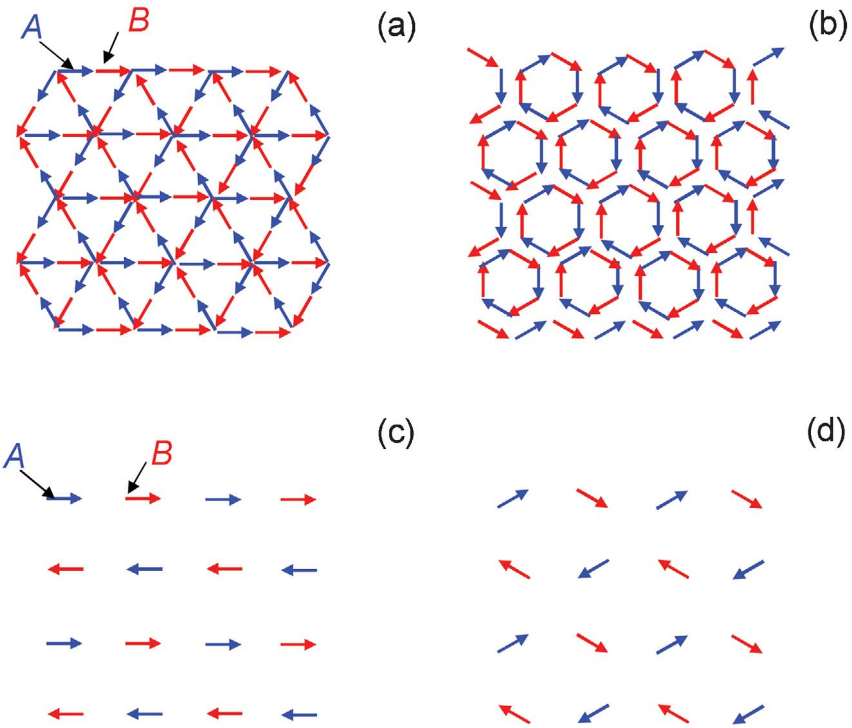

**Fig. 2.20** Two examples of the class of continuously degenerate ground states ($\phi=0$, $\pi/6$) of a dipolar magnet on a honeycomb (a, b) and a square (c, d) lattice.

been found in a nanomagnetic array [56], where the microvortex configuration is addressed as a "spin ice" according to the nomenclature utilized elsewhere [37–39]. The density of states on a honeycomb lattice does not depend on a specific lattice direction, and the ground state is degenerate with respect to continuous rotations of opposite sense on both sublattices [57]. Therefore, a low-temperature Monte-Carlo structure on a honeycomb lattice shows different degenerate states in the same sample (see Fig. 2.21 b).

What question remains as to what happens with dipoles on a triangular and a kagome lattice? For open boundary conditions, a planar vortex structure appears in both cases, which is formed to avoid free magnetic poles at the boundaries of the sample (see Fig. 2.22 a, b). The ground state of an infinite sample is a ferromagnetic-like monodomain structure. Figure 2.22 (c) shows an experimental verification of the dipolar system made from 364 small magnets on a triangular lattice. The Monte-Carlo simulations and the experiment reveal identical structures. Thus, due to the geometric frustration of the lattice – which commonly leads to a disorder or a non-collinearity – the perfectly ordered vortex is formed.

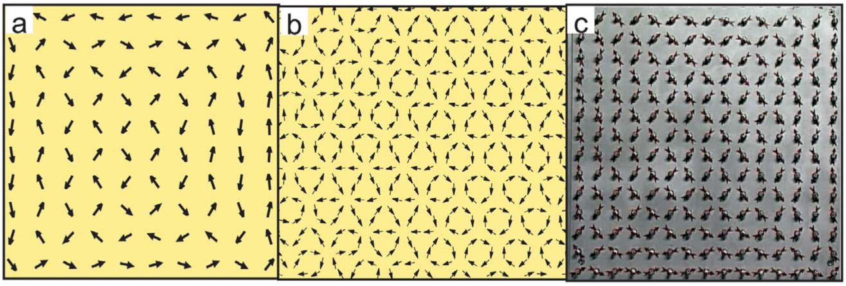

**Fig. 2.21** Pure dipolar coupling: top view of a portion of low-temperature ($kT = 0.05\ D$) Monte-Carlo configuration on (a) a square lattice and (b) a honeycomb lattice. (c) An experimental dipolar model on a square lattice. The model belongs to the physical collection of J. Kirschner at the Max-Planck Institute for Microstructure Physics in Halle, Germany.

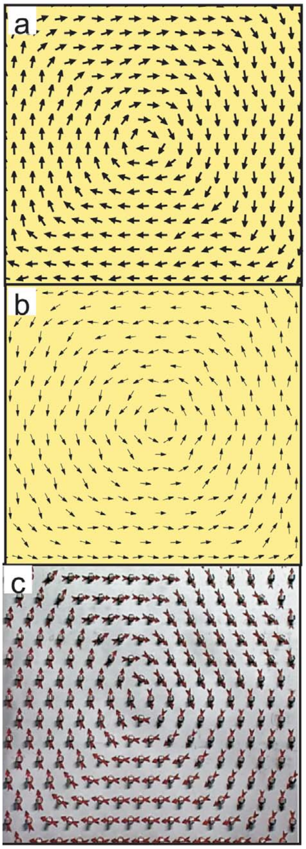

**Fig. 2.22** Pure dipolar coupling: top view of a portion of low-temperature ($kT = 0.05\ D$) Monte-Carlo configuration on (a) a triangular lattice and (b) a kagome lattice. (c) An experimental dipolar model on a triangular lattice. The model belongs to the physical collection of J. Kirschner at the Max-Planck Institute for Microstructure Physics in Halle, Germany.

In conclusion, although the dipolar coupling has an antiferromagnetic nature, the ground states of vector spins for pure antiferromagnetic and pure dipolar interactions are completely different. Square and honeycomb geometries which are unfrustrated in case of pure antiferromagnetic coupling lead to frustrated, non-collinear ground states in the pure dipolar case. Strongly frustrated, non-collinear for a pure antiferromagnetic interaction triangular and kagome lattices lead to ordered collinear low-temperature dipolar configurations.

#### 2.6.1.3 **Localized Vector Moments on Aperiodic Tilings**

An analytical description of the dipolar structure on an aperiodic tiling is hardly feasible, and therefore Monte-Carlo simulations function well to identify equilibrium spin configurations. Especially important is the possibility of introducing temperature into the calculations, as this allows the stability of the obtained structures to be checked. First, we discuss a dipolar magnet on a prominent Penrose tiling, as the theoretical results obtained may be verified using the macroscopic experimental model developed at the Max-Planck Institute for Microstructure Physics in Halle, Germany [23]. This experimental model involves a 480 mm×480 mm Penrose tiling of magnets of 4 mm length separated by 30 mm. The large distance between the magnets is chosen deliberately in order to minimize the multipolar terms that can trap the system into metastable states. The magnets are placed on to nonmagnetic vertical axes and can rotate in the XY plane. Figure 2.23 shows examples of relaxed dipolar configurations obtained in the numerical (Fig. 2.23 a) and in experimental (Fig. 2.23 b) models. Both studies show that, after different relaxation procedures, a magnetic pattern can have a different local arrangement of dipoles, although the total energy is always identical. Thus, the ground state is highly degenerate. All patterns – whether theoretical or experimental – have features in common. Magnetic moments are ordered in circular loops, the diameters of which are identical all over the sample. The loops also overlap, such that the overlapping magnetic decagon chains form a quasiperiodic pattern. This overlapping is not accidental but rather follows certain rules which, amazingly, coincide with the recently proposed "decagonal model" of quasicrystals [58–60]. In 1991, it was realized [58] that the planar Penrose tiling could be generated using a single type of tile, a decagon, with each decagon consisting of Penrose rhombuses (see Fig. 2.7). In contrast to the conventional tiling description, the decagonal atomic clusters overlap, which means that they share atoms with their neighbors. The overlapping rules have been mathematically proven [59]. Only two types of overlap (A and B) are allowed, and the decagons can be easily recognized in the magnetic microstructure of Figure 2.23. The locations of "A" and "B" in a Penrose tiling are marked in Figure 2.23 a.

The most interesting observation about the decagonal structure relates to its stability. In order to observe the time-dependent changes in a magnetic structure in the simulations, an extremely slow annealing procedure has been applied [25]. The overlapping rings of magnetic moments have been found to be very stable.

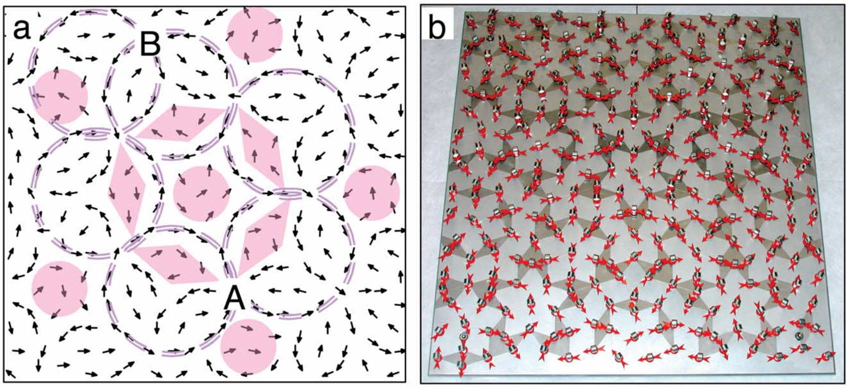

**Fig. 2.23** (a) Monte-Carlo simulations. Top view of the portion of the low-temperature magnetic structure in a sample of finite size for pure dipolar interaction. The microstructure has been obtained for a square sample of about 10500 vector spins on the Penrose tiling. The spins belonging to the perimeter of decagons (marked) form closed chains are stable. The two types of chain overlap are marked as A and B. The spins inside the decagons (marked) are unstable and fluctuate for $kT > 0.3$ D. (b) Experimental model. The perspective view of the magnetic structure. The red arrows represent the orientation of dipolar moments of magnets fixed onto the nodes of the Penrose tiling (rhombuses). The magnets can rotate in the horizontal plane. The model belongs to the physical collection of J. Kirschner at the Max-Planck Institute for the microstructure physics in Halle, Germany.

The decagons can have the same or opposite sense of rotation, although once the sense of the rotation has been chosen it remains unchanged. The orientation of the moments that do not belong to the perimeter of decagons is highly disordered, and varies from cluster to cluster. In a zero magnetic field this state is degenerate and represents manifold spin configurations. Orientations of disordered dipoles are not static at temperatures $kT > 0.2$ D; rather, they change continuously during the Monte-Carlo run while the decagon chains remain stable and the total energy oscillates around its minimal value. In the experimental model, the temperature has been simulated by the application of an alternating magnetic field. When a very weak field is applied the magnetic moments inside the rings begin to oscillate. The moments on the perimeter of decagons, in contrast, remain stable to very high values of the field. In addition to the alternating magnetic field, a constant external magnetic field can be also applied to the structure (see the snapshots for different fields in Fig. 2.24). Even a strongest possible in-plane magnetic field was not enough to destroy the experimental decagonal pattern while the frustrated inner dipoles were immediately aligned (see Fig. 2.24b). In the simulations, the field necessary for alignment of the chains must be at least an order stronger than that needed for alignment of the frustrated moments. Thus, in the quasiperiodic magnetic structure the stable decagonal pattern coexists with a highly frustrated, glass-like phase.

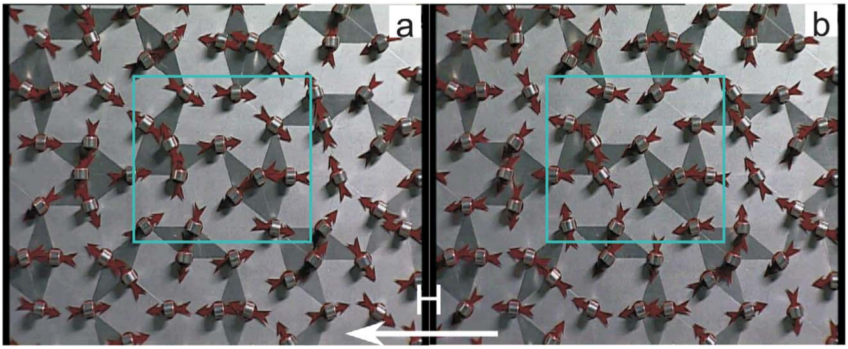

**Fig. 2.24** Two snapshots of a decagon from the experimental model of Figure 2.23 for different strengths of the applied permanent in-plane magnetic field: (a) $H = 0$; (b) $H > 1$ T. Frustrated moments (highlighted) change their orientation while the ring remains stable.

Usually, frustrated systems have either a continuously degenerated, periodic ground state (antiferromagnetic spins on a honeycomb, a kagome, a triangular, and a pyrochlore lattice) or a completely disordered one (spin glasses). The superposition of both types of frustration has not been reported for either periodic or disordered systems. Thus, a magnetic system on a Penrose tiling belongs to a new class of frustrated systems where the degenerated ground state is aperiodic and consists of two parts: ordered decagon rings and disordered spin-glass-like phase inside the decagons. The Penrose tiling is not an exception. The coexistence of ordered and frustrated parts is characteristic of dipolar or antiferromagnetic ensembles on many aperiodic tilings. Two examples are provided in Figure 2.25.

#### 2.6.1.4 **Delocalized Moments with Given Orientation: Two-Dimensional Electron Wigner Crystal**

The systems we have dealt with in previous chapters were restricted to magnetic or electric moments localized on a lattice, and the question posed was “What is the magnetic/electric structure for different lattice symmetries?” Mother Nature offers a variety of other possibilities, however. For example, there are many structures having constituents which can move. These include dipolar and magnetorheological fluids, liquid crystals, gels, water-oil mixtures, or electron-liquids. The orientation of mobile moments may be fixed by an external magnetic/electric field, but one has then an inverse problem – namely, what happens to the spatial ordering of charged particles for a given direction of their moments? The palette of solutions is large and depends on many factors. An example of a system coupled by one single interaction provides electrons that are confined to a two-dimensional surface, that is the so-called two-dimensional electron gas (2DEG).

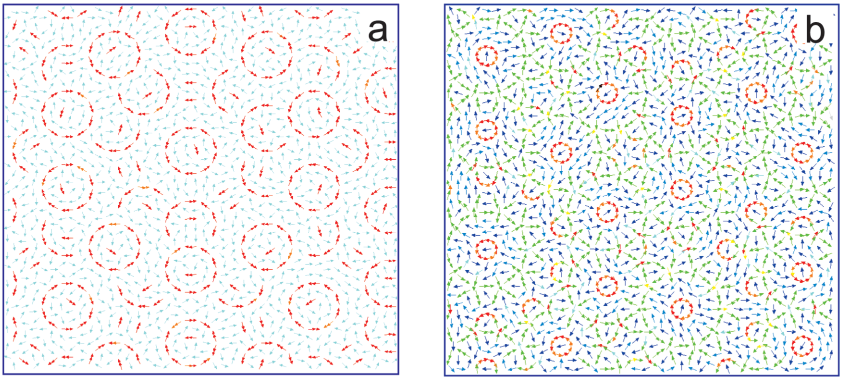

**Fig. 2.25** Portions of the low-temperature pure dipolar configurations for an Anti-Penrose (a) and a Tie-Navette (b) tilings. The color scheme defines an average energy per magnetic moment: from lowest energy (red) to the highest energy (dark blue). Red moments are stable, and blue moments frustrated.

Experimentally, 2DEG can be formed in the presence of a strong magnetic field at the interface between GaAs and AlGaAs layers [61], above the surface of liquid helium [62], or in a microchannel capillary filled with liquid helium [63]. While the electrons are bound in the direction normal to the surface with a binding energy which is of order of 0.6 mEv in case of liquid helium, they are free to move parallel to the surface. For a bound electron the extension of its wave function is at least one order of magnitude smaller than the average distance between electrons. Therefore, the electrons interact like point charges.

Although point charges of the same sign simply repel each other, these classical interactions are strongly influenced by the kinetic energy of the electrons. The thermodynamic state of this classical two-dimensional Coulomb system is determined by the quantity $\Gamma$, which is a measure of the ratio of the Coulomb potential energy to the kinetic energy per particle. For the two-dimensional system this ratio becomes $\Gamma = \frac{\pi^{1/2} N_s^{1/2} e^2}{kT}$, with $N_s$ as the electron areal desnity, $e$ the electron charge, and $kT$ thermal energy. For $\Gamma = 1$, the kinetic energy predominates and the system behaves like an electron gas, whereas at $1 < \Gamma < 100$ the electron motion become liquid-like and for $\Gamma > 100$ the Coulomb energy predominates. The latter case mostly corresponds to our inverse problem as the potential interaction energy strongly dominates but the particles are free to move. In 1934 it was proposed that, for $\Gamma > 100$, the electrons should form an ordered array in three dimensions [64]. An electron-liquid to electron-solid phase transition in a three-dimensional electron system has been predicted to occur at *low* densities. Later, the analogous phase has been found (theoretically) for two-dimensional systems at sufficiently *high* electron densities [65]. The question is, how do the formed two-dimensional periodic array appear? Bearing in mind that all electrons have the same charge,

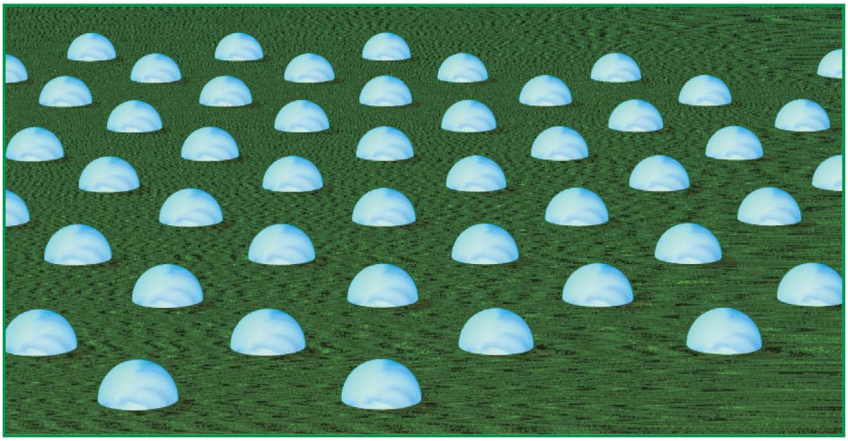

**Fig. 2.26** Two-dimensional electron Wigner crystal on the He surface.

the repulsive Coulomb interaction leads to an ordered array of hexagonal symmetry or to a triangular electron lattice (see Fig. 2.26).

This lattice of electrons, or a Wigner electron crystal, may be detected experimentally by means of so-called plasmon-ripplon modes [62, 66]. When the electrons have formed a crystal, then driving the crystal up and down against the He surface with a uniform electric field can produce a series of resonances due to excitation of the standing capillary waves (ripplons). Standing capillary waves will become resonantly excited when an integral number of capillary-wave wavelengths equals the spacing between the rows of electrons. Another possible means of confirming the existence of the Wigner crystal is to detect the so-called “plasmon modes”; these involve horizontal motions of the electrons due to the external electric field, which is parallel to the He surface, rather than vertical ripplon motions. Indeed, coupled plasmon-ripplon modes have been observed in most experiments.

The detection of a Wigner crystal from the phason-ripplon modes is indirect. Although the direct optical observation of an electronic crystal is still not possible, a two-dimensional Coulomb crystal can be modeled with the help of so-called colloid crystals. These colloidal systems consist of small particles of one material dispersed in a second material [67]. In the most common situation, the particles of the dispersed phase are solid, while the continuous phase, or dispersion medium, is liquid. Colloid dispersions have usually slow dynamics; this corresponds to the case of 2DEG with $\Gamma > 100$. Strictly speaking, apart from the repulsive interactions in the colloidal systems, different types of attractive forces may be present. Moreover, the two interactions can compete, and this topic will be discussed further in Chapter 3 (Section 3.2.5).

## 2.6.2
## Multipolar Interactions: Why Might that be Interesting?

Among the interactions in many-body atomic, molecular or nanoparticle systems, those of electrostatic or magnetostatic nature are very important. Recently, arrays of nanoparticles or adsorbates have been proposed for a number of applications as storage [51], high-speed nonvolatile magnetic memory (MRAM) [52], and logic functions for computations [53]. Different applications require different properties of an array. Whilst in storage applications every particle should be individually addressed (i.e., the nanoelements should not interact), for logic schemes strong interactions are necessary. In both cases the control of interactions between nanoparticles is very important. In order to derive the theory of these interactions one needs to know the charge distribution of a particle. One of the simplest and most effective ways to do this is to describe a distribution of charges as a series of multipole moments. There exist different ways to explain what are the multipole moments; this subject is first addressed from a mathematical point of view.

- Multipole moments: Spherical coordinates

Any two-dimensional periodic function can be expanded in terms of an infinite sum of sines and cosines with corresponding coefficients. This expansion is known as the Fourier series.

$$f(x) = \frac{1}{2} a_0 + \sum_{n=1}^{\infty} a_n \cos(nx) + \sum_{n=1}^{\infty} b_n \sin(nx) \,. \tag{2.17}$$

The coefficients $a_n$ and $b_n$ can be described as integrals of the periodic function Eq. (2.17) multiplied with $\cos(nx)$ or $\sin(nx)$

$$\begin{aligned} a_n &= \frac{1}{\pi} \int_{-\pi}^{\pi} f(x) \cos(nx) dx \,, \\ b_n &= \frac{1}{\pi} \int_{-\pi}^{\pi} f(x) \sin(nx) dx \,. \end{aligned} \tag{2.18}$$

Similarly, any scalar field on a sphere, which is periodic by definition, can be expressed in spherical coordinates $r = f(r, \theta, \varphi)$ (a description of spherical coordinates is provided in Fig. 2.27) as a series of *spherical harmonics* with corresponding coefficients,

$$H(\theta, \varphi) = \sum_{l=0}^{\infty} \sum_{m=-l}^{l} Q_{lm} R_{lm}(r) = \sum_{l=0}^{\infty} \sum_{m=-l}^{l} Q_{lm} Y_{lm}(\theta, \varphi) \frac{4\pi}{2l+1} r^l \,. \tag{2.19}$$

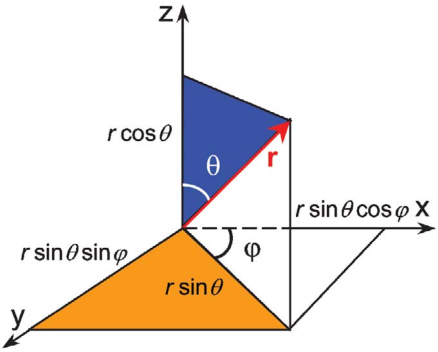

**Fig. 2.27** Definition of the spherical polar coordinates.

The coefficients $Q_{lm}$ are the multipole moments, $R_{lm}(r) = \sqrt{\frac{4\pi}{2l+1}} r^l Y_{lm}(\theta, \varphi)$ are *normalized spherical harmonics*, and $Y_{lm}(\theta, \varphi)$ are *simple spherical harmonics*. The spherical harmonic with $-l < m < l$ is a function of the two coordinates $\theta, \varphi$ on the surface of a sphere and can be modeled by special set of polynomials known as Legendre functions $P_{lm}(\cos\theta)$. Spherical harmonics are natural functions to describe a system with spherical symmetry. For example, with spherical harmonics the 3D motion of an electron around a nucleus can be described. In that case, a spherical harmonic can be thought of as a 3D-path along which a particle can travel without "destroying" itself energetically. This 3D-path is not fixed, and can take on many different shapes, even for one energy level. In this sense the spherical harmonics correspond to the angular part of the atomic orbitals. An example of typical representation of, for example, $d_{z^2}$ orbital in physics is shown in Figure 2.28 a. The orbital corresponds to the spherical harmonic $Y_{20}$, and is uniformly colored as it represents simply a volume of space within which an electron would have a certain probability density of being (the wave-function of electron).

On the other hand, with the spherical harmonics a spatial distribution of electric charges due to a molecule can be represented. In that case, a charge distribution is usually two-colored, as in Figure 2.28 b. The colors correspond to positively and negatively charged parts of the distribution. This representation is typical for quantum chemistry or molecular biology. The multipole expansion plays an important role in the geosciences, and also in cosmology. With help of multipoles, gravity fields can be expanded and the linear polarization of the sky predicted. In the geosciences and astronomy, multipoles are defined with slightly different constants which lead to so-called zonal, tesseral and sectoral representations. A typical zonal image of $Y_{20}$ is provided in Figure 2.28 c. There are many other applications of the multipole calculus throughout the physical sciences, including nuclear physics and radio physics. The graphical representation, however, can be attributed to one of three examples given in Figure 2.28.

Similarly to the Fourier coefficients of Eq. (2.18), a multipole moment is nothing else than a volume integral of a charge distribution multiplied by the normalized spherical harmonic

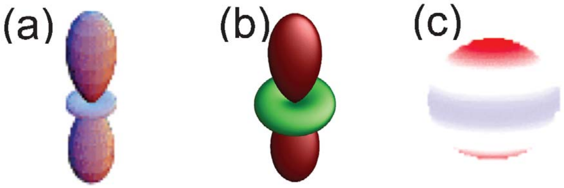

**Fig. 2.28** Representation of the spherical harmonic $Y_{20}$ for the description of (a) atomic orbital, (b) distribution of charges, (c) sky polarization (zonal spherical harmonic).

$$Q_{lm} = \int_V \rho(r) R_{lm}(r) dV \, . \tag{2.20}$$

Hence, the multipoles themselves can be visualized as spherical harmonics, whereupon Figure 2.28 then represents $Q_{20}$.

- Multipole moments: Cartesian coordinates

For calculation of the electrostatic potential $\varphi$ of a charge density $\rho$ at the distance $R \gg r$ where $r$ is the maximal size of the charge distribution $\rho$ in Cartesian coordinates, one can use so-called multipole expansion. An electrostatic potential as a function of $R$ can be expanded in integral powers of a small parameter $r/R$; .e., $\varphi(R)$ can be represented as a number series of a sum where higher terms include higher powers of $r/R$: $\varphi(R) = \varphi_0/R + \varphi_1/R^2 + \varphi_2/R^3 + \dots$ and become less and less important at large distances. This is known as the multipole expansion with:

- 0th order: Monopole potential (falls off like $1/R$, corresponds to $Q_0$)
- 1st order: Dipole potential (falls off like $1/R^2$, corresponds to $Q_1$)
- 2nd order: Quadrupole potential (falls off like $1/R^3$, corresponds to $Q_2$)
- 3rd order: Octopole potential (falls off like $1/R^3$, corresponds to $Q_3$)
- etc…

Shapes of multipoles to the third order in terms of electric charges are shown in Figure 2.29. The first term corresponds to a single charge and is called a "monopole moment"; it is a scalar. The dipole moment is a vector. In general, the order-$n$ term in the sum is the *$2^n$-pole moment* of the configuration of charges.

#### 2.6.2.1 **Multipolar Moments of Molecular Systems and Bose–Einstein Condensates**

Polar molecules with an asymmetric charge distribution – that is, with one end of the molecule relatively negative with respect to the other – possess a permanent dipole moment. Examples are HF, $H_2O$, FCl (where the F atom is negative with respect to the Cl atom), the polyatomic molecule $HCCl_3$ (where the H end of the molecule is positive with respect to the three Cl atoms), three isomers of

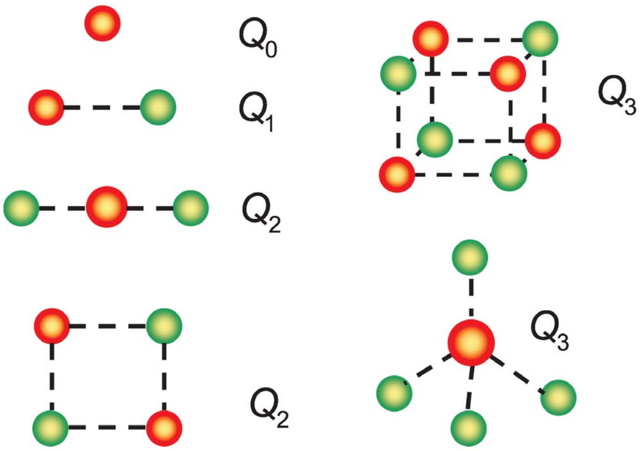

**Fig. 2.29** Possible shapes of multipoles composed of several electric charges. $Q_0$ monopole, $Q_1$ dipole, $Q_2$ quadrupole, $Q_3$ octopole.

1,1-dichloroethene, *cis*-1,2-dichloroethene, *trans*-1,2-dichloroethene, and many others. As a dipole is a vector quantity, a total molecular dipole can be obtained by summing up all individual bond-dipoles, as shown in Figure 2.30.

Although linear molecules such as $CO_2$ or acetylene (H–C≡C–H) and the planar molecule benzene ($C_6H_6$) do not have molecular dipole moments (Fig. 2.30), they have non-zero quadrupole moments [68]. Another example of organic quadrupoles is that of 3,4,9,10-perylenetetracarboxylicdianhydride (better known as PTCDA), which can be adsorbed onto various substrates [69, 70]; $H_2$, $N_2$, CO on salts or metal surfaces; *ortho-para* hydrogen molecules adsorbed onto hexagonal boron nitride, solid hydrogen, $N_2Ar$ mixtures, and many others [71–73]. There exist more complicated cases. For example, the total quadrupole moment of the water molecule is zero. However, $Q_2^{xx}, Q_2^{yy}, Q_2^{xy}, Q_2^{xz}, Q_2^{yz}$ tensor components of the quadrupole moments in Cartesian coordinates have non-zero values. For more symmetrical molecules, the first non-zero multipole moments have higher orders; examples are the methane molecule ($CH_4$) and the giant Keplerate molecule $Fe_{30}$, which has no dipole or quadrupole moment, but has a non-zero octopole moment [74, 75].

More complicated molecular charge distributions have different multipolar contributions. For example, a charged "American football" has non-zero even multipolar contributions $Q_{\text{football}} = Q_0^{\text{football}} + Q_2^{\text{football}} + Q_4^{\text{football}} + Q_6^{\text{football}} + Q_8^{\text{football}} + \ldots$ The same is true for a discus or any other charged object, which is rotationally symmetric and at the same time symmetric around its own equatorial axis. Rotationally symmetric but not equatorially symmetric objects such as a bowling pin possess as even as odd multipolar moments $Q_{\text{b.pin}} = Q_0^{\text{b.pin}} + Q_1^{\text{b.pin}} + Q_2^{\text{b.pin}} + Q_3^{\text{b.pin}} + Q_4^{\text{b.pin}} + \ldots.$

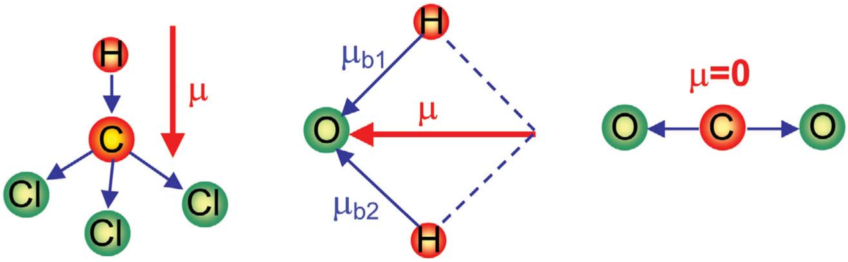

**Fig. 2.30** Molecular dipole moments $\mu$ of polyatomic molecules.

A Bose–Einstein condensate is a phase of matter formed by bosons cooled to temperatures very near to absolute zero. At low temperatures, bosons can behave very differently from fermions because an unlimited number of them can collect into the same energy state – a phenomenon termed "condensation". The first experimental verification of this phase (which had been predicted by A. Einstein and S. Bose) led to the award of the Nobel Prize in Physics for 2001 to Eric A. Cornell, Wolfgang Ketterle and Carl E. Wieman, who succeeded in cooling 2000 rubidium atoms to a temperature less than 100 billionths of a degree above absolute zero. This forced the atoms to lose for 10 s their individual identities and behave as though they were a single "superatom". Nowadays, magneto-optical traps for gas condensation have become much more sophisticated, and the drops of condensate can be arranged in a cubic structure in the potential minima of an optical lattice. Recent experimental and theoretical studies have established that $^{87}$Rb spinor condensate may be ferromagnetic at zero temperature. This means that the expectation value of total spin of a condensate drop $\mathbf{F}$ is finite $\langle \mathbf{F} \rangle \neq 0$ [76, 77]. As a result, an ensemble of condensates acts much like large spins or dipoles on a crystalline lattice. The very latest investigations [78] have shown that, under certain circumstances, Bose–Einstein condensate columns may have quadrupolar moments.

#### 2.6.2.2 **Multipolar Moments of Nanomagnetic Particles**

Magnetic particles with a lateral size less than the characteristic exchange length $d < \chi_{ex}$ have a single domain magnetization configuration with a macroscopic magnetic moment. In case of an ideal single domain, all elementary dipoles inside a particle are compensated, and only appear at the boundary as uncompensated positive and negative magnetic poles (see Fig. 2.31).

Isolated magnetic poles have never been observed in Nature; rather, they always occur in pairs, as in the described example. However, it is often convenient to use instead of magnetic poles and the vector field quantity $\mathbf{H}$ the notion of magnetic charges and a scalar potential $\varphi$. The quantity $\varphi$ is defined so that its negative gradient is the magnetic field $\mathbf{H} = -\nabla\varphi$, where the operator $\nabla$ is $\nabla = \mathbf{i}\frac{\partial}{\partial \mathbf{x}} + \mathbf{j}\frac{\partial}{\partial \mathbf{y}} + \mathbf{k}\frac{\partial}{\partial \mathbf{z}}$. Here, $\mathbf{i}$, $\mathbf{j}$, $\mathbf{k}$ are the unit vectors of a Cartesian coordinate system, and $(x, y, z)$ are the coordinates at the point where the field or potential is under consideration. In the framework of this approximation the macroscopic moment of a polarized or magnetized particle can be obtained by means of the multipole expansion of a continuous magnetization distribution within a dot, as described in Section 2.6.2 (i) or (ii). As can be seen from Eq. (2.20), the strength of a multipole moment depends solely on a charge distribution – that is, on the shape of an object and on its magnetization/polarization configuration. Hence, for typical magnetization distributions corresponding multipolar moments can be calculated on the basis of Eq. (2.20).

Figure 2.31 represents a nanoparticle with $n$-fold symmetry ($n > 1$) within the $x$-$y$ plane, which is magnetized in $z$-direction. The symmetry-axis is parallel to the polarization. The upper surface of the particle is positively charged, with the surface charge density $\sigma = \mu_0 \mathbf{n} \cdot \mathbf{M}(\mathbf{r})$ due to uncompensated dipoles, the unit vector perpendicular to the surface, and the magnetization vector field $\mathbf{M}(\mathbf{r})$. With this definition the unit for the magnetic charge is *Volt-second*, and the magnetic dipole moment is measured in *Volt-second-meter.* The bottom charge is the mirror image of the positive charge distribution at the top of the particle. To find the integral Eq. (2.20) explicitly, the charged surface can be divided into $n$ identical triangles (Fig. 2.31). Then, $Q_{lm}$ are calculated by the sum over the triangles ($0 \leq j \leq n-1$) of the top and bottom surfaces. As the charged surfaces are planar, the volume charge density $\rho$ and the volume integration in Eq. (2.20) can be substituted by the surface charge density $\sigma$ and integration over the surface element $dS$

$$Q_{lm} = \sum_{j=0}^{n-1} \left( \int\limits_{j_{th}\text{top}-\text{triangle}} dS|\sigma(\mathbf{r})|R_{lm}(\mathbf{r}) - \int\limits_{j_{th}\text{bottom}-\text{triangle}} dS|\sigma(\mathbf{r})|R_{lm}(\mathbf{r}) \right). \tag{2.21}$$

After several simplification steps this integral can be evaluated analytically. The details of the calculation can be found in [79].

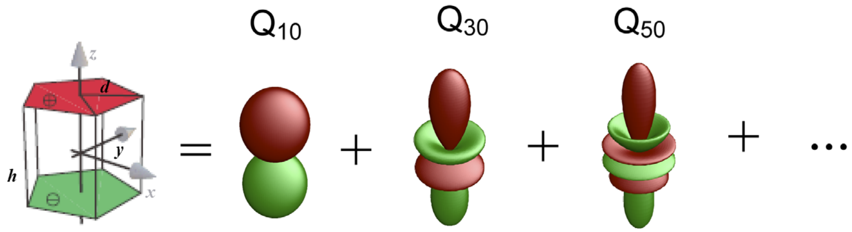

**Fig. 2.31** Scheme of a nanoparticle with $n$-fold symmetry. Every surface can be divided into $n$ equivalent isosceles triangles with edge length $d$. The particle is magnetized in $z$-direction. Such a particle possesses only odd multipolar contributions.

A similar procedure can be applied to the in-plane magnetized discs shown in Figure 2.32. Due to the natural symmetry of a disc it is trivially proportional to $\cos\varphi$ in cylindrical coordinates. Furthermore, the cosine charge distribution can be easily generalized for non-uniform onion states as the charge distribution can be expanded as $\rho(\mathbf{r}) \propto \sum_p c_p \cos^p \varphi$ with expansion coefficients $c_p$. Due to the symmetry of the onion configuration (Fig. 2.32 b), only the odd integer $p$ appears. The non-uniformity of the magnetization increases with increasing $p$. By expressing the volume element and normalized spherical harmonics of Eq. (2.20) in cylindrical coordinates, one obtains the following integral:

$$Q_{lm}^{p} = \mu_0 M_S \int\limits_{-h/2}^{h/2} dz \int\limits_{0}^{2\pi} r_0 d\varphi \left( \cos^p \varphi \cdot R_{lm} \left( \sqrt{r_0^2 + z^2}\,, \frac{\pi}{2} - \arctan \frac{z}{r_0}\,, \varphi \right) \right) . \tag{2.22}$$

The integral in Eq. (2.22) has polynomial solutions for all integers $p$, including $p=1$ for uniform magnetization [80]. The low order moments of a particle in Figure 2.31 (Eq. (2.21)) with fourfold and cylinder symmetry as a function of a surface area and a height are brought together in Table 2.2. The dependency of the strength of multipole moments on the effective aspect ratio $h/a$ of a particle with out-of-plane magnetization (Fig. 2.31) is shown in Figure 2.33 a, and for an in-plane magnetized disc (Fig. 2.32) in Figure 2.33 b.

The most important conclusions are as follows. First, all homogeneously out-of-plane magnetized prismatic particles with even rotational symmetry (Fig. 2.31) and all in-plane magnetized discs (Fig. 2.32) do not possess multipolar moments with even $l$; that is, the quadrupoles ($Q_{20}$), the hexadecapoles ($Q_{40}$) etc. are not allowed (see Fig. 2.31). The lowest moment with $l$ even is $(l, m)=(4, 3)$ for an odd, threefold prism. The first possible multipole moment with even $l$ for a fivefold symmetry is $(l, m)=(6, 5)$. The functions $Q_{lm}(h, a)$ may cross zero. This occurs, for example, with the octopole moments of a cube (see Fig. 2.33 a). For vertically magnetized particles the octopole moment reaches 25% of the dipole moment in the limit of small thicknesses. This

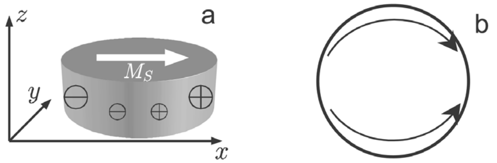

**Fig. 2.32** (a) Scheme of a disk within the *x*-*y*-plane (magnetized in *x*-direction). Due to the magnetization, magnetic surface positive and negative charges emerge. In the case of a uniform magnetization, the charge is cosine distributed. (b) Top view of an onion magnetization configuration.

**Table 2.2** The multipole moments $Q_{lm}$ in units of the surface charge density up to the order $(l, m) = (7,0)$ of isotropically magnetized in $z$-direction particles with fourfold and cylindrical symmetry.

| l | m = 0 (fourfold symmetry) | M = 0 (cylindrical symmetry) |
|---|---|---|
| 1 | $2hd^2$ | $\pi hd^2$ |
| 3 | $hd^2\left(\frac{h^2}{2} - d^2\right)$ | $\frac{\pi}{4}hd^2(h^2 - 3d^2)$ |
| 5 | $\frac{h^5d^2}{8} - \frac{5h^3d^4}{6} + \frac{7hd^6}{12}$ | $\frac{\pi}{16}hd^2(h^4 - 10h^2d^2 + 10d^4)$ |
| 7 | $\frac{h^7d^2}{32} - \frac{7h^5d^4}{16} + \frac{49h^3d^6}{48} - \frac{3hd^8}{8}$ | $\frac{\pi}{64}hd^2(h^6 - 21h^4d^2 + 70h^2d^4 - 35d^6)$ |

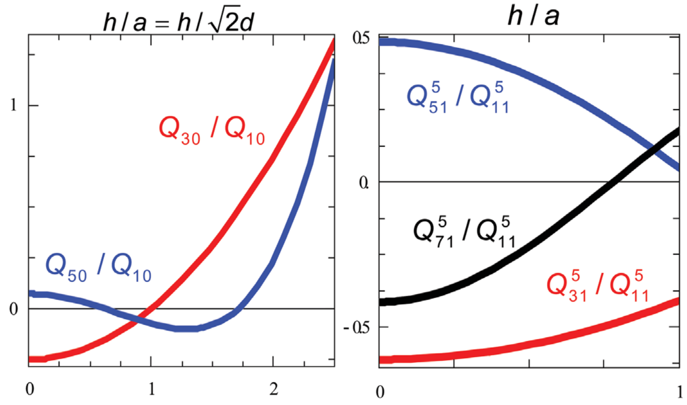

**Fig. 2.33** (a) The low order multipole moments $Q_{lm}$ (normalized to dipolar moment $Q_{10}$) of particles with fourfold symmetry with height $h$ and edge length $a$. For $h \to 0$ $Q_{30} \approx -0.25\ Q_{10}$. (b) The multipole moments $Q^p_{lm}$ in units of the dipolar moment of the in-plane magnetized discs with height $h$ and radius $a$. Magnetization configuration $Q^p_{11}$ is a non-uniform onion state with the measure of the non-uniformity $p$.

geometry corresponds to sizes of particles often used in experimental studies [81–84]. For vertically elongated particles, such as arrays of magnetic nanocolumns [82, 85] or liquid colloidal crystals with rod-like components [86], the magnitude of the octopole moments exceeds that of the dipolar one. Similar results have been obtained for in-plane magnetized dots. For $h \approx a$ the multipolar moments are smaller than the dipolar one. However, in the limit of small thickness ($h \ll r_0$) the octopole moment $Q^p_{31}$ reaches –61% of the dipole moment $Q^p_{11}$ for all odd p, and even the dotriacontapole ($Q^p_{51}$) is of the order of $0.5Q^p_{11}$ (see Fig. 2.33 b). Hence, the multipole moments of ultrathin, in-plane magnetized discs may also be comparable with their dipolar counterparts. The described geometry is typical for on-going experimental studies on magnetic arrays.

#### 2.6.2.3 **Multipole–Multipole Interactions**

By knowing the multipole moments of two particles, the multipole–multipole interaction energy can be calculated. The most general formulation of the interaction energy between two non-intersecting charge distributions is given by [87]:

$$E_{AB} = \frac{1}{4\pi\mu_0} \sum_{l_A l_B m_A m_B} T_{l_A l_B m_A m_B}(R_{AB}) Q^A_{l_A m_A} Q^B_{l_B m_B} \tag{2.23}$$

with the geometric interaction tensor $T_{l_A l_B m_A m_B}$ [68, 88]

$$T_{l_A l_B m_A m_B}(\mathbf{R}_{AB}) = \\ (-1)^{-l_B} l^*_{l_A+I_B m_A+m_B}(\mathbf{R}_{AB}) \sqrt{\frac{(l_A+l_B-m_A-m_B)!(l_A+l_B+m_A+m_B)!}{(l_A-m_A)!(l_B-m_B)!(l_A+m_A)!(l_B+m_B)!}} \, . \tag{2.24}$$

The multipole–multipole interaction is long-ranged, and therefore for an ensemble of particles having higher-order multipolar contributions the coupling between every pair of constituents must be calculated. For large systems this is impossible, although the strength of the interaction between higher-order multipoles decreases rather quickly with distance. This dependence on distance is given by the complex conjugate of the irregular normalized spherical harmonic function

$$I^*_{l_A+l_B m_A+m_B}(\mathbf{R}_{AB}) = \sqrt{\frac{4\pi}{2l+1}} \frac{Y_{lm}(\theta,\varphi)}{r^{l+1}} \, . \tag{2.25}$$

From Eqs. (2.24) and (2.25) it follows that the interaction energy between moments $Q^A_{l_A}$ and $Q^B_{l_B}$ of order $l_A$ and $l_B$ respectively decreases with increasing distance as $R_{AB}^{l_A+l_B+1}$. Consequently, higher-order multipole moments are important for $R \geq d$. Therefore, for multipoles of order $l \geq 3$ a so-called cut-off procedure is appropriate – that is, the calculations of interaction energy may be restricted to several nearest neighbors only. In order to calculate the ground states of multipolar systems, it is necessary either to guess a configuration, to calculate its energy and compare with other guesses, or to introduce the Hamiltonian (Eq. (2.24)) into the Monte-Carlo scheme [89].

#### 2.6.2.4 **Ground States for Multipoles of Even Symmetry: Quadrupolar and Hexadecapolar Patterns**

Figure 2.34 shows the low-temperature Monte-Carlo configurations of a pure quadrupolar system on a triangular and a square lattice for three-dimensional and *XY* planar moments [90]. The consideration is restricted to rotationally symmetric $Q_{20}$ quadrupoles observed in Nature [69, 71, 91, 92]. For 3D moments on a triangular lattice, a long-range, 3D configuration consisting of seven-atomic rotors or “pinwheels”, with the central atom oriented vertically and the others lying in the film plane, has a minimal energy (Fig. 2.34 a). The vertical moments form a triangular superstructure which corresponds to the so-called “4-phase” of hydrogen molecules on a triangular lattice found in mean-field and molecular-dynamics approximations [72, 73]. Every vertical quadrupole occupies the center of a hexagonal pinwheel. For an ideal configuration, every pinwheel element belongs simultaneously to two adjacent pinwheels – that is, the unit cell has three in-plane moments and one vertical moment. Therefore, the perfectly ordered pinwheel phase has an average vertical projection per moment $\langle Q_{20z} \rangle = 0.25$.

The three-dimensional pinwheel structures have been observed experimentally, by means of nuclear magnetic resonance spectroscopy studies in *ortho*-hydrogen adsorbates [93] and $Ar_{1\text{-}x}(N_2)_x$ quantum crystals [71, 72, 93]. Hence, the symmetry of the ground state confirms the pure quadrupolar nature of the pinwheel phase in those systems. The phase is double degenerate as the rotors can have either a clockwise or counter clockwise sense of rotation. In contrast to previous studies [72, 73], a 3D quadrupolar system on a triangular lattice easily admits domains

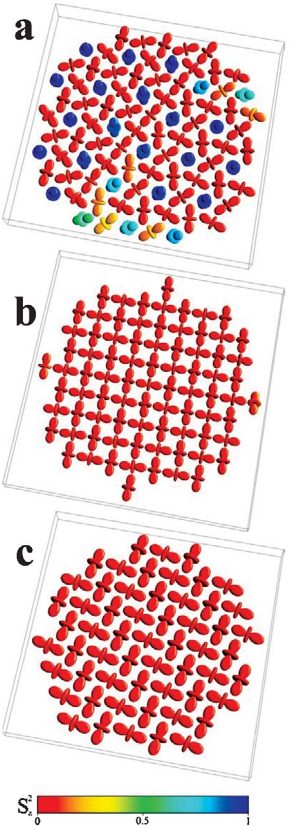

**Fig. 2.34** The low-temperature pure quadrupolar Monte-Carlo configurations on a triangular (a, c) and a square (b) lattice. The quadrupoles are represented by the spherical harmonic $Y_{20}$ corresponding to the equipotential surface of a charge distribution with $Q_{20}$ quadrupole moments; the two clubs represent positive charge, while the belly is negatively charged. The color scheme denotes the squared vertical component of the projection of a moment. The quadrupoles are 3D moments in (a, b) and XY moments in (c).

(Fig. 2.34 a), with different senses of rotation. A domain wall consisting of moments with T-like mutual orientation is formed between the domains (Fig. 2.34 a). The T-orientation is the energetically most favorable one for two quadrupoles. Therefore, the total energy of the domain structure is close to that of a monodomain, while the entropy of the domain structure is higher. According to the principle of maximal entropy, the domain structure represents the state of lowest free energy at finite temperatures. Crossing of the domain walls is, however, not allowed as this will lead to an increase in internal energy due to the deviation of moments from their equilibrium orientation in the neighborhood of the crossing point. Two parallel domain walls cannot come closer than two primitive cells of the pinwheel structure ($4a$) without increasing the internal energy of the system. Therefore, the low-temperature configuration of a large $Q_{20}$ quadrupolar system on a triangular lattice consists of an array of clock-wise and counter-clockwise “pinwheel” domains separated by parallel domain walls.

In contrast to the triangular lattice, the ground state configuration of quadrupoles on a square lattice is completely planar (Fig. 2.34 b). The twofold lattice symmetry permits the T-configuration for every pair of nearest neighbors; that is, the configuration is non-frustrated and monodomain. As the moments have not been constrained to lie in the XY plane it can be concluded that the quadrupolar interaction induces very strong easy-plane anisotropy for a square lattice. As this is not the case for a triangular lattice, a low-temperature configuration of a quadrupolar *XY* system with threefold symmetry has been additionally calculated. Experimentally, this situation corresponds, for example, to organic PTCDA molecules adsorbed onto Ag(111) [69] having some freedom of the rotation only in the XY-plane. The calculated ground state configuration is given in Figure 2.34 c. Instead of the pinwheel phase, we find a “herringbone” structure consisting of lines of quadrupoles with two possible orientations. The moments make an angle of 15° to the principal lattice axes, and 45° to the direction joining the atomic sites. Within the accuracy of calculations the angle between two adjacent rows of moments is exactly 90°. The “herringbone” pattern found in these simulations is very similar to that reported in [69]. However, the molecules in the experiment are oriented parallel to the principal axes and, consequently, the mutual angle between the rows is 60°. The analytical calculation of the energies for all possible relative orientations of rows of the “bones” shows that the absolute minimum belongs to the Monte-Carlo solution with the angle of 90°. From this finding it can be concluded that the configuration of [69] cannot be explained only from the minimization of electrostatic interactions originating from the quadrupolar field of a molecule. One possible explanation is that rotation of the molecules is not free, but another is that the molecules possess higher-order multipolar contributions.

Hexadecapolar ($Q_{40}$) ground states on a triangular and a square lattice for moments which are free to rotate in the 3D space are given in Figure 2.35. Both configurations are planar, and a “herringbone” structure consisting of lines of hexadecapoles with two possible orientations is formed on both lattices. For a triangular lattice, the moments make angles of 69° and 157° to the X axis, while

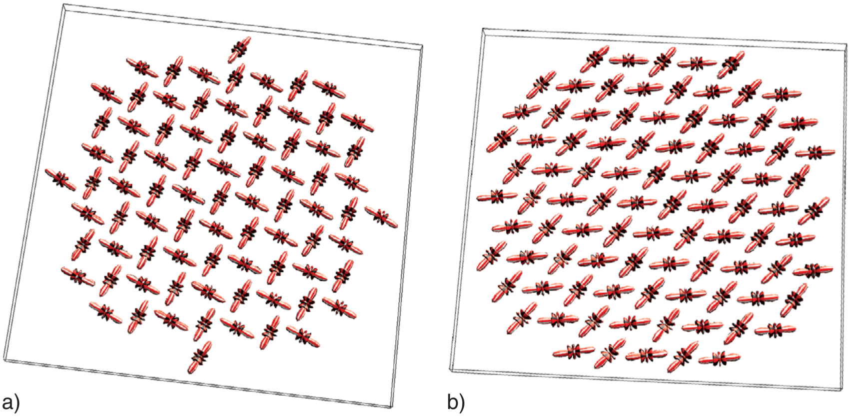

**Fig. 2.35** The low-temperature pure hexadecapolar Monte-Carlo configurations on a square (a) and a triangular (b) lattice. The hexadecapoles are represented by the spherical harmonic $Y_{40}$ corresponding to the equipotential surfaces of a charge distribution with $Q_{40}$ moments; the two white-gray clubs represent positive charge, while the bellies are alternately positively (white-gray) or negatively (black-gray) charged. Top perspective view of a portion of a configuration. The hexadecapoles were free to rotate in space. However, the configurations are planar.

for a square symmetry angles of 9.5° and 49.5° are favorable. Within the accuracy of calculations [90], the angle between two adjacent rows of moments are 88° and 40°, correspondingly. Hence, a hexadecapolar contribution supports the herringbone structure of a planar pure quadrupolar state on a triangular lattice (Fig. 2.34 c). However, the symmetry of the structure changes significantly. Thus, the higher-order $Q_{40}$ contribution is another possible explanation for the experimentally found herringbone pattern of PTCDA adsorbates.

#### 2.6.2.5 Ground States for Multipoles of Odd Symmetry: Octopolar and Dotriacontapolar Patterns

The octopolar moments ($Q_{3m}$) are unidirectional – that is, they can be represented as vectors. The low-temperature configurations consist of moments oriented in principal directions of the underlying lattice, and hence the octopolar interaction introduces not only an easy-plane but also a three- and twofold in-plane anisotropy, respectively. On a square lattice, octopoles form lines being aligned antiparallel (such as in Fig. 2.19 a), whilst on a triangular lattice the domains show parallel alignment of the moments (Fig. 2.19 b). The dotriacontapolar interactions ($Q_{5m} - Q_{5m}$) break the isotropic behavior of dipoles on square and triangular lattices in the same way. Anti-parallel alignment is one of the ground states of an *infinite* pure dipolar system on a square lattice [53], whilst on its triangular counterpart the ferromagnetic alignment has minimal energy. Hence, the octopolar interaction selects some of the dipolar ground states. The principal difference between the two interactions is that the dipolar energy, because of its long-range character, can be minimized, thereby avoiding free poles in *finite* samples. Due to this property a vortex on a triangular and a microvortex state on a square lattices are formed in finite dipolar systems (see Section 2.6.1.2). A finite octopolar system, in contrast, in most geometries is not sensitive to the formation of free poles. The main reason for this is that octopoles do not interact with a field but rather with the field curvature. Therefore, the gain in internal energy due to the compensation of free magnetic poles at the sample boundary is weaker than for pure dipolar systems, and low-temperature configurations in finite samples are still parallel lines for a triangular and antiparallel lines for a square lattice.

## 2.7
## Summary

Despite the increasing configurational entropy, systems with three-dimensional freedom of orientation are often more ordered than Ising-like systems. The reasons for such phenomena include order by disorder, and order by frustration. The self-competition due to geometric frustration may lead to a number of non-trivial ordered patterns in nanosystems, and can alter macroscopic properties such as switching behavior or thermal stability.

## 2.8
## Exercises

1. Calculate the configurational entropy of the structure in Figure 2.21 c.

*Solution*

Every magnetic moment on the lattice may have four possible configurations. The total number of all possible states for a lattice with $N$ moments is $4^N$. Thus, the configurational entropy is $S = k \ln W = k \ln 4^N$.

2. Bipartite lattices can be decomposed into two sublattices, such that the spins on the A sublattice interact only with the spins on B sublattice. Then, if the short-range exchange interaction is antiferromagnetic – that is, the sign of $J$ favors antiparallel alignment of vectors – a simple “gauge” transformation can transform the model into a ferromagnet in the new, transformed spins. Which “gauge” transformation could convert the structure (Fig. 2.21 c) into a “ferromagnet”?

*Solution*

In case of collinear configurations it is usually sufficient to apply a gauge transformation to one of the sublattices. In this non-collinear case, such a simple transformation is not enough. In order to obtain new spin variables $S(\mathbf{r})$, all oriented in the same direction, initial spin variables $\sigma$ must be transformed as

$S_x(\mathbf{r}) = (-1)^{n_y}\sigma_x(\mathbf{r})$ and $S_y(\mathbf{r}) = (-1)^{n_x}\sigma_y(\mathbf{r})$, where $n_x$ and $n_y$ are the numbers of rows in $x$ and $y$ direction.

3. Calculate multipole moments $Q_{lm}$ of the linear change distribution $Q_2$ given in Figure 2.29 for two cases: (a) the charge distribution is parallel to the $z$-axis; (b) the charge distribution is parallel to the $y$-axis. Consider the central charge as $-2q$, while all of the two other charges are $+q$. The distance between the smaller charges is $2a$.

*Solution*

$$\text{(a)} \quad Q_{lm} = \sum_i q_i r_i^l Y_{lm}(\theta_i, \varphi_i) = -2qY_0^0 + qa^l\{Y_l^m(0,0) + Y_l^m(\pi, 0)\}\ ,$$

$$Y_l^m(\theta, \varphi) = \sqrt{\frac{2l+1}{4\pi}\frac{(l+m)!}{(l-m)!}}P_l^m(\cos\theta)e^{im\varphi}\ .$$

Hence,

$$Q_{lm} = -2q\frac{1}{2\sqrt{\pi}} + qa^l\left[\frac{2l+1}{4\pi}\right]^{1/2}(P_l^m(0) + P_l^m(\pi))$$

with

$$P_l^m(x) = (-1)^m(1-x^2)^{m/2}\frac{d^m}{dx^m}P_l(x)\ \text{(Rodriges' formula)}\ .$$

For axially symmetric charge distributions the multipole moments are nonzero only for $m = 0$, therefore $P_l^0(1) = (-1)^0(1-x^2)^{0/2}\frac{d^m}{dx^m}P_l(1) = P_l(1)$ and $P_l^0(-1) = p_l(-1)$.

Finally, $Q_l^0 = -\frac{2q\delta_{l0}}{\sqrt{4\pi}} + qa^l\sqrt{\frac{2l+1}{4\pi}}(P_l(1) + P_l(-1))$. As $P_l(-1) = (-1)^l P_l(1)$ and $P_l(1) = 1$ $Q_l^0$ is nonzero only for even l. It is then equal to $Q_l^0 = 2qa^l\sqrt{\frac{2l+1}{4\pi}}$, i.e., l cannot be smaller than zero.

$$\begin{aligned}
\text{(b)} \quad Q_{lm} &= -2q\frac{\delta_{l0}}{2\sqrt{\pi}} + qa^l\left[Y_l^m\left(\frac{\pi}{2}, 0\right) + Y_l^m\left(\frac{\pi}{2}, \pi\right)\right] \\
&= -2q\frac{\delta_{l0}}{2\sqrt{\pi}} + qa^l\sqrt{\frac{2l+1}{4\pi}\frac{(l-m)!}{(l+m)!}}P_l^m(0)(e^{i0\varphi} + e^{i\pi\varphi}) \\
&= -2q\frac{\delta_{l0}}{2\sqrt{\pi}} + qa^l\sqrt{\frac{2l+1}{4\pi}\frac{(l-m)!}{(l+m)!}}P_l^m(0)(1 + (-1)^m)\ .
\end{aligned}$$

Hence, the higher order multipole moments are nonzero only for $m$-even. In addition, from Rodriges' formula $P_l^m(0)$ differs from zero only for $l + m = even$, therefore $l$ should also be even.

## References

1 G. Toulouse, *Commun. Phys.* **1977**, *2*, 99.
2 C. Lacroix, Magnetic Systems: Lattice Geometry originated Frustration. In: *Encyclopedia of Materials: Science and Technology Updates*, Elsevier, Oxford, **2005**.
3 S.C. Abrahams, L. Guttman, J. S. Kasper, *Phys. Rev.* **1962**, *127*, 2052.
4 U. Gonser, et al., *J. Appl. Phys.* **1963**, *34*, 2373.
5 A. Kubetzka, et al., *Phys. Rev. Lett.* **2005**, *94*, 87204.
6 W. Heisenberg, *Z. Phys.* **1928**, *49*, 619.
7 B.P. Burton, Order-disorder Phenomena and Phase Separation. In: *Encyclopedia of Materials*, K.H.J. Buschow, R.W. Cahn, M.C. Flemings, B. Ilschner, E.J. Kramer, S. Mahajan, P. Veyssière (Eds.), Elsevier, Oxford, **2003**.
8 K. Binder (Ed.) Applications of the Monte Carlo method in statistical physics. In: *Topics in Current Physics*, Springer, Berlin, **1987**.
9 J.J. Binney, N.J. Dowrick, A.J. Fisher, M.E.J. Newman, *The theory of critical phenomena: An introduction to the renormalization group*, Oxford University Press, Oxford, **1998**.
10 N.D. Mermin, H. Wagner, *Phys. Rev. Lett.* **1966**, *17*, 1133.
11 E.Y. Vedmedenko, U. Grimm, R. Wiesendanger, *Phys. Rev. Lett.* **2004**, *93*, 76407.
12 S. Kobe, T. Klotz, *Phys. Rev. E* **1995**, *52*, 5660.
13 S. Kobe, K. Handrich, *Phys. Stat. Sol. (b)* **1976**, *76*, K65.
14 D. Greywall, P. Busch, *Phys. Rev. Lett.* **1989**, *62*, 1868.
15 J. Atwood, *Nature Materials* **2002**, *1*, 91.
16 R.P. Millane, A. Goyal, R.C. Penney, *Phys. Lett. A* **2003**, *311*, 347.
17 G.H. Wannier, *Phys. Rev.* **1950**, *79*, 357.
18 M. Mekata, *Phys. Today* **2003**, *February*, 12.
19 I. Syôzy, *Prog. Theoret. Phys.* **1951**, *6*, 306.
20 R. Liebmann, Statistical mechanics of periodic frustrated Ising systems. In: *Lecture notes in physics*, H. Araki, J. Ehlers, K. Hepp, R. Kippenhahn, H.A. Weidenmüller, J. Zittartz (Eds.), Springer, Berlin, **1986**.
21 C. Godréche, J.M. Luck, H. Orland, *J. Stat. Phys.* **1986**, *45*, 777.
22 E.Y. Vedmedenko, Quasicrystals: Magnetism. In: *Encyclopedia of Materials: Science and Technology Updates*, Elsevier, Oxford, **2005**.
23 E.Y. Vedmedenko, H.P. Oepen, J. Kirschner, *Phys. Rev. Lett.* **2003**, *90*, 137203.
24 G.G. Naumis, R.A. Barrio, C. Wang, *Phys. Rev. B* **1994**, *50*, 9834.
25 E.Y. Vedmedenko, *Ferroelectrics* **2004**, *305*, 129.
26 U. Grimm, M. Baake, Aperiodic Ising Models. In: *The Mathematics of Long-Range Aperiodic Order*, R.V. Moody (Ed.), Kluwer, Dordrecht, **1997**.
27 E.Y. Vedmedenko, U. Grimm, R. Wiesendanger, *Phys. Rev. Lett.* **2004**, *93*, 76407.
28 K. Niizeki, *J. Phys. A: Math. Gen.* **1990**, *23*, 5011.
29 M. Baake, D. Joseph, *Phys. Rev. B* **1990**, *42*, 8091.
30 P. Kurz, B. Bihlmayer, K. Hirai, S. Blügel, *Phys. Rev. Lett.* **2001**, *86*, 1106.
31 F. Keffer, in: *Handbuch der Physik XVIII/2*, S. Flugge, H. P. Wijn (Eds.), Springer, Berlin, **1966**.
32 S. Shakravarty, B.I. Halperin, D.R. Nelson, *Phys. Rev. B* **1988**, *60*, 1057.
33 P. Chandra, P. Coleman, I. Ritchey, *J. Physique* **1993**, *3*, 591.
34 S.E. Palmer, J.T. Chalker, *Phys. Rev. B* **2000**, *62*, 488.
35 A. Chubukov, *Phys. Rev. Lett.* **1992**, *69*, 832.
36 J. Delft, C.L. Henley, *Phys. Rev. B* **1993**, *48*, 965.

**37** M.J. Harris, S.T. Bramwell, D.F. McMorrow, T. Zeiske, K.W. Godfrey, *Phys. Rev. Lett.* **1997**, *79*, 2554.

**38** M.J. Harris, S.T. Bramwell, P.C.W. Holdsworth, J.D.M. Champion, *Phys. Rev. Lett.* **1998**, *81*, 4496.

**39** A.S. Wills, R. Ballou, C. Lacroix, *Phys. Rev. B* **2002**, *66*, 144407.

**40** A.B. Harris, C. Kallin, A.J. Berlinsky, *Phys. Rev. B* **1992**, *45*, 2899.

**41** Ch. Waldtmann, et al., *Eur. Phys. J. B* **1998**, *2*, 501.

**42** E.Y. Vedmedenko, U. Grimm, R. Wiesendanger, *Phil. Mag.* **2006**, *86*, 733.

**43** S. Blügel, M. Weinert, P.H. Dederichs, *Phys. Rev. Lett.* **1988**, *60*, 1077.

**44** N.W. Ashcroft, N.D. Mermin, *Solid State Physics*, Holt, Rinehart and Winston, New York, **1973**.

**45** Ph. Kurz, G. Bihlmayer, K. Hirai, S. Blügel, *Phys. Rev. Lett.* **2001**, *86*, 1106.

**46** R. Moessner, J.T. Chalker, *Phys. Rev. Lett.* **1998**, *80*, 2929.

**47** I. Mirebeau, I.N. Goncharenko, P. Cadavez-Peres, S.T. Bramwell, M.J.P. Gingras, J.S. Gardner, *Nature* **2002**, *420*, 54.

**48** E.Y. Vedmedenko, A. Ghazali, J.C.S. Lévy, *Surf. Sci.* **1998**, *402–404*, 391.

**49** K. Nielsch, et al., *J. Magn. Magn. Mater.* **2002**, *249*, 234.

**50** R.E. Rosensweig, M. Zahn, R. Shumovich, *J. Magn. Magn. Mater.* **1983**, *39*, 127.

**51** J.-C. Bacri, R. Perzynski, D. Salin, *Recherche* **1987**, *18*, 1150.

**52** V.M. Ogenko, V.M. Rosenbaum, A.A. Chuiko, *Theory of oscillations and reorientations in atomic groups at the surface* (in Russian), Naukova Dumka, Kiev, **1991**.

**53** K. De'Bell, A.B. MacIsaac, I.N. Booth, J.P. Whitehead, *Phys. Rev. B* **1997**, *55*, 15108.

**54** G.O. Zimmerman, A.K. Ibrahim, F.Y. Wu, *Phys. Rev. B* **1988**, *37*, 2059.

**55** S. Prakash, C.L. Henley, *Phys. Rev. B* **1990**, *42*, 6574.

**56** R.F. Wang, C. Nisoli, R.S. Freitas, J. Li, W. McConville, B.J. Cooley, M.S. Lund, N. Samarth, C. Leighton, V.H. Crespi, P. Schiffer, *Nature* **2006**, *439*, 303.

**57** H.B. Braun, B. Roessli, unpublished results.

**58** S.E. Burkov, *Phys. Rev. Lett.* **1991**, *67*, 614.

**59** P. Gummelt, in: *Proceedings of the 5th International Conference on Quasicrystals*, C. Janot, R. Mosseri (Eds.), World Scientific, Singapore, **1995**.

**60** K.W. Urban, *Nature* **1998**, *396*, 14.

**61** C.C. Li, J. Yoon, L.W. Engel, D. Shahar, D.C. Tsui, M. Shayegan, *Phys. Rev. B* **2000**, *61*, 10905.

**62** C.C. Grimes, G. Adams, *Phys. Rev. Lett.* **1979**, *42*, 795.

**63** P. Glasson, et al., *Phys. Rev. Lett.* **2001**, *87*, 176802.

**64** E.P. Wigner, *Phys. Rev.* **1934**, *46*, 1002.

**65** R.S. Crandall, R. Williams, *Phys. Lett.* **1971**, *34A*, 404.

**66** V.B. Shikin, *JETP Lett.* **1974**, *19*, 335.

**67** P.N. Pusey, Colloidal Systems: Ordered. In: *Encyclopedia of Materials: Science and Technology Updates*, Elsevier, Oxford, **2005**.

**68** A.J. Stone, *The Theory of Intermolecular Forces*, Clarendon Press, Oxford, **1996**.

**69** M. Eremtchenko, J.A. Schaefer, F.S. Tautz, *Nature* **2003**, *425*, 602.

**70** F. Würthner, *Chem. Commun.* **2004**, *1*, 1564.

**71** K. Kim, N.S. Sullivan, *J. Low Temp. Phys.* **1999**, *114*, 173.

**72** S. Raugei, G. Cardini, V. Schettino, *J. Chem. Phys.* **1997**, *106*, 8196.

**73** A.J. Berlinsky, A.B. Harris, *Phys. Rev. Lett.* **1978**, *40*, 1579.

**74** S.F. O'Shea, *J. Chem. Phys.* **1979**, *71*, 2399.

**75** A.S. Mishenko, A.S. Chernyshov, A.K. Zvezdin, *Europhys. Lett.* **2004**, *65*, 116.

**76** K. Gross, C.P. Search, H. Pu, W. Zhang, P. Meystre, *Phys. Rev. A* **2002**, *66*, 033603.

**77** V. Dunjko, V. Lorent, M. Olshanii, *Phys. Rev. Lett.* **2001**, *86*, 5413.

**78** K. Bongs, unpublished results.

**79** N. Mikuszeit, E.Y. Vedmedenko, H.P. Oepen, *J. Phys.: Condens. Matter* **2004**, *16*, 9037.

**80** N. Mikuszeit, E.Y. Vedmedenko, H.P. Oepen, R. Wiesendanger, *J. Appl. Phys.* **2005**, *97*, 101502.

**81** T. Aign, P. Meyer, S. Lemerle, J.P. Jamet, J. Ferré, V. Mathet, C. Chappert, J. Gierak, C. Vieu, F. Rousseaux, H. Launois, H. Bernas, *Phys. Rev. Lett.* **1998**, *81*, 5656.

**82** C.A. Ross, M. Hwang, M. Shima, J.Y. Cheng, M. Farhoud, T.A. Savas, H.I. Smith, W. Schwarzacher, F.M. Ross, M. Redjdal, F.B. Humphrey, *Phys. Rev. B* **2002**, *65*, 144417.

**83** J.P. Jamet, S. Lemerle, P. Meyer, J. Ferré, B. Bartenlian, N. Bardou, C. Chappert, P. Veillet, F. Rousseaux, D. Decanini, H. Launois, *Phys. Rev. B* **1997**, *57*, 14320.

**84** K. Koike, H. Matsuyama, Y. Hirayama, K. Tanahashi, T. Kanemura, O. Kitakami, Y. Shimada, *Appl. Phys. Lett.* **2001**, *78*, 784.

**85** K. Nielsch, R.B. Wehrspohn, R. Barthel, J. Kirschner, S.F. Fischer, H. Kronmüller, T. Schweinböck, D. Weiss, U. Gösele, *J. Magn. Magn. Mater.* **2002**, *249*, 234.

**86** J.S. van Duijneveldt, A. Gil-Villegas, G. Jackson, M.P. Allen, *J. Chem. Phys.* **2000**, *112*, 9092.

**87** P. Popelier, D. Kosov, *J. Chem. Phys.* **2001**, *114*, 6539.

**88** D.A. Varsalovich, A.N. Moskalev, V.K. Khersonskii, *Quantum Theory of Angular Momentum*, World Scientific, Singapore, **1988**.

**89** E.Y. Vedmedenko, N. Mikuszeit, H.P. Oepen, R. Wiesendanger, *Phys. Rev. Lett.* **2005**, *95*, 207202.

**90** E.Y. Vedmedenko, unpublished results.

**91** I.E. Dzyaloshinskii, E.I. Kats, J. Lajzerowicz, *JETP Lett.* **1998**, *68*, 785.

**92** V.E. Klymenko, V.M. Rosenbaum, V.V. Kukhtin, O.V. Schramko, *Sol. State Commun.* **1993**, *88*, 373.

**93** J.A. Hamida, N.S. Sullivan, M.D. Evans, *Phys. Rev. Lett.* **1994**, *73*, 2720.

# 3

# Competition Between a Short- and a Long-Range Interaction

Diverse systems in physics and chemistry display a remarkable variety of ordered patterns having common structural features as stripes, labyrinths, bubbles or vortices on scales from several nanometers to several centimeters (see Fig. 3.1). The structural similarity suggests a possible universal underlying mechanism. As follows from numerous investigations, those patterns arise from the competition between short- and long-range interactions with the Hamiltonian

$$\mathbf{H} = H_{\text{short}} + H_{\text{long}} . \tag{3.1}$$

Short-range interactions [the first term in Eq. (3.1)] include magnetic exchange, van der Waals attractive interactions, the short-range part of Coulomb interaction, the attractive part of the Lennard–Jones potential, and hard-core steric repulsion. Magneto- and/or electrostatic interactions and the repulsive part of the Lennard–Jones potential can be attributed to the long-range couplings [the last term in Eq. (3.1)]. The competition arises from the fact that the short- and long-range interactions often favor opposite phenomena, for example, attraction and repulsion. A periodic pattern then becomes a compromise between the two forces. The details of a pattern depend heavily on the strength of ingredients, the temperature, and whether some mediators exist such as an underlying lattice or other physical restrictions. One of the most widespread physical restric-

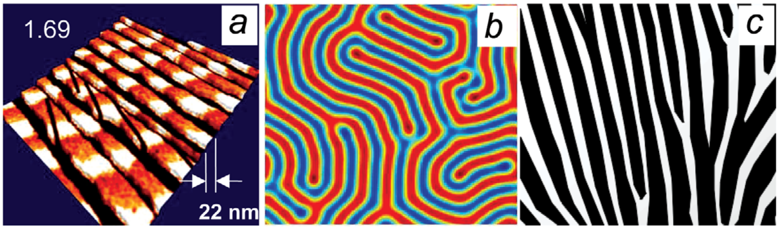

**Fig. 3.1** (a) Magnetic stripe pattern in a two monolayer-thick Fe magnetic film, width of order of 20 nm (reprinted with permission from [1]). (b) Theoretical presentation of a µm large neural network, (c) cm large zebra stripes.

tions is that of crystalline anisotropy. In this chapter only extreme cases will be discussed – infinite anisotropy or no anisotropy at all. All other anisotropic effects will be highlighted in Chapter 5.

## 3.1
## Localized Particles

### 3.1.1
### Competition Between the Ferromagnetic Exchange and the Dipolar Interaction: Ising Spins

First, we return to systems of magnetic or electric moments on a lattice. Now, however, instead of one single interaction the moments are coupled by two terms:

$$\mathbf{H} = -2J\sum_{\langle i,j\rangle} \mathbf{S}_i \cdot \mathbf{S}_j + D\sum_{i,j}\left(\frac{\mathbf{S}_i \cdot \mathbf{S}_j}{r_{ij}^3} - 3\frac{(\mathbf{S}_i \cdot \mathbf{r}_{ij})(\mathbf{S}_j \cdot \mathbf{r}_{ij})}{r_{ij}^5}\right), \tag{3.2}$$

the short-range exchange interaction and the long-range dipolar interaction.

In the simplest case, the vectors can have only two orientations, *up* or *down*. All other possibilities are forbidden. Such a situation arises in ferroelectrics (see Section 1.1.2), where dipole moments are induced by the piezoelectric distortion of a lattice, where the distortion is usually uniaxial, or in magnets with infinitely strong uniaxial crystalline anisotropy such as magnetic garnets and ultrathin magnetic films Co/Au(111), Fe/W(110), Mo/W(110), Co/Pt(111).

The ground state of a pure dipolar Ising system is an antiferromagnetic configuration – that is, an atomic checkerboard pattern on a square lattice and a labyrinth on a triangular lattice (see Section 2.6.1.1). The ground state of a pure ferromagnet is all spins up or all spins down, but if both interactions are present then the compromise is to orient several parts of the sample (domains) up and several down. At that point, at the inside of the homogeneously polarized regions the exchange energy will be satisfied, whereas on the interfaces between the domains the dipolar energy will be "happy". In other words, a compromise between the loss in exchange energy due to the formation of domain walls and the gain in the dipolar energy due to the interaction between magnetization currents generated at the domain walls will be found. The question is, how large should these areas be in the optimal case, which form should they have, and how they should be spatially ordered?

#### 3.1.1.1 **Stripes or Checkerboard?**

The shape of the vertically magnetized domains in Ising-like systems was intensively discussed during the early 1990s. To make a reliable suggestion about the possible shape of domains, it should be borne in mind that the dipolar interaction favors an antiferromagnetic alignment of magnetic moments in order to avoid uncompensated magnetization. Hence, even if some parts of the sample were to be unfavorable for the dipole–dipole coupling uncompensated magnetic poles, the dipolar energy could be minimized by allowing the total magnetic charge of a sample to be zero. This means that the total area of up- and down-domains should be equal. According to this reasoning, two possible domain configurations have been suggested: (i) a stripe pattern with up- and down-magnetic moments ordered in parallel stripes of the width *w*; and (ii) a checkerboard domain pattern with up- and down-magnetized regions of square shape with the edge length *w*.

In both cases the opposite domains have identical surface areas and, therefore, the total magnetic charge of a system is zero. The next step is to calculate the energy of both configurations and to compare them. Ground-state energy calculations [3, 4], renormalization-group-based arguments [5] and Monte-Carlo simulations [6–8] all predict the existence of a striped phase at low temperatures for systems with dipolar coupling and ferromagnetic exchange interactions. Qualitatively, the stability of the stripe domains is caused by the fact that, for identical *w*, the total length of domain walls of a checkerboard pattern is larger than that of a stripe configuration. Hence, the exchange energy – which is usually much stronger than the dipolar one – is minimized in case of a stripes comparable to the checkerboard configuration. Stripe interfaces have the lowest energy when aligned along favored directions of a lattice, thereby introducing a *p*-fold symmetry-breaking orientational field. Hence, the configurational entropy of a perfect stripe pattern on a triangle-based lattice is higher than that on a lattice with a square base. As follows from the Monte-Carlo simulations at finite temperatures, a system may further increase the entropy by the formation of more complicated structures which also belong to the class of stripe configurations. These are the superdomains and labyrinthine patterns shown in Figure 3.2.

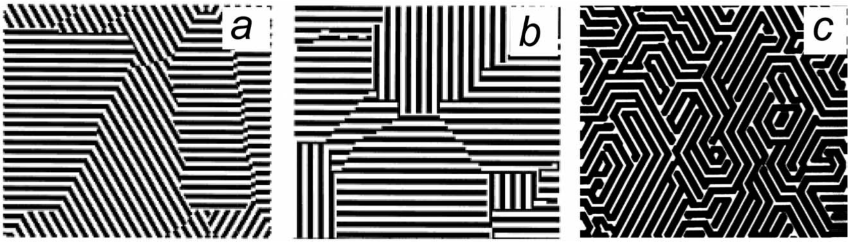

**Fig. 3.2** Portions of $100 \times 100$ Ising spins at low temperature on square (b) and triangular (a, c) lattices. The black stripes indicate up-spins; the white stripes down-spins. The exchange constant of configuration (c) is twice as strong compared to the exchange constant of pattern (a).

#### 3.1.1.2 **Scaling Theory**

The next fundamental question to answer is the following. If the ratio of the dipolar and exchange interaction parameters $D/J$ gives rise to domains with a particular length scale, is there another set of interaction parameters that gives rise to the same domain configurations as the original parameters, only scaled in size by a factor $b$ (see Fig. 3.3)?

A number of different approaches have been developed to answer this question. For example, scaling relations have been obtained by describing the domain energy as a sum of contributions coming from the domain areas and the domain contours [9]. Elsewhere, an effective dimensionless parameter was introduced into the Hamiltonian Eq. (3.1) [10]. Both approaches lead to the conclusion that the scaling parameter $b$ is mainly determined by the ratio between the dipolar and the exchange interaction constants.

The dimensionless parameter of [10] is defined through the coupling constants of the exchange and the dipolar interaction $q = D/(J \cdot a^3)$ with the lattice parameter $a$. In a system with competing short- and long-range interactions, the scaling parameter $a$ remains the only free variable, as the expressions under the summation contain only relative angle cosines and the distances between lattice points. Therefore, different ratios of $D/J$ can be considered as issued from a single case with a given $q$ value, but with different effective lattice parameters $a = b \cdot a_0$. Then, $D_0/Ja_0^3 = D_1/Ja^3$ and $b^3 = D_1/D_0$. Thus, increasing the dipolar coupling $D$ while keeping the exchange coupling $J$ constant amounts to a mere increase in the effective lattice parameter $a$ or, in other words, to a homothetic increase of the domain length scale by a factor $b$. For example, in the usual $3d$ magnets such as *Co* or *Fe*, the ratio $q = D/(J \cdot a_0^3)$ is of the order of $10^{-3} \ldots 10^{-4}$, where $a_0$ is a typical atomic distance in metals. For $D/J = 0.1$, $b = 5 \ldots 10$ and $a \approx 5a_0 \ldots 10a_0$. For $D/J = 1$, $b = 10 \ldots 20$ and $a \approx 10a_0 \ldots 20a_0$. Hence, the larger values of $D/J$ correspond to the larger domains. This result can be also interpreted as a slightly different way, however, in that the larger the ratio $D/J$ the coarser the calculation mesh and the coarser the resolution of the structure. By using this method it is possible to examine the structures at several scales. For example, Figure 3.4 provides a portion of a labyrinthine structure on a trian-

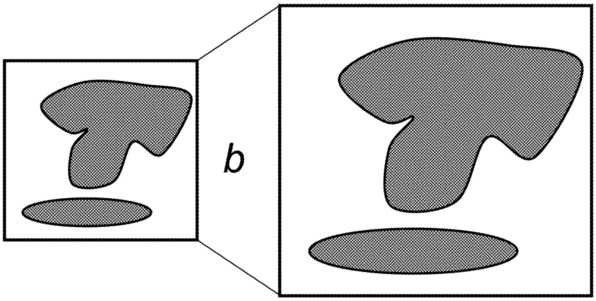

**Fig. 3.3** Two-domain configurations scaled by a factor $b$.

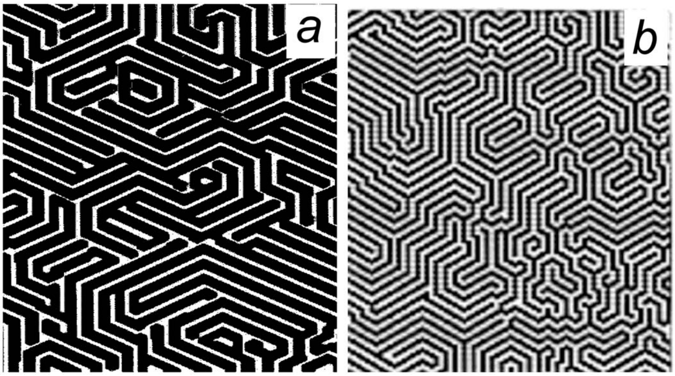

**Fig. 3.4** Portions of an Ising labyrinthine pattern on a triangular lattice for (a) $D/J \rightarrow \infty$ and $D/J < 1$, corresponding to lower and higher resolutions, respectively.

gular lattice for: (a) the pure dipolar case, $D/J \rightarrow \infty$ corresponding to a low resolution; and (b) for $D/J < 1$ corresponding to a higher resolution. The scaling allows us to change the mesh of the calculation, depending upon the specific objectives of the system.

#### 3.1.1.3 **Stripes in an External Magnetic Field: Bubbles**

Figure 3.5 summarizes the results obtained if an external field is applied to a stripe pattern. The simulations [8] show evidence of a hysteresis and the appearance of so-called "bubble domains". The progressive change from stripes to bubbles is initiated by stripe indentations that transform into closed bubbles when there are sufficient numbers of them. This process requires a higher energy than bubble shrinkage and wall motion, and therefore the indentations have a very short lifetime and are difficult to observe. By comparison, wall motions have a larger lifetime and can be easily observed.

The size and periodicity of bubble domains depends on the strength of the applied magnetic field and the ratio between film thickness and characteristic magnetic exchange length [11]. It transpires that, beyond a relative magnetization $m$ of about 0.3 and reduced perpendicular fields of about $H = 0.2J$, the bubble lattice is energetically advantageous compared to the stripe array [12]. However, the energy difference is small and negligible as a driving force for domain rearrangement processes. Only at higher fields can a bubble array be stable. At zero field the bubble lattice remains metastable. Usually, the bubbles in a lattice are arranged in a close-packed, hexagonal manner, as shown in Figure 3.5. In the presence of in-plane anisotropies, bubbles may also form other lattices or irregular, amorphous structures.

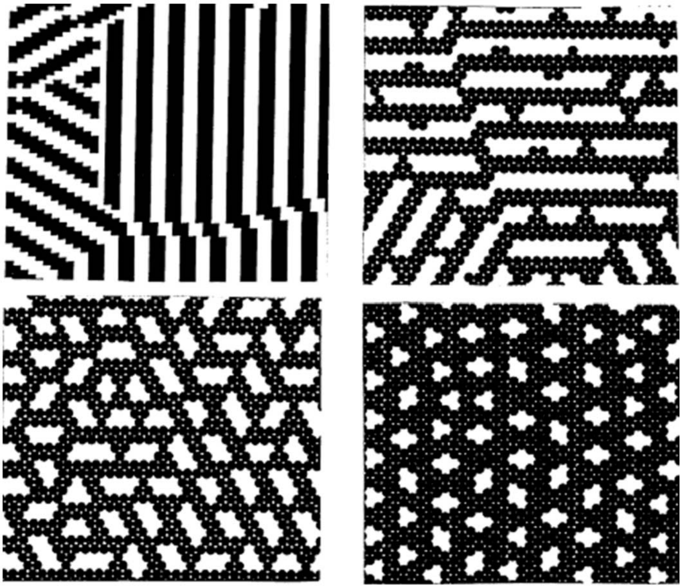

**Fig. 3.5** Magnetic field effects: portion of 100×100 system of Ising spins on a triangular lattice. $D/J=1$, $kT/J=0.05$. The external magnetic field is continuously increased from $H/J=0$ to $H/J=2$.

### 3.1.2

### Competition Between the Ferromagnetic Exchange and the Dipolar Interaction: Vector Spins

#### 3.1.2.1 Films: Dominating Exchange Interaction

##### 3.1.2.1.1 Periodic Lattices

The competition between ferromagnetic exchange and dipolar interaction without any significant anisotropic contributions is typical of magnetic materials such as 5 to 20 nm-thick Permalloy ($Ni_{80}Fe_{20}$), Supermalloy ($Ni_{80}Fe_{14}Mo_5$) or Co(0001) films [13, 14]. In ferromagnets, the exchange interaction dominates $k=J/D\geq 50$. Therefore, a typical ground state of an *infinitely* large two-dimensional film made from soft ferromagnetic material is just tediously ferromagnetic for all lattice types. The magnetization of such magnets lies in the film plane in order to reduce the stray field energy.

##### 3.1.2.1.2 Aperiodic Tilings

Recently it has been demonstrated [15] that in quasicrystals the situation may be more delicate than is usually expected, even for the dominating ferromagnetic coupling. The main reason is that, in contrast to the periodic lattices, a unique nearest-neighbor distance and correspondent exchange integral cannot be defined for the aperiodic structures. Atoms on quasiperiodic tilings have not only a varying number of neighbors but also several different nearest-neighbor distances (see Fig. 2.1). Accordingly, there are several different values of the exchange force which can even change sign. The existence of several exchange constants $J$ can also exert a significant influence on the magnetic structure. In one study [15], five different values of the exchange constant – that is, for the sides and all diagonals of the rhombuses – have been considered. The coupling along the sides of the Penrose rhombuses has been taken to be unity. It has also been assumed that the ferromagnetic exchange interaction decreases exponentially with the distance between magnetic moments. The strength of the exchange interaction has been defined as $J_{\mathrm{ij}}=J \cdot \exp(1-\rho_{\mathrm{ij}})$, where $\rho_{ij}=r_{ij}/a$, the distance between two neighboring moments normalized to the length of the side of the rhombuses $a$. $\rho_{ij}$ takes the lengths of the diagonals of the Penrose tiles. The shortest diagonal has a length of $\rho_{ij}=\tau^{-1}<1$, where $\tau$ is the golden mean. Therefore, $J'=J \cdot \exp(1-\tau^{-1})$ – that is, $J'$ is larger than $J$. Further interactions become weaker than $J$ with increasing distance as in the case of $\rho_{ij}>1$.

According to the Mermin–Wagner theorem [16], no long-range order exists in two dimensions with continuous symmetry, because thermal fluctuations result in a mean-square deviation of the spins from their equilibrium positions, which increases logarithmically with the size of the system. The addition of a very weak anisotropy stemming, for example, from the dipolar interactions, does not alter the distribution of the exchange energy, but does anchor the absolute spatial orientation of the magnetization. Magnetic ordering depends on the ratio of exchange to dipolar constant $k$ and on the radius of the cut-off in the exchange coupling ($\rho$). In the first approximation, the cut-off radius in the exchange interaction can take one of three values: $\rho=a$, which means that the exchange coupling is considered only along sides and the shortest diagonal of the Penrose rhombuses; $\rho=0.727\,a\tau$; or $\rho=1.176\,a\tau$. The latter distance corresponds to the exchange coupling along the longer diagonals, and the previous distance to the interaction along the shorter diagonals.

In the quasiperiodic Penrose lattice with high $k=J/D$, that is, with the strong exchange interaction, a single domain for all cut-off radii $\rho_{ij}$ is found. This means that the exchange coupling acting along the two shortest bonds ($J$ and $J_0$) is sufficient to ensure the ferromagnetic order. However, the degree of magnetic order increases remarkably with increasing $\rho$. While the average magnetization per moment at low temperature ($J/kT=100$) and high ratio $k\approx 100$ is almost unity for the exchange cut-off radius $\rho=1.176\,a\tau$, it is only $\bar{\mathbf{M}}=0.85$ for $\rho = a\tau$. Hence, in contrast to periodic lattices, the ferromagnetic order in quasicrystals depends heavily on the cut-off radius in the exchange interaction. In the case of small $\rho$, a high magnetic frustration of the quasiperiodic structure leads to significant deviation of the average magnetization from unity, even for very high $k$-ratios. An example of a ferromagnetic configuration on a Penrose tiling is shown in Figure 3.7 c.

#### 3.1.2.2 **Films: Dominating Dipolar Interaction**

Interesting equilibrium structures appear for dominating dipolar interactions which can be found in rare-earth-based compounds, in some molecular magnets, and in arrays of exchange-coupled magnetic nanodots. Although, in order to obtain a non-trivial magnetic pattern, the lattice structure of a system must be different from a triangular structure for which both interactions favor a ferromagnetic alignment of magnetic moments (see Section 2.6.1.2).

The ground state configuration of a magnet with dominating dipolar interactions on a two-dimensional square lattice is shown in Figure 3.6a. It consists of domains with opposite polarization. Although the exchange interaction is spatially isotropic the domains are in-plane magnetized – that is, the dipolar interaction introduces effective in-plane anisotropy in the system. The domain size increases with increasing ratio of two interaction constants $k = J/D$. In monolayer films the domains may exist only for $D > J$. In thicker films with, for example, simple cubic stacking, the critical $k$-ratio is slightly reduced, although it is still very high compared to the Ising-like systems with strong perpendicular anisotropy. The reason for this is that the gain in dipolar energy due to domain formation is relatively small for the in-plane magnetized samples without uncompensated magnetic poles. Another geometry, which leads to the formation of domains is that of a honeycomb. A typical equilibrium magnetic configuration for $D > J$ is shown in Figure 3.6b. While the domain size increases with decreasing $k$ as on the square lattice, the spatial orientation of domains and their shape are different. Similar to the square lattice, possible orientations of magnetic moments inside a domain follow the sixfold symmetry of the lattice. In contrast to the square counterpart, the orientation of the domain walls is, in most cases, at variance with the principal crystallographic directions of the un-

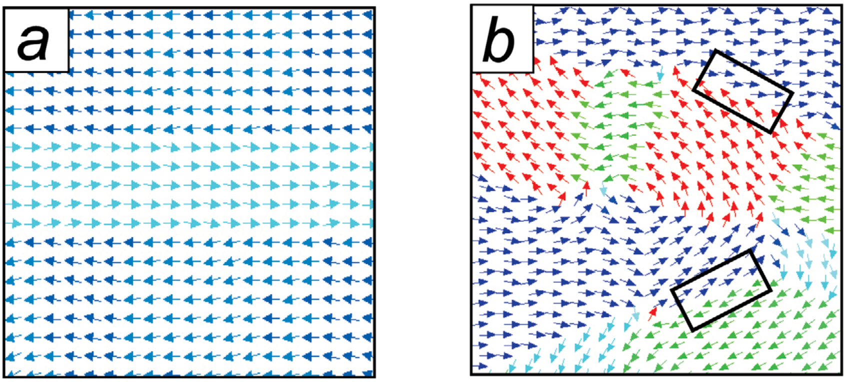

**Fig. 3.6** Low-temperature stable magnetic configurations on a square (a) and a honeycomb (b) lattice for dominating dipolar interactions $D/J = 1.4$, $kT/J = 0.05$. Different colors indicate the different azimuthal orientations of magnetic moments. The two boxes highlight 180° and 120° domain walls.

derlying lattice (compare the two highlighted domain walls in Fig. 3.6 b). This occurs for two reasons. First, the statistical weight of having 180° domain walls between two adjacent domains is lower than that of 60° (120°)-walls. Second, the dipolar interaction favors the 60° (120°) configurations (see Section 2.6.1.2). As a consequence, the domain walls can run either along principal crystallographic directions or under the angle of 30° to them. Hence, there are 12 possible orientations of magnetic domain walls, and many possibilities for their intersection, and this leads to a complicated situation which is very different from the ideal stripe pattern domain shapes. Very often, the domains form closer vortex-like structures on a large scale. Thus, the square and honeycomb lattices belong to the class of two-dimensional systems, which lead to the formation of in-plane domains for $D > J$.

The kagome lattice represents a different class of a non-trivial magnetic symmetry for competing dipolar and ferromagnetic exchange interactions. As shown in Section 2.6.1.2, the kagome lattice supports a ferromagnetic-like magnetic ordering, and therefore at first glance it seems that a ground state for dominating dipolar interactions is simply ferromagnetic. In reality, however, the situation is more complicated, with the whole configuration being divisible into three sublattices denoted as green, blue and red in Figure 3.7 a. The orientation of the more diluted sublattice (green in Fig. 3.7 a) coincides with one of the principal crystallographic directions. Two other sublattices make an angle $\theta$ with the selected principal orientation. The angle $\theta$ depends on $k$, and increases exponentially from 0° for pure ferromagnetic interactions to 30° for pure dipolar configuration (see Fig. 3.7 b).

Thus, the competition between dipolar and ferromagnetic exchange interaction leads to two principal types of magnetic structure: macroscopic domains, and antiferromagnetic-like sublattice ordering. Magnetization in the domains is

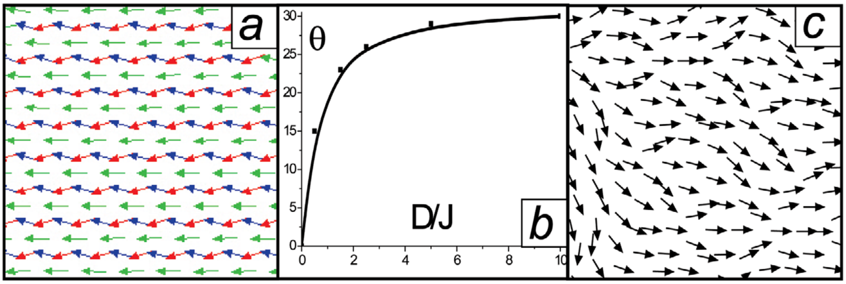

**Fig. 3.7** Low-temperature stable magnetic configurations on a kagome (a) and a Penrose (c) lattice for dominating exchange interactions $D/J = 0.2$, $kT/J = 0.05$. The cut-off in the exchange interactions for the Penrose tiling (c) is $\rho = a\tau$. The X component of the average magnetization is $\bar{\mathbf{M}}_x = 0.85$. Different grades of gray indicate different azimuthal orientations of magnetic moments. Inset (b) provides an angle $\theta$ made by two sublattices on a kagome lattice relative to the third sublattice, which coincides with one of the principal crystallographic directions, as a function of the ratio between the dipolar and the ferromagnetic exchange interactions.

usually oriented along the principal crystallographic directions of an underlying lattice, while the domain walls can have intermediate orientations. The magnetization of sublattices in the second type of ordering is not always directly related to the crystallographic axes. The dipolar coupling usually induces strong in-plane anisotropy.

#### 3.1.2.3 **Nanoparticles with Periodic Atomic Structure**

The situation is more complicated if a two-dimensional ferromagnet has finite dimensions. On a large length scale, the total dipolar (magnetostatic) energy may be much larger than the dipolar coupling between two spins, as the interaction energies between all pairs of neighbors on a lattice must be summed. In contrast, the short-range exchange interaction is important only for nearest-neighboring pairs of magnetic moments. Due to the long-range character, weak dipolar interaction can compete with the ferromagnetic exchange, thus favoring stray field-free magnetic configurations. The question is, what type of configurations are to be expected – domains with distinct domain walls similar to Ising-like systems, or rather a continuously flowing divergence-free magnetization pattern?

This question can be answered by postulating [11] that the magnetization vector field $\mathbf{m}(x,y)$ must: (i) lie parallel to the film surface ($m_z = 0$); (ii) be divergence-free in the interior ($div\,\mathbf{m} = \partial m_x/\partial x + \partial m_y/\partial y = 0$) and at the edges ($\mathbf{m} \cdot \mathbf{n} = 0$, $\mathbf{n}$ – edge normal); and (iii) have a constant length $|\mathbf{m}| = 1$. Intuitively, some smoothly varying vector field might be always expected, but it transpires that in structures with lateral dimensions on the micrometer scale all three conditions cannot be satisfied simultaneously and a continuous planar pattern can appear only for certain shapes of a sample. A comprehensive analysis of such thin-film elements of arbitrary shape was achieved by van den Berg and Vatvani [17], and subsequently reviewed by Hubert and Schäfer [11]. It has been proven that the conditions explained above can only be met if the magnetization remains parallel to the edges on every point along the edge normal, as long as no other edges interfere. This means that if an edge is straight, then a domain with magnetization parallel to this edge appears. Between two adjacent domains, discontinuities (i.e., domain walls) emerge (see Fig. 3.8). The magnetization configuration inside the walls is also dependent upon the shape of the sample and the $k$ ratio. A detailed analysis of wall width and wall magnetization profiles can be found in [11].

In thin magnets of circular shape and with thickness much less than the diameter, a continuous curling spin configuration – that is, a magnetization vortex – has been proposed to occur in place of domains. In the vortex, the spin directions change gradually in the film plane so as not to lose too much exchange energy, but rather to minimize the total dipole energy. In the vicinity of the dot center, the angle between adjacent spins becomes increasingly larger when the spin directions remain confined in-plane. This leads to a strong local increase in the exchange energy. Therefore, it has been predicted [11] that at the core of the vortex structure, the magnetization will turn out-of-plane, thus forming a continuous transition between two in-plane regions with opposite in-plane magnetization.

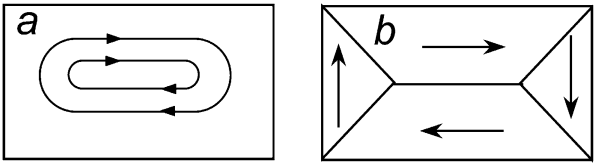

**Fig. 3.8** Schematic representation of (a) a continuously flowing magnetization pattern and (b) so-called Landau–Lifshitz in-plane domain structure consisting of four domains and five discontinuous domain walls.

Although this analytical statement has been confirmed by numerical simulations (an example of a stable Monte-Carlo vortex configuration is shown in Fig. 3.9), an experimental verification of this interesting phenomenon has been conducted only recently [18, 19]. Magnetic force microscopy imaging of circular dots of permalloy ($Ni_{80}Fe_{20}$), 0.3–1 μm in diameter and 50 nm thick, has revealed contrast spots at the center of each permalloy dot corresponding to the turned-up magnetization of a vortex core [18]. Subsequent Spin Polarized Scanning Tunneling Microscopy (SP-STM) experiments have succeeded in resolving the size of the vortex core [19] (see Fig. 3.10). For supermalloy islands with lateral size of order of 200 nm and thicknesses of 2–5 nm, the diameter of the vor-

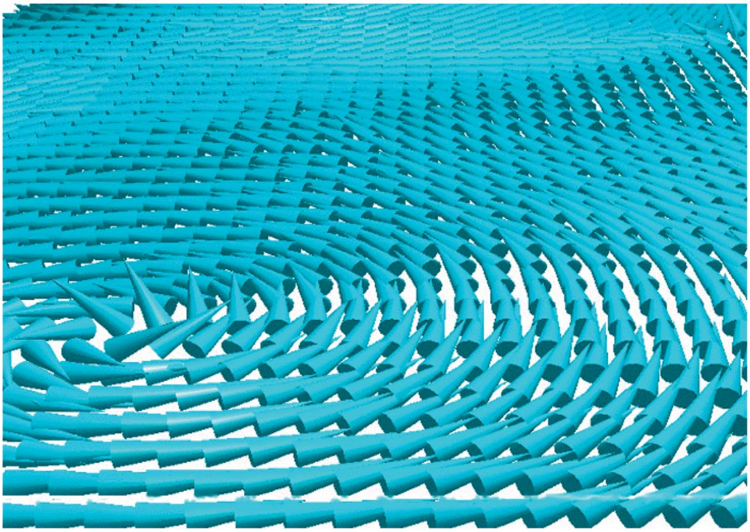

**Fig. 3.9** Monte-Carlo simulation for a monolayer of Heisenberg 50×50 spin structure at $kT/J=0.15$. For clarity, only one of six cones is shown. Because of the rather elevated temperature the ideal vortex structure is not yet reached. However, the core of the vortex already has distinct out-of-plane magnetization.

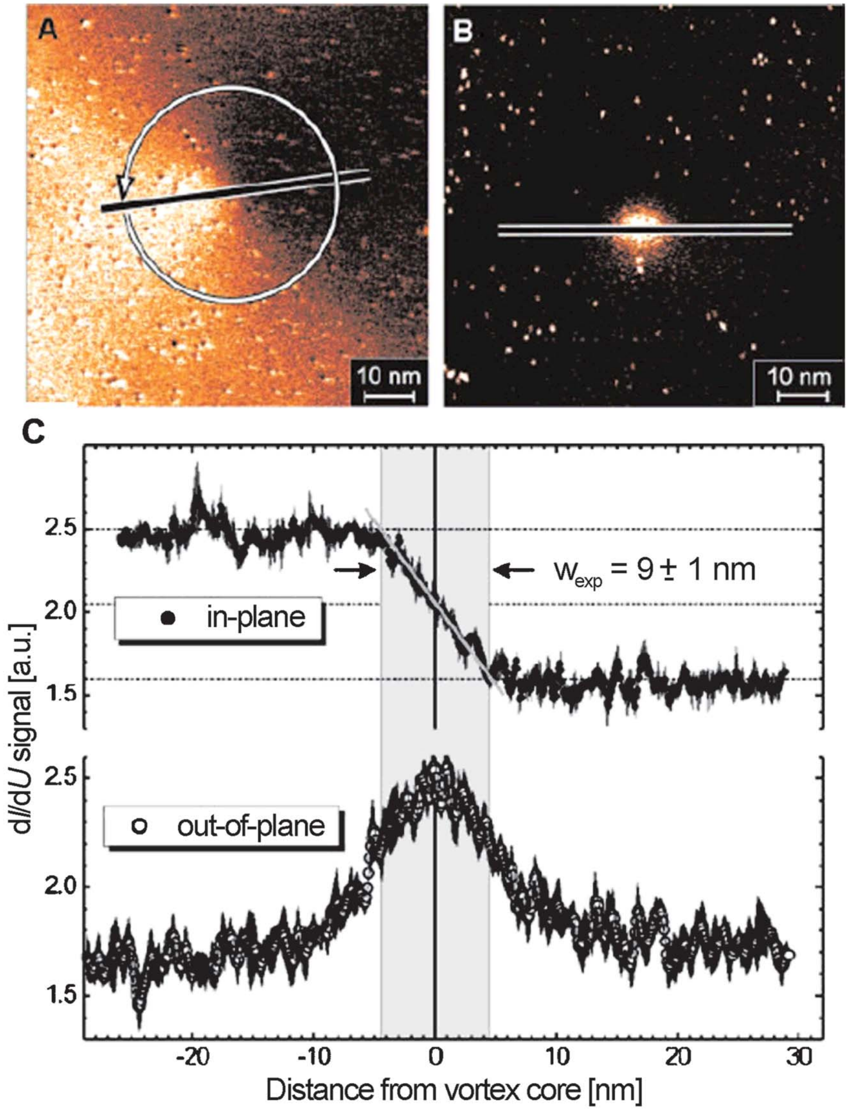

**Fig. 3.10** Spin Polarized Scanning Tunneling Microscopy (SP-STM) measurements. Magnetic d$I$/d$U$ maps as measured with (A) an in-plane and (B) an out-of-plane sensitive Cr tip. The curling in-plane magnetization around the vortex core is recognizable in (A), and the perpendicular magnetization of the vortex core is visible as a bright area in (B). (C) The d$I$/d$U$ signal along the lines in (A) and (B) gives changes in the in-plane and out-of-plane components of magnetization with the distance from the center of the vortex, and hence defines the diameter of the vortex core. Reprinted with permission from [19]: A. Wachowiak et al., *Science*, **2002**, *298*, 577. © 2002 AAAS.

tex core has been found to be 9 ± 1 nm, which is slightly larger than the domain wall width in an extended thin film with the same exchange and dipolar constants. Interestingly, these experiments and simulations indicate that in magnets – which are only several tenths of nanometer wide – a curling spin structure can be realized even for dots of square or elongated shape [18, 19]. Hence, the configurations of Figure 3.8 are mainly restricted to magnets on the micrometer scale, while continuous magnetization configurations evolve in nanomagnets.

One of the most important theorems in micromagnetics – one describing the magnetic ordering of a magnet on a micrometer scale – is referred to as "Brown's fundamental statement" [20]. This claims that, because of competition between the dipolar energy and the quantum mechanical exchange energy, magnetic domain formation should be entirely suppressed in very small $\approx 10^{-8}$ m magnetic particles (nanomagnets). Such nanomagnets should then behave as single giant spins. However, knowing that the dipolar interaction leads to smooth magnetic configurations instead of domains, the question arises: "what is the critical size for the transition from a vortex to a single domain configuration?" The related question is whether this transition is abrupt, or if some intermediate configurations occur?

Recent advances in nanometer-scale fabrication technology and computer simulations with atomic resolution have opened up the possibility of testing this fundamental theorem on artificially fabricated zero-dimensional magnetic systems in which all three dimensions are geometrically constrained on a nanometer length scale [18, 19, 21]. The experimental results can be compared with Monte-Carlo or micromagnetic simulations performed at high resolution. The first such study to be performed was with circular nanomagnets [21], and the main result was an experimental phase diagram in diameter and thickness which identified a vortex phase and a single-domain phase of supermalloy nanoplatelets. It has been shown that, with decreasing thickness, the critical diameter of the transition vortex → single domain increases. The next important conclusion is that for small thicknesses (< 6 nm) the state with the non-zero macroscopic magnetization can be achieved for platelets of 200 nm diameter and smaller. However, 200 nm is a relatively large size, and therefore – as follows from the simulations [14] – an ideal ferromagnetic configuration should lead to rather strong surface charges and, hence, to large losses in magnetostatic energy. The high energetic cost of the magnetostatic surface charges means that magnetostatic energy can often be reduced by introducing non-uniformity to the magnetization field. These so-called incoherent magnetization fields can reduce the net moment carried by a nanomagnet without driving it to zero, as in a vortex structure.

A series of subsequent experiments on magnets of different shapes [14] have confirmed those results, and shown that the hysteretic properties of nanomagnets depend significantly on their shape, size, and thickness. The magnetic ordering of a nanomagnet is shown to be linked to its shape by two distinct phenomena. The first phenomenon is called *configurational anisotropy*, and describes

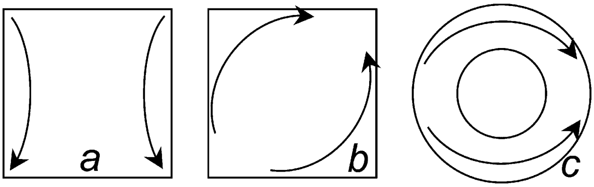

**Fig. 3.11** Schematic representation of non-uniform magnetization vector fields with non-zero net magnetization: (a) a "flower" state; (b) a "leaf" state; and (c) an "onion" state.

the role played by small deviations from uniformity in the magnetization field within the nanostructures. The second phenomenon is the *competition* which exists between the exchange and the magnetostatic energy. This competition determines whether a nanomagnet exhibits single domain or incoherent magnetization, and also controls the non-uniformities in magnetization leading to the configurational anisotropy. The configurational anisotropy allows unexpected higher-order anisotropy terms to appear, which can dominate the magnetic properties. A schematic representation of three non-uniform configurations in nanomagnets – the flower, the onion and the leaf structure – is provided in Figure 3.11.

In conclusion, due to its long-range characteristics, the dipolar interaction is able to compete with the dominating exchange coupling until very small sample sizes. This competition leads to a non-uniformity of the ferromagnetic magnetization in single domain limit, to the appearance of additional configurational anisotropy, and to out-of-plane magnetization in the transition regions between the uniformly in-plane magnetized domains.

#### 3.1.2.4 **Nanoparticles with Aperiodic Atomic Structure**

As stated in Section 3.1.2.1, the ferromagnetic order in quasicrystals depends on the cut-off radius taken for the exchange interaction. This can cause strong inhomogeneities of the magnetization at the boundaries of laterally confined magnet with quasiperiodic structure, where some of the neighboring moments are missing. In finite samples on periodic lattices of sizes which exceed the single domain limit, the in-plane vortex structures dominate (see Section 3.1.2.3). The vortex phase arises as a result of the influence of sample boundaries. The dipolar interaction preferentially keeps the magnetic moments in the film plane and parallel to the sample edges in order to avoid the formation of magnetic poles. The exchange energy then controls the parallel orientation of neighboring moments. The interplay of these different contributions leads to the formation of a vortex structure with dimensions of the sample size.

The situation is completely different for the Penrose tiling, however. For all $J/D$-ratios and cut-off radii the macroscopic vortex configuration is energetically unfavorable with regard to the exchange interaction. When the dipolar energy becomes strong enough to compete with the exchange coupling ($J/D < 0.5$), the microscopic decagonal pattern described in Section 2.6.1.3 begins to form (compare Figs. 2.23 and 3.12a). The decagonal pattern in the presence of an exchange interaction shown in Figure 3.12a differs from that of the pure dipolar case shown in Figure 2.23. The strong exchange coupling lifts the degeneracy of the decagonal magnetization configuration found for $J = 0$. The magnetic moments are almost coplanar with the sides of the decagons, as in the pure dipolar case. The average magnetization, however, is not zero – that is, the magnetic moments have some preferential direction (see Fig. 3.12a). We refer to such magnetization configuration as a “quasiferromagnetic decagonal structure”. A further decrease in the ratio $k$ leads to an increasing influence of the dipolar interaction on the magnetic structure. In order to minimize the magnetostatic energy, the dipoles form lines at the edges of the sample, as in a conventional vortex. However, a macroscopic vortex does not form for any shape of the sample, with small local vortices perhaps appearing inside only some decagon rings.

Thus, according to Monte-Carlo simulations [15], the influence of the boundaries does not lead to the formation of a macroscopic vortex in a Penrose tiling. To understand this phenomenon, the energies of a ferromagnetic single domain, ideal macroscopic vortex and Monte-Carlo microvortex structure have been calculated numerically. The data versus $k = J/D$ are presented in Figure 3.12b for the maximal value of $\rho$. As soon as the energy of the vortex or the quasiferromagnetic structure becomes less than that of a single domain, a crossing of curves will occur. The point of intersection produces a critical ratio $k_c$ where the transition between different configurations occurs, though no values of either $k_c$ or $\rho$ have been found where the macroscopic vortex is preferred. The shaded area in Figure 3.12b separates the phases of the monodomain and the decagonal pattern. The center of the interval where all three configurations have comparable energy is denoted as $k_c$. Hence, for $k \approx k_c$ the magnetic struc-

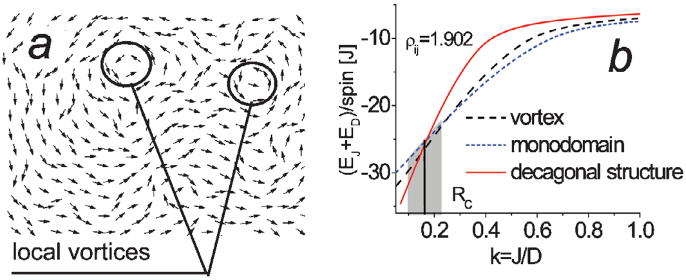

**Fig. 3.12** (a) An example of a planar spin configuration in the region of transition from the single domain to the decagonal structure for $\rho = 1.176\,a\tau$ and $J/D = 0.4$. The magnetic structures have been obtained for square and disk-shaped samples of 400 and 10 500 magnetic moments at $J/kT = 100$. The magnetic moments at the edges are oriented mainly parallel to the boundary, as in a conventional vortex structure. However, only local vortices inside the decagons exist.
(b) Total energy per spin for a monodomain, an ideal vortex and a Monte-Carlo decagonal structure as a function of $k = J/D$.

ture should contain ordered regions coexisting with the decagonal pattern and local vortices [22]. Thus, the dipolar energy can compete with the exchange energy only on the scale of the quasiperiodic decagonal microstructure. The reason for this phenomenon is the spatial variation of the number of nearest neighbors and the exchange interaction strength. As the strength of the exchange interaction decreases exponentially with the distance, $J$ becomes much stronger for neightbors with $\rho \leq a$ (i.e., with $J \geq 1$) than for neighbors with $\rho < a$. The magnetic moments with $\rho = a$ are situated mainly on the perimeter of the decagons. It is energetically more preferable to keep these moments parallel rather than the other moments, as this causes the appearance of decagonal chains and local vortices.

In conclusion, in contrast to periodic lattices, the formation of macroscopic vortex configuration is suppressed in favor of the microscopic quasiferromagnetic pattern. For low $k$ ratios a new microscopic structure – the quasiferromagnetic decagonal pattern – represents the minimum of the free energy.

### 3.1.3
### Competition Between the Antiferromagnetic Exchange and the Dipolar Interaction

The dipolar interaction of Ising spins has an antiferromagnetic character, which means that in many cases the two interactions will act almost identically. Therefore, the discussion in this section will center on vector magnetic moments.

#### 3.1.3.1 Periodic Lattices

As has been shown in Chapter 2, an antiferromagnet with only nearest-neighbor exchange interactions can possess multiple ground states of equal energy due to the geometric frustration. Often, there is no finite-temperature transition to a phase with a static ordering [23–25], and therefore the smaller energies – quantum fluctuations, long-range dipolar interactions and temperature – can be challenging for lifting the degeneracy and ordering at low temperatures [25–29].

On a square lattice the antiferromagnetic exchange cooperates with $D < J$ the dipolar coupling instead of competition. The ground state of a system with on a square lattice is just out-of-plane checkerboard configuration. This configuration is bipartite and non-frustrated (see Fig. 3.13 a). Similar bipartite configuration (see Exercise 2 and Fig. 3.13 b) with vertical magnetization is typical of the honeycomb symmetry. Interestingly, those out-of-plane ground states arise without the application of vertical anisotropy. Hence, in contrast to the usual situation in which the dipolar coupling constrains a system to in-plane configurations, the antiferromagnet with dipolar interaction on a square and a honeycomb lattice possess a strong out-of-plane anisotropy. For higher strengths of dipolar interaction $D$, such systems pass into the typical in-plane dipolar configurations described in Chapter 2.

For dipolar antiferromagnets on lattices with triangular symmetry, there are indications that the dipolar coupling can reduce the number of accessible degener-

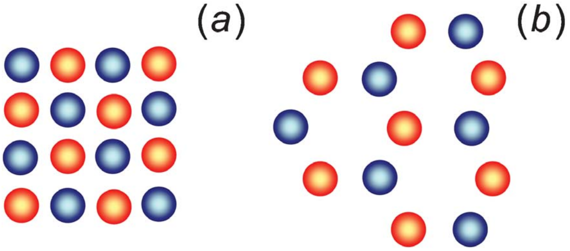

**Fig. 3.13** Schematic representation of the bipartite ground states on a square (a) and a honeycomb (b) lattice for $D<J$. The blue balls represent up-moments, and orange balls down-moments.

ate states [27, 30]. These investigations [27, 30], however, have treated the long-range dipolar coupling in a non-general manner, starting with the assumption that the spin structure of the model has a certain period that is known from the pure antiferromagnetic case. Namely, a rhombic $(\sqrt{3}a, \sqrt{3}a)$ superstructure where $a$ is the interatomic distance for a triangular lattice [30], and a triangular $2a$ superstructure for a kagome lattice [27]. The spin configurations were then determined by minimization of a total spin moment and a total energy on each rhombus/triangle. In these studies only one particular ratio between exchange and dipolar constants has been used. For the pure dipolar case, the same periodicity has been adopted, but the dipolar interaction can cause long-periodic or even non-periodic structures due to its long-range nature. Thus, the approximation made in [27, 30] may break down if the dipolar interactions are treated without any periodic limitations. In subsequent Monte-Carlo simulations [31], neither periodicity of the unit cell nor configurational space were restricted.

The dipolar energy per bond can vary from $D/J \approx 0.01$ in $\mathrm{SrCr_{8-x}Ga_{4+x}O_{19}}$ [27] or $D/J \approx 1$ in rare-earth compounds up to $D/J \to \infty$, that is, pure dipolar interactions in magnetic dot arrays. Therefore, in the following text the magnetic structure will be discussed as a function of $k$. The magnetic, low-temperature ordering has been found to differ from that reported elsewhere [30, 32] and to depend on the ratio $D/J$. The reason for such disagreement was shown to be the break down of the approximation for dipolar interactions made in those references for low temperatures.

Figure 3.14 provides the frequency distributions of the angle $\alpha$ between nearest-neighboring moments on a triangular lattice and the top views of typical magnetization configurations for different $D/J$ ratios. For dominating exchange coupling ($D \leq 0.1J$) a $120^\circ$ Néel ordering has been found (Fig. 3.14 a). In contrast to the usual Néel configuration (see Fig. 2.9), the in-plane components of all magnetic moments are collinear and parallel to one of the closed packed directions of a lattice, while adjacent moments still lie $120^\circ$ one to another. Hence, the magnetization rotates in a plane which is spanned by the z-axis and by one of the principal crystallographic axes of the triangular lattice. The dipolar

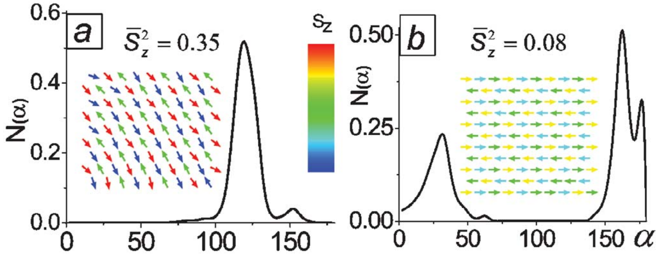

**Fig. 3.14** The frequency distribution of the angle $\alpha$ between the nearest-neighboring moments of Monte-Carlo configurations on a triangular lattice at $kT = 0.01J$. Top views of the configurations are shown as insets. The color scheme denotes the vertical component of magnetization $S_z$: (a) $D/J = 0.05$; (b) $D/J = 1$.

interaction, even if very weak, brings an anisotropy into the problem and selects six possible configurations from an infinite set of Néel structures. These six configurations are unique up to the global rotation of the whole structure, whereas in a normal Néel ordering two out of three sublattices may also admit any orientation on a cone (as shown in Fig. 2.10).

For $0.1J < D \leq J$, the dipolar interaction (which is still smaller than the exchange coupling) is able to alter the short-range order due to its long-range character. An example of such a configuration is shown in Figure 3.14b. The row-wise ordering is similar to that of the previous case ($D \leq 0.1J$), but the relative orientation of the moments inside of a row departs from that of the Néel state. There are three characteristic angles: 30°, 160° and 180° in the $\alpha$-distribution. Inside of a row, a translationally invariant cell consists of three spins: one of these lies in the film plane (green in Fig. 3.14b), two others are canted and make an angle of 30° to the film plane (yellow and blue, respectively). Magnetic moments belonging to neighboring rows have mutual angles of 160° or 180°. The angle distribution changes as a function of $D/J$. Generally, $\alpha$ increases with increasing strength of the dipolar interaction, which means that the dipolar interaction induces an in-plane anisotropy in an antiferromagnet on a triangular lattice. Although the squared vertical magnetization $S_z^2$ decreases from 0.35 for $D = 0.05J$ to 0.08 for $D = J$, the vertical component remains finite. The configuration becomes completely planar for $D > J$. For $D \approx 2J$ there are only two characteristic angles of 0° (inside of a row) and 180° (between rows). For $D \gg J$, an ideal row-wise antiparallel configuration becomes distorted, and stripes of parallel, planar magnetic moments are formed for periodic boundary conditions. For open boundaries, a multi-vortex structure appears, which goes continuously into a single vortex for $D \to \infty$.

Similar to the triangular lattice, its kagome counterpart shows a 120° order with a $(\sqrt{3}a, \sqrt{3}a)$ supercell for dominating exchange coupling (Fig. 3.15a). In contrast to the triangular lattice, however, the configuration is completely planar,

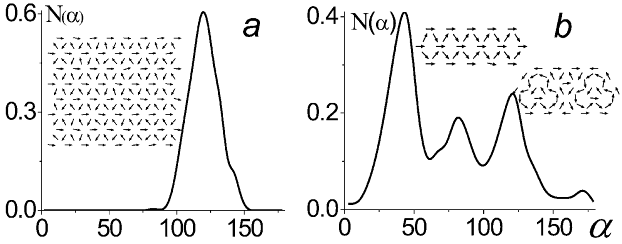

**Fig. 3.15** Monte-Carlo simulations. The frequency distribution of angle $\alpha$ between nearest-neighboring moments on a kagome lattice at $kT=0.01J$. Top views of stable configurations are shown as insets. The color scheme denotes the vertical component of magnetization $S_z$: (a) $D/J=0.05$; (b) $D/J=5$.

has a lower degeneracy, and corresponds to the phase found in [27]. In contrast to the data of Ref. [27], magnetic moments have not been constrained to lie in the $xy$ plane. Hence, we can conclude that the dipolar interaction induces a very strong easy-plane anisotropy in an antiferromagnetic kagome system. The micro-vortex, planar configuration persists until rather high values of dipolar strength $D \approx 5J$. For $D > 5J$, complex multi-domain planar configurations appear. The $\alpha$ distribution becomes much more complicated (the two main patterns of that state are illustrated in Fig. 3.15 b), and the structure is frustrated – that is, above the blocking temperature the system walks between many energetically similar configurations. Below the blocking temperature, however, the system becomes frozen in one of the multidomain states. At $D > 10J$ the frustrated state passes continuously into a vortex configuration, as detailed in Chapter 2.

In conclusion, the dipolar interaction introduces an out-of-plane anisotropy in square and honeycomb lattices, and an easy-plane anisotropy for triangular and kagome symmetry. A row-wise, chiral antiferromagnetic structure arises for $0 < D \leq 5J$ on a triangular lattice. The kagome symmetry leads to strong frustration for $D > 5J$ and a microvortex $60^\circ$ configuration for smaller $D$.

### 3.1.3.2 **Aperiodic Lattices**

In quasicrystals both the antiferromagnetic exchange and dipolar interaction lead to a hierarchical magnetic ordering consisting of ordered and frustrated sublattices. However, sublattices that are stable in an antiferromagnetic system are usually different from the stable subtilings of a pure dipolar system with the same atomic symmetry. For example, the most stable part of a Penrose lattice coupled by pure dipolar interaction is the subtiling consisting of decagonal rings (see Fig. 2.23). In a pure antiferromagnetic case, the decagonal subtiling does not exist; rather, it is divided into three subtilings of different symmetry. Additionally, these three antiferromagnetic successors of the decagonal structure can have relatively high energy. Thus, while stable in the dipolar case, subtilings may be completely unstable in an antiferromagnetic system, and vice versa.

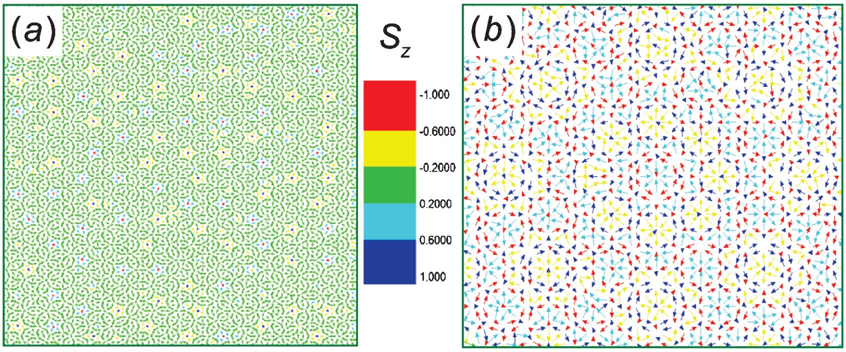

**Fig. 3.16** Top views of the Monte-Carlo stable configurations on (a) a Penrose and (b) octagonal tilings for $D=J$ and $kT=0.01J$. The color scheme denotes the vertical component of magnetization $S_z$.

If the two interactions of similar strength are applied at the same time to a two-dimensional quasicrystal, the magnetic structure becomes more ordered. Two examples of a Penrose and an octagonal tiling in case of $D=J$ are provided in Figure 3.16. Both magnetic configurations are three-dimensional and non-collinear, in spite of the absent anisotropy. Similar to the case of pure couplings, the whole tiling can be subdivided into interpenetrating subtilings, although the criterion is now the order parameter rather than the energy range. In Figure 3.16 the role of an order parameter plays the vertical component of magnetization $S_z$. The energy of all magnetic moments forms a very narrow band and the whole system becomes more stable. In spite of its long-range character, the dipolar energy can compete/cooperate with the antiferromagnetic coupling only for $D \approx J$. With increasing $D$ or $J$, the orientational order visible in Figure 3.16 is destroyed in favor of pure dipolar or antiferromagnetic patterns (as discussed in Chapter 2).

### 3.1.4
### Neural Networks

The main privilege of a human being is the capability for thought. Thinking is the main use of the human brain – a network of $\approx 10^{10}$ *neurons* allocated in a volume of approximately 0.001 $m^3$. Each of the brain's $10^{10}$ neurons receives signals from other neurons via a five-place number of entries, processes the data, and provides an output impulse through a long, thin stand known as an *axon* to a structure called a *synapse*. Synapses convert the signal from the axon into electrical effects that either inhibit or excite the activity of a further $10^5$ neurons.

In order to deduce the essential features of neurons and their interconnections, so-called Artificial Neural Networks (ANN) have been proposed [33]. In

ANN, a neuron is reduced to a variable $S_i \in \{+1,-1\}$. In the model, every neuron $i$, $i=1,\dots,N$ receives a signal $S_j$ from other neurons $j$, weights the signal with the synapse-strength $J_{ij}$, and sums the result. This construction is formally analogous to the Ising spin model, where the exchange couplings between the spins take the role of synapses. The excitatory or inhibitory nature of synapses in this construction corresponds to a ferromagnetic or an antiferromagnetic nature of the spin-spin interaction.

The neurons are concentrated in the cerebral cortex, the so-called *neocortex*, that serves as the center of higher mental functions for humans. The neocortex is the structure in the brain that differentiates mammals from other vertebrates, and it is assumed that the neocortex is responsible for the evolution of intelligence. The cells in the neocortex are arranged in several layers, within which different regions permit vision, hearing, touch, the sense of balance, movement, emotional responses, and every other feat of cognition. The simplest mathematical model of this layered structure is a two-dimensional film on a square lattice, where the "atomic" rows represent the layers of neurons. The state of activity of the first layer is entirely determined by external sources. They are entry neurons. At time 0, an input signal $\{S_{1,n}\}$ is given; at this initial time other neurons are either randomly distributed with given probability, or all at rest. At any time during the presentation of an entry, the input neurons keep the same state of activity, while the other neurons follow an interaction process according to the field value $h_i(t) = \sum_j J_{ij} S_j(t)$. If $h_i(t)$ is larger than a threshold reference value $h$, the neuron becomes active (excited) at times $t+1: S_i(t+1)=1$. If not (inhibited), then $S_i(t+1)=0$. This process defines a cellular automata network [34]. The convergence to a stable configuration for large times is not ensured; however, the system finds either a ground state or a metastable one for $J_{ij}=J_{ji}$, that is, convergence governed by the input occurs. The final configuration realizes an analysis of the entry. Hence, the final configuration provides information about some entry configuration at the initial time or represents memory states.

For a very simple Ising-like synapse behavior the number of accessible memory states is not large. Numerous estimations of the number of memory states $N_m$ for such types of simple model gives $N_m \approx 0.13\, N_n$, where $N_n$ is the number of neurons [35]. Everyday experience contradicts this statement, however, and suggests that the number of memory states in a real brain should be much larger. Taking as an example a sentence from A. Christie, "He let it be thought his visit was in connection with the Trust – but that's nonsense. He was here for that only a month ago. And nothing of importance has arisen since. So he must have come on some private business. He saw Walter on his last visit, and he may have recognized him – or perhaps made inquiries about him in the States…" Numerous associations on the details of previous events lead to several suggestions on the aim of a visit, which could be made on other details such as color, odor, or sounds. In such trees of associations the convergence between elements "States" and "visit" occurs in a very casual manner through many intermediate links. In a physical language, this indirect dependence corresponds to a familiar long-range coupling such as a dipolar one. The long-range interactions, which compete with the stronger short-range couplings, increases the number of conflicts and thus the number of memory states [36].

The main influence of the long-range interactions is the appearance of a hierarchy of branching structures (see Fig. 3.4). In ANN models with long-range interactions, this branching is even more pronounced as the first layer is pinned and supports certain pinned entry-configurations for the formation of labyrinthine structures. After several hundred iterative steps, a stable configuration with some residual fluctuation, which is localized in space and time, appears. The end-configuration is then analyzed in terms of stripes, angles between stripes, vortices, and ensembles of vortices. This analysis enables one to decode some part of the final configuration as unambiguously due to the entry. For example, an entry with a series of several 0 or several 1 leads locally to stripes that are parallel to the entry layer. An entry with alternated 0 and 1 leads locally to stripes that are perpendicular to the entry layer. The first layers are mainly associated with the short-term memory. The internal arrangement of singularities (i.e., knick points of chevrons or centers of vortices) are stabilized by long-term memory effects (long-range interactions). The spatial arrangements of memorized shapes allow the reconstruction of entries or, in other words, will reveal the casual, long-range links between different entry elements. This is one of the main applications of the Neural Networks – pattern recognition. The pattern of the initial signal is recognized by the topology of a final configuration. There exists also an entry-independent part of the final structure, so-called “ego” or “noise” of the network [36], which hampers the progress of recognition. For pattern recognition applications it is important that the system can recognize the sample, despite the fact that the final configuration is noisy – that is, it differs from an ideal one. For this purpose the system should be “trained”, which means that the real final configuration should be compared to several ideal configurations. The deviations of the real finite state from every ideal one must be weighted, and from several possible initial configurations the version with minimal deviations should be chosen [37]. These types of task, however, belong to engineering applications rather than to an understanding of pattern formation.

## 3.2
## Delocalized Particles

### 3.2.1
### Self-Assembled Domain Structures on a Solid Surface: Dipolar Lattice Gas Model

There is considerable current interest in fabricating perfect arrays of nanometer-sized structures on surfaces. One attractive approach is to form patterns of nanometer dimensions on solid surfaces and then to grow the nanostructures on these templates. In this case, large numbers of identical nanostructures can be formed simultaneously. The formation of nanotemplates on surfaces is complicated by the fact that for two-dimensional, two-phase systems with only short-range attractions between atoms, an ordered nanoarray consisting of small domains is not thermodynamically stable. In time, these small domains can coarsen into larger ones, this being true whether the two phases are islands of one material on top of another, or two different structures on the same surface [38]. The reason for this is the high energetic cost of domain boundaries between the two phases. If, however, in addition to the short-range coupling there are longer-range repulsive forces, the competition between the two interactions can lead to a stabilization of domains and two-dimensional self-assembly [39–42].

This type of domain stabilization is very similar to that discussed previously for spin-systems on a lattice. However, the atoms are not localized – that is, they may change their position, and the short- and long-range interactions have elastic origin. It is understandable from a qualitative viewpoint how stress differences can lead to domain stabilization by considering the situation where one phase is under compressive and the other under tensile stress. At each domain boundary there will be elastic relaxation which will lower the surface energy and favor the domain boundaries where the compressive and tensile surface phases are at equilibrium. Analytically, the equilibrium domain size $I_0$ is determined by the ratio of the boundary and surface stress difference. For a relatively sharp boundary $I_0 \approx \pi a \exp(C_1/C_2+1)$, where $C_1$ is the boundary energy per unit length, $C_2$ is proportional to the square of the difference in stress between two phases, and $a$ is a length which measures the sharpness of the interface between the boundaries [38]. Numerically, the interplay of attractive and repulsive forces is often studied in the framework of the Monte-Carlo simulations of the two-dimensional dipolar lattice gas with the following Hamiltonian

$$H = -J' \sum_{\langle \mathbf{R},\mathbf{R}' \rangle} n_{\mathbf{R}} n_{\mathbf{R}'} + \frac{A}{2} \sum_{\mathbf{R},\mathbf{R}'} \frac{n_{\mathbf{R}} n_{\mathbf{R}'}}{|\mathbf{R}-\mathbf{R}'|^3} - \mu \sum_{\mathbf{R}} n_{\mathbf{R}} \,. \tag{3.3}$$

Here, $J'$ is attractive coupling constant, $A$ is the repulsive coupling constant (analog of the repulsive part of the dipolar interaction $D$), $\mu$ is the chemical potential (analog of the magnetic field $H$), and $n_{\mathbf{R}}$ the occupational variable of a lattice site $\mathbf{R}$ which can take the values 0 (cell empty) and 1 (cell occupied) in contrast to Ising-like variables $S_{\mathbf{R}} = \pm 1$. Rewriting the Hamiltonian (Eq. 3.3) in the Ising form

$$H = -J \sum_{\mathbf{R},\mathbf{R}'} S_{\mathbf{R}} S_{\mathbf{R}'} + \frac{D}{2} \sum_{\mathbf{R},\mathbf{R}'} \frac{S_{\mathbf{R}} S_{\mathbf{R}'}}{|\mathbf{R}-\mathbf{R}'|^3} - H \sum_{\mathbf{R}} S_{\mathbf{R}} \tag{3.4}$$

one sees immediately the similarity between $J$ and $J'$, $A$ and $D$ and $H$ and $\mu$.

In order to derive the exact relationship between Ising and lattice gas variables the function $n_{\mathbf{R}} = f(S_{\mathbf{R}})$ must be defined: $S_{\mathbf{R}} = 2n_{\mathbf{R}} - 1$ and hence $n_{\mathbf{R}} = \frac{1}{2}(S_{\mathbf{R}} + 1)$ (3.5). By substituting Eq. (3.5) into Eq. (3.3), one finds

$$
\begin{aligned}
-J'\sum_{\langle \mathbf{R},\mathbf{R}'\rangle} n_{\mathbf{R}} n_{\mathbf{R}'} &= -\frac{1}{4}J'\sum_{\langle \mathbf{R},\mathbf{R}'\rangle}(S_{\mathbf{R}}+1)(S_{\mathbf{R}'}+1) \\
&= -\frac{1}{4}J'\sum_{\langle \mathbf{R},\mathbf{R}'\rangle} S_{\mathbf{R}} S_{\mathbf{R}'} - \frac{1}{2}qJ'\sum_{i} S_{\mathbf{R}} + \mathrm{const}\,,
\end{aligned}
\tag{3.6}
$$

$$
\begin{aligned}
\frac{A}{2}\sum_{RR'}\frac{n_{\mathbf{R}} n_{\mathbf{R}'}}{|\mathbf{R}-\mathbf{R}'|^3} &= \frac{1}{4}\frac{A}{2}\sum_{RR'}\frac{C_3}{a^3}(S_R+1)(S_{R'}+1) \\
&= \frac{A}{8}\sum_{RR'}\frac{C_3}{a^3} S_{\mathbf{R}} S_{\mathbf{R}'} + q\frac{A}{4}\frac{C_3}{a^3}\sum_{i} S_{\mathbf{R}} + \mathrm{const}\,,
\end{aligned}
\tag{3.7}
$$

$$
\mu\sum_{\mathbf{R}} n_{\mathbf{R}} = \frac{1}{2}\mu\sum_{\mathbf{R}} S_{\mathbf{R}} + \mathrm{const}
\tag{3.8}
$$

with $C_3 = \sum_{\mathbf{R}\neq\mathbf{R}'}\frac{a^3}{|\mathbf{R}-\mathbf{R}'|^3}$, and $a$ is the nearest-neighbor distance of a lattice and $q$ is the number of nearest neighbors. Physically, $C_3$ is the dimensionless interaction strength of a perpendicular to the plane dipole at site $\mathbf{R}$ with an infinite two-dimensional array of parallel dipoles. $C_3$ has the numerical value of 9.0336217 for a square lattice, and 11.0341757 for a triangular lattice [6]. By rewriting $\mu \equiv \mu_0 + \delta\mu$, one finds the following correspondence between Ising magnetic and lattice gas models:

- Exchange coupling constant corresponds to the attractive interaction energy of the strength $J' = 4J$;
- Dipolar coupling constant corresponds to the repulsive interaction of the strength $A = 4D$;
- External magnetic field corresponds to the chemical potential with

  $$
  \mu_0 = 2\left(\frac{C_3}{a^3}D - qJ\right) \quad \text{and} \quad \delta\mu = 2H\,;
  $$

- Magnetization $M = \sum_{\mathbf{R}} S_{\mathbf{R}}$ corresponds to the particle density $\rho$. For $N$ as the number of sites, this can be expressed mathematically as

  $$
  \sum_{\mathbf{R}} n_{\mathbf{R}} = \rho N
  \tag{3.9}
  $$

  and

  $$
  \sum_{\mathbf{R}} S_{\mathbf{R}} = N(2\rho - 1)\,;
  \tag{3.10}
  $$

- Free energy corresponds to the pressure and the susceptibility to the compressibility.

The calculations made on the basis of the model Eq. (3.3) show that the dipolar lattice gas supports both disk and stripe domain phases, as well as more complicated domain textures. The spatial ordering of the patterns depends on the chemical potential, the strength of the interactions, and the fractional coverage $\rho$ [6, 9, 42]. Examples of numerical structures are shown in Figure 3.17.

Experimentally, self-assembled domain structures have been found in a Pb/Cu system [38]. The surface alloy phase has been obtained by vapor deposition of Pb on the clean Cu(111) surface at room temperature, and above. According to the experimental verification, the domain pattern changes with increasing area fraction of one phase with respect to the other. As shown in Figure 3.18, the pattern evolves from circular islands of one phase within the matrix of the other to alternating rows of the two phases (stripes) to circular islands of the phase reversed. The real-time experimental observations provided important new insights into the atomic processes at the interface. For example, the size of the domains has been found to depend exponentially on temperature, and the close connection between surface morphology and domain structure has been found [38].

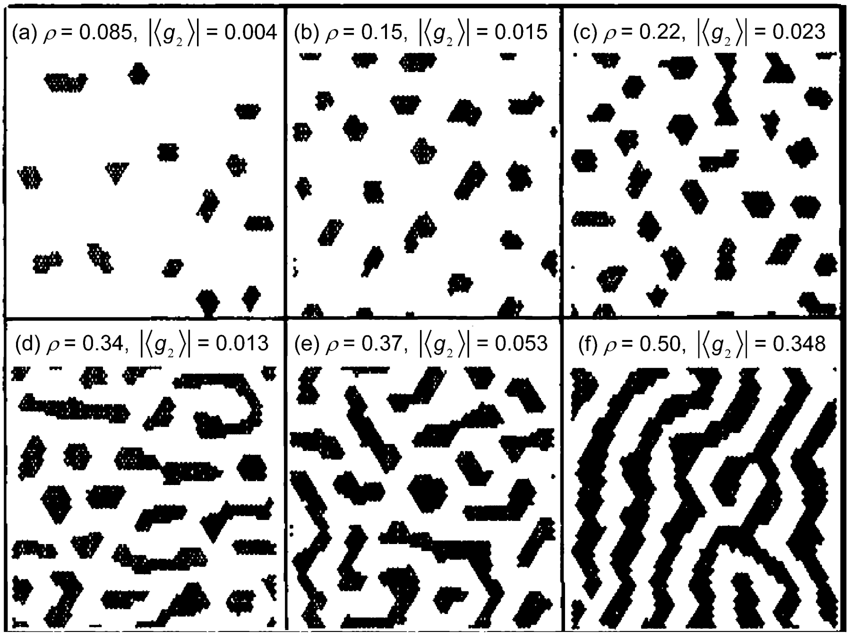

**Fig. 3.17** Snap-shots of domain configurations at several values of the chemical potential $\mu$, $J' = 9.5$, and $A/J' = 3.7$. The average coverage $\rho$ and orientational order parameter are shown next to each figure. Reprinted with permission from [6].

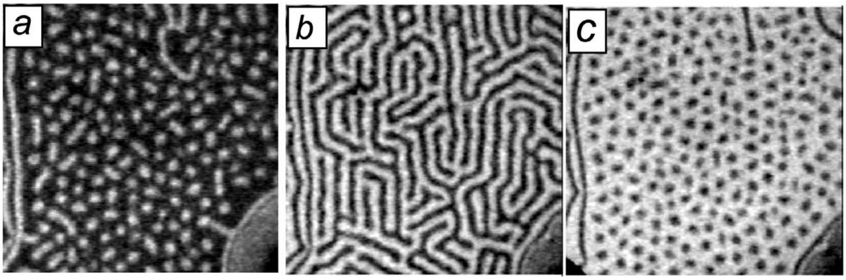

**Fig. 3.18** Low-energy electron diffraction images of domain pattern evolution as a function of Pb coverage of Cu(111) at 673 K. The images correspond to Pb coverage of (a) 0.33, (b) 0.39, and (c) 0.48 ml. Reprinted with permission from Macmillan Publishers Ltd: *Nature*, © 2001 [43].

### 3.2.2
### Self-Organization in Langmuir Monolayers

A Langmuir monolayer is a monomolecular film formed at the air–water interface, usually composed of amphiphilic molecules. Langmuir films are most commonly formed on the surface of water by molecules, called lipids or amphiphiles, which consist of two dissimilar parts. One part is hydrophilic (usually polar) and is commonly referred to as the "head". The rest of the molecule is hydrophobic and, for example, contains one or more saturated alkane chains ("tails") [44]. Such asymmetric molecules naturally prefer the surface of water – that is, they are surfactants. If the tail is sufficiently hydrophobic the material is insoluble, such that the molecules on the surface of the water form an isolated two-dimensional system.

So, why are Langmuir monolayers interesting? To a physicist, a Langmuir monolayer represents an excellent model system for studying ordering in two dimensions. The water surface provides an ideally smooth substrate, while two thermodynamic variables – temperature and surface pressure – can be directly controlled. The surface pressure is varied simply by moving a barrier along the surface, keeping the monolayer molecules on one side but letting the water freely below it (see Fig. 3.19). Such direct mechanical compression, which is a straightforward analog of hydrostatic compression in three dimensions, is not possible in any other two-dimensional system. Moreover, the intramonolayer and the monolayer sub-phase interactions can be varied widely by changing the head or tail parts of the molecule (e.g., the length of a hydrocarbon chain can be varied in small steps), or by changing the pH or ion content of the sub-phases.

As an ideal two-dimensional system, the Langmuir monolayer is used to model the biomembranes. For that purpose, monomolecular films [45] or mixtures of different immiscible amphiphiles (e.g., cholesterol and phospholipids) are utilized [46]. Equilibrium-modulated phases, such as stripes and bubbles, have been found in both systems. For monomolecular systems, the modulated phases correspond to the appearance of periodic intralayer density modulations,

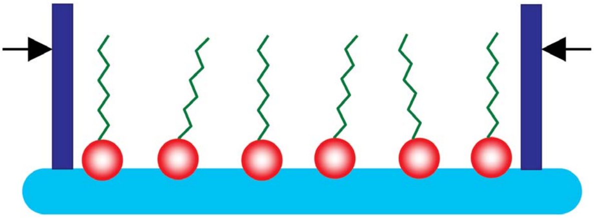

**Fig. 3.19** Langmuir monolayer on the water surface. The surface pressure can be changed by two sliding barriers.

**Inset 3.1** Van der Waals Forces and Lennard–Jones Potential

The origin of van der Waals dispersion forces are fluctuating multipoles. On average, a symmetrical molecule such as hydrogen has no electric moment. However, the electrons are mobile, and at any one instant they might find themselves towards one end of the molecule, making that end negatively charged, $-\delta$. The other end obtains, temporarily, a charge $+\delta$. In the next instant, the electron may move to the other end of the distorted molecule, and it is due to this redistribution of electron density that the molecule becomes a fluctuating multipole. Such a multipole might polarize approaching neutral molecules, while adjacent molecules will tend to attract each other.

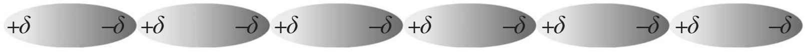

When molecules are close together, this synchronized movement of electrons can occur over huge numbers of molecules. This phenomenon is the only attractive intermolecular force at medium distances present between neutral atoms and molecules. Van der Waals (London) forces are weak, but become stronger as the atom (or molecule) in question becomes larger. This is due to the increased polarizability of molecules with larger, more dispersed electron clouds.

Weak van der Waals attraction at larger separations together with strong repulsion for smaller separations $r$ can well parameterized by the Lennard–Jones potential of the form $V(r)=4\varepsilon[(\sigma/r)^{12}-(\sigma/r)^{6}]$, where $\sigma$ is a characteristic length of the transition from steric core repulsion to the van der Waals attraction and $\varepsilon$ is the energy constant. Despite the fact that the van der Waals forces act on distances larger than the core repulsion, they are still "short-range" interactions compared to dipolar coupling.

and for lipid mixtures they correspond to the modulations of the composition. The patterns are very similar to those in magnetic films, with perpendicular anisotropy and self-assembled domain structures on solid surfaces (see Figs. 3.17 and 3.18). The mechanism of their formation is also similar, namely the competition between the short-range attraction and the long-range repulsion. At short length scales the attractive forces dominate, but as the domain size increases the overall repulsive energy becomes dominant. Hence, the growth leads to a certain selected size, although the origin of those forces is different.

Attraction typically originates from the van der Waals interactions, which belong to a class of feeble dispersion forces that stem from the attraction between temporary, fluctuating multipoles of neighboring molecules (see Inset 3.1). The strength of the attraction increases with decreasing intermolecular distance, and is proportional to the line tension $\lambda$ in a 2D system. The line tension expresses the energy cost incurred in forming boundaries between regions of different composition or different density, and thus favors minimization of the total length of the boundary. As a result, "black"-rich and "white"-rich regions tend to grow. The long-range interaction is derived from the electrostatic repulsion between the charged molecular "heads". These interactions try to repel like-species one from another, and hence the dipolar forces try to increase the length of the boundaries. The line tension can be tuned by the sliding barriers shown in Figure 3.19. Therefore, the ratio between two interactions can also be easily changed and the evolution of the domain pattern can be observed experimentally.

In the case of the two-component Langmuir film, the domains consist of molecules of different sorts. In an "equivalent dipole" model, a lipid molecule in different (black and white) domains has an average electrostatic dipole moment density $m_B$ or $m_W$ oriented perpendicular to the water interface [41]. At a critical pressure $\Pi_C$ the difference $m=|m_B-m_W|$ approaches zero with critical exponent $\beta$: $m=m_0(1-\Pi/\Pi_C)^{\beta}$. The dipole density difference is proportional to the composition difference for ideal mixtures. The exponent is $\beta\approx 0.25$ for a binary mixture of cholesterol and phospholipids. The dipole density difference and the line tension play against each other to determine the size of domains. The line tension can be related to the critical exponent $\mu: \lambda=\lambda_0(1-\Pi/\Pi_C)^{\mu}$, where $\lambda_0$ is a line tension at zero pressure. In two dimensions, $\mu$ is close to unity for a wide palette of mixtures [46]. A large dipole density difference favors narrow stripe domains, while a large tension favors compact domains of larger width [46]. A change in the width of the stripe domains in a Langmuir layer with the line tension is demonstrated in Figure 3.20.

In addition to controlling the period of modulated phases, the balance of competing interactions also determines the stability of the shapes of individual, isolated domains. Consider an isolated two-dimensional circular "white" domain embedded in a matrix of "black" component. As long as line tension predominates, a circular domain shape will be preferred because this minimizes the length of the domain boundary. As repulsive interactions between individual particles of the "white" subphase grow in relation to the line tension, however, instabilities ensue to produce elongated and branched shapes [47].

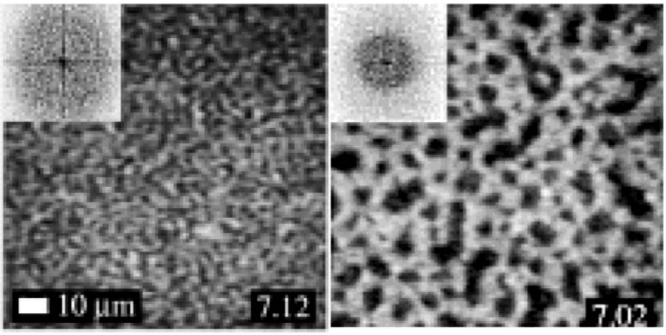

**Fig. 3.20** Experimental determination of stripe width. Micrographs of stripe domains at different pressures (inset values in dyne cm$^{-1}$). At high pressure $\Pi = 7.12$ dyne cm$^{-1}$ (left), near critical points the stripes are thin, while at $\Pi = 7.02$ dyne cm$^{-1}$ (right) the stripe width is increased and many of the stripes become circular domains. Stripe width is proportional to the radii of the rings in the Fourier transform, as measured from the peak intensity of the ring. Reprinted with permission from [46].

### 3.2.3
### Self-Organization in Block Copolymer Systems

Block copolymers are composed of long sequences ("blocks") of the same monomer unit, covalently bound to sequences of unlike type. The blocks can be connected in a variety of ways; schematics of AB diblock and ABA triblock structures are shown in Figure 3.21. The blocks can sometimes intermix freely at sufficiently high temperature or, when sufficiently diluted with solvent, generate the "disordered" structure shown in Figure 3.21 (right). However, it is common for the blocks spontaneously to self-assemble (Fig. 3.21, left) into a diversity of mesophases, with the size scale governed by the chain dimensions (order of tens of nanometers). One of those mesophases is a familiar nanometer-scale stripe pattern, although spherical, cylindrical and/or lamellae structures have also been observed [48]. Initially, the patterns amount to no more than a random dappling of the film, but with time the dark and light regions organize themselves into the swirling fingerprint patterns shown in Figure 3.22. As time passes, the swirls become smoother and the defects become fewer. In this way the film progresses towards a regular parallel stripe pattern.

The stripe patterns shown in Figure 3.22 result from the competition between an *effective* long-range and an *effective* short-range interaction. The couplings of both ranges comprise several specific molecular contributions such as osmotic compressibility, electrostatic repulsion, or strength of the covalent linkage. The long-range part [49–51] reflects the connectivity of the copolymer molecular blocks, which precludes compositional fluctuations on large length scales [40, 52]. In diblock copolymers, for example, the long-range part includes the repulsion between the two halves of each polymer molecule. The short-range effective interactions include, amongst other contributions, an attraction between the

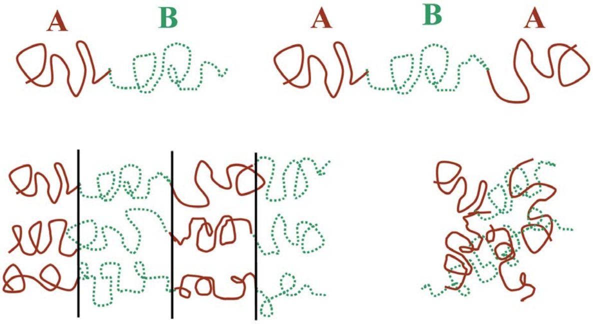

Fig. 3.21 Schematic representation of a diblock (AB), and a triblock (ABA) copolymer molecule (top) and of a stripe-like and a disordered copolymer mesophase (bottom).

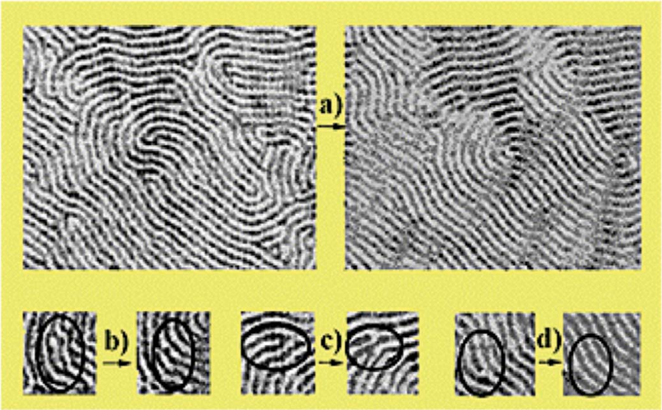

Fig. 3.22 Defect evolution by relinking and joining of defects in polystyrene (PS)-block-polymethylmethacrylate (PMMA) diblock copolymers. Bright domains are PMMA, dark domains are PS. (a) 2 µm × 1.5 µm atomic force microscopy images of microdomains annealed for 2 h (left-hand side) and 3 h (right-hand side) at 523 K. (b–d) 0.5 µm × 0.5 µm images of the defect change. Adapted from [48].

like-parts of two different copolymer molecules [51]. Whilst the shape of domains is determined by the competition between the short- and long-range interactions, the width of the stripes is determined by the length of the polymer chains in the film. The ordering can be controlled either by the composition or by the concentration of copolymers in the solution.

### 3.2.4
### Self-Organization in Colloidal Systems

As discussed previously in Section 2.6.1.4, the electrostatic repulsive long-range order interactions can lead to formation of the so-called Wigner crystal in two-dimensional electron system. Similar phenomena can occur in two-dimensional arrays of nanometer-sized colloidal particles confined to a surface of a liquid. During the past few years, many examples of such systems have been reported, including: electrorheological fluids consisting of suspensions of electrically polarizable particles in insulating solvents [53]; polar amphiphiles at an air–water interface [54]; suspensions of small (~100 Å) permanently magnetized particles in a non-magnetic solvent or ferrofluids [55]; and magnetorheological fluids [56], that is, dispersions of a ferrofluid in a non-magnetizable fluid. Depending upon the system objectives in all of these diverse media, ordered structures can be formed. The most characteristic examples will be outlined in the following sections.

#### 3.2.4.1 Planar Colloidal Crystals

One of the first such systems has been studied by Pieranski [57], who investigated a monolayer of polystyrene spheres trapped at a water–air interface. The radius of spheres was approximately 1000 Å, and the concentration of the solution $20\times10^{12}$ particles $\text{cm}^{-3}$. In spite of the Brownian motion, the particles never penetrated into the bulk. Photographs of the surface monolayer showed an ordered array of hexagonal symmetry (see Fig. 3.23 a). Interactions in this experiment are short-range steric repulsion of the hard spheres and long-range dipolar interaction. Due to the combination of two interactions, distances between the colloidal particles are larger than their radius (see Fig. 3.23). The electrostatic dipolar interaction comes from the formation of effective dipoles near the surface of polystyrene spheres immersed in water. Dissociation of the sulfonic acid groups coming from the polymer leads to an asymmetric (with respect to the interface) but axially symmetric distribution of charges (see Fig. 3.23 b). This

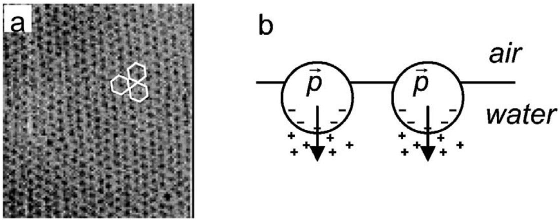

**Fig. 3.23** (a) Portion of a microscopic image of the polystyrene colloid crystal with hexagonal symmetry; the dipolar interactions are repulsive (reprinted with permission from [57]). (b) Formation of electric dipoles at the sphere–water interface.

charge distribution is associated with vertical dipole moments of strength of approximately 1000 $e$. As all dipoles are confined to a plane and oriented along its normal, the second term in Eq. (3.2) vanishes. This means that the dipole–dipole interactions have a purely repulsive character, just as the simple Coulomb repulsion of like charges. The only difference is that the dipolar interactions decrease with distance as $1/r^3$ instead of $1/r$. However, this does not change the structure of the colloid crystal.

Recently, it has been shown that two-dimensional crystals can be formed on a fluid surface, not only with hexagonal symmetry but also with all other planar crystal symmetry such as the oblique, centered-rectangular, rectangular, and square lattices [58]. These lattice structures, some of which are metastable, can be reversibly tuned by adjusting the polar and azimuthal angles of the magnetic field relative to the surface normal and the symmetry direction of the 2D lattice. Furthermore, by using two different-sized magnetic particles, local formations of 2D quasicrystallites with fivefold symmetry were observed. In this study [59], spherical magnetic particles have been fabricated by coating 25- to 50 μm-sized spheres with 1.5 μm-thick nickel layers. The competing interactions included long-range magnetic repulsion and "attractive" interaction due to the weight of the particles projected along the surface tangent.

#### 3.2.4.2 **Patterns in Ferrofluids**

Magnetic fluids are colloidal suspensions of magnetic particles; the liquid carrier may be either polar or non-polar. If the particles are very fine they are usually classified as ferrofluids. Suspensions of larger particles or ferrofluid droplets in a non-magnetizable fluid are denoted as magnetorheological fluids; these are often used in dampers, brakes and clutches as their viscosity is greatly increased under the application of a strong magnetic field. This occurs due to the structural and magnetic instability of the large, micron-sized grains. Colloidal particles in ferrofluids are stable both structurally and magnetically [55]; therefore, ferrofluids maintain their fluidity even if subjected to strong magnetic fields [59]. In order to keep the colloidal ferrofluid stable and prevent aggregation processes from increasing the viscosity, the magnetic particles are either coated with surfactant agents (usually magnetite, $Fe_3O_4$) or electrically charged (usually maghemite, $\gamma$-$Fe_2O_3$ or ferrites).

The stability and properties of a magnetic colloid are determined by the balance between the attractive and repulsive interactions. There are basically two main attractive interactions between magnetic particles in a ferrofluid: van der Waals forces, and magnetic dipole–dipole interactions. The van der Waals–London force has a shorter range, and the strength of attraction increases with the particle size. The magnetic dipole–dipole interaction may be attractive for certain orientations of two magnetic dipoles, and is of long-range order. The repulsive interactions include long-range electrostatic interactions between charged particles in ionic ferrofluids, or steric repulsion forces of the short-range order in surfacted ferrofluids. The total interaction potential is dominated by the van der Waals attraction for distances $r$ of the order of the average particle diameter $\bar{d}$, and by the magnetostatic interaction for larger distances. The temperature ($T$) also plays an important role. In order to evaluate the typical particle diameter ($D$) to avoid magnetic agglomeration, the thermal energy must be compared with the dipole–dipole pair energy [55]: $\bar{d} \leq \left(\frac{72k_BT}{\pi\mu_0M^2}\right)^{1/3} \leq 10$ nm with $M$ the magnetization.

For calculations related to the dynamic properties of the system (e.g., for molecular dynamic simulations), it must be borne in mind that there exist two distinct mechanisms for the rotation of magnetic moments in magnetic fluids. The first mechanism is rotation of the magnetic particle inside the liquid carrier, referred to as *Debye* or *Brownian* rotation. This type of torque is derived from the Brownian motion and collisions of particles. The relaxation time for this rotation is, for spherical particles, $\tau_B = 3V\eta/k_BT \approx 10^{-2}\ldots10^{-3}$ s [55], where $V$ is the particle's hydrodynamic volume and $\eta$ is the liquid's dynamic viscosity. The second mechanism is rotation of the magnetic moment with respect to the particle; this is known as *Néel* rotation. The relaxation time for this rotation is heavily dependent on the particle volume and on the temperature, namely $\tau_N = 2\pi f_0 e^{(kV/k_BT)}$, where $f_0$ is the attempt frequency in the $10^7\ldots10^{12}$ Hz range and $K$ is the anisotropy constant of the particle. In the case of a magnetite particle [60], $K = 1.1 \cdot 10^4$ J/m$^3$, at room temperature $\tau_N$ increases from $4 \cdot 10^{-9}$ s to $7 \cdot 10^{-5}$ s upon increasing the particle's diameter from 10 nm to 20 nm. In absence of magnetostatic interactions for dominating Néel rotation, the particle is superparamagnetic and, hence, the ferrofluid is also superparamagnetic. By lowering the temperature one arrives at a temperature $T_B$, known as blocking temperature, below which $\tau_N$ is larger than the typical observation times. Below $T_B$ the particle itself is no longer superparamagnetic, but the magnetic fluid remains superparamagnetic because of the Brownian rotation. When the magnetostatic interactions become comparable with the temperature, they stabilize the long-range magnetic ordering in ferrofluids. At low temperatures the stable magnetic pattern is determined by the magnetostatic interactions, and does not depend on the type of the rotation. Moreover, the higher-order magnetostatic moments can be neglected for two reasons: first, due to the rather large interparticle distances; and second, due to the spherical form of the particles (see Section 2.6). Therefore, the ferrofluids can be nicely modeled as a dilute gas of dipolar hard spheres. In this model the particles are specified by their center position and their magnetization. The particle–particle interaction has two components: (i) the repulsive hard-core interaction $H_{hc} = \sum_{ij} V_{ij}$, where $V_{ij} = A\left[\frac{||\mathbf{r}_j - \mathbf{r}_i||}{\sigma}\right]^{-n}$ for $||\mathbf{r}_j - \mathbf{r}_i|| = r_{ij} < \sigma$ and $V_{ij} = 0$ for $r_{ij} > \sigma$; and (ii) the dipole–dipole interaction [given in Eq. (3.2)]. $A$ is the repulsive intensity with an excluded sphere of grain diameter $\sigma$, and $n$ is usually considered to between 5 and 10 [61].

The symmetry of stable magnetic patterns depends heavily on the presence of an external magnetic field. If the ferrofluid droplet is confined between two glass slides and a perpendicular magnetic field is applied, the magnetic particles are polarized in the field direction. Hence, all dipoles are parallel, and these repel each in same way as colloidal particles or two-dimensional electron gas (see

Section 2.6.1.4). In contrast to the two-dimensional electron gas or charged colloids, however, there exist in the ferrofluids significant attractive van der Waals interactions which, similar to Langmuir films, cause strong surface tension in the constrained magnetic fluid. Surface tension maintains the topology of a single disc-like droplet of a ferrofluid in the center of cell, although at the perimeter – where the dipolar repulsion is able to compete with the line tension – a typical labyrinthine structure is formed [62]. In the labyrinth, the "black" regions of magnetic phase alternate with the "white" regions of the liquid carriers. Hence, the origin of the stripe pattern is phase separation, just as in the Langmuir films or stripe domains on the solid surfaces.

In the absence of an external field, the magnetic particles are free to rotate. In the Monte-Carlo simulations, the magnetic particles easily find the energetically most favorable head-to-tail configurations. However, for strongly interacting ferrofluids the individual magnetic particles tend to align into chains, loops, or branched networks. The chains are confined to the plane in the case of the two-dimensional glass cell described above. The pattern depends heavily on the particle density, and three typical theoretical configurations for different particle concentrations are illustrated in Figure 3.24. The dipole–dipole coupling favors straight lines which can be curved due to either temperature or Brownian mo-

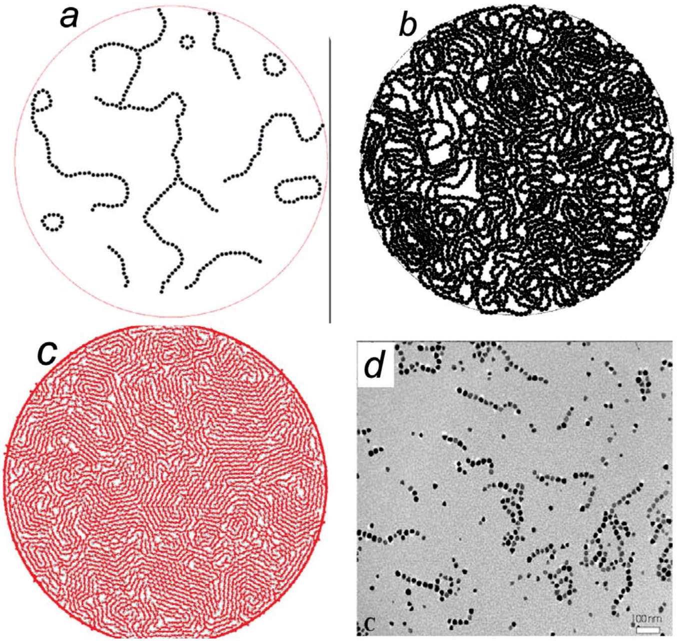

**Fig. 3.24** (a)–(c) Theoretical chain configurations in ferrofluids (courtesy of A. Ghazali). (d) Experimentally found chain structure (adapted from [63]).

tion. The energy loss due to the curvature of rings is balanced by the energy gain due to the closure of ending connections. Dipoles are always aligned along the chain, with the dipolar energy per site close to $\zeta(3)=1.2$, where $\zeta(s)$ is the Riemann zeta function. This corresponds to the connectivity of just two nearest neighbors [61]. The connectivity increases with increasing concentration of the magnetic particles such that, for high concentration the chains interact to form many metastable vortex structures. The centers of the vortices often coincide with the vacancies in the particle distribution (see Fig. 3.24 b, c). Recently, similar chain structures have been visualized experimentally in laboratory-prepared magnetite dispersions [63] (see Fig. 3.24 d). Here, the 20-nm particles form dynamic structures that are comparable to those of the simulations in Figure 3.24 a, b, while the 16-nm particles form droplet-shaped structures due to prevailing van der Waals attractions.

#### 3.2.4.3 **Systems of Magnetic Holes**

In all of the examples described in the previous sections, it is the dispersion of charged or magnetic particles in a *non-magnetic* media that has been discussed. The reverse situation with non-magnetic particles in a *magnetic* fluid or ferrofluid represents another concept for model studies of phase transitions. In that case, instead of a system of magnetic/electric particles, a system of charged holes appears (see Fig. 3.25 b). The pioneering steps in this direction were made by A. T. Skjeltorp [64], who studied a thin layer of magnetic fluid containing a monolayer of monodisperse polystyrene spheres in an external magnetic field – that is, a system of magnetic holes. Subsequently, similar results have been obtained for polystyrene spheres suspended in an aqueous medium, to which a high-frequency uniform electric field has been applied. At high frequencies a single sphere distorts the field in such a way that it is equivalent to a dipole pointing along the external field [65]; thus, the spheres act as dielectric holes in the water.

The ordering of magnetic holes depends on the orientation of an external magnetic field, since the effective magnetic dipolar interactions between the

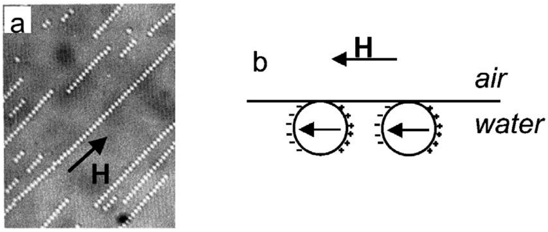

**Fig. 3.25** (a) Part of a microscopic image of a system of magnetic holes in an external in-plane magnetic field **H**. The dipolar interactions between the holes are attractive (reprinted with permission from [64]). (b) Formation of magnetic dipoles at the sphere–ferrofluid interface.

spheres may be made attractive or repulsive by an external field $H$ parallel or perpendicular to the layer, respectively. The case when the external field is perpendicular to the layer is analogous to that of Section 2.6.2.1. This situation includes a two-dimensional system of repulsive dipoles forming a triangular lattice. If, however, the field is parallel to the layer, the situation is different, and all dipoles align themselves in the layer plane. This means that the product $(\mathbf{S}_i \cdot \mathbf{r}_{ij})(\mathbf{S}_j \cdot \mathbf{r}_{ij})$ in the second term of Eq. (3.2) is no longer zero, and hence the dipole–dipole interaction energy will decrease with decreasing distance between moments or, in other words, the dipolar term becomes attractive. Depending on the density of spheres and the external field, a variety of crystalline-like and amorphous-like configurations can be formed. These crystalline structures consist mainly of chains (see Fig. 3.25 a), the density of which increases with increasing concentration of the solution.

### 3.2.5
### Two-Dimensional Electron Systems

In two-dimensional electron gas systems long-range Coulomb repulsion leads to the formation of Wigner crystal of hexagonal symmetry (see Section 2.6). There exist, however, electronic systems with intrinsic attractive interactions; an example of this is metal oxides and doped itinerant antiferromagnets. In the case of the metal oxides, holes with repulsive Coulomb interaction move in an antiferromagnetic background and produce during the movement a distortion of the antiferromagnetic bonds. This magnetic distortion in turn gives rise to the dipolar attraction between the holes. In similar fashion, an antiferromagnetic bond can be broken during the movement of charge carriers in a doped itinerant antiferromagnets, leading to a short-range attraction. The interaction energy of such systems can be successfully simulated by the simple Hamiltonian [66], $H = 1/r - B\exp(-kr)$, where $r$ is the distance and $k$ the inverse range, while the parameter $B$ is used to vary the relative strength of the attractive interaction. In the absence of disorder, the Wigner crystal for $B=0$ has been found. As $B$ is increased, the lattice becomes increasingly distorted until for $B=0.25$ to $B<0.325$ dynamics stripes form, and for $B\geq 0.325$ clumps form. The characteristic for different coupling strength patterns are shown in Figure 3.26; these correspond to a slow velocity of electrons (i.e., a quasi-stationary pattern). Increasing the drive force and hence the kinetic energy leads to distortions of the lattice and net-like particle configurations.

### 3.2.6
### Patterns in Animal Colors

Many animals have patterns of coloration on their external surface. Both, predator (tigers, leopards) and prey (zebras, giraffes) mammals can have patterned skin. Large (cheetahs, giraffes), small (ladybird) or nanometer-sized animals (bluetongue virus) may have a strictly regular geometrical coloration. Often, the patterns

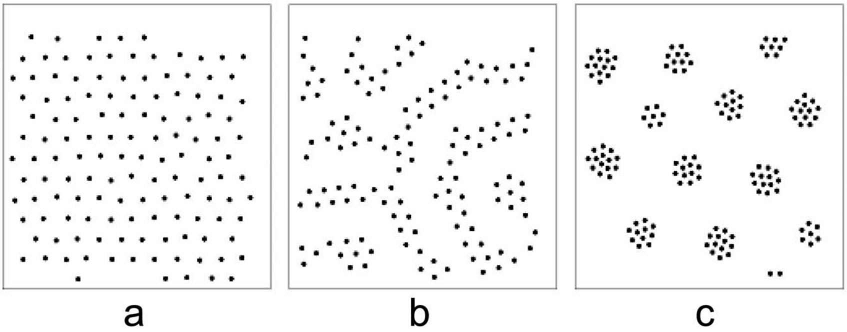

**Fig. 3.26** Individual snapshots of the two-dimensional electron sysetm for the ratio between the attractive and the repulsive interactions $B$ for (a) $B=0$ (Wigner crystal); (b) $B<0.325$ (stripes); and (c) $B\geq0.325$ (clumps). Adapted from [66].

are composed of only two colors, though in some cases there are more, and they can vary in a subtle way between different individuals. Explanations of this phenomenon have been proposed based on the concepts of evolutionary theory, suggesting that such physiological attributes as coloring arise from a survival advantage. A typical example is that color is used as a camouflage, but this does not appear to be true for all species. An alternative explanation relies upon forms of social or collective behavior; the coloration of zebras, for example, might serve to confuse predators because it inhibits the distinction between one sole individual and a group of animals. As the herd as a whole is not readily attacked, the individuals are protected. This is, however, not true for predators [67]. It may also be that individuals are identified through the specific distinctions in coloring patterns.

Regardless of the purpose of coloring, the process of coloration should be determined on the scale of individual cells as color is result of pigment produced in cells. On the one hand, it seems that the pattern of an animal's skin is secondary in comparison to the formation of limbs or neural and vascular networks. On the other hand, different patches of color require sometimes different functions of the cells and, hence, only after a pattern has been established can the processes associated with differential functions of the cells proceed. Thus, the patterns in animal colors relate to important questions of developmental biology [67].

An excellent review of the models describing color self-organization in animals is provided in [67]. Here, a cellular model will be presented as it fits well into the topic of competing short- and long-range interactions. A mathematical model describing the formation of animal colors might use a cellular space, with a variable representing the color of each cell in an array. As many of these animals have essentially two colors, a binary variable $s_i$ can be used. This type of model is suggestive of a simple cellular automation or Ising procedure, where the individual cell determines its state as a consequence of interactions with neighboring cells. Indeed, the local intercellular influence in biology is strong. The migration of cells or changes in their shapes can be neglected in most cases, and hence the principal issues are not dynamic but rather revolve around constructing a model with complex pattern as its equilibrium or steady-state structure. Although the most direct model represents each biological cell by a lattice cell, a homogeneous region of biological cells can be represented by a single lattice cell. The simplest spot-like color pattern is a checkerboard, and within the framework of the lattice model with local interactions this can be produced by an antiferromagnetic exchange coupling between nearest-neighbor cells on a square lattice (see Chapter 2). The most basic feature of color patterns in animals – the existence of different length scales – is not captured by this model with short-range interactions only. An alternative, straightforward method to create a new length scale is to introduce longer-range interactions. But, is this reasonable for a biological system?

Interaction in biological systems mainly occurs via the emission of chemicals into the intercellular fluid; these chemicals are then detected by adjacent cells. These interactions, however, are not necessarily local, because the distance over which the chemicals travel is controlled not only by their diffusion constant but also by their lifetime in the cell matrix and intercellular fluid. Thus, an individual cell can interact with a region of cells in its vicinity, where the size of this region is controlled by the diffusion constant of the chemicals, as well as any reactions in which they might participate. Hence, long-range interactions exist in biological systems.

There are two possible types of pairwise interactions between cells. When one cell producing pigment causes other cells to produce pigment, the interaction is defined as *activating*. When a cell causes others *not* to produce pigment, the interaction is *inhibiting*. The interactions must achieve two effects. First, they must cause nearby cells to have a bias toward having the same color, so that the regions of color are formed. Second, they must cause regions that are further away to have the opposite color. This suggests a short-range activating and a long-range inhibiting interaction. The mathematics of activation clearly corresponds to the ferromagnetic exchange interactions that cause the spins to be aligned. For inhibition, there are two possibilities – either antiferromagnetic or dipolar interactions. Within the framework of the Ising model, both couplings force the spins to be anti-aligned, the only difference being that the dipolar interaction always decreases proportionally to $1/r_{ij}^3$ while the $r_{ij}$-dependence of the antiferromagnetic interaction depends on the objectives of the system. The best fit provides calculations using local ferromagnetic and long-range antiferromagnetic interactions according to the Hamiltonian

$$H = -h \sum_i s_i - \frac{1}{2} J_{ff} \sum_{r_{ij} \leq R_1} s_i s_j + \frac{1}{2} J_{af} \sum_{R_1 < r_{ij} < R_2} s_i s_j \; . \tag{3.11}$$

The existence of long-range antiferromagnetic interactions causes patches of color or stripes, depending on parameters $J_{ff}$, $J_{af}$, $h$, $R_1$ and $R_2$. The most obvious changes occur with $R_2$. The characteristic size of the pattern increases and is di-

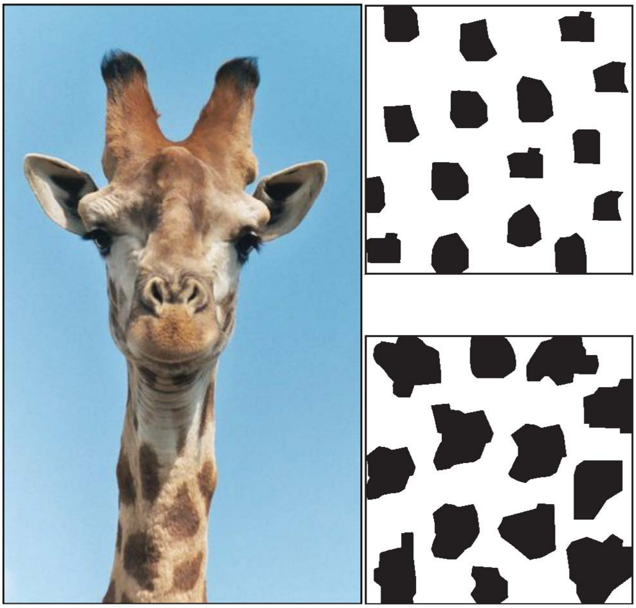

**Fig. 3.27** The giraffe color patterns generated by starting from points that are regularly spaced in the plane (upper right inset). The parameters of the activation-inhibition model of Eq. (3.11) are $R_2=11$, $R_1=1$, $h=-24$.

rectly controlled by $R_2$. Increasing $R_1$ does not affect the size of the pattern but rather the shape of the boundaries between regions of different color. Increasing $R_1$ ensures that the boundaries are smoother. For realistic color patterns of large animals, the size of $R_1$ should be larger than the size of cells, to avoid sharp corners [67].

The initial conditions of the simulations can be important. For example, while a striped tiger pattern can be obtained without specific initial conditions, the best simulation of the Ugandan giraffe pattern is generated by starting from points that are rather regularly spaced in the plane and then relaxing to the equilibrium configuration (see Fig. 3.27). If the simulation is started with low density of random "black" cells for the same set of parameters, then the pattern will be much more disordered and in than sense dissimilar to the giraffe pattern.

## 3.3
## Exercises

1. Calculate the exchange energy per spin of a line of mutually parallel and perpendicular to the chain magnetic moments $\mathbf{S}=1$ as a function of number of spins in the chain $N$.

*Solution*

The exchange energy of a chain consisting of $N$ moments is $E_J = -\frac{J}{2}\sum_{\langle i,j\rangle} \mathbf{S}_i\mathbf{S}_j = -\frac{J}{2}\sum_{\langle i,j\rangle} \cos\alpha$; $\cos\alpha = 1$ as the spins are all parallel. Then, the exchange energy per spin is $E_J^{\text{spin}} = -\frac{(2NJ-J-J)}{2N} = \frac{J(N-1)}{N}$.

2. Calculate the dipolar energy per spin of a line of mutually parallel and perpendicular to the chain magnetic moments $\mathbf{S}=1$ as a function of number of spins in the chain $N$.

*Solution*

The dipolar energy of a chain consisting of $N$ moments is $E_D = \frac{D}{2}\sum_{\langle i,j\rangle}\frac{\mathbf{S}_i\mathbf{S}_j}{r^3} = \frac{D}{2}\sum_{\langle i,j\rangle}\frac{\cos\alpha}{r^3}$; $\cos\alpha = 1$ as the spins are all parallel. The sum $\sum_j \frac{1}{r^3} = \sum_{r=1}^{N}\frac{1}{r^3} = \sum_{r=1}^{\infty}\frac{1}{r^3} - \sum_{r=N}^{\infty}\frac{1}{r^3}\Delta\xi(3) - \int_N^\infty \frac{dr}{r^3} = 1.2020569032 - \frac{1}{2N^2}$, where $\xi(p) \equiv \sum_{n=1}^{\infty} n^{-p}$ is called zeta Riemann function. The dipolar energy per spin is

$$E_D^{\text{spin}} = \frac{D}{2}\sum_{i,j}\frac{1}{r^3} = \frac{D\sum\limits_{r=1}^{N}\left(2\cdot\xi(3) - \frac{1}{2(N-r)^2} - \frac{1}{2r^2}\right)}{2N} \, .$$

3. Calculate the exchange and dipolar energies of a line of mutually antiparallel and perpendicular to the chain magnetic moments. Plot all four calculated functions and make a conclusion about the favorable and non-favorable configurations of magnetic moments in such a system for three cases: $D<J$; $D>J$ and $D\approx J$. Discuss the role of number of moments $N$ in the chain for possible configurations.
4. Perform the same calculations as in Questions 1 and 2, considering that angle $\beta$ of moments with respect to the distance vector $\mathbf{r}_{ij}$ varies between 0 to $\pi$. Find the ground state configuration.

*Solution*

$$E_D = \frac{D}{2}\sum_{\langle i,j\rangle}\frac{\mathbf{S}_i\mathbf{S}_j - 3\mathbf{S}_i\cdot\mathbf{r}_{ij}\mathbf{S}_j\cdot\mathbf{r}_{ij}}{r^3} = \frac{D}{2}\sum_{\langle i,j\rangle}\frac{\cos\alpha - 3\cos^2\beta}{r^3} \, . \quad \text{Hence}$$

$$E_D^{\text{spin}} = \frac{D}{2}\sum_{i,j}\frac{1-3\cos^2\beta}{r^3} = \frac{D\sum\limits_{r=1}^{N}\left(2\cdot\xi(3) - \frac{1}{2(N-r)^2} - \frac{1}{2r^2}\right)(1-3\cos^2\beta)}{2N}$$

$$= \frac{DNf(N)(1-3\cos^2\beta)}{2N} = Df(N)(1-3\cos^2\beta) \, .$$

By minimizing $E_D^{\text{spin}}$ with respect to $\beta : dE_D^{\text{spin}}/d\beta = 0$, one finds that the ground state corresponds to $\beta = 0$, that is, the magnetization/polarization must lie parallel to the chain.

## References

1 A. Kubetzka, M. Bode, O. Pietzsch, R. Wiesendanger, *Phys. Rev. Lett.* **2002**, *88*, 057201.
2 J. Delacour, J.-C. Lévy (Eds.) *Systems with Learning and Memory Abilities*, Elsevier (North-Holland), Amsterdam, **1988**.
3 B. Kaplan, G.A. Gehring, *J. Magn. Magn. Mater.* **1993**, *128*, 111.
4 A.B. MacIsaac, J.P. Whitehead, M.C. Robinson, K. De'Bell, *Phys. Rev. B* **1995**, *51*, 16033.
5 A.B. Kashuba, V.L. Pokrovsky, *Phys. Rev. B* **1993**, *48*, 10335.
6 M.M. Hurley, S.J. Singer, *J. Phys. Chem.* **1992**, *96*, 1938.
7 I.N. Booth, A.B. MacIsaac, K. De'Bell, J.P. Whitehead, *Phys. Rev. Lett.* **1995**, *75*, 950.
8 E.Y. Vedmedenko, A. Ghazali, J.-C.S. Lévy, *Surf. Science* **1998**, *402–404*, 391.
9 A.D. Stoycheva, S.J. Singer, *Phys. Rev. E* **2001**, *64*, 016118.
10 E.Y. Vedmedenko, A. Ghazali, J.-C.S. Lévy, *Phys. Rev. B* **1999**, *59*, 3329.
11 A. Hubert, R. Schäfer, *Magnetic Domains: The Analysis of Magnetic Microstructures*, Springer, Berlin, **1998**, pp. 310–312.
12 J.A. Cape, G.W. Lehman, *J. Appl. Phys.* **1971**, *42*, 5732.
13 C.L. Dennis, R.P. Borges, L.D. Buda, U. Ebels, J.F. Gregg, M. Hehn, E. Jouguelet, K. Ounadjela, I. Petej, I.L. Prejbeanu, M.J. Thornton, *J. Phys. C: Condens. Matter* **2002**, *14*, R1175.
14 R.P. Cowburn, *J. Phys. D: Appl. Phys.* **2000**, *33*, R1.
15 E.Y. Vedmedenko, H.P. Oepen, J. Kirschner, *Phys. Rev. Lett.* **2003**, *90*, 137203.
16 N.D. Mermin, H. Wagner, *Phys. Rev. Lett.* **1966**, *17*, 1133.
17 H.A.M. van den Berg, D.K. Vatvani, *J. Appl. Phys.* **1981**, *52*, 6830.
18 T. Shinjo, T. Okuno, R. Hassdorf, K. Shigeto, T. Ono, *Science* **2000**, *289*, 930.
19 A. Wachowiak, J. Wiebe, M. Bode, O. Pietzsch, M. Morgenstern, R. Wiesendanger, *Science* **2002**, *298*, 577.
20 W.F. Brown, Jr., *J. Appl. Phys.* **1968**, *39*, 993.
21 R.P. Cowburn, D.K. Koltsov, A.O. Adeyeye, M.E. Welland, D.M. Tricker, *Phys. Rev. Lett.* **1999**, *83*, 1042.
22 E.Y. Vedmedenko, *Ferroelectrics* **2004**, *305*, 129.
23 A.P. Ramirez, *Nature* **2003**, *421*, 483.
24 A.P. Ramirez, in: *Handbook of Magnetic Materials, Vol. 13*, K.H.J. Buschow (Ed.), Elsevier, Oxford, **2001**.
25 B.C. den Hertog, M. Gingras, *Phys. Rev. Lett.* **2000**, *84*, 3430.
26 A. Chubukov, *Phys. Rev. Lett.* **1992**, *69*, 832.
27 N. Gov, *J. Phys.: Condens. Matter* **2002**, *14*, 6931.
28 S. Sachdev, *Phys. Rev. B* **1992**, *45*, 12377.
29 J.C.S.E. Palmer, *Phys. Rev. B* **2000**, *62*, 488.
30 Y. Sasaki, F. Matsubara, *J. Phys. Soc. Jpn* **1998**, *67*, 1134.
31 E.Y. Vedmedenko, unpublished results.
32 S.R.E. Rastelli, A. Tassi, *Phys. Rev. B* **2002**, *66*, 054431.
33 J.J. Hopfield, *Proc. Natl. Acad. Sci. USA* **1982**, *79*, 2554.
34 P. Rujan, Cellular automata and models of memory. In: *Systems with Learning and Memory Abilities*, J. Delacour, J.-C. Lévy (Eds.), Elsevier (North-Holland), Amsterdam, **1988**.
35 L.N. Cooper, A possible organization of animal memory and learning. In: *Proceedings of the Nobel Symposium on Collective Properties of Physical Systems*, B. Lundquist, S. Lundquist (Eds.), Academic Press, New York, **1973**.
36 J.-C.S. Lévy, D. Mercier, Neural Networks with Selforganization. In: *Systems with Learning and Memory Abilities*,

J. Delacour, J.-C.S. Lévy (Eds.), Elsevier (North-Holland), Amsterdam, **1988**.

**37** C.M. Bishop, *Neural Networks for Pattern Recognition*, Clarendon Press, Oxford, **1995**.

**38** R. Plass, N.C. Bartelt, G.L. Kellogg, *J. Phys.: Condens. Matter* **2002**, *14*, 4227.

**39** T. Garel, S. Doniach, *Phys. Rev. B* **1982**, *26*, 325.

**40** M. Seul, D. Andelman, *Science* **1995**, *267*, 476.

**41** H.M. McConnell, *Annu. Rev. Phys. Chem.* **1991**, *42*, 171.

**42** S.L. Keller, H.M. McConnell, *Phys. Rev. Lett.* **1999**, *82*, 1602.

**43** R. Plass, J.A. Last, N.C. Bartelt, G.L. Kellogg, *Nature* **2001**, *412*, 875.

**44** V. Kaganer, H. Möhwald, P. Dutta, *Rev. Mod. Phys.* **1999**, *71*, 779.

**45** H.M. McConnell, L. Tamm, R.M. Weis, *Proc. Natl. Acad. Sci. USA* **1984**, *81*, 3249.

**46** S.L. Keller, H.M. McConnell, *Phys. Rev. Lett.* **1999**, *82*, 1602.

**47** K.J. Stine, C.M. Knobler, R.C. Desai, *Phys. Rev. Lett.* **1990**, *65*, 1004.

**48** J. Hahm, W.A. Lopes, H.M. Jaeger, S.J. Sibener, *J. Chem. Phys.* **1998**, *109*, 10111.

**49** L. Leibler, *Macromolecules* **1980**, *13*, 1602.

**50** A.N. Semenov, *Sov. Phys. JETP* **1985**, *61*, 733.

**51** J. Zhang, G. Jin, Y. Ma, *J. Phys.: Condens. Matter* **2006**, *18*, 837.

**52** T. Ohta, K. Kawasaki, *Macromolecules* **1986**, *19*, 2621.

**53** P. Glasson, et al., *Phys. Rev. Lett.* **2001**, *87*, 176802.

**54** V.B. Shikin, *JETP Lett.* **1974**, *19*, 335.

**55** R.E. Rosenzweig, *Ferrodynamics*, Cambridge University Press, Cambridge, London, **1985**.

**56** P.N. Pusey, Colloidal Systems: Ordered. In: *Encyclopedia of Materials: Science and Technology Updates*, Elsevier, Oxford, **2005**.

**57** P. Pieranski, *Phys. Rev. Lett.* **1980**, *45*, 569.

**58** W. Wen, L. Zhang, P. Sheng, *Phys. Rev. Lett.* **2000**, *85*, 5464.

**59** C. Scherer, A.M. Figueiredo Neto, *Braz. J. Phys.* **2005**, *35*, 718.

**60** B. Berkovski, V. Baschtovoy (Eds.) *Magnetic Fluids and Applications Handbook*, Begell House, Wallingford, **1996**.

**61** A. Ghazali, J.C. Lévy, *Phys. Rev. B* **2003**, *67*, 064409.

**62** J.A. Miranda, M. Widom, *J. Stat. Phys.* **1998**, *93*, 411.

**63** M. Klokkenburg, C. Vonk, E.M. Claesson, J.D. Meeldijk, B.H. Erné, A.P. Philipse, *J. Am. Chem. Soc.* **2004**, *126*, 16706.

**64** A.T. Skjeltorp, *Phys. Rev. Lett.* **1983**, *51*, 2306.

**65** S. Fraden, A.J. Hurd, R.B. Meyer, *Phys. Rev. Lett.* **1989**, *63*, 2373.

**66** C. Reichhardt, C.J. Olson, I. Martin, A.R. Bishop, *Europhys. Lett.* **2003**, *61*, 221.

**67** Y. Bar-Yam, *Dynamics of Complex Systems*, Westview Press, Oxford, **1997**.

# 4

# Competition Between Interactions on a Similar Length Scale

The Heisenberg model for the exchange interactions discussed in the previous chapters is appropriate for two neighboring atoms with direct overlap of their electron densities. Therefore, this interaction is termed *direct exchange*. The best examples of direct exchange interaction can be found in the ferromagnetic *3d* metals Fe, Co, and Ni, which order at rather high temperature even in nanostructures. In reality, many magnetic ions are unable to interact by direct exchange; for example, the magnetic orbitals of the rare earth ions lie well inside the ion (within a radius of about 0.3 Å) and are therefore unable to overlap with the corresponding orbitals of neighboring atoms. However, those materials that do not show direct exchange coupling might show magnetic ordering due to so-called *indirect exchange* and *super-exchange* interactions. These types of interaction have a longer range than the direct exchange and, in some cases, may compete with it.

## 4.1

## Two Short- or Mid-Range Interactions

### 4.1.1

### Super-Exchange and Indirect Exchange Interactions

Electronic interaction between two molecular or atomic entities mediated by one or more different molecules or ions is called *super-exchange*. It can be illustrated by the divalent transition metal oxides with rock salt crystals (e.g., NiO). The interaction between nearest-neighbor magnetic Ni ions is very weak because of the small magnitude of the direct ferromagnetic exchange. The second nearest-neighbor Ni ions are separated by an oxygen ion (see Fig. 4.1). This oxide is semiconducting, and thus Ni and O ions are joined by covalent bonds showing sufficient electronic overlap between cations and anions. Therefore, magnetic moments on the Ni ions interact most strongly with the second nearest neighbors via the 180° Ni–O–Ni bonds. The relevant electronic orbitals are shown in Figure 4.2. The degenerated *d* orbitals of a Ni ion are coupled via the *p* orbital of an O ion. The two lobes of the *p* orbital must have opposite spins in order to satisfy the exclusion principle. Therefore, the electrons in the overlap-

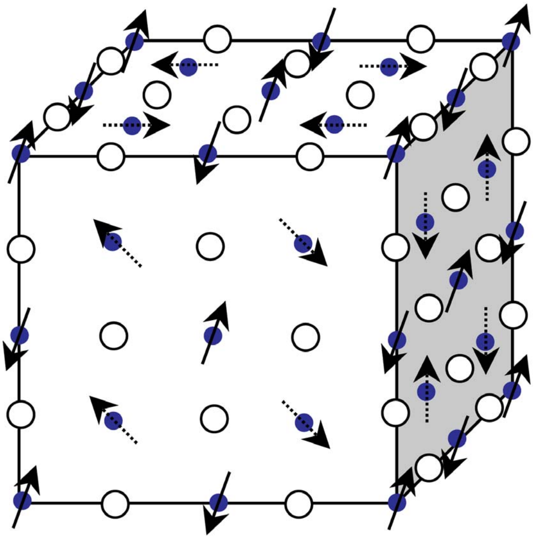

**Fig. 4.1** Crystal and magnetic structure of NiO. The hollow circles represent O ions; filled circles correspond to the Ni ions.

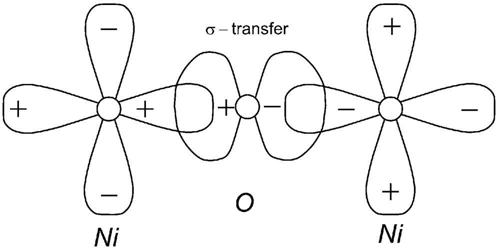

**Fig. 4.2** Example of super-exchange interactions with next-nearest-neighbor ions via 180° σ-bond.

ping lobes of the nearest-neighbor Ni ions will also have opposite spins – that is, the coupling is antiferromagnetic. This type of overlapping is known as σ-bonding or σ-transfer. There exists also an antiferromagnetic super-exchange via the 90° Ni–O–Ni bonds (see Fig. 4.1), though this feeble interaction must compete with the direct ferromagnetic exchange of the similar strength, and the two couplings simply cancel each other out.

A particular analogy of super-exchange is the *indirect exchange* in intermetallic materials called "hybridization-mediated exchange interaction", which is frequently reported in actinide intermetallics [1] or quasicrystals [2]. In this case, the interaction between two magnetic ions is mediated by polarization of the valence states of an ion between them due to hybridization of relevant magnetic ion and ligand states. Consequently, a non-negligible magnetic moment is also observed on the originally non-magnetic atom (ion). Whilst the super-exchange interactions are typical for materials in which the magnetic atoms are surrounded by ligands that do not carry permanent magnetic moments [3], the indirect exchange interactions may also arise in monolayers of *3d* metals on non-magnetic substrate due to strong hybridization effects. An example of such a system gives a Fe/W(001) monolayer. In contrast to bulk *bcc* iron, which is a prototypical ferromagnet, a monolayer of Fe on top of the W(001) crystal possess antiferromagnetic interactions [4]. Moreover, apart from the direct exchange interactions an antiferromagnetic coupling with the next-nearest-neighbors exists in this system [5]. The origin of this magnetic trend is attributed to the nature of the *3d–5d* hybridization between the overlayer and the substrate. In other systems [e.g., Fe/Ir(111)], even further situated magnetic moments can be addressed via the indirect exchange interactions [6].

A particular example of indirect exchange gives the *Ruderman–Kittel–Kasuya–Yosida* (RKKY) interaction. The weak RKKY interaction refers to a coupling mechanism of nuclear magnetic moments or localized inner *d* shell electron spins in magnetic material by means of an interaction through the conduction electrons [7]. Owing to the properties of the conduction electrons, the RKKY interaction is long-range and oscillates with respect to the distance from the magnetic ion as, $J_{ij} \propto \cos\,(k_F|\mathbf{r}_i - \mathbf{r}_J|)/|\mathbf{r}_i - \mathbf{r}_J|^3$, where $k_F$ is the Fermi wave vector. As a consequence, the ordered arrangements of magnetic moments determined predominantly by the RKKY interaction are complex and may have long periodicity.

The super- and indirect-exchange interactions can be successfully described by the Heisenberg model, which takes into account not only nearest neighbors but also further-situated magnetic moments. Some examples of these systems will be discussed in the following sections.

### 4.1.2
### Spin Glass

In many strongly diluted magnets, where magnetic ions (e.g., Mn or $\mathrm{Eu_x}$) are randomly distributed in a host (e.g., Cu or $\mathrm{Sr_{1-x}S}$, respectively), the magnetic interaction is RKKY-like. Since in such a dilute alloy the distances between magnetic ions are random, both ferromagnetic and antiferromagnetic $J_{ij}$ occur with approximately equal probability. Such materials – termed "spin glasses" – are disordered magnetic systems with competing ferromagnetic and antiferromagnetic interactions, which generate frustration [8]. But why are such systems are called "glass"? Loosely speaking, glass is a material which is in an amorphous state and has local, but no global, order. The local order appears with decreasing temperature and therefore is called "local freezing". Hence, spin glass exhibits a *freezing* transition to a low-temperature phase where the spins are aligned in fixed but random directions. Disorder and frustration are the two key features of spin glasses. Concepts and techniques developed in the study of these complex systems have impacted on a variety of other subjects, including combinatorial optimization, neural networks and protein folding.

Qualitatively, spin glasses are modeled by an Ising or a Heisenberg system with Gaussian or simply random distribution of ferro- and antiferromagnetic interactions $P(J_{ij}) = \exp(J_{ij}^2/2(\Delta J)^2)$ with width $\Delta J$. This random character, or disorder, together with the frustration generated by the competing character of interactions, serve as the main ingredients for the strange characteristics observed in spin glasses. Their most salient features are:

- A paramagnet-spin glass phase transition in which non-linear responses diverge instead of the usual linear susceptibility. The spin glass order is not the simple alignment order of a ferromagnet or a non-collinear Néel structure, but is rather a complicated one in which although the global magnetization is zero, a type of long-term memory of the local magnetizations exists.
- Due to disorder and frustration, spin glasses present a huge multiplicity of ground states. At finite temperature, the mean field theory of spin glasses predicts the existence of many stable thermodynamic states below $T_c$.

For a spin system, the multiplicity of ground states means that the average *local* magnetizations $\langle\sigma_i\rangle$ are non-zero, while the spontaneous magnetization of the whole system $m = (1/N)\sum_i \langle\sigma_i\rangle$ may be zero. The magnetic structure of spin glasses appears highly disordered; the typical spin glass configuration is shown in Figure 4.3. An Ising plaquette of four bonds on a square lattice with three ferromagnetic and one antiferromagnetic interactions between nearest-neighboring spins has an energy $-2J$ and eightfold degenerate ground state. The ground state energy of an unfrustrated antiferromagnetic or ferromagnetic plaquette has energy $-4J$, and is only twice degenerated.

Experimentally, the susceptibility of spin glasses shows a sharply defined, frequency-dependent cusp at the temperature $T_f$ indicating a sudden freezing of the spins. On the other hand, the specific heat does not indicate any phase transition at $T_f$, and neutron scattering shows no long-range order [9]. Another hallmark of the spin glass system is an S-shaped virgin branch of the hysteresis loop with a positive curvature at low fields [10] and a time-dependence of the thermoremanent magnetization. In order to measure the thermoremanent magnetization, the spin glass is cooled in the presence of a magnetic field to the freezing temperature. After temperature stabilization, the field is reduced to

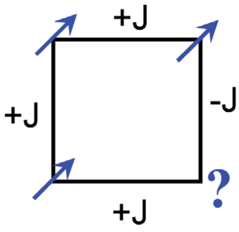

**Fig. 4.3** Frustrated Ising plaquette with competing ferromagnetic and antiferromagnetic bonds.

zero and the magnetization recorded. In spin glasses, in contrast to magnets, the magnetization decays with time.

Monte-Carlo simulations and mean-field calculations of spin glasses are very difficult to perform due to slow relaxation caused by the existence of many states with low-lying energy. However, by using an improved averaging procedure, Monte-Carlo simulations can provide a good approximation for the description of the critical properties of spin glasses. No analytic method has yielded results competitive with the Monte-Carlo treatment [11].

### 4.1.3
### Non-Collinear Magnetism at Surfaces

As mentioned in Section 4.1.1, as the dimensionality of magnets decreases – that is, within the context of nanomagnetism – there arise an increasing number of cases where the ferromagnetic and antiferromagnetic interactions coexist in one and the same system. In contrast to the spin glasses, these interactions are usually not random but rather follow a certain periodicity. In *fcc* iron, for example, the competition between ferromagnetic and antiferromagnetic interactions of the two nearest-neighbor shells of different symmetry, leads to a non-collinear, spiral magnetic ground state. Depending on thickness, the lateral size of a magnet, crystal structure, substrate and overlayer properties, multiple sets of such coexisting couplings may exist. Each set of interactions will lead to different magnetic structures, which may be much more complex than simply parallel or antiparallel, and this in turn means that the phase space is huge. In the following sections, the magnetic structures formed in a monolayer on a hexagonal and a square lattice with interactions between the first-, second- and third-nearest neighbors will be analyzed. This situation corresponds to many experimental systems, including for example Mn, Fe or Cr films on Ir(111), Pt(111), Ag(111), Cu(001), etc. As the reader will realize, even this rather modest part of the enormous phase space leads to a very large variety of non-trivial magnetic structures.

#### 4.1.3.1 **Competing Heisenberg Exchange Couplings (Hexagonal Lattice)**

Even with only three exchange constants it is very difficult to construct a comprehensible phase diagram, as this requires a fourth dimension. Therefore, it is instructive to discuss the phase space in terms of the separate contributions of $J_1$, $J_2$ and $J_3$ respectively, where the indices of the exchange parameters denote between which pairs of nearest neighbors the corresponding exchange coupling acts. Here, the discussion is limited to the first three nearest-neighboring pairs on a hexagonal lattice. For the first time, these diagrams have been derived by Ph. Kurz and coworkers [12, 13] on the basis of the Fourier transform of the Heisenberg exchange Hamiltonian. These authors have shown that the fundamental solutions of the Heisenberg exchange model on a periodic lattice are spiral spin structures. For a given reciprocal vector $\mathbf{Q}$ of a spin spiral, the magnetic moment of at atom at site **R** is given by $\mathbf{m}(\mathbf{R}) = m_s\,(\cos(\mathbf{QR}),\ \sin(\mathbf{QR}), 0)$, that is, the magnetization vector at the lattice position **R** is described by its three components: $m_x$ is the cosine of an angle between the vectors **Q** and **R**, $m_y$ is sine of the same vector, and $m_z = 0$. One supposes that the **Q** vector is directed along one of the directions of high symmetry on the triangular (hexagonal) lattice (see Fig. 4.4). In order to obtain all possible solutions, the length of the **Q** vector is changed in certain limits and the corresponding spirals are formed. For example, one of the possibilities is that $|\mathbf{Q}|$ is equal to an interatomic distance $a$. Then, the spin at the next atomic site to the reference point should be rotated by 360° or, in other words, be parallel to the initial one. The same is true for all spins lying in the planes perpendicular to the vector **Q** as is shown in Figure 4.4. The remaining atomic sites belong to another set of planes, which are situated at the half-period of the spiral. This means that spins belonging to these planes should be rotated only by 180° with respect to initial one. They are denoted as green in Figure 4.4. Altogether, the so-called row-wise antiferromagnetic structure has been constructed. In this formalism the famous Néel configuration shown in Figure 2.9 a is simply a spiral along a principal direction of the hexagonal (triangular) lattice with the period $Q = 3a$ which gives rotation by 120° between nearest neighbors. Spiral states which can be constructed with the help of a single **Q** vector are often denoted as $1Q$ states.

In the area between the lines $J_2 = 1/8 J_1$ and $J_2 = J_1$ (for antiferromagnetic $J$) the so-called row-wise antiferromagnetic configuration (see Fig. 4.5) has been predicted to be a ground state [11, 12]. A consequent Monte-Carlo study [14] confirmed this prediction. In the simulations, apart from the classical row-wise configuration other magnetic states have been found. Two examples of these configurations are shown in Figure 4.6, their energy being identical to that of the row-wise structure (Fig. 4.5). However, in contrast to the collinear row-wise pattern, which has two spins in the unit cell these structures have four spins per unit cell and are noncollinear. The most common characteristic of these degenerated states is that they cannot be constructed by means of a single **Q** vector. Generally, the noncollinear configurations result from the superposition of

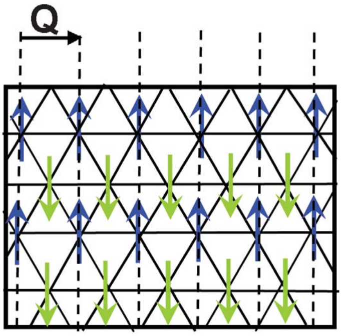

**Fig. 4.4** Construction of the row-wise antiferromagnetic structure.

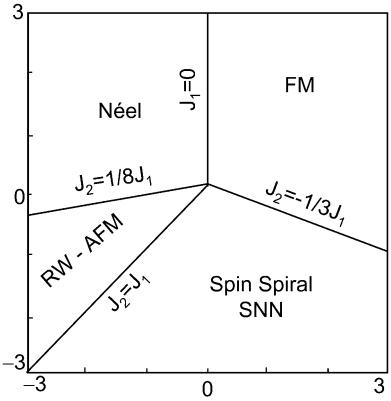

**Fig. 4.5** The three-dimensional magnetic phase diagram of the Heisenberg model on a triangular lattice, including interactions up to the second-nearest neighbor. The minus sign of a $J$ constant corresponds to the antiferromagnetic coupling [12].

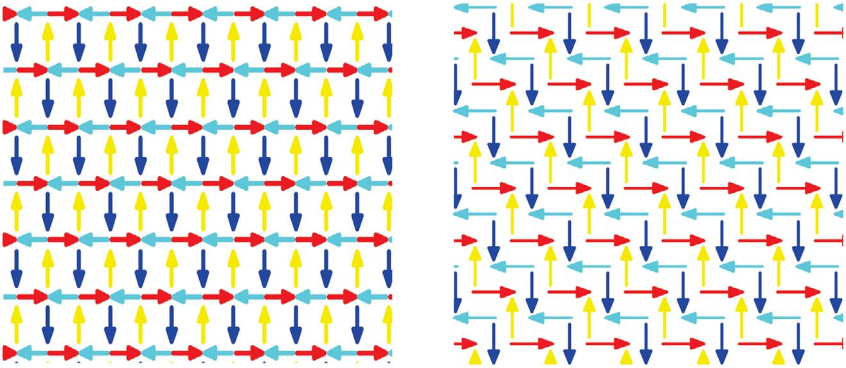

**Fig. 4.6** Monte-Carlo configurations in the framework of the Heisenberg model with antiferromagnetic $J_2$=$J_1$=2 on the triangular lattice. The energy of those configurations is identical with that of a row-wise configuration.

$N$ spirals with different vectors $\mathbf{Q}$, and therefore they can be addressed to as $NQ$ states.

It is possible to show that the patterns of Figure 4.6 do belong to the class of $NQ$ configurations and more precisely to the 2$Q$ subclass. The construction of the state shown in Figure 4.6 (left) from two $Q$ vectors is demonstrated in Figure 4.7.

We choose the vector $Q_1 = a$ (black in Fig. 4.7) to run along one of the high symmetry directions of the triangular lattice. We also choose the orientation of an initial magnetic moment to be at –45° with respect to the axis $Oy$. With these assumptions, the $Q_1$ row-wise structure is formed (black arrows in Fig. 4.7). In the same way, the $Q_2$ pattern of the same periodicity can be formed along one of two other densely packed crystallographical directions of the lattice (light arrows in Fig. 4.7). In the next step, the two spirals are geometrically added at

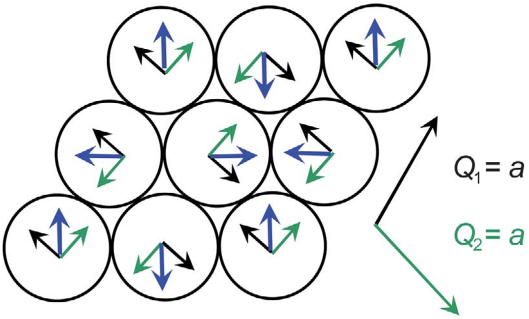

**Fig. 4.7** Construction of a typical Monte-Carlo 2$Q$ configuration on a triangular lattice for $J_2$=$J_1$=2 by superposition of the two spin spirals with vectors $Q_1$=$a$ and $Q_2$=$a$ running along two principal lattice directions. The black arrows denote $Q_1$ and the first spin-spiral (row-wise configuration); light gray arrows denote $Q_2$ and the second spin spiral; the large gray arrows indicate the resulting configuration.

each atomic site and the superposition of the two spin spirals is identified (large blue arrows in Fig. 4.7). This structure is thought to be a solution of the Heisenberg model, in which case an important condition must be fulfilled: namely that the resulting spin at each atom site must have the same magnitude, that is, $|S_i|^2 = \text{const}$. This condition is trivially fulfilled for the chosen $Q_1$ and $Q_2$. The pattern formed by blue arrows coincides with the Monte-Carlo configuration. Hence, it has been demonstrated that the Monte-Carlo structures of Figure 4.6 are the result of superposition of the two spin spirals of the same periodicity running along principal lattice directions.

In the bottom region of the phase diagram a spin spiral (SS) running along the direction of Second Nearest Neighbors (SNN) has been predicted. An example of such a structure, found in Monte-Carlo simulations, is shown in Figure 4.8. The angle between nearest neighbors is approximately 140°, and the period of rotation is non-commensurate with the underlying lattice structure with $Q = 2\sqrt{3a}$. Monte-Carlo simulations go beyond the prediction [12] revealing complicated patterns degenerated in energy with that of the spin spiral along SNN bonds (SS_SNN). Similar to the previous example, the state shown in Figure 4.7 (right) is the superposition of $N$ simple spiral states.

The next interesting case is the competition of the exchange interaction between the second and the third nearest neighbors $-3 \leq J_2, J_3 \leq 3$ for constant ferromagnetic or antiferromagnetic interaction between nearest neighbors $J_1$. The phase diagrams for these two cases are shown in Figure 4.9. Again, in the diagrams the regions with ferromagnetic, Néel, row-wise antiferromagnetic structures and the SSs with $Q$ directed along the second-nearest-neighbor bonds are identified. Additionally, for negative $J_2$ and $J_2 > 2J_3$ a SS along the nearest-neighboring bonds has been predicted. Monte-Carlo simulations reveal the periodicity of this structure to be $Q = 3a$. A typical SS_FNN configuration is plotted in Figure 4.10.

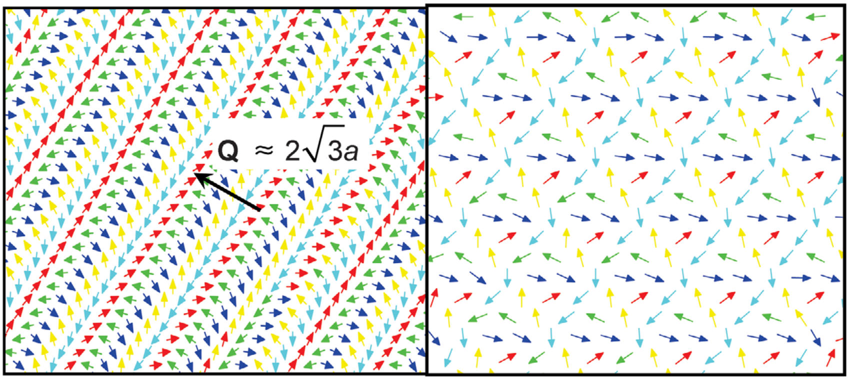

**Fig. 4.8** Spin Spiral state found in Monte-Carlo simulations for the Heisenberg model with ferromagnetic $J_1=1$ and antiferromagnetic $J_2=2$ on a triangular lattice.

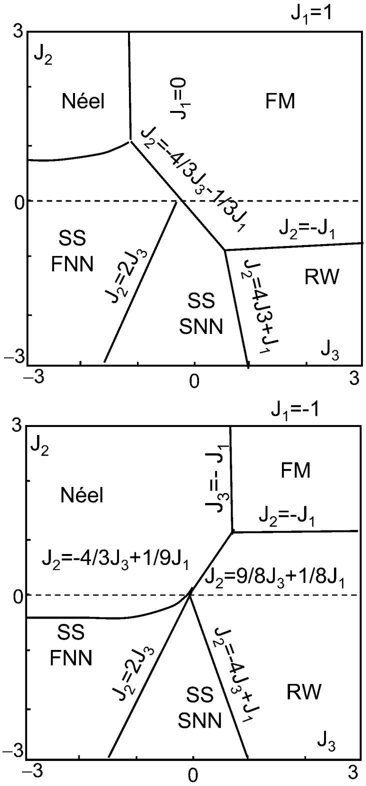

**Fig. 4.9** The three-dimensional magnetic phase diagrams of the Heisenberg model on the triangular lattice including interactions up to the second-nearest neighbor. The phase diagrams are plotted in the $J_2$–$J_3$ plane for $J_1=1$ (top) and $J_1=-1$ (bottom). The minus sign of a $J$ constant corresponds to the antiferromagnetic coupling [12].

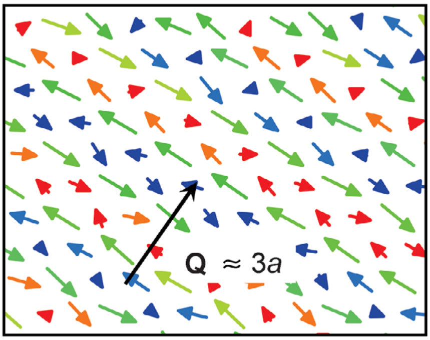

**Fig. 4.10** Typical Monte-Carlo configuration of a SS_FNN configuration: $J_1 = 1$ (ferromagnetic); $J_2 = J_3 = -2$. The color scheme and vector length denote $z$ and $xy$ projections of the moments, respectively.

Thus, the higher-order Heisenberg contributions that arise in magnetic nanostructures due to the indirect exchange interactions via a substrate are very important for nanomagnetic ordering. The ground states of nanomagnets are often non-collinear spiral configurations, with $Q$ vectors along the high symmetry lines of the Brillouin zone or their complicated superposition.

### 4.1.3.2
### Competing Heisenberg Exchange Couplings (Square Lattice)

The ground state of an antiferromagnetic spin system on a square lattice coupled by nearest-neighbor interactions only is a non-frustrated checkerboard pattern. The addition of a second nearest-neighbor ferromagnetic interactions does not alter the ground state pattern. Hence, for $J_3 = 0$ the competition can arise only from the $J_1$ ferromagnetic and $J_2$ antiferromagnetic.

Ground state structures for the ferromagnetic ($J_1 > 0$) and antiferromagnetic ($J_2 > 0$) interactions are provided in Figure 4.11. For $J_1 = -J_2$, many degenerated ground states are found (see Fig. 4.11 a). Similar to the triangular lattice, these ground states belong to the class of $NQ$ states. The spiral states may be either planar as the row-wise configuration of Figure 4.11 a (center pattern) or three-dimensional, as in Figure 4.11 a (left and right patterns). Whilst the inset Figure 4.11 a (center) is a $1Q$ pattern, the other two patterns represent linear combination of spirals with different $Q$ vectors. In order to dominate the ferromagnetic interaction $J_1 \geq -2J_2$, the structure is just ferromagnetic, but for dominating the antiferromagnetic coupling between second-nearest neighbors $J_1 \leq -J_2$ the spiral state is altered. The main tendency is to increase the mean mutual angle between nearest-neighbor spins due to weakening of the ferromagnetic coupling.

The ground state for an antiferromagnetic $J_1$ and a ferromagnetic $J_2$ is just row-wise antiferromagnetic configuration, as shown in Figure 4.12. It should be noted that, whilst in the case of the ferromagnetic $J_1$ the rows run along the first nearest-neighbor bonds (i.e., along [100] or an equivalent direction), for the antiferromagnetic $J_1$ they are oriented along the second nearest-neighbor bonds (i.e., along [110]) or an equivalent direction.

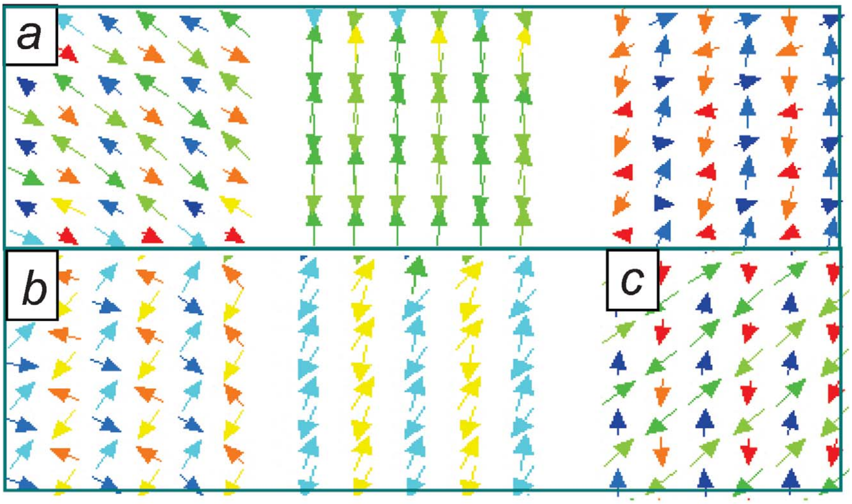

**Fig. 4.11** Typical Monte-Carlo configurations on a square lattice for ferromagnetic $J_1$ and antiferromagnetic $J_2$ (a) $J_1=-J_2$; (b) $J_1=-2J_2$; (c) $J_1=-3J_2$. The color scheme and vector length denote $z$ and $xy$ projections of the moments, respectively.

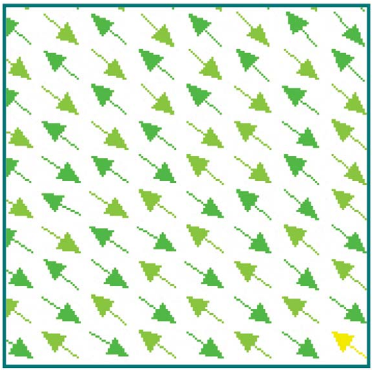

**Fig. 4.12** Typical row-wise Monte-Carlo configuration on a square lattice for antiferromagnetic $J_1$ and ferromagnetic $J_2$.

### 4.1.3.3
### Antiferromagnetic Domain Wall as a Spin Spiral

As mentioned in Section 4.1.3.2, for $J_1 \gg J_2$ both antiferromagnetic, the ground state is the checkerboard antiferromagnetic configuration. One of the lowest exited states is a domain structure with so-called phase domains and phase domain walls (p-DW). A schematic representation of the orientational and p-DW is provided in Figure 4.13 A. In the phase domains the checkerboard spin structure shifts laterally by one structural lattice constant. Experimentally, this can only be detected indirectly by the presence of domain walls. Recently, such do-

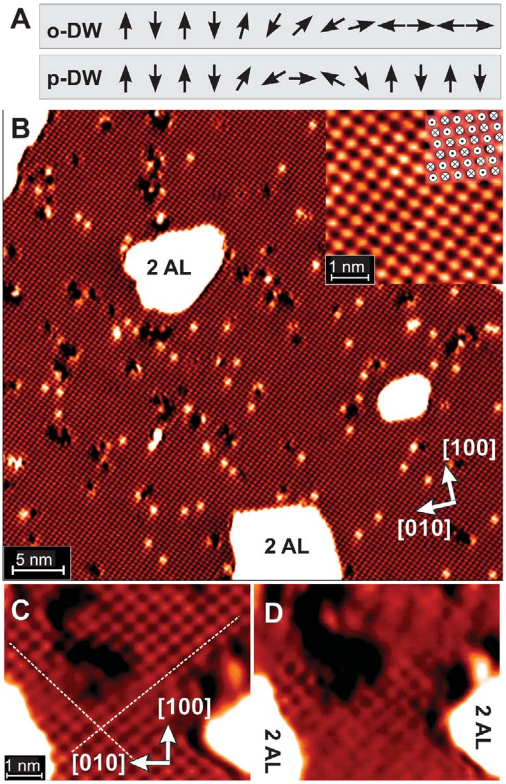

**Fig. 4.13** Schematic representation and experimental observation of domain walls at antiferromagnetic surfaces. (A) Scheme of an orientational domain wall (o-DW) and a phase domain wall (p-DW). (B) SP-STM image of 1.1 atomic layer Fe/W(001). The antiferromagnetic structure (shown at higher resolution in the inset) exhibits long-range periodicity without any domain wall visible in the field of view. Only at higher defect density do p-DWs appear that can be imaged with (C) out-of-plane ($\mu_0 H = 2T$) and (D) in-plane sensitive tips (no field). In the constriction between the two double-layer islands, a p-DW can be recognized which runs along the [010] direction. At the position of the p-DW the magnetic structure shifts by one atomic site, that is, half the magnetic periodicity (see the dashed lines).

main walls have been found by means of the spin-polarized scanning tunneling microscopy (SP-STM) [5]. Here, an exciting question is whether the phase domain walls can lead to the uncompensated magnetic moments, or not. This question is important as it has been postulated [15, 16] that the small amount of uncompensated magnetic moments at the antiferromagnet/ferromagnet interface is responsible for the exchange bias effect [17] which is widely used in state-of-the-art magnetic storage devices. The exchange bias is based on the direct exchange interaction between an antiferromagnet and a ferromagnet with which it is in contact, and leads to a sign-dependent magnetic coercivity of the latter. As will be shown in the following, the experimental data together with Monte-Carlo simulations can infer the existence of uncompensated spins in p-DWs which are oriented along [110] crystallographic direction. The uncompensated magnetization appears due to the spiral-like rotation of antiferromagnetic moments in a wall. Depending on the surface density of these p-DWs, the resulting moment may lead to a significant contribution to the exchange bias.

It has been shown recently that one atomic layer of Fe on W(001) is an antiferromagnet with the nearest- and next-nearest-neighbor exchange parameters $J_1 = 20.3 \cdot 10^{-3}$ and $J_2 = 2.4 \cdot 10^{-3}$ meV/atom, respectively [5, 18]. STM with non-magnetic tips is sensitive only to the spin-averaged local density of states (DOS) $n(\mathbf{r}, E_F)$ at the Fermi level (low-voltage approximation) and tip position **r**. The intrinsic spin-polarization of magnetic tips, $P_T \equiv (n^{\uparrow} - n^{\downarrow})\,(n^{\uparrow} + n^{\downarrow})$ where $n^{\uparrow}$ and $n^{\downarrow}$ are the majority and minotity density of states, introduces a spin-polarized contribution to the tunneling current $l(r)$ which scales with the projection of the unit vector of tip magnetization $\mathbf{u}_T$ onto the local magnetization DOS at $E_F$, $\mathbf{m}(\mathbf{r}, E_F)$ [18]:

$$\mathbf{I}(\mathbf{r}) \propto n(\mathbf{r}, E_F) + P_T \mathbf{u}_T \cdot \mathbf{m}(\mathbf{r}, E_F)\ . \tag{4.1}$$

This gives a magnetic contribution to constant-current mode images of periodic magnetic structures which is superimposed on the conventional topographic image. The magnetic contrast image of the sample consisting of iron film [nominal thickness of 1.1–1.4 pseudomorphic atomic layers (AL)] deposited onto a stepped W(001) single crystal is shown in Figure 4.13 B. While the topography appears flat if measured with a non-magnetic tip (not shown here), the use of an out-of-plane sensitive magnetic tip leads to the checkerboard superstructure visible in the inset of Figure 4.13 B. Hence, the experimental results prove that the Fe monolayer on W(001) is indeed a perpendicular antiferromagnet with the magnetic moments of nearest-neighbor atoms pointing alternately up and down (see inset). Although numerous defect sites such as impurities and adatoms as well as ferromagnetic second layer islands are visible, perfect long-range magnetic order without any domain wall is found on a scale of about 2 μm×1 μm. Only if the defect density was increased, for example by increasing the Fe coverage to 1.3 AL, short (1–2 nm) segments of p-DWs have been occasionally found, as shown in Figure 4.13 C. This particular DW is clamped between two double-layer islands and extends along the [010] direction. By following the dashed lines in Figure 4.13 C it becomes apparent that the phase of the magnetic lattice shifts at the position of the wall by one atomic site.

The internal spin structure of domain walls was investigated theoretically by the MC method, which is capable of simulating complex spin structures of antiferromagnets [19]. The $J_1$ and $J_2$ exchange constants given above have been used in the calculations. Apart from the exchange interaction, a perpendicular anisotropy and a dipolar interaction have been included into the simulations. The anisotropy energy density has been set to be $K_1 = 2.4$ meV/atom, while the strength of the magnetic dipole–dipole coupling is calculated by $D = (\mu_0 g^2 \mu_{Fe}^2)/(4\pi d^3)$

with $\mu_0$ the permeability of the vacuum, $\mu_{Fe} = 2.67\,\mu_B$ the magnetic moment of antiferromagnetic iron and $d = 0.3165$ nm the interatomic Fe–Fe distance.

In order to avoid the sample eventually relaxing into a single domain state, it must be quenched rapidly from a random start configuration to the measurement temperature, that is $T \approx 13K$. A characteristic result is shown in Figure 4.14 A. The magnetic structure inside the wall is spiral-like, but no preferred orientation of the domain wall has been found. The three wall segments are oriented approximately along: (a) the [110]; (b) the [100]; and (c) an intermediate direction. In order to compare the theoretical spin structures with experimental STM data, SP-STM images of Monte-Carlo non-collinear magnetic structures have been modeled. The details of calculations can be found in [18]. The calculated STM images shown in Figure 4.14 B and C are in good qualitative agreement with the experiment (cf. Fig. 4.13 C and D): the checkerboard superstructure is clearly observed in the domains (domain walls) with an out-of-plane (in-plane) sensitive tip. As also found experimentally, the apparent domain wall width is slightly larger for in-plane than for out-of-plane sensitive tips. This can be explained on the basis of Eq. (4.1): the magnetic corrugation at the domain wall scales cosine-like for an out-of-plane sensitive tip, but sine-like for an in-plane sensitive tip, with the former having a rather steep zero-crossing at the domain wall position. The very weak topographical (non-magnetic) atomic contrast observed wherever $\mathbf{u}_T \perp \mathbf{m}_r$ (see, e.g. the domains in Fig. 4.14 C) is below the experimental resolution limit.

To discuss the question of whether the non-collinear p-DWs can cause uncompensated magnetic moments, four principal types of p-DWs are illustrated schematically in Figure 4.15. The p-DWs may be centered between (top row of Fig. 4.15) or on top of atomic rows (middle row), and either oriented along the [010] (left column of Fig. 4.15) or along the [110] direction (right column), respectively. For the ease of illustration, Figure 4.15 shows a fully coplanar situation, but the following arguments are also valid for a system such as Fe/W(001), where the easy axis is perpendicular to the surface and to the wall direction. The sketch reveals that, irrespective of their symmetry, [010]-oriented DWs are always compensated because adjacent spins within any row parallel to the wall point in opposite directions. The situation is different for p-DWs along [110] directions as their magnetic moments do not cancel. The direction of the uncompensated moment depends on the position of the p-DW center: if the p-DW center is on top of an atomic row it points along the spins that form the domain wall center. In the case of a wall which is centered between two atomic rows this is along the quantization axis within the domains. The bottom row of Figure 4.15 shows the perpendicular component of the magnetization as obtained from MC simulations for p-DWs which run almost perfectly along the [010] (left column) and the [110] direction (right column). In agreement with the above-mentioned arguments, the [010]-oriented wall is compensated (average total magnetization $\leq 10^{-4}\,\mu_B$ per nm domain wall length). Although not perfectly mirror-symmetric, the domain wall center of [110]-oriented p-DWs is always found between two atomic rows and, in agreement with the uncompen-

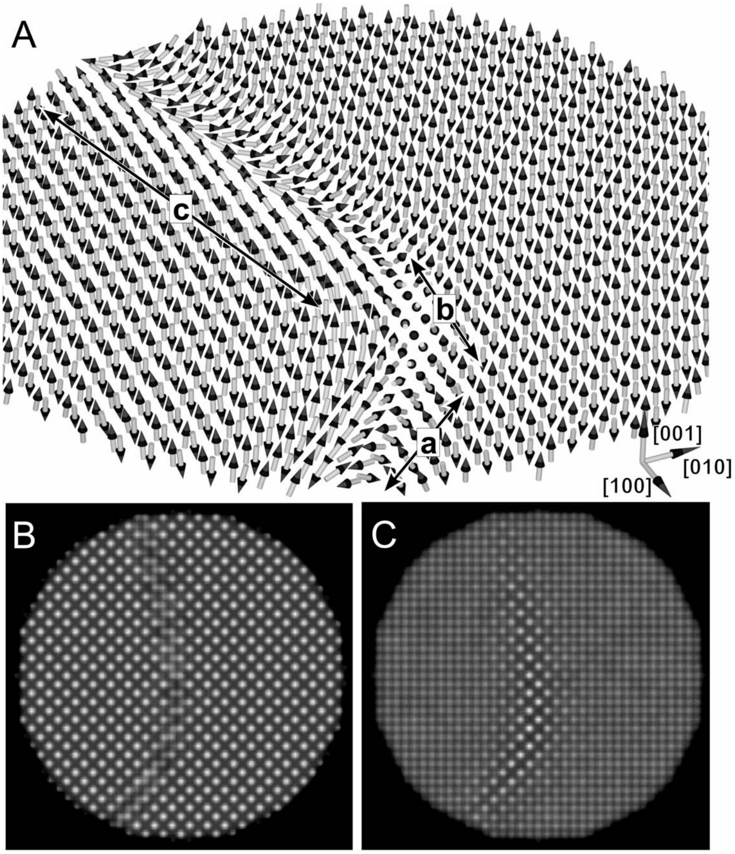

**Fig. 4.14** Monte-Carlo (MC) simulation of antiferromagnetic domain walls. (A) Rendered perspective image of the quenched spin structure of an antiferromagnetic material as obtained by MC simulation. A domain wall can be recognized which exhibits three different orientations: (a) along the [110]; (b) [100]; and (c) an intermediate direction. Calculated SP-STM images for (B) out-of-plane and (C) in-plane sensitive magnetic tips.

sated moment in the simple sketch, a finite perpendicular moment of about 0.6 $\mu_{Fe}$ per nm domain wall length remains.

A wall directed approximately along [110] will be discussed in the next section. The azimuthal orientation of spins within the wall of Figure 4.14 A [middle of segment (a)] is shown in closer view in Figure 4.16 A. As mentioned above, the MC simulations find the DW center between two atomic rows. In Figure 4.16 A, for clarity, the atomic rows are numbered successively (1) to (5) with respect to their distance from the DW center. The wall center is formed by two rows (1) with a predominant in-plane orientation ($\theta > 65^\circ$). With increasing distance from the DW center, the moments tilt more and more in the out-of-plane direction; the in-plane component of rows (4) and (5) is already very small. Apparently, the wall is six to eight atomic rows wide and Bloch-like. By comparing

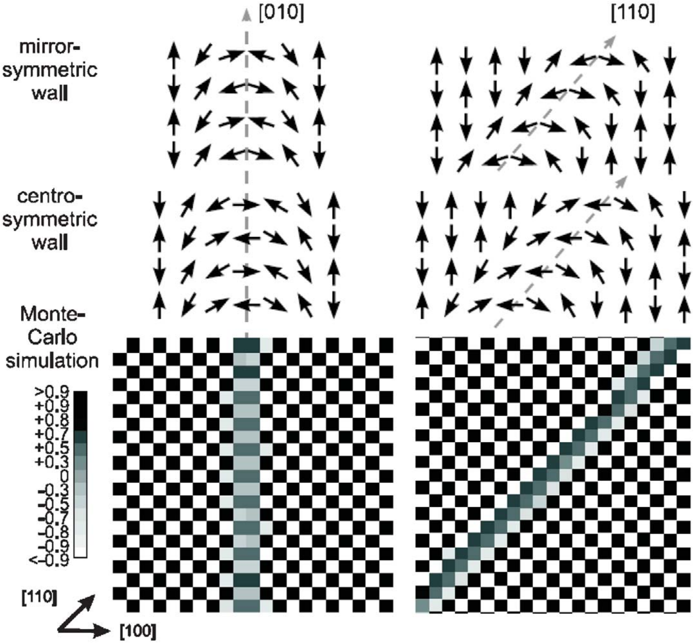

**Fig. 4.15** Spin configuration of [010]- and [110]-oriented domain walls. Schematic representation of p-DWs which are centered between (top row) and on top of atomic rows (middle row). Bottom row: Part of a p-DW oriented along the [010] (left) and the [110] direction (right) from Monte-Carlo simulations. The gray scale gives the calculated out-of-plane component of the magnetization.

equidistant atomic rows located on opposite sides of the DW center, it becomes clear that the in-plane component is reversed while the out-of-plane component is equal. Thereby, the integrated in-plane component of magnetization is perfectly canceled but, interestingly, a non-vanishing net magnetic moment remains for the out-of-plane component.

Figures 4.16 B and C show calculated and experimental SP-STM images of such a wall, respectively. Although there are some differences with regard to the details of the contrast within the domain wall, the width and general appearance of the DW is well-reproduced. In order to gain a better understanding of the experimentally observed structure, two experimental line sections taken on adjacent atomic rows along the [110] direction have been plotted – that is, perpendicular to the wall (Fig. 4.16 D (upper panel)). These two rows are approximately equally distant from the termination points of the domain wall. The middle panel shows the sum and the difference of these lines in black and gray, respectively. The difference (gray) shows an almost constant signal of opposite sign at the left and right rim of the line section, that is, far away from the domain wall center. These regions (domains) are connected by a constant slope

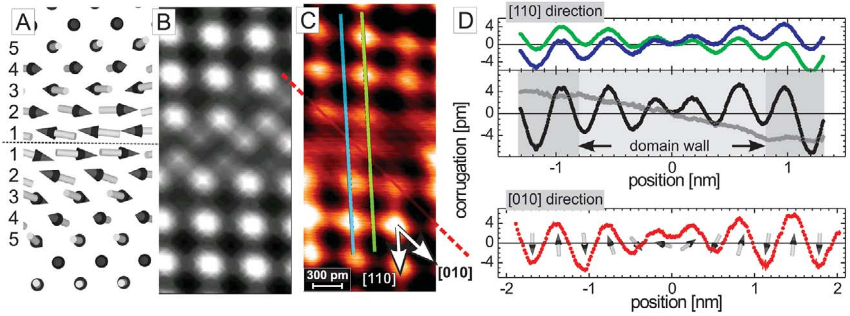

**Fig. 4.16** Detailed view of a [110]-oriented spiral p-DW. (A) Theoretical spin structure, (B) simulated, and (C) experimental SP-STM image of a p-DW in the out-of-plane antiferromagnetic Fe monolayer on W(001). (D) Height profiles drawn at the positions of the correspondingly colored lines in (C) along the [110] (upper panel) and the [010] direction (lower panel). Middle panel: Sum (black) and difference (gray) of the line profiles shown in the upper panel. The wall is about 1.6 nm wide and its out-of-plane component exhibits mirror symmetry.

that extends over approximately 1.6 nm and corresponds to the wall width of six to eight atomic rows mentioned above. The sum (black) reveals that the average out-of-plane component of these atomic rows is mirror-symmetric. The mirror-symmetric appearance, which is also found in the line profile taken along the [010] direction (lower panel of Fig. 4.16 D) indicates, in agreement with the above-mentioned MC calculations, that the domain wall center is located between two atomic rows. This is also confirmed by an interpolation of the atomic periodicity from the two domains into the domain wall (arrows in lower panel of Fig. 4.16 D). It is possible that the position of the DW center moves out of a mirror-symmetric position between two atomic rows when approaching the termination points of the DW, which are outside the field of view of Figure 4.16 C. A similar effect appears in the MC simulations, and is best visible at the bottom left edge of the spin disk in Figure 4.14.

Due to the fact that domains walls in antiferromagnets cost exchange energy but cannot lower the dipolar energy, they are very rare and short on clean surfaces. It is, however, likely that they may occur much more frequently in a typical exchange-bias situation. Here, the antiferromagnet is covered with a ferromagnetic film which typically exhibits a higher magnetic ordering temperature than the antiferromagnet. Consequently, the antiferromagnet is in contact with a ferromagnet when it orders magnetically. It is expected that in this case the exchange coupling to the ferromagnet induces a relevant number of p-DWs.

#### 4.1.3.4 **Spin Spiral State in the Presence of Dipolar Interactions**

It follows from the discussions of Sections 4.1.3.1 and 4.1.3.2 that spin spiral states often arise in antiferromagnets. Previously, only spin spirals in systems with exchange interactions were detailed, the main conclusion being that, depending on exchange constants, the 1$Q$ spin spirals may be oriented either along the principal crystallographic directions of a lattice or along the second-nearest-neighbor bonds. The strength of the competing ferro- and antiferromagnetic couplings determines the period of a spiral. The 1$Q$ spirals can be superimposed, forming complicated $NQ$ states.

In these previous discussions, the dipole–dipole coupling was not considered. However, long-range dipolar interaction has long been recognized in magnetic systems. The strength of the exchange coupling in nanosystems is very often reduced because of fewer neighbors at the edges, and hybridization with substrate. For example, as follows from the DFT calculations [7], the strongest exchange energy per atom in Fe/Ir(111) is less than 5 meV. At the same time, the strength of dipolar interaction between two Fe magnetic moments $D = (\mu_0 g^2 \mu_{Fe}^2)/(4\pi d^3) \approx 0.1$ meV. As the dipolar energy has a long-range character, the dipolar interactions between all pairs of magnetic moments in the sample must be added. The total dipolar energy of a ferromagnetic, perpendicular to the film plane configuration, is close to 1 meV per atom, which is comparable with the short-range exchange contributions. Hence, the dipolar energy is able to compete with the exchange coupling in nanosystems and must be included in the calculations.

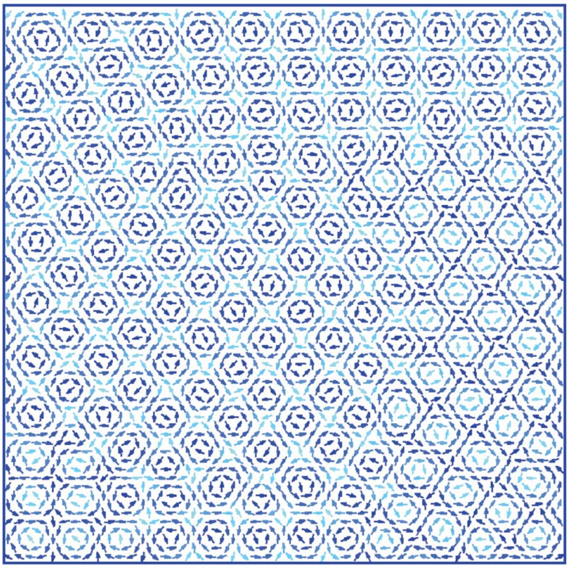

**Fig. 4.17** Typical Monte-Carlo magnetization configuration of a vortex lattice with a four-fold symmetry on a triangular atomic lattice for $J_1 = +3.9$ meV, $J_2 = -0.1$ meV, $J_3 = -1.7$ meV, and $D = +0.2$ meV. The dark areas denote up-magnetization orientation; light areas down-magnetization orientation.

The main "task" of the dipolar interaction is to avoid uncompensated magnetic poles, and a spin spiral is rather favorable from this point of view configuration. Therefore, it seems that the dipolar contribution is not able to change the spiral state. The Monte-Carlo simulations, however, demonstrate that the dipolar coupling can provide a significant energy gain by formation of the regular lattice of magnetic vortices in systems with competing ferro- and antiferromagnetic interactions. The typical vortex lattice for $J_1 = +3.9$ meV (ferromagnetic), $J_2 = -0.1$ meV, $J_3 = -1.7$ meV and $D = +0.2$ meV is shown in Figure 4.17 a. Interestingly enough, the inclusion of dipolar interactions leads to the formation of a *square* lattice of vortices on a *triangular* atomic lattice. On a large scale, there exist three rotational domains of vortex structure. In different domains the up- (light-colored) and down-oriented (dark-colored) parts of the vortices can trade places, and the domains can also be phase-shifted. The unusual structure found in the Monte-Carlo simulations is similar to an experimental finding of so-called mosaic structure in Fe/Ir(111) [20].

In conclusion, the dipolar interactions significantly alter the spin spiral configurations, and this may lead to formation of the vortex superstructure on a nanometer scale.

### 4.1.4
### Two Short-Range Repulsive Interactions

Stripe formation is generally attributed to competition between the short-range attractive forces and the long-range repulsion (see Chapter 3). Here, it will be shown that stripe phases may result from a different mechanism based on a purely repulsive isotropic short- to medium-range pair potential with two characteristic length scales.

Consider a two-dimensional system of hard discs surrounded by a soft circular repulsive corona – that is, the particles interact through a radially symmetric pair potential which consists of an impenetrable hard core of radius $\sigma_0$ plus a repulsive interaction extending to the distance $\sigma_1$ (see Fig. 4.18).

Monte-Carlo simulations of such a system with $\sigma_0/\sigma_1 = 2.5$ have been performed in [20]. The spatial configurations of the system at different densities, but fixed temperature, are shown in Figure 4.19. With increasing density the system rapidly turns from the disordered configuration into a triangular lattice

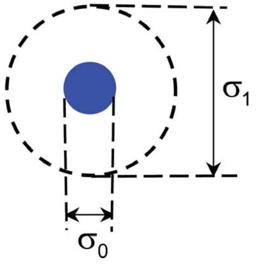

**Fig. 4.18** Pair potential $V(\mathbf{r})$ as a function of the distance $\mathbf{r}$ between two particles. $\sigma_0$ is the hard core radius, $\sigma_1$ is the soft core radius.

with lattice constant $\sigma_1$. In this regime, the particles just touch each other with their coronas. At the next density considered, the system is composed of dimers and short linear chains. For this concentration the formation of dimers is energetically preferable. In a dimer, a soft corona of a particle overlaps with only one other soft corona of the neighboring particle. In a chain there are two nearest neighbors, and hence two overlaps, which is energetically more unfavorable. With increasing density, more frequent overlaps are unavoidable and therefore the dimers align in worm-like filaments and eventually form stripe domain patterns similar to those in systems with competing short-range and long-range interactions (see Chapter 3). If the particle density is further increased (Fig. 4.19 e), the system is composed mainly of loose aggregates of three or more particles. Thus, in spite of the isotropic nature of the interaction, the effective coupling in the stripe phase is anisotropic. This allows penetration of the soft core along the stripe, but not orthogonal to it.

The structure order of a system can be analyzed through the structure factor, a quantity that provides a measure of order parameter correlations in wave vector (Fourier) space. A similar analysis was carried out in Section 2.5.2.2 for antiferromagnetic structures on aperiodic tilings. Here, the distance between particles has been chosen as an order parameter, and therefore the structure factor is a function of one sole variable (Fig. 4.19, lower). The main peak provides an estimate of the nearest-neighbor length scale, while other peaks reflect the progressive turning on or off of different effective length scales as the mean distance between the dimers or stripes. At low densities the coronas are scarcely penetrable, and the system behaves as an assembly of hard discs of effective diameter $\sigma_1$. This can be seen from the dominance of the first peak, centered at wave vector $k \approx 2\pi/\sigma_1$. In contrast, at very high densities, the system resembles

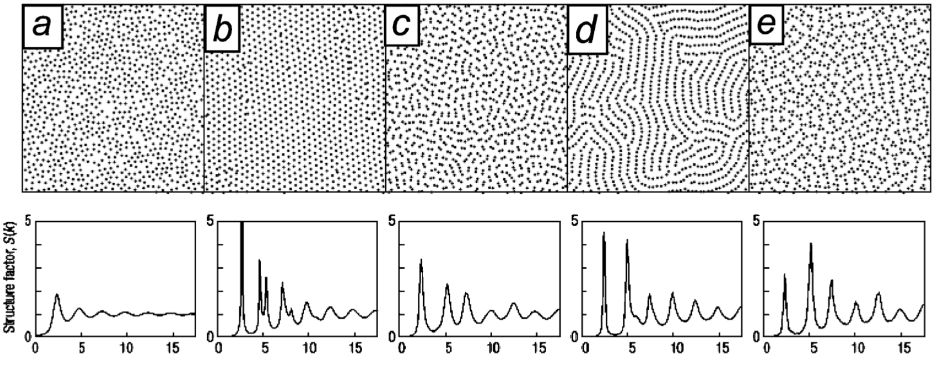

**Fig. 4.19** Spatial configurations and corresponding structure factors of a two-dimensional hard core particles with the soft core repulsive interactions. The density of particles is (a) 0.1; (b) 0.15; (c) 0.227; (d) 0.291; and (e) 0.38. Reprinted with permission from Macmillan Publishers Ltd: *Nature Materials*, © 2003 [20].

an assembly of hard discs of diameter $\sigma_0$ (dominance of the third peak with $k \approx 2\pi/\sigma_0$). Intermediate densities are characterized by other distribution of the peaks and hence, by the competition between the inner hard core and the external soft core radii.

## 4.2
## Two Long-Range Interactions

A prototypical example of the long-range interactions provides the magnetostatic or electrostatic coupling. Different contributions of these interactions require different ground state configurations (see Chapter 2), and therefore, if there exist several magnetostatic/electrostatic contributions in the same system, they may compete. The competition between quadrupolar and dipolar interactions, as well as between octopolar and dipolar contributions, will be discussed in the following section.

### 4.2.1
### Systems with Dipolar and Quadrupolar Interactions

The dipolar and quadrupolar interactions may exist in the fluids or liquid crystals composed of polar molecules [21]. As demonstrated in Chapter 2, although both dipolar and quadrupolar terms require a micro-vortex like ground state, these micro-vortex patterns have different symmetry. The comparison of the two structures is provided in Figure 4.20. In a pure quadrupolar pattern (thick, gray elements in Fig. 4.20), vortices with left and right senses of rotation appear alternately along each row (left-upper scheme). Together, they form a square vortex superlattice with the period of $p_q = \sqrt{2}a$, with $a$ the interparticle distance. The principal directions of this superstructure are rotated by 90° with respect to the original square lattice. The pure dipolar ground state (black arrows in Fig. 4.20) forms the sequences of the vortices with same sense of rotation separated by the anti-vortices. Therefore, the vortex superstructure has larger period $p_d = 2a$, and its principal directions coincide with those of an initial square lattice.

For dominating dipolar interactions the $2a$ structure prevails, whereas for dominating quadrupolar forces the $\sqrt{2}a$ superstructure exists. If the two interactions are of comparable strength, a compromise must be found. A typical Monte-Carlo stable configuration for $Q_{20} \approx Q_{10}$ is shown in Figure 4.21 a. The $Q_{20} + Q_{10}$ moments are represented by the corresponding spherical harmonics in Figure 4.21 where, instead of the microvortex structure a macroscopic vortex with small amount of defects emerges. A similar picture emerges for the combined quadrupoles and dipoles on a triangular lattice, as shown in Figure 4.21 b. Thus, the addition of quadrupolar interactions breaks the ground state degeneracy of the pure dipolar system, and vice versa. This phenomenon should lead to changes in the spectrum of orientational vibrations in polar liquids and liquid crystals, when measured experimentally.

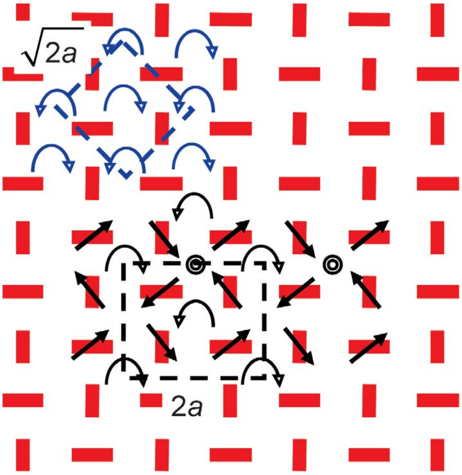

**Fig. 4.20** Comparison of the ground states of a pure quadrupolar and a pure dipolar system. The quadrupoles are represented by blue elements, and dipoles by black arrows. The micro-vortices are denoted by their sense of rotation. The anti-vortices are marked by the small circles. Unit cells of the quadrupolar and the dipolar superstructure are shown by the dashed lines.

### 4.2.2
### Systems with Dipolar and Octopolar Interactions

The next higher order magnetostatic/electrostatic contribution is an octopolar one. The octopolar contribution is extremely important for rotationally symmetric homogeneously magnetized particles [22, 23], and hence the following discussion will focus on nanomagnetic arrays with dipolar and octopolar interactions.

#### 4.2.2.1 **Combined Multipoles in Nanomagnetic Arrays**

As shown in Chapter 2, the in-plane magnetized nanodiscs with height-to-diameter ratio $h/a \leq 0.5$, that are often used in modern experimental studies on nanoarrays, possess dipolar and octopolar moments with $Q_3/Q_1 \geq 0.5$. Hence, for a real nanomagnetic array neither pure dipolar, nor pure octopolar configurations are relevant. Instead, ground states of an ensemble of combined multipoles should be calculated. Recently, these calculations have been carried out by means of Monte-Carlo simulations for the case of rotationally symmetric multipoles [22]. Arrays of combined multipoles show maxima of specific heat and susceptibility at the same temperature, thus confirming the existence of a phase transition. Whereas the zero-temperature ground state on a square lattice consists of antiparallel lines (as in a pure octopolar system), at finite temperatures alternating regions of uniaxial parallel and antiparallel lines (as in Fig. 4.22 c)

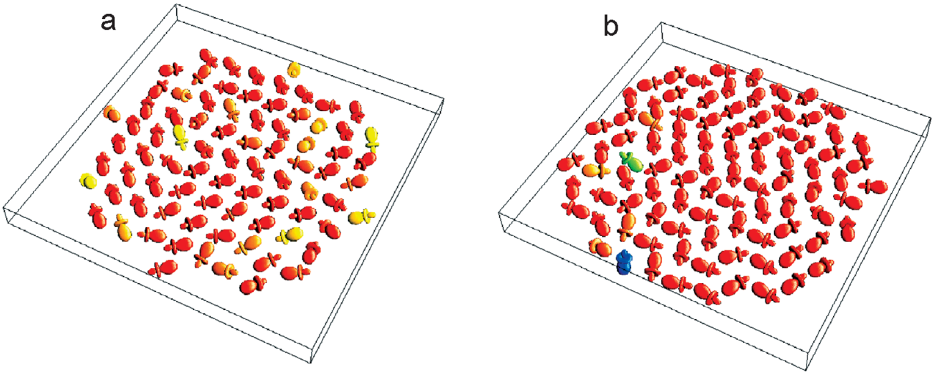

**Fig. 4.21** Monte-Carlo stable low-temperature configurations for $Q_{20}$+$Q_{10}$ moments with $Q_{20} \approx Q_{10}$ on a square (a) and a triangular (b) lattice.

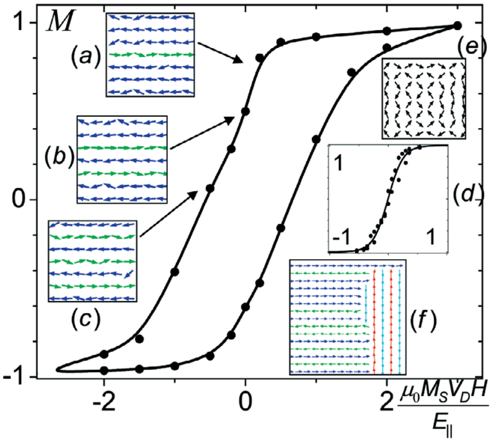

**Fig. 4.22** Hysteresis loops for a 20×20 square nanoarray with $Q_{30}=0.5\,Q_{10}$ and a pure dipolar system (inset (d)). The magnetic field is applied in the *x*-direction. Insets (a–c) provide the central part of intermediate magnetic configurations; (f) and (e) show stable zero-field configurations for combined multipoles and the pure dipolar case, respectively. The thermal energy is $kT=0.6\,E_{||}$. The field is expressed in $\mu_0 M_S V_d/E_{||}$, with $\mu_0$ as the permeability of free space and $V_d$ as the volume of a dot.

have been found. The width of regions with parallel lines is usually two to three lattice parameters. In ∼ 10% of calculations, despite a very long relaxation procedure, superdomains appear (Fig. 4.22 f). On an infinite triangular lattice the ground state is a ferromagnetic single domain, as in a pure dipolar system, although in finite systems the vortex configuration is never formed for $Q_3/Q_1 \geq 0.5$. Instead, large collinear domains appear. Hence, the interaction of

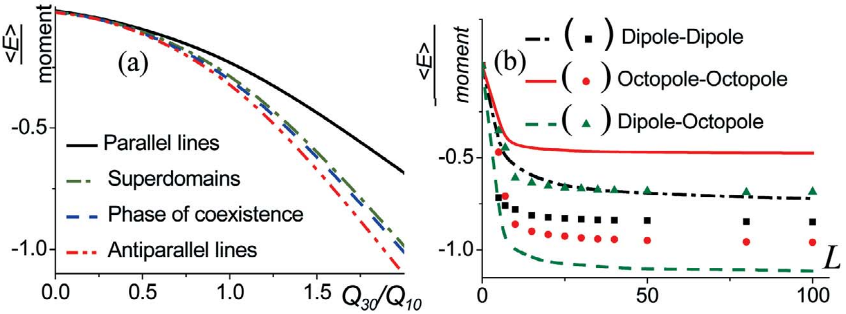

**Fig. 4.23** (a) Internal energy of ideal parallel, antiparallel, coexisting and superdomain MC configurations for $L=20$ as a function of $Q_{30}/Q_{10}$ on a square lattice. (b) Size-dependence of different contributions of the magnetostatic energy for parallel (solid lines) and antiparallel lines (scatter graph) for $Q_{30}/Q_{10}=0.5$.

dipoles with demagnetizing field is still too weak compared to the anisotropy induced due to octopole–octopole coupling.

In order to understand why the state of coexisting parallel and antiparallel lines has the lowest internal energy, different energetic contributions (dipole–dipole, dipole–octopole, octopole–octopole) and the entropy must be analyzed. The energy of ideal and MC configurations on a square lattice as a function of $Q_{30}/Q_{10}$ is plotted in Figure 4.23 a. All energies are expressed in the pair interaction energy $E_{\|}$ between two dots magnetized mutually parallel but perpendicular to the bond $E_{\|} \propto 1/R_{AB}^{I_A+I_B+1}$. Figure 4.23 b indicates the size-dependence of all energy contributions for parallel (solid curves) and antiparallel (scatter graph) lines. It has been found that the dipole–octopole energy contribution $E_{d\text{–}o}$ is minimal for the parallel lines, but maximal for antiparallel lines. The dipole–dipole ($E_{d\text{–}d}$) and octopole–octopole ($E_{o\text{–}o}$) interactions, in contrast, prefer antiparallel lines. Therefore, for sample sizes $L<9$ and $Q_{30}/Q_{10}<0.8$ the state of coexisting parallel and antiparallel lines has the lowest total internal energy. For $L>9$ the antiparallel lines are preferable for all $Q_{30}/Q_{10}$ as the long-range dipolar contribution increases. The energy difference between antiparallel lines and coexisting phases or superdomains $\delta E$ grows with increasing $Q_{30}/Q_{10}$ (Fig. 4.23 a). However, for $Q_{30}/Q_{10} < 0.6\,\delta E$ is very small ($\sim 2\%$), while the configurational entropy in a system of parallel or antiparallel lines increases drastically with the system size $S = k \cdot \ln(2 \times 2^L)$. As the entropy increases boundless with $L$, in contrast to the slow convergence of the dipolar sum, the free energy of the coexistence is lower for non-zero temperatures.

The formation of superdomains provides an additional contribution to the entropy, and one which depends on the size of the superdomains. Superdomain size in finite dipolar systems is driven by the pole avoidance principle. While the energy cost due to wall formation increases only linearly with domain size, the gain in long-range dipolar interaction increases with the square of the domain size, and only rarely is the formation of superdomains observed at low temperatures. The additional entropy for large superdomains is small. When approaching the critical temperature the domain size decreases, the corresponding entropy increases, and the superdomains appear more frequently. This finding is in accordance with the experiment [24] providing evidence for the formation of large in-plane collinear domains extending across several dots.

Thus, unlike the non-collinear ground states of pure dipolar systems, their odd multipolar counterparts select collinear configurations from the dipolar manifold. The reason for this selection is two-fold. First, the octopolar/dotriacontapolar interaction on a triangular and a square lattice introduces an easy-plane and a tri- and a biaxial in-plane anisotropy, respectively. Second, the octopoles do not interact with the field. Rather, they interact with the second derivative of the field, that is, its curvature. Therefore, systems with strong octopolar contribution are less sensitive to the formation of uncompensated magnetic poles at the sample boundary than systems with dominating dipolar interactions. Despite the collinearity, the lattice structure plays an important role. Whilst the ground state for $Q_{30}/Q_{10} \approx 0.5$ multipoles on a square lattice consists of antiparallel lines of magnetic moments, the triangular symmetry leads to the parallel ferromagnetic configuration.

#### 4.2.2.2 **Magnetization Reversal in Nanomagnetic Arrays**

Experimental investigations have shown that, in comparison to an infinite film, the interparticle interactions usually lead to a decrease in the switching field in patterned media with out-of-plane magnetization [25, 26], and to an increase of the coercivity for in-plane magnetized particles [27–29]. Although in some cases an agreement of switching behavior with theoretical predictions has been obtained, it is often found that measured switching fields deviate significantly (by 10–15%) from those expected with pure dipolar interactions. In the following section the field dependence of magnetization in square and triangular array of dots with in-plane magnetization and $Q_{30}/Q_{10} \geq 0.5$ will be analyzed and compared with hysteretic properties of a pure dipolar system.

Figure 4.22 shows the magnetization reversal of a square lattice with $Q_{30}/Q_{10} = 0.5$ corresponding to an array of ultrathin particles with height to diameter ratio $h/a \leq 0.5$ and interparticle distance $d \leq 1.5a$; and for a pure dipolar system $(h/2a \approx 1$ (or) $d > 1.5a)$ (Fig. 4.22 d). A pure dipolar system does not show any easy-axis hysteresis; the reason for this is clear from Figure 4.24, where several snapshots of a hysteresis on a pure dipolar square lattice are shown. In a pure dipolar case all magnetic moments rotate coherently, and therefore the total magnetization decreases continuously from unity at saturation field $H_S$ to zero for $H=0$. In a multipolar array, on the contrary, the hysteresis loop is quite open. The squareness $s$ depends on the composition, the strength of the multipoles, and on the temperature. The field is scaled with $E_{\|}$, as described in the previous section. Therefore, contributions from moments of different order in combined multipoles scale differently with $R_{AB}$. All values are given for $Q_{30} = 1$, $Q_{10} = 2$, and $R_{AB} = 1$. This gives $s \approx 0.5$ and $H_c \mu_0 M_S V_d \approx 0.7\, E_{\|}$ . By calculating $E_{\|}$ this result can be scaled to a square array of any material with any interdot distance. For example, for an array of permalloy particles at room temperature $M_S = 8 \cdot 10^5$ A m$^{-1}$, and vanishing anisotropy $K_1 < 1000$ J m$^{-3}$ with $h = 20$ nm, $d = 2a = 70$ nm and $R = 100$ nm, a coercive field $H_c \approx 20$ mT has been found.

Magnetic moments do not rotate continuously, as in a pure dipolar system (see Fig. 4.22 d, Fig. 4.24), but are reoriented line-by-line (Fig. 4.22 a–c) as non-collinear configurations are energetically unfavorable. From the Monte-Carlo calculations it follows that the competition between dipolar and octopolar contributions $E_{d\text{–}o}$ and combined $E_{d\text{–}d} + E_{o\text{–}o}$ interaction energy plays an important role for the magnetization reversal. As demonstrated in Figure 4.23 a, the total energy of the configuration in Figure 4.22 b is close to or even lower than that of Figure 4.22 c, where all chains are antiparallel. Hence, to go from the configuration of Figure 4.22 b to that of Figure 4.22 c, an external magnetic field must be applied and the hysteresis appears. $H_c$ increases with decreasing temperature; this effect is similar to superparamagnetic temperature-assisted switching, and thus the hysteretic behavior is predefined by competition between the octopole–dipole contribution of the magnetostatic energy and its dipole–dipole and octopole–octopole counterparts. Pure dipolar systems do not show any significant hysteresis.

On a triangular lattice, $H_c$ increases by $\sim 10\%$ compared to the pure dipolar system, and in good accordance with experimental data [28]. However, the magnetization reversal is different from that on a square lattice. Hence, the ground states and magnetization reversal in densely packed nanomagnetic arrays is strongly influenced as much by the order of magnetostatic interactions as by the underlaying lattice symmetry.

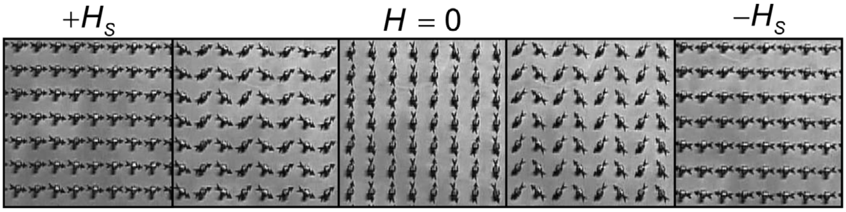

**Fig. 4.24** Snapshots of the central part of an experimental dipolar model on a square lattice during magnetization reversal. The magnetic field is changed from $+x$ to $-x$ direction. The left and right panels indicate the saturated configurations for positive and negative field, respectively. The center panel shows stable zero-field configuration, while two other panels represent intermediate configurations.

## 4.3
## Summary

Competing interactions of the same range may significantly alter pure ground state configurations and, hence, the macroscopic physical properties of a material. Competing ferromagnetic-like and antiferromagnetic-like interactions of short and medium ranges lead to the spiral states. Competing long-range electrostatic/magnetostatic forces, in contrast, relieve the degeneracy of the pure interactions and promote the formation of collinear structures.

## 4.4
## Exercises

1. Find the two superimposed $Q$ vectors of the $2Q$ structure in Figure 4.6 (right).

*Solution*
See Fig. 4.25.

2. Consider a chain with antiferromagnetic first and second-nearest-neighbor interactions (negative $J$ constants). Calculate the optimal angle between the nearest-neighboring spins and make conclusions about the type of magnetic order. Is it commensurate, or not (see Chapter 1)?

*Solution*

$$E = -J_1 \sum_i \mathbf{S}_i \cdot \mathbf{S}_{i+1} - J_2 \sum_i \mathbf{S}_i \cdot \mathbf{S}_{i+1} = J_1 S^2 \sum_i \cos\, \theta_{i+1} - J_2 S^2 \sum_i \cos\, \theta_{i+2}$$

$$= -NS^2 [J_1 \cos\, \theta + J_2 \cos\, 2\theta]$$

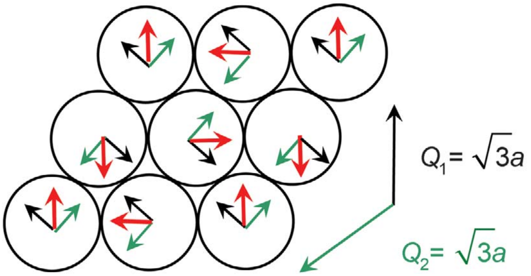

**Fig. 4.25** The spirals with the wave vectors $Q_1 = \sqrt{3a}$ and $Q_2 = \sqrt{3a}$ run along two directions of second-nearest-neighbor bonds. The black arrows denote $\mathbf{Q}_1$, the green arrows represent $\mathbf{Q}_2$, and the red arrows give the resulting configuration.

where the angle between nearest neighbors $\theta$ is the same. The optimal angle can be obtained from the minimization of the internal energy:

$$\frac{dE}{d\theta} = NS^2\left[J_1 \sin\theta + 2J_1 \sin 2\theta\right] = 0 \Rightarrow$$

$$J_1 \sin\theta = -2J_2 \sin 2\theta = -4J_2 \sin\theta \cos\theta \Rightarrow \cos\theta = -J_1/4J_2$$

The solution gives the spiral order. Generally it is incommensurate with the interatomic spacing.

3. Write down the classical Heisenberg Hamiltonian on a periodic lattice representing the spin variables in terms of their Fourier components. Show that the fundamental solution of the Heisenberg model on a Bravais lattice are helical spin structures.

*Solution*
The spins on the lattice sites can be written in terms of their discrete Fourier components by

$$\mathbf{S}_i = \sum_{\mathbf{q}} \mathbf{S}_q \cdot e^{i\mathbf{q}\mathbf{R}_q}\,, \tag{4.2}$$

where the sum is over the reciprocal lattice vectors $\mathbf{q}$ and $\mathbf{R}_i$, is the real-space coordinate of lattice site $i$. The inverse Fourier transform is given by:

$$\mathbf{S}_q = \frac{1}{N}\sum_i \mathbf{S}_i \cdot e^{-i\mathbf{q}\mathbf{R}_i} \tag{4.3}$$

Since spins are real quantities

$$\begin{aligned}\sum_i \mathbf{S}_i \cdot e^{-i\mathbf{q}\mathbf{R}_i} &= \sum_i \mathbf{S}_i \cdot (\cos(-\mathbf{q}\mathbf{R}_i) - i\sin(-\mathbf{q}\mathbf{R}_i))\\ &= \sum_i \mathbf{S}_i \cdot (\cos(\mathbf{q}\mathbf{R}_i) - i(-\sin(\mathbf{q}\mathbf{R}_i)))\end{aligned} \tag{4.4}$$

Therefore,

$$\mathrm{S}_q = \mathbf{S}^*_{-q} \tag{4.5}$$

replacing the localized spin by its Fourier components in the Heisenberg Hamiltonian yields

$$H = \sum_{i,j} -J_{ij} \sum_{\mathbf{q}\mathbf{q}'} \mathbf{S}_{\mathbf{q}}\mathbf{S}_{\mathbf{q}'} e^{i\mathbf{q}\mathbf{R}_i} e^{i\mathbf{q}'\mathbf{R}_j} = \sum_{i,j} -J_{ij} \sum_{\mathbf{q}\mathbf{q}'} \mathbf{S}_{\mathbf{q}}\mathbf{S}_{\mathbf{q}'} e^{i(\mathbf{q}+\mathbf{q}')\mathbf{R}_i} e^{i\mathbf{q}'(\mathbf{R}_j-\mathbf{R}_i)}$$

$$= -N \sum_{\mathbf{q}} \mathbf{S}_{\mathbf{q}} \mathbf{S}_{-\mathbf{q}} \left( \sum_{\delta} J_{0\delta} e^{-i\mathbf{q}\mathbf{R}_{\delta}} \right) \tag{4.6}$$

where $\sum_i e^{i(\mathbf{q}+\mathbf{q}')\mathbf{R}_i} = N\delta_{\mathbf{q},-\mathbf{q}}$ holds for all lattice sites and $\mathbf{R}_\delta = \mathbf{R}_i - \mathbf{R}_j$, that is, using summation over Kroneker $\delta$-function $q'$ can be replaced by $-q$. The Fourier transform of the exchange constants are defined by:

$$J(\mathbf{q} = \sum_{\delta} J_{0\delta} e^{-i\mathbf{q}\mathbf{R}_{\delta}} = J(-\mathbf{q}) = J(\mathbf{q})^* \tag{4.7}$$

They are real quantities. Here, the relationship $J_{0\delta} = J_{0-\delta}$ has been used, which is consequence of the translational symmetry and the fact that the interaction is symmetric $J_{ij} = J_{ji}$. With Eq. (4.7) the Hamiltonian can be written in the simple form

$$H = -N \sum_{\mathbf{q}} J(\mathbf{q}) \mathbf{S}_{\mathbf{q}} \mathbf{S}_{-\mathbf{q}} \tag{4.8}$$

In order to find the magnetic ground state, the energy of Eq. (4.8) has to be minimized under the condition that the spins on all lattice sites have the same magnitude $\mathbf{S}_i^2 = S^2$ as they are classical vectors. This equation represents a system of N independent equations

$$\sum_{q} \mathbf{S}_{\mathbf{q}} \mathbf{S}_{-\mathbf{q}} = S^2 \sum_{q} \mathbf{S}_{\mathbf{q}} \mathbf{S}_{\mathbf{q}'-\mathbf{q}} = \mathbf{0}\,,\ \mathbf{q}' \neq \mathbf{0} \tag{4.9}$$

The lowest energy is given by $E = -NS^2 J(\mathbf{Q})$, where $\pm\mathbf{Q}$ are the values of $\mathbf{q}$ that maximize $J(\mathbf{Q})$. To recover the spin structure that corresponds to $\mathbf{S}_{\mathbf{Q}}$ and $\mathbf{S}_{-\mathbf{Q}}$ the real and imaginary parts of $\mathbf{S}_{\mathbf{Q}}$ should be introduced as

$$\mathbf{S}_{\mathbf{Q}} = \mathbf{R}_{\mathbf{Q}} + i\mathbf{I}_{\mathbf{Q}}\,,\ \mathbf{S}_{-\mathbf{Q}} = \mathbf{R}_{\mathbf{Q}} - i\mathbf{I}_{\mathbf{Q}} \tag{4.10}$$

From the conditions in Eq. (4.9)

$$\mathbf{S}_{\mathbf{Q}} \mathbf{S}_{-\mathbf{Q}} = \mathbf{R}_{\mathbf{Q}}^2 + \mathbf{I}_{\mathbf{Q}}^2 = S^2$$

$$\mathbf{S}_{\mathbf{Q}} \mathbf{S}_{\mathbf{Q}} = \mathbf{R}_{\mathbf{Q}}^2 - \mathbf{I}_{\mathbf{Q}}^2 + 2i\mathbf{R}_{\mathbf{Q}} \mathbf{I}_{\mathbf{Q}} = 0 \tag{4.11}$$

The second equation shows that $\mathbf{R}_{\mathbf{Q}}$ and $\mathbf{I}_{\mathbf{Q}}$ are perpendicular and have the same magnitude. Finally,

$$\mathbf{R}_{\mathbf{Q}}^2 = \mathbf{I}_{\mathbf{Q}}^2 = S^2/2\,,\ \mathbf{R}_{\mathbf{Q}} = \mathbf{I}_{\mathbf{Q}} = 0 \tag{4.12}$$

Substituting this into Eq. (4.2) yields the spins on the lattice sites:

$$\mathbf{S}_i = 2(\mathbf{R}_{\mathbf{Q}} \cos(\mathbf{Q}\mathbf{R}_i) - \mathbf{I}_{\mathbf{Q}} \sin(\mathbf{Q}\mathbf{R}_i)) \tag{4.13}$$

Hence, the fundamental solutions of the Heisenberg model on a Bravais lattice are helical spin structures [12].

## References

1 V. Sechovsky, Magnetism in Solids: General Introduction. In: *Encyclopedia of Materials: Science and Technology Updates*, Elsevier, Oxford, **2005**.
2 P. Hässler, E. Kay, *Z. Physik. Chemie Neue Folge* **1988**, *157*, 377.
3 B. Barbara, D. Gignoux, C. Vettier, *Lectures on Modern Magnetism*, Springer, Berlin, **1988**.
4 A. Kubetzka, P. Ferriani, M. Bode, S. Heinze, G. Bihlmayer, K. von Bergmann, O. Pietzsch, S. Blügel, R. Wiesendanger, *Phys. Rev. Lett.* **2005**, *94*, 087204.
5 M. Bode, E.Y. Vedmedenko, K. von Bergmann, A. Kubetzka, P. Ferriani, S. Heinze, R. Wiesendanger, *Nat. Mater.* **2006**, *5*, 477.
6 K. von Bergmann, S. Heinze, M. Bode, E.Y. Vedmedenko, G. Bihlmayer, S. Blügel, R. Wiesendanger, *Phys. Rev. Lett.* **2006**, *96*, 167203.
7 J. Jensen, A.P. Makintosch, *Rare Earth Magnetism*, Clarendon Press, Oxford, **1991**.
8 K. Binder, A.P. Young, *Rev. Mod. Phys.* **1986**, *58*, 801.
9 W. Kinzel, *Phys. Rev. B* **1979**, *19*, 4595.
10 C.A. Cardoso, F.M. Araujo-Moreira, V. P.S. Awana, E. Takayama-Muromachi, O.F. de Lima, H. Yamauchi, M. Karppinen, *Phys. Rev. B* **2003**, *67*, 020407.
11 D.P. Landau, K. Binder, *A Guide to Monte Carlo Simulations in Statistical Physics*, Second Edition, University Press, Cambridge, **2005**, p. 167.
12 Ph. Kurz, *Non-Collinear Magnetism at Surfaces and in Ultrathin Films*, Dissertation, Aachen, **2000**.
13 Ph. Kurz, G. Bihlmayer, S. Blügel, K. Hirai, T. Asada, *Phys. Rev. B* **2001**, *63*, 096401.
14 E.Y. Vedmedenko, unpublished results.
15 M. Kiwi, *J. Magn. Magn. Mater.* **2001**, *234*, 584.
16 H. Ohldag, et al. *Phys. Rev. Lett.* **2003**, *91*, 017203.
17 W.H. Meiklejohn, C.P. Bean, *Phys. Rev.* **1956**, *102*, 1413.
18 A. Kubetzka, P. Ferriani, M. Bode, S. Heinze, G. Bihlmayer, K. von Bergmann, O. Pietzsch, S. Blügel, R. Wiesendanger, *Phys. Rev. Lett.* **2005**, *94*, 087204.
19 E.Y. Vedmedenko, U. Grimm, R. Wiesendanger, *Phys. Rev. Lett.* **2004**, *93*, 76407.
20 G. Malescio, G. Pellicane, *Nature Materials* **2003**, *2*, 97.
21 A.R. Massih, G.A. Mansoori, *Fluid Phase Equilibria* **1983**, *10*, 57.
22 E.Y. Vedmedenko, N. Mikuszeit, H.P. Oepen, R. Wiesendanger, *Phys. Rev. Lett.* **2005**, *95*, 207202.
23 N. Mikuszeit, E.Y. Vedmedenko, H.P. Oepen, R. Wiesendanger *J. Appl. Phys.* **2005**, *97*, 10J502.
24 Y.B. Xu, et al., *IEEE Trans. Magn.* **2001**, *37*, 2055.
25 T. Aign, P. Meyer, S. Lemerle, J.P. Jamet, J. Ferré, V. Mathet, C. Chappert, J. Gierak, C. Vieu, F. Rousseaux, H. Launois, H. Bernas, *Phys. Rev. Lett.* **1998**, *81*, 5656.
26 C.A. Ross, M. Hwang, M. Shima, J.Y. Cheng, M. Farhoud, T.A. Savas, H.I. Smith, W. Schwarzacher, F.M. Ross, M. Redjdal, F.B. Humphrey, *Phys. Rev. B* **2002**, *65*, 144417.
27 R.P. Cowburn *J. Phys. D: Appl. Phys.* **2000**, *33*, R1.
28 J.Y. Cheng, W. Jung, C.A. Ross, *Phys. Rev. B* **2004**, *70*, 064417.
29 C. Miramond, C. Fermon, F. Rousseaux, D. Decanini, F. Carcenac, *J. Magn. Magn. Mater.* **1997**, *165*, 500.

# 5
# Interplay Between Anisotropies and Interparticle Interactions

Anisotropy is the property of having a different value when measured in different directions. Anisotropy breaks the symmetry of a system and therefore strongly affects its physical properties, such as the shape of hysteresis loops, conductivity, and diffusion, transmission of the light, or mechanical properties. When the dimensionality of a system is reduced, additional surface or edge anisotropy contributions come into play. These new effects are of considerable practical importance because they can be exploited in the design of materials or devices of commercial significance. Two striking examples of anisotropic systems are two-dimensional liquid crystals and nanomagnets. The effects of anisotropy on the structural ordering in these materials will be discussed in the following sections.

## 5.1
## Interplay Between the Structural Anisotropy and the Short-Range Repulsion/Attraction: Liquid Crystals

When light passes through a body with a uniaxial anisotropy it splits into two beams that vibrate perpendicular to each other. Because each of these beams travels in different directions, they will encounter different resistance to their motion and so will travel at different speeds through the body. Due to this effect, the two polarizations of light in most transparent crystalline materials possess slightly different indices of refraction and therefore the crystals show birefringence – that is, optical anisotropy. As the properties of isotropic materials (e.g., glasses, liquids and amorphous materials) do not depend on direction, birefringence can be used to distinguish crystalline media from non-crystalline media. This method, however, fails for one class of materials, namely liquid crystals (LCs). Liquid crystals are a phase of matter the order of which is intermediate between that of a liquid and that of a crystal. These materials show strong birefringence – that is, they are anisotropic and at least partially ordered – but they flow as a liquid. Thus, the question to be asked is “What is the reason for such an unusual behavior?”

In contrast to isotropic liquids, LCs consist of molecules/molecular complexes of anisotropic shape (rod-like, columnar, disc-shaped, etc.). The anisotropic components (mesogens) cannot penetrate one into another – that is, there exists a hard-core repulsion between them. The interplay between shape anisotropy and hard-core repulsion is the essential prerequisite for the liquid crystalline ordering. A simple model predicting phase transition from the liquid to the liquid crystalline state is the hard-rod model proposed by Lars Onsager [1]. In this model, the volume excluded from the center-of-mass of one idealized cylinder as it approaches another is calculated. Specifically, if the cylinders are oriented parallel to one another, there is very little volume that is excluded from the center-of-mass of the approaching cylinder (it can come quite close to the other cylinder). If, however, the cylinders are at some angle to one another, then there is a large volume surrounding the cylinder where the approaching cylinder's center-of-mass cannot enter. Thus, this angular arrangement leads to a decrease in the net positional entropy of the approaching cylinder (there are fewer states available to it). While parallel arrangement of anisotropic objects leads to a decrease in orientational entropy, there is an increase in positional entropy. Thus, in some cases a greater positional order will be entropically favorable. This theory predicts that a solution of rod-shaped objects will undergo a phase transition, at sufficient concentration, into a so-called nematic LC phase. Liquid crystals which undergo a phase transition with increasing concentration are called *lyotropic* LCs.

Despite its simplicity and clarity, the Onsager theory yields rather poor predictions for the properties of *thermotropic* LCs – liquid crystals which undergo a temperature-driven phase transition [2]. The thermotropic LCs are usually studied on the basis of the Maier–Saupe theory [3], which includes contributions from an attractive intermolecular potential of the type $H = 1/2\varepsilon \sum_{<i,j>} P \cos\theta_{ij}$, where $\varepsilon$ is dielectric constant, $P$ the strength of the interaction, and $\theta_{ij}$ the angle between nearest-neighbor mesogens $i,j$. The anisotropic attraction stabilizes parallel alignment of neighboring molecules, and the theory then considers a mean-field average of the interaction. When solved self-consistently, the Maier–Saupe theory predicts thermotropic phase transitions, consistent with experiment.

Thus, both lyotropic and thermotropic liquid crystalline phases (mesophases) can be theoretically described in the framework of the interplay between the structural anisotropy and the repulsive or attractive interaction potential between mesogenic molecules. In addition to these main interactions, a long-range electrostatic forces between mesogens may exist in ferroelectric/antiferroelectric or in some polymer LCs [4–6]. Therefore LCs can be simulated like a system of hard ellipses/cylinders [7] or like a system of electric dipoles on a lattice with Maier–Saupe and dipolar potential [8]. Sometimes, it is suggested that the anisotropic Maier–Saupe potential has a Lennard-Jones-type (see Inset 3.1) distance-dependence [9].

### 5.1.1
### Liquid Crystal Phases

There are many types of liquid crystal state, depending upon the amount of order in the material and the geometry of the mesogens. The main phases of thermotropic LCs with elongated molecules are nematic, smectic, and cholesteric. The *nematic* (from the Greek nematos, meaning "thread") liquid crystal phase is characterized by molecules that have no positional order but tend to point in the same direction. An example of such a configuration is shown in Figure 5.1 a. To make the analysis of liquid crystalline order quantitative, an orientational order parameter – the so-called "director" – is usually defined based on the average of the second Legendre polynomial.

$$S = \langle P_2(\cos\theta)\rangle = \left\langle \frac{3\cos^2\theta - 1}{2} \right\rangle, \tag{5.1}$$

where $\theta$ is the angle between the axis of a mesogen molecule and the local director. In the *smectic* phase (from the Greek smectos, meaning "soap"), molecules of liquid crystal form orderly layers; that is, in addition to the orientational ordering they show a degree of translational organization (see Fig. 5.1 b). The director can be either perpendicular to or tilted with respect to the smectic layer, and the tilting angle can change from one layer to another. *Cholesteric* LCs are sometimes also called "chiral nematics"; this phase is typically composed of nematic layers with directors aligned at a slight angle to one another. This leads to the formation of a structure that can be visualized as a stack of very thin, two-

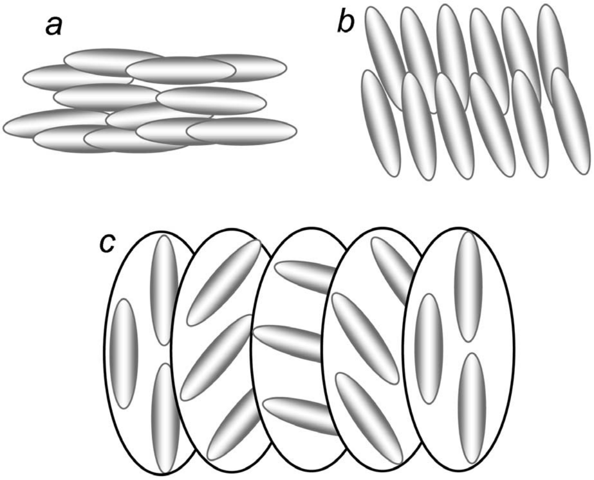

**Fig. 5.1** Phases of thermotropic liquid crystals: (a) nematic; (b) smectic; (c) cholesteric.

dimensional, nematic-like layers with the director in each layer twisted with respect to those above and below. In this structure, the directors form a continuous helical pattern about the layer normal (see Fig. 5.1 c). Disk-like thermotropic mesogens form different kinds of columnar phases.

Lyotropic LCs are found in countless everyday situations. For example, soaps and detergents form lyotropic LCs when they combine with water, while biological membranes and many biological liquids such as bile, saliva, and pancreatic juice display lyotropic liquid crystalline behavior. The molecules from which lyotropic liquid crystals are formed are surfactants that consist of two distinct parts: a polar, often ionic, hydrophilic head; and a non-polar, often hydrocarbon, hydrophobic tail. If the tail is sufficiently hydrophobic, the material is insoluble, and then for concentrations $C > C_L$ the molecules on the surface of water form an isolated two-dimensional system (i.e., Langmuir monolayer described in Section 3.2.2). At a critical concentration of amphiphiles in the water $C_M > C_L$, which is larger than the Langmuir concentration, the molecules begin to arrange themselves in hollow spheres, rods, or disks called *micelles* (see Fig. 5.2 a). The surface of a micelle is a layer of polar heads dissolved in the water, while the inner portion consists of hydrophobic tails screened from the water by the hydrophilic heads. In non-polar solvents, *inverse micelles* (see Fig. 5.2 b, d) appear. As the concentration increases further, the micelles begin to arrange themselves into loose patterns. This means that an isotropic micellar liquid turns into a lyotropic LC with anisotropic properties. Several possible types of lyotropic ordering are illustrated schematically in Figure 5.2, these being either face-centered or body-centered cubic crystal lattice and hexagonal structure. Usually, the ordered structures are formed under a critical temperature, $T_c$. For organic mesogens (e.g., lipids), the critical temperature is lower than the room temperature ($\sim 15\,^\circ\mathrm{C}$). At even higher concentrations the molecules move into another liquid crystalline phase, the lyotropic liquid crystal *bilayer* (Fig. 5.2 g), which is a prototype of biological membranes. This pattern is similar to that of smectic liquid crystals in the thermotropic category. Because the sheet-like layers can slide easily past each other, this phase is less viscous than the hexagonal phase, at least in the direction of the sliding, despite its lower water content. By further water evaporation the bilayer (or lamellar) phase becomes a gel (Fig. 5.2 h) and then a solid crystal. More detailed descriptions of liquid crystalline phases can be found in some excellent text books [5, 6, 10].

### 5.1.2
### Liquid Crystal Patterns: Textures and Disclinations

As shown above, mesogens tend to arrange themselves in ordered structures with a common direction of orientation. Imagine that a column of nematic liquid crystal is suspended between two transparent glasses and two polarizing filters the axes of polarity of which are perpendicular to each other. In a homeotropically aligned LC, where the director is normal or parallel to the glass surface, no birefringence is observed because the phase is uniaxial. The planar cell

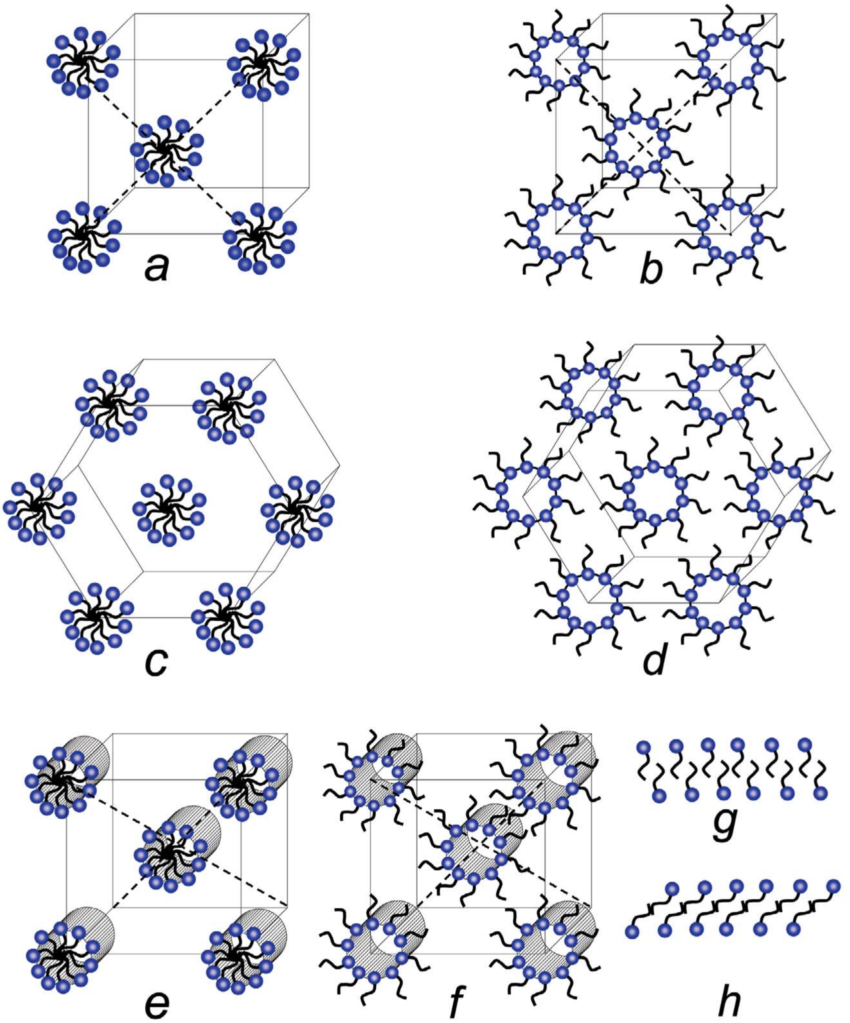

**Fig. 5.2** Lyotropic phases. (a) Micellar face-centered; (b) inverse micellar phase-centered; (c) micellar hexagonal; (d) inverse micellar hexagonal; (e) body-centered rod-like; (f) inverse body-centered rod-like; (g) lamellar liquid crystal (bilayer); (h) lamellar gel.

appears just as a dark field. However, if the nematic is replaced by the chiral nematic with helical structure (Fig. 5.1c), the LC changes the twist of the light passing through the molecules, and allows varying degrees of light to pass (or not pass) through the polarizing filters. It is said that liquid crystals belong to the class of optically active materials, which can rotate the axis of light polarization. However, by controlling the twist of the LCs in such a column, light may be allowed to pass through in varying amounts, correspondingly illuminating the field of view. This principle is used in liquid crystalline displays (LCD), where each such column is a pixel, the simple glass is replaced by the transparent electrodes, and the degree of molecular twisting is controlled by an applied electric field.

Without an ordering field it is almost impossible to obtain a single textured material in which all of the molecules in the sample have a common orientation. Although this is the lowest energy state, it is unlikely for kinetic reasons. First, the orientational ordering of LCs does not require a positional organization. Second, dispersive Maier–Saupe forces are not very strong and compete with the temperature; thus, one usually achieves a "multi-textured" arrangement in which there is local orientation in domains that are randomly oriented with respect to each other. Abrupt discrete boundaries between domains would have a very high energy and be unstable; however, the energy can be lowered by more or less continuous rotation of the director around the singular points, called *disclinations*.

The first quantitative theory of disclinations was developed by F.C. Frank [11] for cholesteric and nematic liquid crystals. Frank showed that disclinations represent arrangements of minimum energy, and were quantized in that there are particular stable disclinations represented by values of parameter $s$ that are integral multiples of 1/2 (see Fig. 5.3), such as $s=1/2$, 3/2, etc., that may have either a positive or negative sign. In order to determine the disclination strength, one should determine by which angle the director rotates when moving around the center of the topological defect [12]. For example, Figure 5.3 a, b illustrates two possible topological configurations where, on the left, the molecules are vertically oriented, while on the right they are horizontal. In both cases the director rotates by $\pi/2$ from the left to the right. The sense of rotation, however, is different: anticlockwise in Figure 5.3 a, but clockwise in Figure 5.3 b. Therefore, the strength of the corresponding disclinations is said to be 1/2 and –1/2. The energy associated with disclinations depends on $s^2$, so that the $s=1/2$ disclinations are most probable.

Disclinations strongly change the appearance of a LC in polarizing light [5, 6, 13, 14]. Due to the optical activity of the LC, the rotation of director in a disclination is seen as a change in light intensity and color. Therefore, when LCs are viewed between crossed polars, arrays of disclinations – or so-called liquid-crystalline *textures* – can be seen. The commonly observed "schlieren texture" found in nematics is shown in Figure 5.4 a. Lines in the schlieren texture correspond to the linear disclination of strength ±1/2, while the dark points are the singularities. A disclination line of strength 1/2 separates regions of the material that differ in rotational distortion by $\pi$. In the lamellar lyotropic crystals, a so-called myelin texture is often produced (see Fig. 5.4 b); this is topologically similar to the schlieren pattern, as it consists of thread-like elements with $\pi$ rotational distortion [15]. However, in contrast to one-dimensional lines of schlieren texture, the myelin "lines" are tubes made from amphiphilic bilayers. If there is a vortex-like disclination of the strength ±1 in the sample, the director will under-

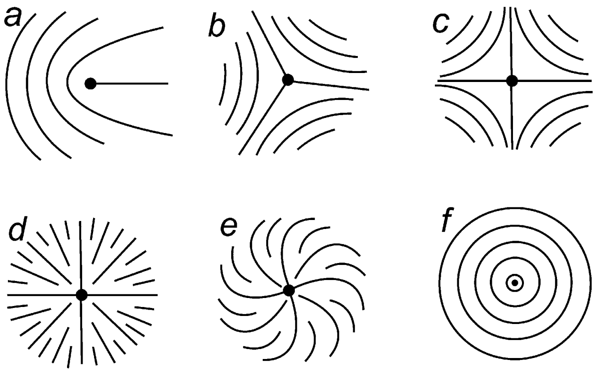

**Fig. 5.3** Disclinations (topological defects) of different strength. (a) $s=1/2$; (b) $s=-1/2$; (c) $s=-1$; (d) $s=1$, phase 0; (e) $s=1$, phase $\pi/4$; (f) phase $\pi/2$.

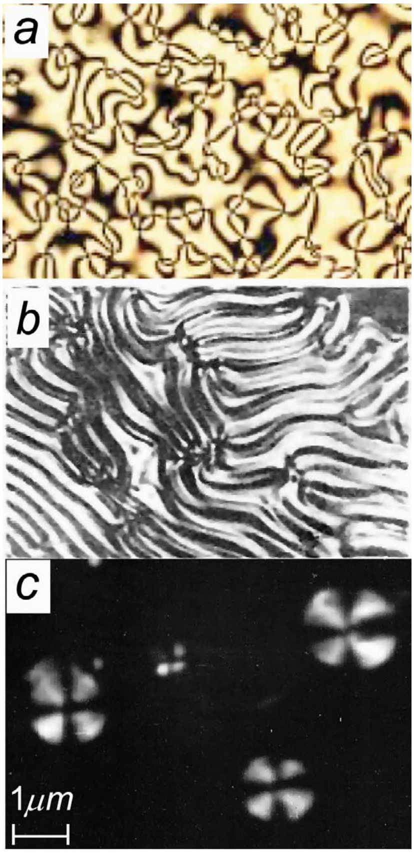

**Fig. 5.4** Disclinations observed by polarizing light microscopy. (**a**) Schlieren texture in a thermotropic nematic ($s=1/2$). (b) Myelin structure in a lyotropic bile ($s=1/2$).
(b) Hedgehog-like vortices in water solution of human saliva under the action of electric field ($s=1$).

go a change of $2\pi$ around a core, and there will be four bright regions at $\pi/4$, $3\pi/4$, $5\pi/4$, and $7\pi/4$ and four dark regions at 0, $\pi/2$, $\pi$, and $3\pi/2$. A photographic image of light reflected from such types of disclination is shown in Figure 5.4c. Disclinations seldom show ordered patterns; rather, their arrays are mainly disordered.

Relatively ordered patterns can also be found in LCs. One example is the prominent focal conic texture usually found in smectic thermotropics and lyotropic lamellar bilayers. In the absence of any constraints, the layers in a smectic LC would be flat and the molecules would tend to lie parallel to one another. In general, however, a smectic placed between microscopic slides does not assume the simple flat form, but becomes bent in order to conform to the boundary conditions. The molecules in the layers would like to be as parallel as possible, and at the same time to retain a constant interlayer distance. However, as shown in Figure 5.5a, this is possible only if the molecules can be aligned with the planes denoted by the dashed lines, assuming the circular bending of the liquid crystal (shown as concentric circles in Fig. 5.5a). This alignment leads to the formation of conical structures that produce the characteristic confocal texture shown in Figure 5.5b. If the bending is ellipsoid rather than circular, the dashed planes will be transformed into the hyperbolic surfaces known as Dupin cyclides [16]. As a consequence, the circular cones become elliptically distorted,

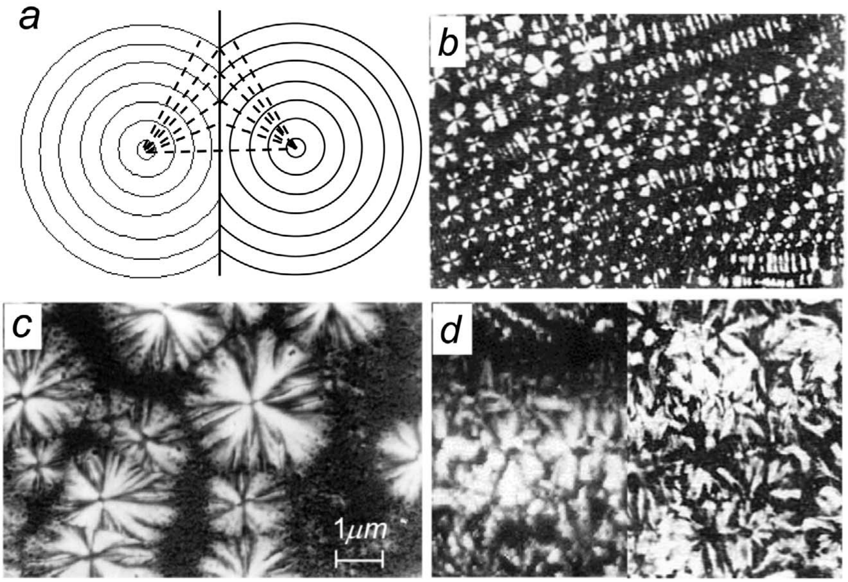

**Fig. 5.5** (a) Schematic representation of layer bending (concentric circles) in thermotropic smectics or lamellar lyotropic liquid crystals. The dashed lines represent planes which are normal to the layers. In general, a cone-shaped region is filled with the liquid crystal. (b–d) Typical focal conic lyotropic textures arising due to the bending of layers, as observed by polarizing light microscopy in lipid solutions.

while the confocal structure remains mainly unchanged but with a slightly different distribution of the light intensity (see Fig. 5.5 c). If the concentration of mesogen in a lyotropic LC is below the optimal value for lamellae formation, the bending of the bilayers becomes irregular, and this leads to distortion of confocal structure. Two examples of distorted focal conic texture are superimposed in Figure 5.5 d.

### 5.1.3
### The Lattice Model of Liquid Crystals

The disclinations can be simulated in the framework of the lattice model of LCs [17–19]. Depending on the dimensionality of the system, two versions of the model have been discussed in the literature. The 3D model consists of a cubic array of cells, each of which is assigned a director orientation [20]. The starting conditions are either random or correspond to a particular arrangement which is written into the model prior to commencement of relaxation. A cell is selected at random and its energy calculated by summing the individual energy contributions due to the orientational distortion between it and each of its six nearest neighbors. The orientation of the central vector is then changed by a small amount (1° or less) down the path of steepest energy gradient.

The energy function which has been found to be most successful in the 3D case is $\sin^2(\Delta\phi)$, where $\phi$ is the angle between neighboring mesogens [20]. The reasons for preference of this harmonic function are as follows:

- It approximates to $E \propto \Delta\phi^2$ at low angles, which is the assumption of the Frank equation for elastic energy.
- The summation of six energy functions corresponding to the surrounding cells corresponds to the summation of six harmonic functions differing in phase and amplitude. The consequence is another harmonic function. This has the advantage of a single minimum, so that gradients at all points on the energy surface lead to this minimum.
- The cubic lattice leads to a symmetrical field with completely flat energy. Hence, the orientation of central director is irrespective of the relative orientation of the disclination and the lattice.

The energy function which has been proposed for the two-dimensional lattice model is

$$E = \sum_i \sin^2(\theta_i - \phi)\,, \tag{5.2}$$

where $\phi$ and $\theta_i$ are the angles to the $x$-axis of the central vector and the $i$-th neighboring vector, respectively [21, 22]. This form can be derived from the Maier–Saupe theory, and an approximate form of the function Eq. (5.1) is

$$E = \sum_i (\theta_i - \phi)^2\,, \tag{5.3}$$

where the angles between neighboring moments are small. Another modification of the function Eq. (5.3) is

$$E = \sum_i (2 - 2\cos(\theta_i - \phi)) \,. \tag{5.4}$$

Close to a disclination core the angle between neighboring vectors may be large, and thus the choice between the three functions above will be significant. Of the functions described, Eq. (5.2) is unique in having a continuous gradient over 180°. Hence, it assures a flat energy distribution that is independent of the lattice mesh. The latter two equations will only produce a flat total energy function if an infinite number of neighbors can be chosen – that is, if there were no mesh. If the mesh is now rotated with respect to the disclination, the minimum energy positions predicted by Eq. (5.3) and (5.4) also rotate, and therefore the resulting orientation of the central director is dependent on the mesh orientation. The function Eq. (5.2) has found to be the most successful in describing the interactions and equilibrium properties of liquid-crystalline patterns.

## 5.2
## Competition Between the Spin-Orbit Coupling and the Long-Range Dipolar Energy: Ultrathin Magnetic Films

In non-relativistic quantum-mechanics the exchange energy has an isotropic character. This means that there is absolute freedom in the choice of the spin quantization axis. In other words, the free energy of the system is independent of the direction of magnetization. This is in contradiction with experience, which tells us that magnetization generally lies in some preferred direction with respect to the crystalline axis and/or to the external shape of the body. This property is known as "magnetic anisotropy". The anisotropy defines the preferential (easy) and difficult directions of magnetization, and is of technological importance for information storage and retrieval. The two main sources of magnetic anisotropy are spin-orbit coupling and magnetic dipolar interaction. Due to spin-orbit interaction, a small orbital momentum is induced which couples the total atomic magnetic moment to the crystal axis. The resultant total energy depends on the orientation of magnetization relative to the crystalline axis, and also reflects the symmetry of the crystal [23]. The dipolar interaction generally results in a shape-dependent contribution to the anisotropy because of its long-range character. The dipole–dipole interactions and spin-orbit coupling are the relativistic corrections to the Hamiltonian, which break the rotational invariance of magnetization with respect to the spin quantization axis.

The energy involved in the rotation of magnetization from a direction of low energy towards that of high energy is typically of the order of $10^{-6} \ldots 10^{-3}$ eV/atom in bulk materials and thin films [24], and may reach values of several meV in nanomagnetic structures [25]. Although the anisotropy energy is only a small correction to the total magnetic energy, it plays an extremely important role for the very existence of spontaneous magnetism in two-dimensional systems such as ultrathin films. Indeed, according to the Mermin-Wagner theorem, two-dimensional systems with only short-range isotropic exchange interactions cannot sustain magnetic order at non-zero temperature. The anisotropy opens a gap at the bottom of the spin-wave spectrum and thus stabilizes the long-range magnetic ordering at finite temperatures.

Anisotropy arising from dipolar interactions and from spin-orbit coupling often favors different orientations of magnetization. This can lead to competition between the two energy contributions, and may lead to many interesting magnetic phenomena such as spin reorientation transition. The magnetic ordering phenomena in single crystal, epitaxial films in the framework of this competition is outlined in the following section.

### 5.2.1
### Shape Anisotropy from Dipolar Interactions

The dipolar coupling introduced in Chapters 1 and 3 is the source of the so-called *shape anisotropy*. Due to the pole avoidance principle, the dipolar energy of a continuous ultrathin ferromagnetic film is minimal when all spins are parallel and lie in the film plane (as in Fig. 5.6 b). The dipolar energy of the configuration in Figure 5.6 a is, in contrast, maximal. In other words, the dipolar energy causes a difficult perpendicular axis but easy plane of magnetization. The shape anisotropy for such a film is defined as the difference between the dipolar energies of configurations of Figure 5.6 a and 5.6 b $\Delta E_D^{\text{film}} = E_D^{\text{up}} - E_D^{\text{in-plane}}$. $\Delta E_D$ of a finite body can be described by the demagnetizing tensor $N$: $\Delta E_D = N \cdot 1/2\,\mu_0 M_s^2 = N \cdot \Delta E_D^{\text{film}}$, with $M_s$ the saturation magnetization and $1/2\,\mu_0 M_s^2$ the shape anisotropy of an infinite continuous magnet. By neglecting the discrete nature of matter, $N$ can be analytically calculated for uniformly magnetized bodies such as ellipsoids. The fullest collection of demagnetizing factors of axially symmetric ellipsoids can be found in [26, 27]. In the continuum approximation, $\Delta E_D$ depends only on the ratio $k = L/t$ with $L$ and $t$ two axes of ellipsoids. Therefore, the shape anisotropy can be represented by a universal curve $\Delta E_D = f(k)$. Figure 5.7 provides an example of such a curve for an oblate spheroid. For the sake of simplicity, the shape anisotropy energy is normalized with respect to $1/2\,\mu_0 M_s^2$. The data in Figure 5.7 show that $\Delta E_D$ deviates from unity only for structures where $L$ and $t$ are comparable. For $L \gg t$, $\Delta E_D$ is close to its saturation value.

Ellipsoids and spheroids are idealized bodies, which are not necessarily relevant for experimental studies. Experimentally, non-ellipsoidal shapes such as a square rectangular prism or a right-circular cylinder are of much practical interest. Both of these shapes exhibit axial symmetry, their shape being similarly specified simply by the ratio of the two axes. It is only fair that in each separate treatment of a cylinder or a spheroid the single shape-characterizing parameter has been called the “aspect ratio”. It has been less fair, though still intuitively

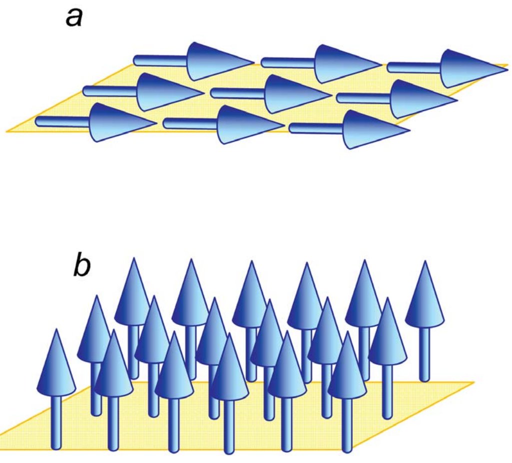

**Fig. 5.6** In-plane (a) and out-of plane (b) isotropic magnetization configurations.

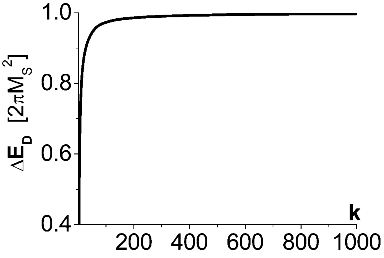

**Fig. 5.7** Analytically calculated magnetostatic energy density (shape anisotropy) $\Delta E_D = (N^{up} - N^{in}) \cdot 1/2\mu_0 M_s^2$ as a function of the dimensional aspect ratio $k = L/t$ for the oblate spheroid in continuum approximation. The demagnetizing energy is normalized with respect to $1/2\mu_0 M_s^2$. $N^{up}$ and $N^{in}$ correspond to the demagnetizing factors of a spheroid magnetized perpendicular to its plane and in-plane, respectively.

appealing, that identical aspect ratios for a cylinder/prism and for a spheroid were taken to imply identical demagnetizing factors for the corresponding distinct shapes. The admitted error in the demagnetization factor due to this switch between shapes has been thought of as small, however.

A particular observation of the inadequacy of the common-sense assumption that "…equal aspect ratios bring about equal demagnetization factors" has been provided by Aharoni [28] where, among other things, it is explicitly stated that the theory of a (square) prism with an aspect ratio of 11 should be compared with that of a prolate spheroid with an aspect ratio of about 6. Recently, the magnetostatic equivalence of non-ellipsoidal bodies to a corresponding uniformly magnetized ellipsoid has been generalized for different shapes [29].

### 5.2.2
### Perpendicular Magnetic Anisotropy

The broken/altered bonds at the top and bottom surfaces of an ultrathin film cause a change in the crystal fields and, hence, the spin-orbit coupling of the atoms at the interface. These interfaces often result in uniaxial anisotropy with perpendicular to the film plane easy axis. In addition, surfaces and interfaces may cause reconstructions and relaxations of the atomic arrangement (see Section 1.1), which may also contribute to the uniaxial anisotropy. Examples of ultrathin systems with perpendicular anisotropy give Fe/Ag(001) [30], Fe/Cu(001) [31, 32] and Co/Au(111) [33, 34].

Whichever the microscopic origin of crystal anisotropy, by following a phenomenological approach one may express the anisotropy energy density as a function of the direction cosines (or sines) of the magnetization component along the anisotropy axis, because the anisotropy energy is invariant under magnetization reversal. In the case of ultrathin films with uniaxial anisotropy, the energy density is

$$K_1 \sin^2\theta + K_2 \sin^4\theta + K_3^1 \sin^6\theta \cos 6\varphi + \ldots \tag{5.5}$$

with $\theta$ and $\varphi$ polar angles with respect to the direction of the anisotropy. The magnitude of anisotropy constants decreases rapidly with increasing order. However, even weak higher-order contributions may change a magnetic ground state of a system if the sign of a higher-order term is different from that of the first-order anisotropy constant $K_1$.

### 5.2.3
### Anisotropy Phase Diagram

Consider a very thin flat film whose easy axis for magnetization **M** is collinear with the normal **n** to the surface. The configuration of magnetization is supposed to be a single domain – that is, all magnetic moments are supposed to be parallel. By defining $\theta$ as the angle between **M** and **n** and assuming that there is no external magnetic field, the complete Hamiltonian can be replaced by the phenomenological expression for the direction-dependent part of the internal-energy density as

$$E_0 = K_1 \sin^2\theta + K_2 \sin^4\theta + \frac{1}{2}\,\mu_0 M^2 \cos^2\theta\,. \tag{5.6}$$

The first two terms involve the first and second anisotropy terms in standard notation, and the last term the demagnetization energy. It proves highly advantageous to redefine the zero of the free energy:

$$E = E_0 - \frac{1}{2}\mu_0 M^2 = K_1^{\text{eff}} \sin^2\theta + K_2 \sin^4\theta\,, \tag{5.7}$$

where now the reference state of zero free energy is the one with $\mathbf{M}||\mathbf{n}$ and

$$K_1^{\text{eff}} \equiv K_1 - \frac{1}{2}\mu_0 M^2 \,. \tag{5.8}$$

Hence, the demagnetizing energy has been absorbed into the expression for the first-order effective uniaxial magnetic anisotropy.

Minimization of the free energy of Eq. (5.7) with respect to $\theta\,(\partial E/\partial\theta = 0$ and $\partial^2 E/\partial^2\,\theta \geq 0)$ reveals the possibility for four different phases which are to be distinguished by the corresponding equilibrium values of $\theta$ [35]:

(i) perpendicular or magnetization up phase $(\theta = 0)$, which is found for $K_1^{\text{eff}} > 0$ and $K_2 \geq -1/2K_1^{\text{eff}}$;
(ii) phase of in-plane magnetization $(\theta = \pi/2)$ for $K_1^{\text{eff}} < 0$ and $K_2 < -1/1/2K_1^{\text{eff}}$;
(iii) phase of canted magnetization $(\theta = \arcsin\sqrt{-K_1^{\text{eff}}/2K_2}$ with $0 \leq -K_1^{\text{eff}}/2K_2 \leq 1)$ for $K_1^{\text{eff}} < 0$ and $K_2 > -1/2K_1^{\text{eff}}$;
(iv) phase of coexisting states $(\theta = 0$ and/or $\theta = \pi/2)$ for $K_1^{\text{eff}} > 0$ and $K_2 < -1/2K_1^{\text{eff}}$.

The anisotropy phase diagram is depicted in Figure 5.8. Typical magnetization configurations for each region are shown as insets. While phases (i), (ii) and

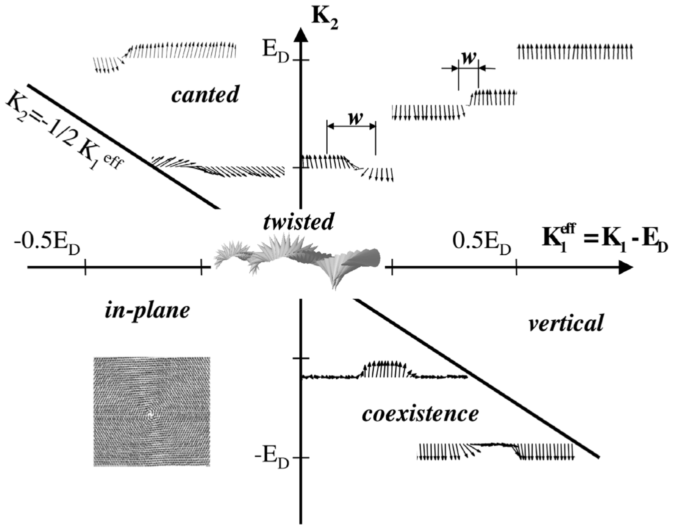

**Fig. 5.8** Possible phases for the free energy of Eq. (5.7). $K_1^{\text{eff}}$ is the difference between the first-order anisotropy and the demagnetizing energy density $\Delta E_D^{\text{film}}$, while $K_2$ is the second-order anisotropy density. The lines $K_2 = -1/2\,K_1^{\text{eff}}$ and $K_1^{\text{eff}} = 0$ separate vertical, canted, in-plane, and coexistence phases (see text). The reorientation transition is characterized by the evolution of magnetic microstructure between vertical and in-plane phases. The insets provide typical magnetic configurations for each region.

(iii) have unique energy minimum, phase (iv) possesses two coexisting energy minima for $\theta = 0$ and $\theta = \pi/2$. The two minima are equally deep for $K_2 = -K_1^{\text{eff}}$ ($K_1^{\text{eff}} > 0$). For $K_2 > -K_1^{\text{eff}}$ the minimum for the out-of-plane magnetization is deeper, whereas for $K_2 < -K_1^{\text{eff}}$ the minimum for the in-plane magnetization prevails.

Typical magnetization configurations for $K_1 \to \infty$ and $K_1 = 0\,(K_1^{\text{eff}} < 0)$ have been discussed in Chapter 3. These are stripe domains in the regime of vertical magnetization, and planar vortex configuration/single domain (depending on boundary conditions) in the regime of in-plane magnetization, as shown schematically in Figure 5.8. In real magnetic systems, $K_1^{\text{eff}}$ and $K_2$ are thickness- and temperature-dependent. Often, the regime of large $K_1^{\text{eff}}$ corresponds to very thin films, and in-plane phase with $K_1^{\text{eff}} < 0$ to thick samples. At intermediate thicknesses $K_1$ becomes comparable to $1/2\mu_0 M_s^2$, i.e., $K_1^{\text{eff}}$ close to zero and the reorientation from the vertical to the in-plane magnetization occurs. This phenomenon is known as the spin reorientation transition (SRT). Inverse SRT is also known [36], but its description is beyond the scope of this section.

### 5.2.4
### Magnetic Structure of the Spin Reorientation Transition

During the past decade, investigations of the spin reorientation in ultrathin films has emerged as an exciting field in basic research. Experimentally, the studies have revealed that the magnetic microstructure at the spin reorientation determines details of the switching of magnetization and thus the macroscopic behavior of the ferromagnet [31, 37–40]. The most complete analysis of magnetic structuring in the SRT-regime has been carried out in an analytical study [41] and in Monte-Carlo simulations [42–45]. A general, spatially resolved, description of magnetization reorientation, based on the framework of competing dipolar and anisotropy energies for a given exchange coupling, will be reviewed in the following section.

#### 5.2.4.1 Regimes of Vertical and Planar Magnetization

In the region of “vertical” magnetization (see Fig. 5.8), for positive $K_1^{\text{eff}}$ and $K_2 > -1/2K_1^{\text{eff}}$ the following microstructure has been found. For dominating $K_1^{\text{eff}}$, mesoscopic or even macroscopic domains with vertical magnetization appear. With $K_1^{\text{eff}}$ decreasing – that is, in the interval $0.2\Delta E_D^{\text{film}} < K_1^{\text{eff}} < 0.5\Delta E_E^{\text{film}}$ – an increasing number of vertically magnetized domains appear and become smaller with decreasing $K_1^{\text{eff}}$. Simultaneously, the domain walls become broader. The domain sizes are in the range from 200 to 400 nm, and the domain walls of the order of 30–40 nm. Domains of that size have been observed experimentally close to the reorientation transition in annealed Co/Au(111) films [38]. In accordance with experiments [33, 38], these domains form neither stripe nor checkerboard pattern but have intermediate arbitrary shape.

If $K_2$ is large, the domain size and domain wall width are mainly determined by $K_2$. The trend is that the stronger the second-order anisotropy, the narrower are the domain walls and the larger the domains. In the close vicinity of $K_1^{\text{eff}} \approx 0$ with non-vanishing $K_2$ the wall width is finite, in contrast to the infinite sinus-like profile of magnetization in the first-order anisotropy approximation (i.e., for $K_2 = 0$) [41, 42, 44]. This means that $K_2$ substitutes for $K_1^{\text{eff}}$ in the definitions of the wall width and energy.

For negative $K_1^{\text{eff}}$ and $K_2 > -1/2K_1^{\text{eff}}$ the "*in-plane*" region in Figure 5.8, the vertical magnetization vanishes and a complete in-plane orientation of the magnetic moments exists. In order to minimize the magnetostatic energy, vortex structures form as the magnetic anisotropy in the film plane is set to zero. In the "in-plane" region, $K_2$ has only a minor influence on the microstructure compared to the former situation with $K_1^{\text{eff}} > 0$.

#### 5.2.4.2 **SRT via the Twisted Phase**

The magnetic structure of SRT via the origin of the anisotropy space is especially interesting, as a non-continuous magnetization change has been postulated in theoretical studies [46–48]. The evolution of magnetic microstructures was not studied in these numerical investigations.

The detailed study of magnetization patterns [44] revealed that, for $K_1^{\text{eff}} = 0$ and $K_2^{\text{eff}} = 0$, the microstructure consists of moments of spatially varying orientation. The arrangement of the magnetic moments is illustrated in Figure 5.9. The magnetization rotates in a helicoidal form along all three principal axes, and the structure formed has been called the "twisted phase" [44]. At this particular point the magnetic moments are evenly oriented in all directions, which is characteristic of the twisted configuration [44, 45]. This yields $\langle S_z^2 \rangle = \langle S_y^2 \rangle = \langle S_x^2 \rangle = 1/3$ in an infinite sample.

The evolution of magnetization along the *x*-axis of the anisotropy space (i.e., for $K_2 = 0$) is presented in Figure 5.10. Here, the averaged values of the vertical component $S_z$ and the squared value $S_z^2$ of the magnetic moment are plotted versus *f*, with $f = E_A/\Delta E_D^{\text{film}}$ as the ratio of perpendicular anisotropy energy $E_A$ to the demagnetizing energy $\Delta E_D^{\text{film}}$. Usually, the MC results are plotted as a function of $K_1/D$. As the behavior of the magnetic sample is governed by the total energy, normalized energies have been found to be more convenient. $S_z$ and $S_z^2$ have been obtained from simulations. While $S_z^2$ is proportional to the total amount of the structure with out-of-plane magnetization orientation, $S_z$ reveals information about the occupation of the two vertical states of magnetization.

These results show that in region C, which corresponds to the reorientation, both $S_z$ and order parameter $S_z^2$ approach zero continuously. The energy of the twisted phase has been compared with energies of different in-plane and out-of-plane configurations, such as stripe or checkerboard domains. At that particular area of the phase diagram the twisted configuration remains the one with the lowest energy among all considered microstructures [44]. Hence, the twisted state represents the minimum of free energy; the configuration is very stable

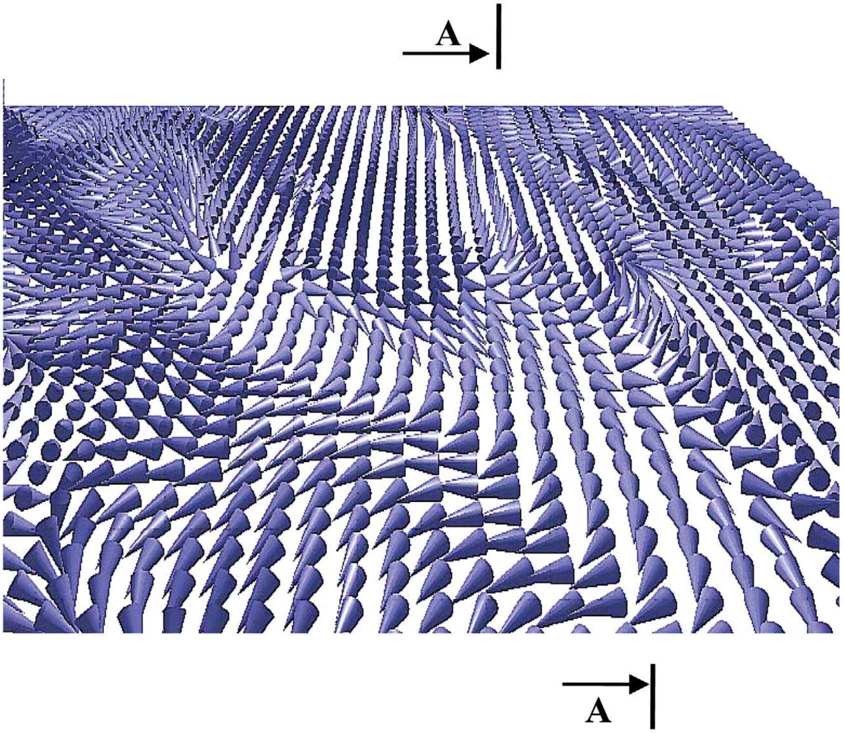

**Fig. 5.9** Twisted spin structure for $K_1^{\text{eff}} = K_2 = 0$. Upper: Perspective view of an enlarged part of the sample. For clarity, only one row out of two and one moment out of two in the row are drawn as cones. Lower: Side-view of the cross-section A–A. The sample size is of order of 500 nm for anisotropy parameters of Co/Au(111), $T \approx 5\,K$.

and allows for a continuous phase transition from the regime of vertical magnetization to the in-plane state.

#### 5.2.4.3 **SRT via the State of Canted Magnetization**

In the region between $K_1^{\text{eff}} < 0$ and $K_2 > -1/2K_1^{\text{eff}}$ (Fig. 5.8), the negative $K_1^{\text{eff}}$ competes with the positive $K_2$. The energy minimization requires a canting of the magnetization to the film normal [35, 45, 49]. The canting angle depends on the balance between $K_1^{\text{eff}}$ and $K_2$. In fact, a canting of magnetic moments has been found in the simulation. The vertical component of magnetization changes continuously from unity at $K_1^{\text{eff}} = 0$ to zero at $K_2 \approx -1/2K_1^{\text{eff}}$. In the literature, this phase is often referred to as the “cone state” as it is generally assumed that the canted magnetic moments are distributed uniformly on a perimeter of the base of a cone. However, the Monte-Carlo simulations [45] provide

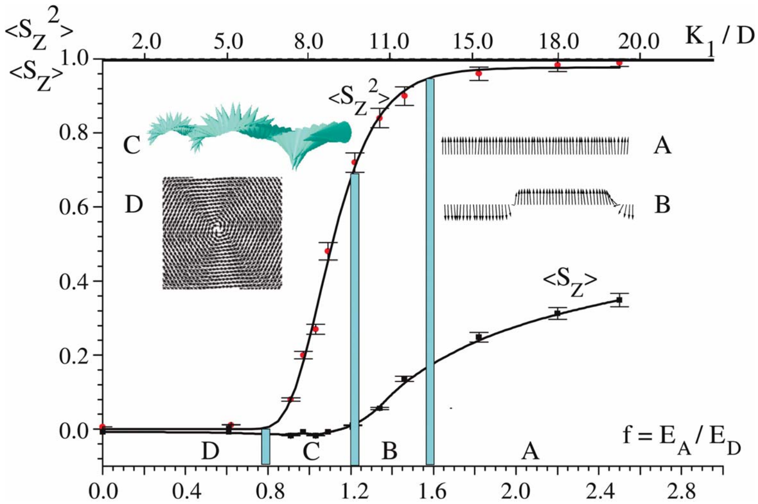

**Fig. 5.10** Plot of $S_z^2$ and $S_z$ versus $f$. $S_z$ is the perpendicular component of magnetization and $f = E_A/\Delta E_D^{\text{film}}$ is the ratio of anisotropy energy to demagnetizing energy. The shaded areas separate the low-temperature phases (A, B, C, D). The phases are characterized by the different microstructures, which are shown as insets in the diagram.

evidence that the canted magnetic moments form domains with in-plane components oriented along the principal directions in the lattice plane, although the in-plane anisotropy was set to zero. This is at variance with the experiment in [50], where no preferred direction of the in-plane components was found. Later experimental investigations confirmed the Monte-Carlo results for ultrathin Fe-Co [40] and Ni(001) [51] films.

The principal axes of the lattice become the in-plane easy axes of magnetization due to the dipolar interaction. It may be concluded that, in the canted phase, the ferromagnetic system is already affected by negligibly small in-plane anisotropies. The in-plane anisotropy causes the appearance of domains with magnetization components along distinct in-plane directions. A top view of the domain structure in the canted regime is presented in Figure 5.11. In Figure 5.11 a different shades of gray represent different orientations of the magnetic moments in the film plane. In Figure 5.11 b the different shades of gray indicate the up- and down-components of the magnetization. The frequency distribution of the in-plane component of magnetization in the down-canted domains is given in Figure 5.11 c. This demonstrates that two main in-plane orientations of the magnetization (ca. 240° and 120° with respect to the $x$-axis) appear. For the vertical component the frequency histogram (Fig. 5.11 d) reveals that the angle to the film normal is identical for all moments in the domains. The angle is equal to the value one obtains from the analytical treatment in case of

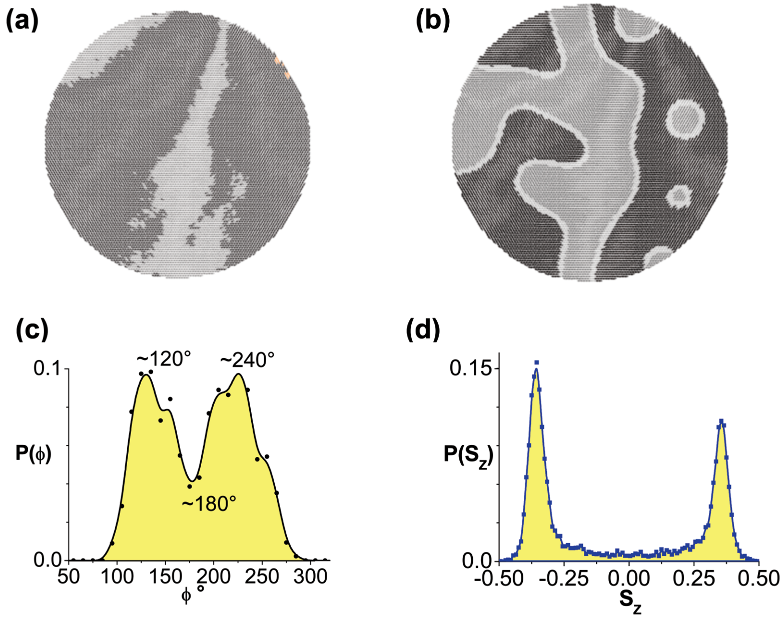

**Fig. 5.11** Top view of the magnetic microstructure in the canted phase for, $K_1^{\mathrm{eff}} = -0.4\,\Delta E_D^{\mathrm{film}}$, $K_2 = -0.65\,\Delta E_D^{\mathrm{film}}$, and $kT/J = 0.05$. (a) Top view of the magnetic structure. In this image the in-plane component of magnetization is coded in gray. The light-gray color indicates the part of the sample with an in-plane component, pointing mainly to left or right in the plane of drawing (azimuthal orientation of 0° or 180°). The dark-gray color indicates the regions having the in-plane components of magnetization at the angle of 60° or 240° to the horizontal within the plane of drawing. (**b**) Out-of-plane components of magnetization in the same sample. Dark- and light-gray arrows represent canted-down and canted-up domains, respectively. (c) The frequency distribution of the in-plane component of magnetization. The abscissa gives the angle of the magnetization to the horizontal within the plane of drawing. (d) The frequency distribution of the out-of-plane component of the magnetization. The abscissa gives the component of the magnetization along the normal.

$0 \leq -K_1^{\mathrm{eff}}/2K_2 \leq 1$, i.e., $\theta = \arcsin\sqrt{-K_1^{\mathrm{eff}}/2K_2}$ (see Section 5.1.3). The small amount of deviating orientations is found in the domain walls.

A three-dimensional representation of the magnetic moments is given in Figure 5.12, where the canted-up and canted-down domains are clearly distinguishable. The domain size increases with increasing $K_2$ for a given $K_1^{\mathrm{eff}}$. The width of the domain walls depends on both $K_1^{\mathrm{eff}}$ and $K_2$. The walls become broader as the ratio $K_1^{\mathrm{eff}}/K_2$ approaches –1/2. The broadening of domain walls causes a slower rotation of magnetization within the wall. As the canting angle is also increasing with $K_1^{\mathrm{eff}}/K_2$ approaching –1/2, the walls fade away and the domains and walls become indistinguishable one from another. The latter process transforms the structure into a planar vortex, which is the charge-free magnetization pattern. Hence, a continuous reorientation transition through the phase of

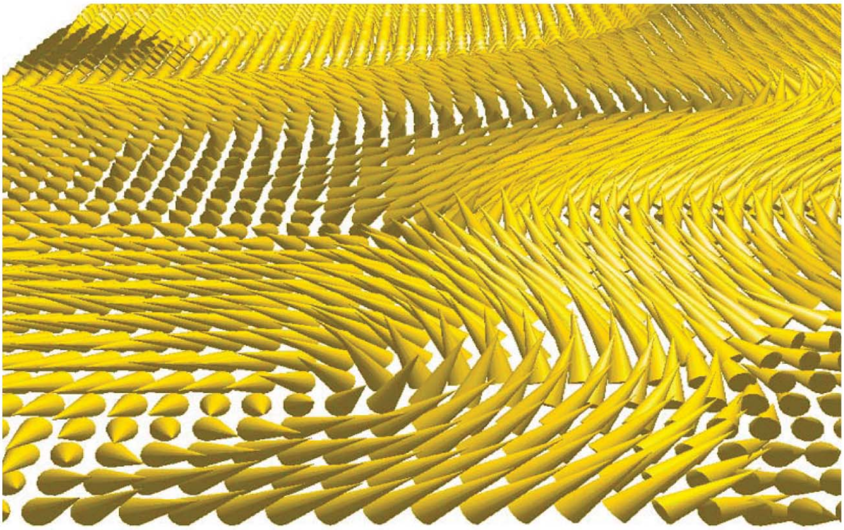

**Fig. 5.12** Perspective view of the canted spin structure for $K_1^{\mathrm{eff}} = -0.4\,\Delta E_D^{\mathrm{film}}$, $K_2 = -0.65\,\Delta E_D^{\mathrm{film}}$, and $kT/J = 0.05$. For clarity, only one row out of two and one moment out of two in the row are drawn as cones.

canted domains occurs. In this region $K_2$ has a strong influence on the microstructure of magnetization.

### 5.2.4.4 SRT via the State of Coexisting Phases

The third possible path for the reorientation of magnetization proceeds via the fourth quadrant of the anisotropy space ($K_1^{\mathrm{eff}} > 0$ and $K_2 < -1/2K_1^{\mathrm{eff}}$). In this region (Fig. 5.8), the average vertical component of magnetization passes gradually from almost unity above $K_2 = -1/2K_1^{\mathrm{eff}}$ to zero at $K_1^{\mathrm{eff}} = 0$. This continuous change of the magnetization component can lead to the erroneous conclusion that reorientation proceeds via the canting of magnetization. The canting phase, however, does not exist in this part of the anisotropy space. In the simulation [45], a magnetic microstructure consists of domains magnetized vertically and in plane – that is, a coexistence of the two phases (see histogram, Fig. 5.13 b). Hence, the very existence of two local minima in the free energy (Fig. 5.8) leads to the appearance of domains with vertical and in-plane orientations of the magnetization.

The existence of domains and the continuous change of magnetization at finite temperatures implies that the magnetic transition is continuous. These results rule out the models discussed in literature for $T = 0$ K – that is, the “perfect delay” and the “Maxwell” convention. Initially, in both models the magnetization occupies the state of the lowest minimum. In the “perfect delay” model the magnetization is believed to stay in that state until the corresponding minimum of the free energy is completely erased. The second model assumes that the orientation of the magnetization is always determined by the lowest-lying energy minimum. A sudden flop appears at the point where both minima have equal depth. Both models have been developed for zero temperature. In the common discussion of discontinuous transition neither the finite temperature nor any microstructure has been taken into account. Thus, in the region of coexisting phases, magnetic structure and entropy each have a major impact on the thermodynamic behavior of the magnetic system.

A typical microstructure of the state of coexistence phases and frequency distribution of the vertical component of magnetization for that state are presented in Figure 5.13. The histogram (Fig. 5.13 b) shows that the majority of magnetic moments build an angle of either 0 or $\pi/2$ with the film normal – that is, both vertical and in-plane magnetized domains are formed. The domain walls cause a small amount of moments with deviating orientations. The depths of the local minima of free energy depend on the values of $K_1^{\mathrm{eff}}$ and $K_2$. In the simulations, an increase/decrease of the in-plane/vertical domains size with decreasing $K_1^{\mathrm{eff}}$ has been found, which means that the frequencies of population of the two phases of magnetization depend on the ratio $K_1^{\mathrm{eff}}/K_2$. A top view of the microstructures of the state of coexisting phases is presented in Figure 5.14; here, Figure 5.14 a represents the situation where the vertical magnetization is favored, which leads to a preponderance of vertically magnetized domains. At first glance the in-plane domains could be misleadingly interpreted as walls, but the magnetization profile deviates completely from that of a domain wall. Whilst in the wall a continuous tilting of the magnetization is expected, all spins lie in the film plane except for a thin region – that is, a wall along the domain con-

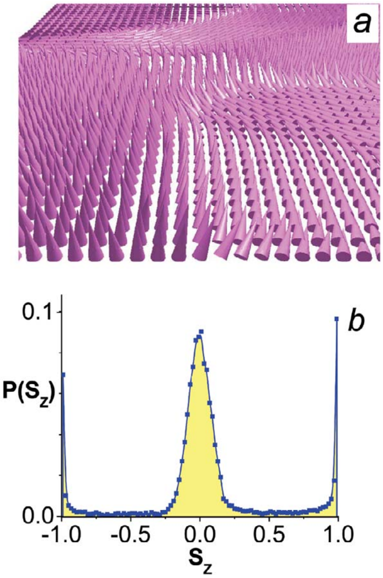

**Fig. 5.13** (**a**) Perspective view of the state of coexisting phases for $K_1^{\mathrm{eff}} = \Delta E_D^{\mathrm{film}}$, $K_2 = -0.8\,\Delta E_D^{\mathrm{film}}$, and $kT/J = 0.05$. For clarity, only one row out of two and one moment out of two in the row are drawn as cones. (b) Frequency distribution of the magnetization orientation. The population frequency is given as a function of the magnetization component along the normal. The plot is generated from the simulation shown in (a).

tours. If the in-plane orientation is more favorable (deeper minimum), an in-plane vortex-like structure appears (Fig. 5.14 b). The vortex-structure is a consequence of the minimization of the magnetostatic energy, as no in-plane anisotropy is assumed. The vertical domains remain in the core of the vortices and at the sample edges. Again, a continuous transition between adjacent phases is achieved via the microstructure.

Exploration of the population of different states of the coexisting phases as a function of time and size of the sample leads to the following results. The relative population of the in-plane and vertical magnetization persists for every relaxation process for a given geometry. The spatial arrangement of the vertical and in-plane domains, however, can change with time. The multidomain state of the coexisting phase transforms into a single domain state when the sample size is smaller than the typical domain size for a given $K_1^{\mathrm{eff}}/K_2$. In that situation, the ratio of $K_1^{\mathrm{eff}}/K_2$ defines the probability of finding the sample in a vertical or an in-plane single-domain state. Domains with an in-plane magnetization do not show a vortex structure in small samples. The monodomain configuration is energetically preferred, as the gain in dipolar energy is less than the loss in exchange energy for small structures.

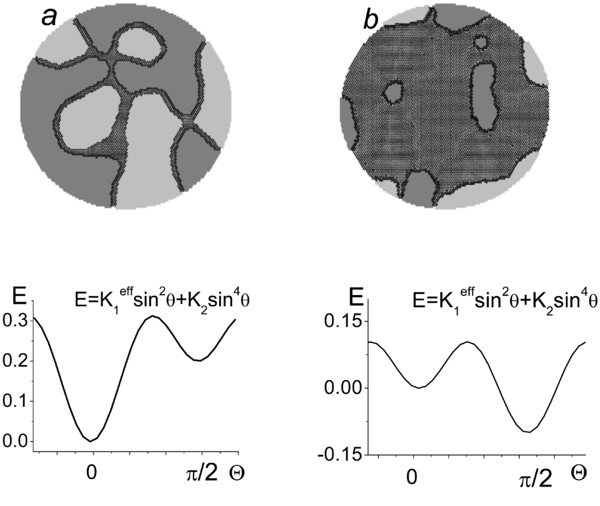

**Fig. 5.14** Top view of the microstructure of the state of coexisting phases and corresponding energetic potential. Dark- and light-gray areas represent spin-up and -down domains, respectively. Black areas show the in-plane domains, $kT/J = 0.05$. In (a) the situation of a deeper minimum for the vertical phase ($K_2 = -0.8\Delta E_D^{\mathrm{film}}$) is shown. The region between the vertical domains are in-plane magnetized domains. (b) The microstructure for the situation that the energy minimum for the in-plane phase is deeper ($K_2 = -1.1\Delta E_D^{\mathrm{film}}$). Note that the vertical domains remain at the edges and in the center of domains with "rotating" in-plane magnetization. These will shrink to the center of vortices found in the in-plane phase.

The borderlines of the phase of coexisting domains in the calculations are in good agreement with the experimentally defined borders of the “gray” zone of SRT in Co/Au(111) [38]. In this zone the contrast has been lost, and one possible explanation is the presence of coexisting domains. The first experimental manifestation of coexisting domains in Co/Au(111)/W(110) [52] and Fe/Cu/Si(111) [53] was published recently.

## 5.3
## Magnetic Nanoplatelets

The SRT may be driven not only by thickness or temperature but also by the size of a sample. The size-driven SRT may appear either due to size-dependence of the anisotropy or to size-dependence of the magnetostatic energy. Both phenomena arise only in very thin films where the discrete nature of matter plays an important role.

### 5.3.1
### Size-Dependence of Shape Anisotropy in Discrete Atomic Approximation

As stated in Section 5.1.1, the shape anisotropy $\Delta E_D^{\text{film}}$ in continuum approximation does not depend on size but rather on the dimensional ratio $k = L/t$. $\Delta E_D^{\text{film}}$ deviates from unity only for structures where the lateral size $L$ and the thickness $t$ are comparable. It has been proposed that, when the film thickness is reduced to a few atomic layers, the system must be treated as a collection of discrete magnetic dipoles, which are arranged on a crystalline lattice [54, 55]. Calculations of shape anisotropy have been performed for an *infinite* number of ultrathin films, and a deviation from the continuum magnetization model was found for films thinner than 16 Å. The consideration of a discrete magnetization yielded reduced stray field energy for perpendicular magnetization of ultrathin films as compared to thick films, and the magnitude of deviation was found to depend on the lattice type [54].

Recently, a study of shape anisotropy of structures with *limited lateral size* has been performed numerically [56]. The platelets were discs of finite diameter $L$ and thickness $t$ on a discrete lattice. Diameter-to-thickness ratios $k = L/t$, ranging from 40 to 1000 with the thickness ranging from one to six monolayers, as well as different crystal arrangements – sc(100), bcc(110), bcc(100), fcc(111), fcc(100), hcp(0001) – were considered. The shape anisotropy (dipolar magnetic anisotropy energy) was calculated as the difference between the dipolar energy of the vertical and in-plane single-domain states: $\Delta\tilde{E}_D = E_D^{\text{up}} - E_D^{\text{in}}$. The results of the calculations for a triangular lattice with *hcp* stacking are shown in Figure 5.15 as a function of $k$ for one- to four-monolayer-thick films. The calculated energies were normalized with respect to $\Delta E_D^{\text{film}} = 1/2\mu_0 M_s^2$. Of note, similar results were obtained for other lattices.

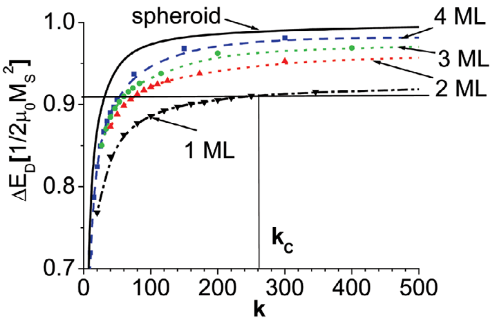

**Fig. 5.15** Numerically calculated demagnetizing energy density $\Delta\tilde{E}_D$ as a function of the dimensional aspect ratio $k = L/d$ for one- to four-monolayer films on a triangular lattice with *hcp* stacking. $\Delta\tilde{E}_D$ is normalized with respect to the demagnetizing energy in the continuum limit $\mu_0 M_s^2/2$. The straight horizontal line corresponds to the perpendicular magneto-crystalline anisotropy $E_A$; the dashed vertical lines denote the critical size $k_c$ of the reorientation.

The exact calculation of the dipolar sums deviates strongly from the magnetostatic energy obtained from the continuum Ansatz (Fig. 5.15). Instead of a unique $\Delta E_D(L, t)$ function, different curves have been obtained for different sample thickness. Thus, the shape anisotropy of discs with diameters of several hundred lattice constants and a few atomic layers thickness (nanoplatelets), depends on both size $L$ and thickness $t$ rather than simply the ratio of the two parameters. For example, $\Delta\tilde{E}_D(L, t)$ of the platelet 100×1 on a *hcp* lattice is 1.2-fold smaller than that of the platelet 300×3, although $k = 100$ is the same for both objects. A remarkable result of these calculations was that the size effect already came into play for rather large monolayer platelets of a few hundred atoms in diameter, and not only for situations where $L/t = 1$. For $t > 5$ monolayers, $\Delta\tilde{E}_D(k, t)$ merges into $\Delta E_D = f(k)$. In all of these cases, the limit of infinite lateral dimensions was studied and the results of previous studies [54, 55, 57] have been retrieved.

In the next step, the rather individual curves, corresponding to different thicknesses at “fixed” lattice structure, were normalized against the value for the dipolar magnetic anisotropy energy of the laterally infinite sample $\Delta E_D^{\text{film}}$. It was then established that all these individual curves collapsed to a single (and thus universal) curve, the precise appearance of which depended only on the ratio $k$ of the cylindrical island. This universal curve for the rescaled dipolar magnetic anisotropy energy was compared to that for the dipolar magnetic anisotropy of an ellipsoid of revolution [56] and the disc [58], with the same aspect ratio in the continuum micromagnetic approximation. Deviations were established and the conclusion drawn that the dipolar sum could be separated into two contributions related to thickness and to geometry. The geometry-dependent demagnetizing factors found by means of discrete summation were identical to those found by continuum approximation. It was pointed out that a combination of these two effects in nanoplatelets might be especially dramatic for ultrathin systems with a SRT.

### 5.3.2
### Multiplicative Separation of Discrete and Continuum Contributions

In order to check numerical results related to the separation of total demagnetizing energy in discrete and continuum contribution, analytical formulae were derived for the demagnetizing factors of circular cylinders [58]. New closed-form analytic expressions for the demagnetization factors of the right-circular cylinder in the continuum limit of micromagnetism have been obtained. From this, the dipolar magnetic anisotropy energy density (shape anisotropy) which depended solely on cylinder shape (as specified by the geometric ratio $k$), was obtained in straightforward manner. It was found that, with very high accuracy and in agreement with the numerical results:

$$\frac{\Delta\tilde{E}_D\,(\text{discrete})}{X\,(\text{lattice},t)} = \Delta E_D\,(\text{continuum}) \cdot N(k)\,. \tag{5.9}$$

The function $N(k)$ is a universal function of the geometry ratio or, in other words, conventional demagnetizing factor. Currently, it has been proven that the following form holds for the discrete mesoscopic system:

$$\Delta\tilde{E}_D\,(k,t) = X\,(\text{lattice},t) \cdot N(k) \cdot \frac{\mu_0 M_s^2}{2}\,. \tag{5.10}$$

Altogether, it has been shown that the exact finite summation of dipolar sums for an essentially discrete dipole lattice (as encountered experimentally for ultrathin ferromagnetic platelets) leads to a clear delineation of the validity of the micromagnetic continuum ansatz, and the quantitative manner in which the discreteness of the lattice bears on the final value of magnetic anisotropy energy density. Indeed, for many lattices the magnetic anisotropy energy density is reduced compared to the continuum limit.

### 5.3.3
### Size-Dependent Spin Reorientation Transition

Generally, magnetic anisotropy is both size- and temperature dependent. Some aspects of the role of temperature dependency for the size-dependent SRT have been studied in [59]. Here, for the sake of simplicity, the description will be limited to a more simple case where magnetic anisotropy is constant for a given thickness. In such a case the anisotropy energy $E_A$ can be represented by a straight line in Figure 5.15. The intersection of $\Delta\tilde{E}_D(k,t)$ and $E_A$ gives a critical length $L_c = k_c \cdot t$ where the magnetization orientation switches (i.e., reorientation) appears. As the shape anisotropy in ellipsoid approximation deviates from unity only at $k \approx 1$, the reorientation can only occur at $L \approx t$ (Fig. 5.15). Thus, it is commonly assumed that the orientation of magnetization in structures with $L \gg t$ depends only on the thickness and the temperature of the sample. However, the shape anisotropy of nanoplatelets, according to these investigations, is reduced for certain lattice symmetries. The reduction of $\Delta\tilde{E}_D(k,t)$ should lead to an enhancement of the effective perpendicular anisotropy $E_A^{\text{eff}} = E_A - \Delta\tilde{E}_D(k,t)$ with shrinking size and, hence, to an increase in $L_c$. For a certain range of $E_A$ the critical size $L_c$ of the reorientation can be very large compared to the film thickness.

Monte-Carlo simulations have been performed to check how the discreteness of the lattice reflects in the orientation of the magnetization [59]. In an extension of the earlier investigations, non-collinear spin states due to thermal disorder have been considered, and the temperature-driven magnetic reorientation discussed in view of the different temperature-dependences of dipolar and magnetic anisotropy energies. The Hamiltonian of the problem included exchange, dipolar interactions and perpendicular anisotropy of the first order. For the chosen strength of dipolar interaction and sample size ($L \leq 350a$ with $a$ as lattice parameter), a single-domain magnetization configuration in samples is expected. In that case the exchange energy for in-plane and out-of-plane configurations is identical, and the magnetization orientation is fully described by the competition between $\Delta\tilde{E}_D$ and $E_A$.

In simulations, the lateral size of the platelets has been chosen to be much larger than the thickness ($L > 100\,t$). A wide range of total anisotropy energy has been explored, but here the case where $E_A$ is slightly smaller than $\Delta E_D^{\text{film}}$ (i.e., $E_A \geq 0.9 \cdot \mu_0 M_s/2$), is described. In the continuum approximation the selected sizes and anisotropy allow any shape effects to become effective at $L_c \approx 20t$. Hence, in all calculated structures with $L > 100t$ an in-plane magnetization configuration should be expected. In contrast to the predictions made in the framework of the continuum theory, a vertical monodomain state in the case of objects with $L < 230t$ on a triangular lattice is found (Fig. 5.16, left). In the case of $L > 300t$, an in-plane configuration of magnetization exists (Fig. 5.16, right). For $230t < L < 300t$, structures with intermediate values of vertical component of magnetization have been revealed. Detailed studies of magnetic structuring in this regime have been reported in [60, 61]. Depending on the sample size and shape, either leaf or vortex magnetization patterns have been found, though for the square lattice the results were completely different. For all structures with $L > 100t$ an in-plane single domain in accordance with the continuum approximation has been found.

Hence, by comparison with the triangular lattice it can be seen that the critical size for reorientation depends on the type of crystalline lattice. According to [56], the shape anisotropy of a triangular lattice with *hcp* or *fcc* stacking is strongly reduced, while $\Delta\tilde{E}_D(k,t)$ of a square lattice with simple cubic stacking is almost equal to that of the continuum. Thus, in contrast to the analytical assumption and in accordance with predictions [56, 58], the critical size of reorientation depends on the type of crystalline lattice, and in some cases takes place far beyond the $k$-range deduced from the continuum approximation. Another important conclusion is that the magnetization direction can change by shrinking the lateral size, without changing parameters such as thickness or temperature.

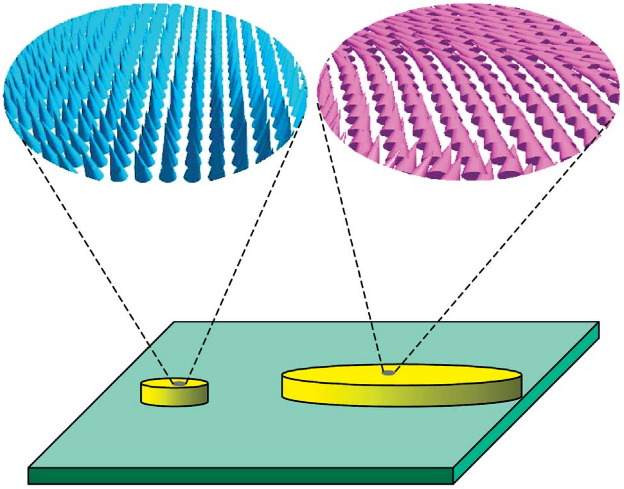

**Fig. 5.16** The low-temperature magnetic microstructure of two discs on a triangular lattice with $L_1 = 100a$ and $L_1 = 330a$; $E_A \approx 0.9 \cdot \mu_0 M_s/2$. The exchange, the anisotropy, the dipolar energy constants and the temperature are identical for both samples. For the sake of an appropriate representation, a perspective view of an enlarged part of each sample is shown. For clarity, only one spin row out of two is drawn as cones. The smaller island has a vertical single-domain structure. The larger structure presents an in-plane single-domain magnetization configuration.

For $E_A \approx 1/2\mu_0 M_s^2$ the magnetization of a nanoplatelet on a triangular lattice will be always out-of-plane, as the maximal possible shape anisotropy of a sample is smaller $\Delta\tilde{E}_D(L \to \infty) \approx 0.91 \cdot \mu_0 M_s/2$. The effective perpendicular anisotropy of a triangular lattice, however, will increase due to the shape and the lattice dependence of $\Delta\tilde{E}_D(k, t)$. The first experimental findings pointing in this direction have been published recently [62].

### 5.3.4
### Size-Dependence of Crystallographic Anisotropy

Previously, perpendicular magnetocrystalline anisotropy has been treated as a local, size-independent property, but recent studies have shown this not always to be correct. For example, the uniaxial perpendicular anisotropy of Co nanostructures on Pt(111) surface is mainly caused by edge atoms having times stronger anisotropy energy than their bulk and surface counterparts [63]. The number of perimeter atoms depends on the size of a particle; hence, the average anisotropy energy per atom and total anisotropy energy per particle of this system are size-dependent. The size-dependence of anisotropy energy is especially important in very small islands consisting only of several tens of atoms. With increasing size, the contribution of the edge atoms to the total anisotropy becomes less important and can be regarded as size-independent. Even today, the influence of size-dependent anisotropy on spin reorientation transition has not yet been studied in detail.

## 5.4
## Summary

Two anisotropic systems – namely, liquid crystals and nanomagnets – have been discussed in this chapter, and in both cases the competition between anisotropies and interparticle interaction was shown to lead to a variety of patterns and different types of reorientation transition. It has been shown that magnetocrystalline anisotropy and shape anisotropy in nanomagnets may be size-dependent, with both effects leading to a shift in reorientation transition to larger sizes for identical thickness. The identification of the role of perimeter atoms and lattice discreteness for the spin reorientation should open new opportunities for material engineering.

## 5.5
## Exercises

1. Construct a disclination of strength $s=3/2$.

*Solution*
See Fig. 5.17.

2. Consider an ensemble of ferromagnetic nanoparticles with uniaxial anisotropy along $z$-axis and without interparticle interactions. The Hamiltonian of such a system reads $H = K\sum_{i=1}^{n}\cos^2\theta_i$, where $K$ is the anisotropy energy per particle and $\theta_i$ is an angle between the $z$ axis and $i$-th particle. The degree of anisotropy in the whole system can be quantified by the so-called nematic order parameter $\sigma = 3/2\langle\cos^2\theta\rangle - 1/2$. Find $\sigma(K)$.

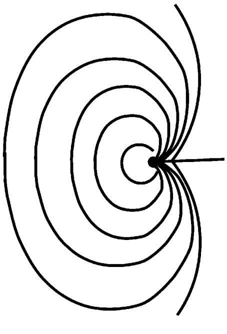

**Fig. 5.17** One possible disclination of strength $s=3/2$.

*Solution*

$$\langle \cos^2\theta \rangle = \frac{\int \cos^2\theta \exp\left(\beta K \cos^2\theta\right) d\Omega}{\int \exp\left(\beta K \cos^2\theta\right) d\Omega},$$

where $\beta$ is the Boltzmann factor and $\Omega$ the volume element. Using $\cos\theta = x$ one can rewrite

$$\langle \cos^2\theta \rangle \approx \frac{\int\limits_{-1}^{1} (1+\beta K x^2) x^2 dx}{\int\limits_{-1}^{1} (1+\beta K x^2) dx} = \frac{1/3 + \beta K/5}{1+\beta K/3} = \frac{5+3\beta K}{15+5\beta K}\,.$$

Hence,

$$\sigma = \frac{3}{2}\langle \cos^2\theta \rangle - \frac{1}{2} = \frac{3}{2}\frac{5+3\beta K}{15+5\beta K} - \frac{1}{2} = \frac{2\beta K}{15+5\beta K} \approx \frac{2}{15}\beta K \quad \text{for } K \ll 1/\beta\,.$$

3. Imagine a liquid crystalline or magnetic two-dimensional system with alternating regions of "vertical" and "horizontal" anisotropy. If the length of these regions is large $L > L_{critical}$, the formation of domains with corresponding orientation of constituents arises. In nanosystems with $L < L_{critical}$ instead of coexistence of domains a non-uniform orientation of mesogens (magnetic moments) with mean angle $\theta_0$ is possible. Determine $\theta_0$ as a function of first-order anisotropies $K_1^1$ and $K_1^2$, supposing that there exists an exchange or Maier–Saupe like angular-independent interaction holding the constituents parallel one to another.

*Solution*

In domains with out-of-plane anisotropy the director rotates in the direction towards the normal by amount $\Delta\theta_1/2$. In the domain with in-plane anisotropy it rotates in the opposite direction by $\Delta\theta_2/2$. In general, these angles are different because the effective anisotropies are not equal. The angular dependence of the anisotropy energy can be written as

$$f(\theta_0) = K_1^1 \sin^2\left(\theta_0 - \frac{\Delta\theta_1}{2}\right) + K_1^2 \sin^2\left(\theta_0 + \frac{\Delta\theta_2}{2}\right) \tag{5.11}$$

As the exchange energy increases with the split angle, the splitting should be very small. In the limit of small splitting $\Delta\theta_1, \Delta\theta_2 \approx 0$ Eq. (5.11) becomes

$$f(\theta_0) \approx (K_1^1 + K_1^2)\sin^2\theta_0 + \frac{K_1^1 - K_1^2}{2}\Delta\theta \sin(2\theta_0) \tag{5.12}$$

with $\Delta\theta = \Delta\theta_1/2 + \Delta\theta_2/2$. Equation (5.12) reduces to Eq. (5.11) if $\Delta\theta$ is zero. For $K_1^1 = -K_1^2$, that is, when the two anisotropies are balanced, Eq. (5.12) re-

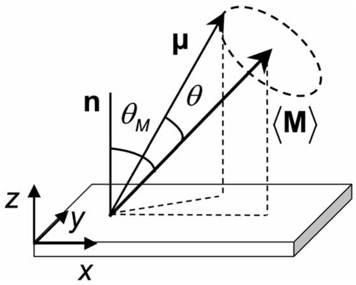

**Fig. 5.18** Illustration of the geometry of the magnetic moment **μ** and the average direction of magnetization ⟨**M**⟩.

duces to $f(\theta_0) \approx -K_1^1 \Delta\theta \sin(2\theta_0)$. This term has a minimum at 45° with respect to the normal with agreement with numerical simulations [64].

4. In the molecular field approximation a magnetic particle is represented by a single magnetic moment $\boldsymbol{\mu}$, which interacts with the average magnetization $\langle \mathbf{M} \rangle$. If the surface normal $\mathbf{n}$ is set along the $z$-axis and the $x$-axis is chosen to be parallel to the in-plane component of $\mathbf{M}$, the average magnetization vector is given by $\mathbf{M} = (\mu/V)(\sin\theta_M, 0, \cos\theta_M)$(see Fig. 5.18), $V$ being the unit-cell volume of the respective lattice. Write spherical coordinates of $\boldsymbol{\mu}$ relative to $\mathbf{n}$ considering that spherical coordinates of $\boldsymbol{\mu}$ relative to $\mathbf{M}$ are $\theta$ and $\varphi$.

*Solution*

$$\boldsymbol{\mu} = \mu \begin{bmatrix} \sin\theta_M \cos\theta + \cos\theta_M \sin\theta \cos\varphi \\ \sin\theta \sin\varphi \\ \cos\theta_M \cos\theta - \sin\theta_M \sin\theta \cos\theta \end{bmatrix}$$

5. Consider a magnetic (or dielectric) specimen of spherical shape with simple cubic arrangement of atoms magnetized by the external field $E_0$ oriented in $z$ direction. (a) Calculate the macroscopic magnetic/electric field inside the sample in continuum approximation (using demagnetizing factors; Section 5.1.1). (b) Calculate the field acting on the atom at the center of the sphere from the discrete dipole approximation (Eq. 3.2). Are the two fields equivalent or not?

*Solution*

(a) The macroscopic field in a sphere is the sum of the external and demagnetizing/depolarization field $\mathbf{E}_1$, which tends to oppose the external applied field in the interior of the system $\mathbf{E} = \mathbf{E_0} + \mathbf{E_1} = \mathbf{E_0} - N_{zz}^{sphere}\,\mathbf{P}$. The trace of the demagnetizing/depolarization tensor is $Tr(N) = N_{xx} + N_{yy} + N_{zz} = 1$ in SI and $4\pi$ in CGS. For a sphere $N_{xx} = N_{yy} = N_{zz} = 1/3$ or $4\pi/3$ correspondingly. Hence, $\mathbf{E} = \mathbf{E_0} - 1/3 \cdot \mathbf{P}$.

(b) If all dipoles are parallel to the $z$-axis and have magnitude $p$, the $z$-component of magnetization at the center of the specimen is

$$\mathbf{E} = \mathbf{E_0} + \mathbf{E}_{dip} = \mathbf{E_0} + \sum_i \frac{3(\mathbf{p} \cdot \mathbf{r}_i)\mathbf{r}_i - \mathbf{r}_i^2 \mathbf{p}}{r_i^5} = \mathbf{E}_0 \, ,$$

i.e., the dipolar sum vanishes. The equality $\mathbf{E}_{dip} = 0$ comes from the fact that in the sum only terms proportional to $y_i x_i$; $z_i x_i$; $z_i y_i$; $x_i^2$; $y_i^2$; $z_i^2$ exist. In the summation, however, these terms vanish because of the symmetry of the lattice and that of the sphere. One finds $\sum_i y_i x_i = \sum_i z_i x_i = \sum_i z_i y_i = 0$ and $\sum_i x_i^2 = \sum_i y_i^2 = \sum_i z_i^2 = 1/3 \sum_i r_i^2$ that leads to $\mathbf{E}_{dip} = 0$.

Thus, the local field is not the same as the macroscopic field. The difference between the two fields may be explained as follows. The field **E** is a macroscopic quantity, i.e., the average being taken over a large number of atoms. The local field is a microscopic field which fluctuates rapidly within the medium. This field is quite large at the atomic sites and small between them.

## References

**1** L.O. Onsager, *Ann. N.Y. Acad. Sci.* **1949**, *51*, 627.

**2** D. Frenkel, *J. Phys. Chem.* **1987**, *91*, 4912.

**3** W. Maier, A.Z. Saupe, *Naturforsch. A* **1958**, *13*, 564.

**4** W. Lehmann, H. Skupin, C. Tolksdorf, E. Gebhard, R. Zentel, P. Krüger, M. Lösche, F. Kremer, *Nature* **2001**, *410*, 447.

**5** S. Chandrasekhar, *Liquid Crystals*, University Press, Cambridge, **1992**.

**6** P.G. de Gennes, J. Prost, *The Physics of Liquid Crystals*, 2nd edition, Clarendon Press, Oxford, **1993**.

**7** J. Vieillard-Baron, *Mol. Phys.* **1974**, *28*, 809.

**8** D. Wei, G.N. Patey, *Phys. Rev. A* **1992**, *46*, 7783.

**9** J.Y. Denham, G.R. Luckhurst, C. Zannoni, J.W. Lewis, *Mol. Cryst. Liq. Cryst.* **1980**, *60*, 185.

**10** G.W. Gray, V. Vill, H.W. Spiess, D. Demus, J.W. Goodby (Eds.) *Physical Properties of Liquid Crystals*, Wiley, Weinheim, **1999**.

**11** F.C. Frank, *Disc. Faraday Soc.* **1958**, *25*, 19.

**12** P.M. Chaikin, T.C. Lubensky, *Principles of Condensed Matter Physics*, Cambridge University Press, Cambridge, **1995**.

**13** R.S. Stein, *Pure Appl. Chem.* **1991**, *63*, 941.

**14** M.V. Kurik, O.D. Lavrentovich, *Sov. Phys. Uspekhi* **1988**, *31*, 196.

**15** V.M. Lisienko, E.V. Zapeckii, E.V. Kononenko, R.I. Mintz, *Extracorporeal Liquid-Crystalline Diagnostic of Cholecystitis*, Ural University, Sverdlovsk, **1989**.

**16** M.J. Stephen, J.P. Straley, *Rev. Mod. Phys.* **1974**, *46*, 617.

**17** S.E. Bedford, A.H. Windle, *J. Chem. Soc. Faraday Trans.* **1993**, *15*, 31.

**18** A. Kilian, S. Hess, *Liquid Crystals* **1990**, *8*, 465.

**19** H.E. Assender, A.H. Windle, *Macromolecules* **1994**, *27*, 3439.

**20** A.H. Windle, H.E. Assender, M.S. Lavine, *Phil. Trans. Royal Soc. London A: Math. Phys. Eng. Sciences* **1994**, *348*, 73.

**21** P.A. Lebwohl, G. Lasher, *Phys. Rev. A* **1972**, *6*, 426.

**22** S.E. Bedford, T.M. Nicholson, A.H. Windle, *Liq. Cryst.* **1991**, *10*, 63.

**23** W.J.M. de Jonge, P.J.H. Bloemen, F.J.A. den Broeder, Experimental investigations of magnetic anisotropy. In: *Ultrathin magnetic structures I*, J.A.C. Bland, B. Heinrich (Eds.), Springer, Berlin, **1994**.

**24** P. Bruno, Physical origins and theoretical models of magnetic anisotropy. In: *Magnetismus von Festkörpern und Grenzflächen*, Forschungszentrum Jülich, Jülich, **1993**.

25 P. Gambardella, A. Dallmeyer, K. Maiti, M. C. Malagoli, W. Eberhardt, K. Kern, C. Carbone, *Nature* **2002**, *416*, 301.

26 J. A. Osborn, *Phys. Rev.* **1945**, *67*, 351.

27 E. C. Stoner, *Philos. Mag.* **1945**, *36*, 803.

28 A. Aharoni, *J. Appl. Phys.* **1998**, *83*, 3432.

29 M. Beleggia, M. De Graef, Y. T. Millev, *J. Phys. D: Appl. Phys.* **2006**, *39*, 891.

30 Z. Q. Qiu, J. Pearson, S. D. Bader, *Phys. Rev. Lett.* **1993**, *70*, 1006.

31 R. Allenspach, A. Bishof, *Phys. Rev. Lett.* **1992**, *69*, 3385.

32 J. Tomassen, F. May, B. Feldmann, M. Wuttig, H. Ibach, *Phys. Rev. Lett.* **1992**, *69*, 3831.

33 R. Allenspach, M. Stampanioni, A. Bischof, *Phys. Rev. Lett.* **1990**, *65*, 3344.

34 C. Chappert, K. Le Dang, P. Beauvillain, H. Hurdequint, D. Renard, *Phys. Rev. B* **1986**, *34*, 3192.

35 Y. Millev, J. Kirschner, *Phys. Rev. B* **1996**, *54*, 4137.

36 B. Schulz, K. Baberschke, *Phys. Rev. B* **1994**, *50*, 13467.

37 D. P. Pappas, K.-P. Kämper, H. Hopster, *Phys. Rev. Lett.* **1990**, *64*, 3179.

38 M. Speckmann, H. P. Oepen, H. Ibach, *Phys. Rev. Lett.* **1995**, *75*, 2035.

39 M. Farle, W. Platow, A. N. Anisimov, B. Schulz, K. Baberschke, *J. Magn. Magn. Mater.* **1997**, *165*, 74.

40 R. Zdyb, E. Bauer, *Phys. Rev. B* **2003**, *67*, 134420.

41 Y. Yafet, E. M. Gyorgy, *Phys. Rev. B* **1988**, *38*, 9145.

42 A. B. MacIsaac, K. De'Bell, J. P. Whitehead, *Phys. Rev. Lett.* **1998**, *80*, 616.

43 A. Hucht, K. D. Usadel, *J. Magn. Magn. Mater.* **1996**, *156*, 423.

44 E. Y. Vedmedenko, H. P. Oepen, A. Ghazali, J.-C. S. Lévy, J. Kirschner, *Phys. Rev. Lett.* **2000**, *84*, 5884.

45 E. Y. Vedmedenko, H. P. Oepen, J. Kirschner, *Phys. Rev. B* **2002**, *66*, 214401.

46 A. Hucht, A. Moschel, K. D. Usadel, *J. Magn. Magn. Mater.* **1995**, *148*, 32.

47 A. Hucht, K. D. Usadel, *J. Magn. Magn. Mater.* **1996**, *156*, 423.

48 A. B. MacIsaac, K. De'Bell, J. P. Whitehead, *Phys. Rev. Lett.* **1998**, *80*, 616.

49 E. Y. Vedmedenko, H. P. Oepen, J. Kirschner *J. Appl. Phys.* **2001**, *89*, 7145.

50 R. Allenspach, *J. Magn. Magn. Mater.* **1994**, *129*, 160.

51 G. Gubbiotti, G. Carlotti, M. G. Pini, P. Politi, A. Rettori, P. Vavassori, M. Ciria, R. C. O'Handley, *Phys. Rev. B* **2002**, *65*, 214420.

52 T. Duden, E. Bauer, in: *Magnetic Ultrathin Films, Multilayers and Surfaces*, J. Tobin, D. Chambliss, D. Kubinski, K. Barmak, P. Dederichs, W. de Jonge, T. Katayama, A. Schuhl (Eds.), MRS Symposia Proceedings No. 475, Materials Research Society, Pittsburgh, **1997**, p. 273.

53 P. Castrucci, R. Gunnella, R. Bernardini, P. Falcioni, M. De Crescenzi, *Phys. Rev. B* **2002**, *65*, 235435.

54 H. J. G. Draaisma, W. J. M. de Jonge, *J. Appl. Phys.* **1988**, *64*, 3610.

55 B. Heinrich, S. T. Purcell, J. R. Dutcher, K. B. Urquhart, J. F. Cochran, A. S. Arrot, *Phys. Rev. B* **1988**, *38*, 12879.

56 E. Y. Vedmedenko, H. P. Oepen, J. Kirschner, *J. Magn. Magn. Mater.* **2003**, *256*, 237.

57 P. J. Jensen, *Ann. Phys.* (Leipzig) **1997**, *6*, 317.

58 Y. Millev, E. Y. Vedmedenko, H. P. Oepen, *J. Phys. D: Appl. Phys.* **2003**, *36*, 2945.

59 E. Y. Vedmedenko, H. P. Oepen, J. Kirschner, *Phys. Rev. B* **2003**, *90*, 12409.

60 A. Maziewski, V. Zablotskii, M. Kisielewski, *Phys. Stat. Sol. C* **2006**, *3*, 9.

61 A. Maziewski, V. Zablotskii, M. Kisielewski, *Phys. Rev. B* **2006**, *73*, 134415.

62 M. Maret, A. Maier, F. Treubel, B. Riedlinger, M. Albrecht, E. Beaurepaire, G. Schatz, *J. Magn. Magn. Mater.* **2002**, *242–245*, 420.

63 S. Rusponi, T. Cren, N, Weiss, M. Epple, P. Buluschek, L. Claude, H. Brune, *Nat. Mater.* **2003**, *2*, 546.

64 F. Porrati, H. P. Oepen, J. Kirschner, *J. Magn. Magn. Mater.* **2004**, *283*, 133.

# 6

# Dynamic Self-Organization

Away from equilibrium, many physical and chemical structures undergo spatial and temporal self-organization. This phenomenon is known by the names of dissipative structures [1], synergetics [2] and self-organization [3], and includes oscillating chemical reactions, convection patterns, bifurcations, electrohydrodynamic instabilities, solidification patterns, flow patterns, propagating interfaces, and spin-wave instabilities. Non-linear dissipative processes can be divided into the three main classes:

- periodic in space and stationary in time;
- uniform in space and periodic in time; and
- periodic in space and oscillatory in time.

In theory, such systems are usually discussed in terms of some appropriate set of non-linear partial differential equations. The quantitative analysis of these non-linear dissipative processes is highly complex, and beyond the scope of this book. However, a detailed review of theoretical models can be found in [4], while a popular introduction is available in [6]. The following sections provide a phenomenological introduction into dynamic patterning in several physical systems from the point of view of competing interactions.

## 6.1

## Diffusion-Limited Aggregation

A perfect crystal is held together mainly by the attractive electrostatic interactions between the negative charges of the electrons and the positive charges of the nuclei. Specialized terms are employed only to categorize distinctive situations: exchange energy (see Chapter 1–3), van der Waals forces (see Chapter 3), resonance stabilization energy or covalent bonds (see. e.g., [5]). At equilibrium, the atoms/molecules of a crystal or dislocations on the surface of a crystal (see Chapter 1) are stacked into orderly arrays. In order to produce these regular stacks during the crystal or array formation, each atom added to the growing object must have the opportunity to find an appropriate, energetically favorable place. This generally requires relatively high temperatures and long times [6]. But, what happens if a crystal is made to grow more quickly, so that each atom sticks close to that place where it hits?

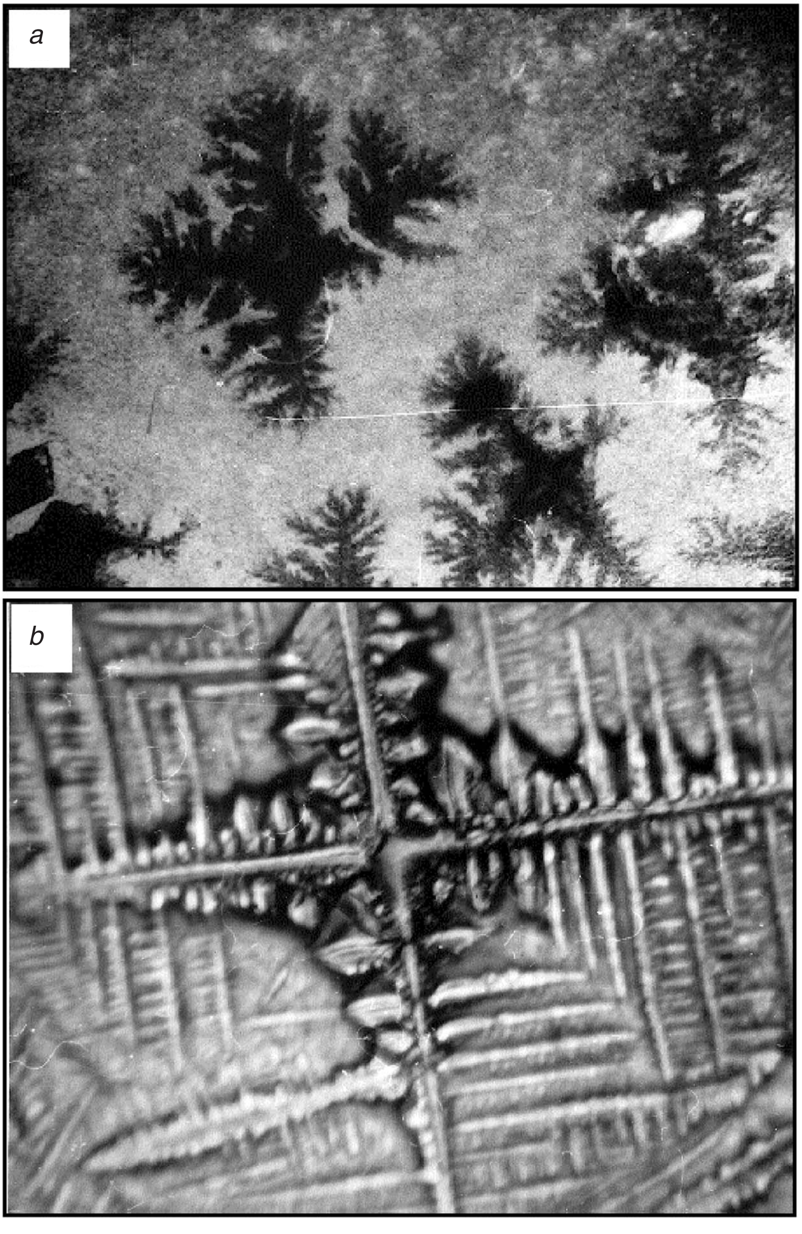

**Fig. 6.1** Crystals obtained after the non-equilibrium crystallization of lipoprotein solution in an external electric field (a) and 0.9% solution of NaCl in bioliquid matrix without an electric field (b).

If the crystallization process is speeded up, the attraction between particles competes with the chaotic character of diffusion – that is, the solidification becomes a non-equilibrium process. The shapes of crystals or geometry of ensembles obtained under non-equilibrium conditions can be very far from facetted perfect crystals or periodic arrays. Many beautiful and bizarre crystal shapes can be found in materials, which are known for their periodic structure under normal conditions. Even such a prominent representative of the simple cubic lattice as table salt (NaCl) becomes unrecognizable after a non-equilibrium crystallization (Fig. 6.1 b). Many other examples can be found in [6, 7] and references therein. Yet these unusual crystals are not disordered; rather, they have been formed according to certain rules and their structure has very interesting properties.

### 6.1.1
### Computer Model

One of the most successful physical models, which helps us to gain some insight into the processes of pattern formation and crystallization close to equilibrium is that of diffusion-limited aggregation (DLA). This model can be applied equally to atomic or molecular crystals as to the systems consisting of subunits of various size, and therefore, one refers to “aggregation” rather than to crystallization. When particles have the ability to attract each other and stick together, they may form aggregates which, in contrast to crystals, may have no distinct shape. The forces between the particles may be either weak (e.g., van der Waals) or strong (e.g., Coulomb), but if the aggregates are formed by charged particles then the forces may be functional over comparatively long distances.

The next ingredient of the model is diffusion, or a random motion. The main characteristic of diffusion is the zero average displacement of all particles. The driving force for such a process is simply a statistical one, as there is no energetic preference for that or another movement direction. Diffusion processes are usually modeled by the random walk model; the simplest random walk being a path constructed according to the following rules:

- there is a starting point depending on objectives of the system;
- the distance between two subsequent points of the walk is a constant;
- the direction from the one point to the next is chosen at random,
- there are no preferable directions.

In a real random walk, any direction is possible, but in a computer simulation the walkers are usually distributed on a lattice and hence, their movements are limited to four or six directions.

The DLA model combines the processes of aggregation and diffusion in order to simulate the non-equilibrium growth of objects by the random addition of subunits. In its original formulation, which was introduced some 25 years ago by T. A. Witten and L. M. Sander [8], the first step is to occupy a site with a seed particle. Next, a particle is released from the perimeter of a large circle, the center of which coincides with the seed. The particle then diffuses until it either leaves the circle or reaches a perimeter site of the seed, and sticks. The process is repeated several thousand times until a large cluster is formed.

Two typical examples of DLA clusters produced by computer simulations are provided in Figure 6.2. Depending on the underlying lattice, the clusters can have different symmetry (see Fig. 6.2). However, the clusters generated by the DLA process have essential features in common, in that they are both highly branched and fractal [9, 10] (see Inset 6.1). The fractal dimension is sensitive to the lattice structure, and for a square lattice it is smaller than for triangular one. The highest fractal dimensionality $D=1.71$ can be obtained without an underlying lattice. However, in all cases the structure consists of branches which sprout, and "fjords" inside the cluster which are never filled. This remarkable geometry arises because the faster-growing parts of the cluster shield the other parts, which therefore become less accessible to incoming particles. An arriving random walker is far more likely to attach to one of the tips of the cluster than to penetrate deeply into one of the cluster inner parts without contacting any surface sites [7]. Thus, tips tend to screen the "fjords". Interestingly enough, this happens on all length scales, which is characteristic for fractals (see Inset 6.1).

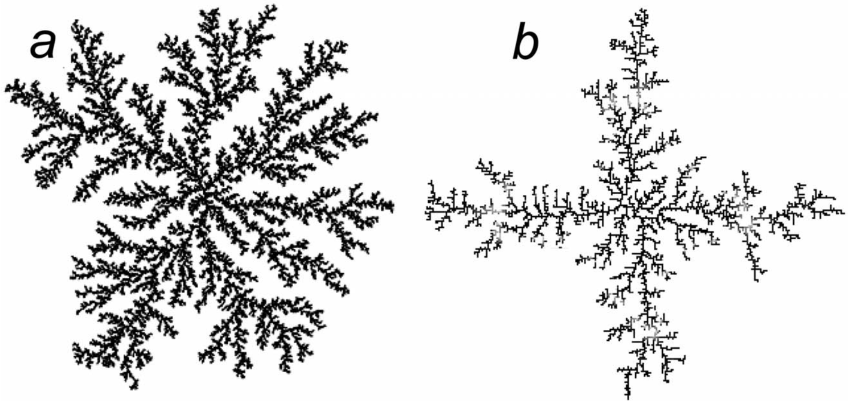

**Fig. 6.2** Examples of a computer realization of DLA clusters on a triangular (a) and a square (b) lattice.

**Inset 6.1** Fractals

Fractals are self-similar geometrical objects, that is, they are objects that have an unchanging structure when viewed at different levels of magnification. Figure 6.3 shows two examples of self-similar objects; in the upper part of Figure 6.3 a DLA cluster is shown, while in the lower part a fern plant is depicted. Looking more closely at the both objects, one finds that increasingly fine levels of the structure become apparent. The cluster and leaf of the fern plant appear the same at many levels of magnification.

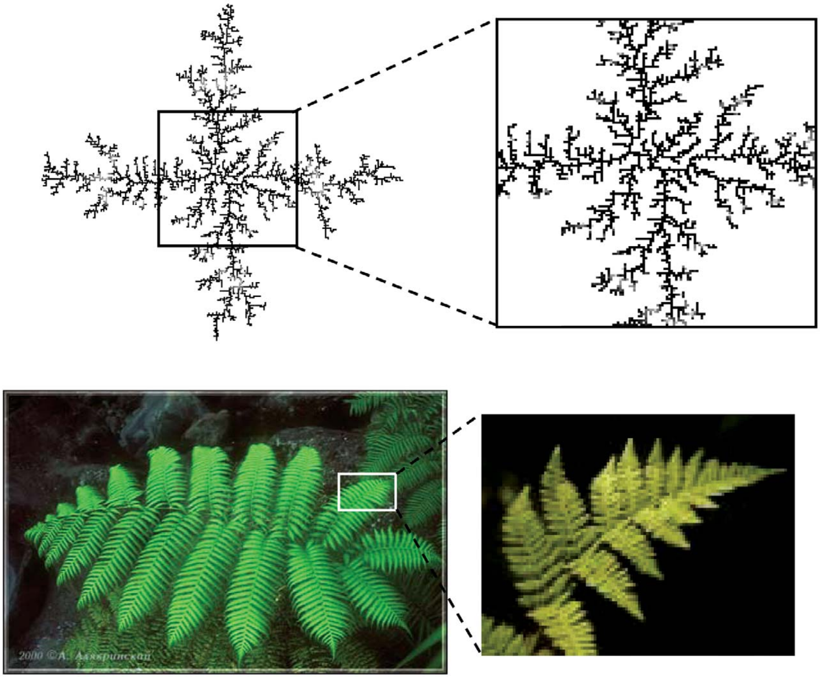

**Fig. 6.3** Self-similarity of the fractal structures.

In mathematics, fractals have a Hausdorff dimension greater than its topological dimension. A comprehensible description of fractals can be found in [9, 10]. Loosely speaking, the Hausdorff dimensionality determines how the mass of the object grows with its radius. The mass of a regular geometric body is proportional to its radius; for example, the mass of a circle is proportional to its area $\pi r^2$ and hence to the squared radius $r^2$; the mass of a sphere is proportional to $r^3$. In these expressions the exponent is an integer and corresponds to the topological dimension. The amount of material in the object of Figure 6.3 does not grow in proportion to the radius, nor in proportion to the radius squared, but rather in proportion to something in between: $\propto t^{1.7}$. This value corresponds to the fractal (Hausdorff) dimension of 1.7.

As can be seen by comparison of Figures 6.1 and 6.2, the DLA model provides a very good approximation of the non-equilibrium growth. This is why it has been successfully applied to many domains of science as gelation, percolation, crystal growth, fracture, sedimentation, viscous fingering, or dielectric breakdown. A comprehensive review of the different applications of the DLA model can be found in [11]. These studies demonstrate that fractal growth is strongly influenced by the presence of interactions between the particles or with external fields, and several examples will be provided in the next section.

### 6.1.2
### Diffusion-Limited Aggregation Altered by Interactions

Branched fractals are known to form during the crystallization of numerous biological systems containing complicated lipid and lipoprotein complexes [12]. Many of these contain different ionized groups, as a result of which they inherently have a quite significant charge [13]. When a biological liquid is subjected to electrophoresis – that is, the action of an external electric field **E** – the polar groups of the molecules and their aggregates are affected. This interaction changes the shape

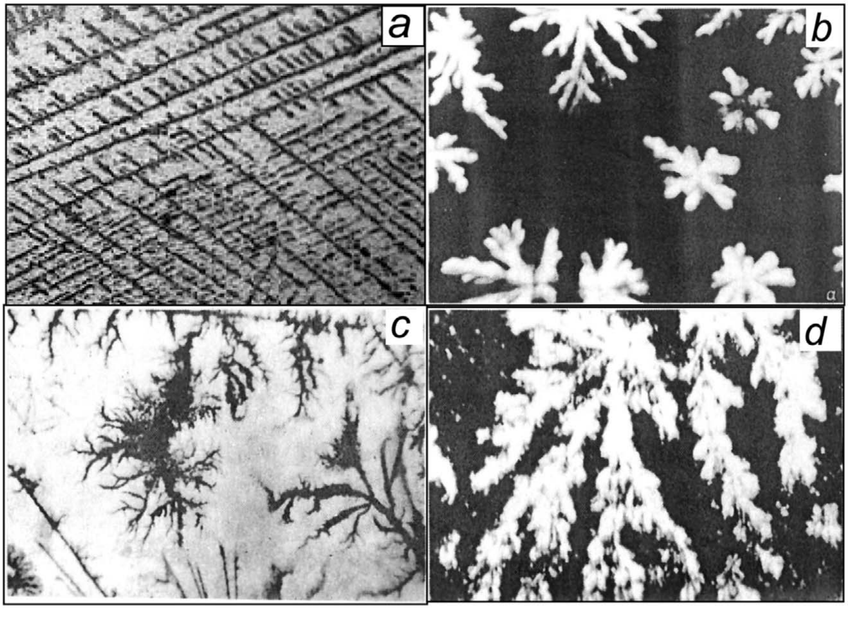

**Fig. 6.4** Micrographs of biological liquids on a solid surface after their crystallization with and without the application of an external electric field. (a, b) Human saliva and pancreatic liquid crystallized without the field. (c, d) Saliva and pancreatic liquid after solidification superimposed with the electrophoresis. The crystal size is of the order of 2 μm. The crystals of pancreatic liquid are optically active; thus, these micrographs have been prepared using a polarizing microscope.

and fractal dimension of the crystals. Figure 6.4 a, b illustrates the typical structures obtained by the crystallization of human saliva and pancreatic liquid of a healthy person on a solid substrate [13]. The crystals have different shapes, although both show significant fractality. The application of an external electric field during the crystallization causes the oppositely charged molecules to move toward the anode or the cathode, respectively – the results is electrophoresis.

The process of electrophoresis is somewhat complicated. In the simplest case, it simply increases the probability of diffusion in certain direction, and this seems to be the case for pancreatic liquid. Figure 6.4 d shows that the branches on one side of fractal crystals become more elongated than on the other sides, while the crystal shape remains mainly unchanged. This situation can be easily modeled by the prescription of different probabilities to movements in different directions $p_x > p_y$. For saliva, the results are different (see Fig. 6.4 a, c), with the crystals obtained after the application of an electric field still having a fractal character. However, the structure induced by the electric field differs significantly from the configuration at $E=0$. This means that, as a result of electrophoresis, either the structure of the lipoprotein complex in solution changes or the thermodynamic equilibrium between the molecules of the lipoprotein complex and solvent molecules is modified. This is not a trivial situation, and it cannot be easily modeled. One of the simplest approximations to such types of problems is the "binary DLA model" [14, 15], which considers two (or several) microscopic entities, attached as a degree of freedom to the diffusing particles. In the binary case, the resulting features can be regarded as "up" and "down". It is expected that neighboring entities interact by means of exchange-like short-range interaction. This formalism has similarities with the Ising model, and therefore it is sometimes referred to as "magnetic DLA".

The magnetic DLA model on a square lattice is defined by the following steps:

(i) An initial particle of size $r_{\max}=1$ with spin $\sigma_0$ is posed on a seed site.

(ii) A diffusing "up" or "down" spin is dropped onto a circle of radius $r_{\max}+\delta$, centered on a seed site.

(iii) A choice is then made for both the next site and the next state orientation of the diffusing spin. The probabilities of jumping to one of the four neighbor sites are proportional to $\exp(\Delta\beta E)$, where $\Delta\beta E$ is the local gain of the dimensionless Ising energy between the initial and the final states defined by

$$\beta E = \frac{\beta J}{2} \sum_{\langle i,j \rangle} \sigma_i \sigma_j - \frac{\beta H}{2} \sum_{\langle i,j \rangle} \sigma_i \,, \tag{6.1}$$

in which the first summation occurs only for nearest-neighbor pairs while the second sum runs over all spins of a cluster. $J$ and $H$ are an exchange integral and an external magnetic field, while $\beta$ is a parameter such that $\beta J$ and $\beta H$ are dimensionless. The probabilities of the eight possible configurations for each jump are renormalized and one specific configuration is chosen through a random number generator.

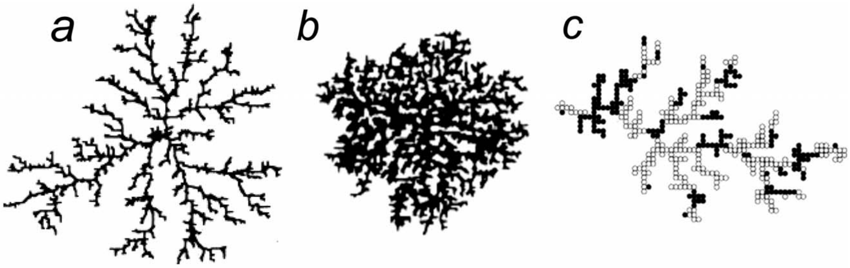

**Fig. 6.5** Typical magnetic diffusion-limited aggregation clusters of 3000 spins grown from an up-spin seed in regime of (a) ferromagnetic exchange ($\beta J>0$) and non-zero magnetic field $\beta H>0$; (b) antiferromagnetic exchange ($\beta J<0$) and non-zero magnetic field $\beta H>0$; (c) ferromagnetic exchange ($\beta J>0$) and zero magnetic field $\beta H=0$. Reprinted with permission from [14].

(iv) If the spin moves outside a circle of radius $n \cdot r_{\max}$, it is removed and one returns to step (ii). If the spin jumps onto a perimeter site of a cluster, it sticks immediately to the cluster and the next diffusing spin is launched. Then, the $r_{\max}$ is adapted to the largest distance between the farthest cluster site, and the seed site.

(v) The launching and diffusing procedures are repeated until a desired number of frozen spins is reached.

Investigation of the model shows that even in the simplest binary case the shape of aggregates depends on the $J$ and $H$. In the case of ferromagnetic $J$, the clusters are DLA-like but they are more extended and less side-branched than the conventional DLA cluster (see Fig. 6.5 a). For the antiferromagnetic interactions the clusters become much more compact (Fig. 6.5 b). In the specific case of $\beta H=0$ and positive $\beta J$, the growing cluster is divided into segments of up- and down-spin species having a characteristic length $\xi$ (see Fig. 6.5 c). This characteristic length scales as a simple power of the mass of the segments with a critical exponent $\mu \approx 1.2$.

## 6.2
## Dynamic Wave Patterns

One of the least-known discoveries of the physicist Michael Faraday is a surface wave instability known as "Faraday waves". Surface waves are standing waves in two dimensions. The basic experimental set-up consists of an open container of fluid which is subjected to uniform vertical oscillations. When the strength or amplitude of these oscillations exceeds a certain threshold, the initially flat surface develops instability and a pattern of standing waves is formed. Originally, only patterns of stripes and squares were observed. Examples of such patterns

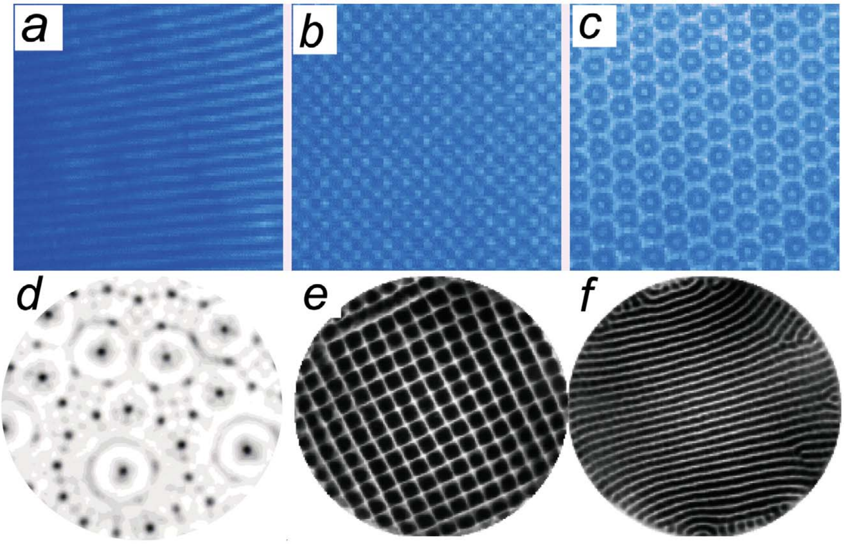

**Fig. 6.6** Experimental images of periodic patterns of standing waves formed at the surface of a vibrated layer of fluid (a–d) and layer of a dry granular material (e, f). The viscosity of the fluid used in these experiments is about 50-fold that of water. The granular material consisted of 0.15–0.18-mm diameter bronze spheres. Reprinted with permission from [17, 18, 20].

are shown in Figure 6.6 a, b. In recent years, using modern experimental techniques, more intricate patterns have been observed. Among those patterns are some showing superstructure ordering, and even some exhibiting quasiperiodic long-range order (see Fig. 6.6 c, d). In these experiments the fluid container is vibrated with a combination of two [16] or even three [17] independent frequencies. Depending on the ratio of the two frequencies, their phase difference, and their relative amplitudes, different patterns are formed.

An interesting variation of the Faraday experiment is to place a dry granular material in a dish and subject it to similar vertical oscillations [19, 20]. Many of the same patterns seen in the liquid version of the experiment are also seen in the granular material. In fact, this technique was used as early as the 17th century by the German physicist Ersnst Chladni, who spread grains of fine sand on a plate from a dismantled violin that was clamped and set vibrating with a bow. The sand grains bounced away from the lively antinodes and accumulated at the relatively quiet nodes. The resulting patterns from different violins were then compared. The aim was to reproduce a pattern similar to those produced by violins of Stradivarius as, presumably, the patterns from better-sounding violins would be similar.

Other examples of pattern-forming systems include Rayleigh-Bénard convection [21], Taylor-Couette flow [22], and reaction-diffusion systems [23]. Surface or parametric wave patterning is a very general phenomenon [4] that is found in a variety of systems with a wide palette of interactions. However, the essential dynamics of those systems can be captured theoretically without specifying any interactions with the help of the Swift-Hohenberg equation [24] and its variants. The Swift-Hohenberg model is of the form

$$\frac{\partial u}{\partial t} = \varepsilon u - (\nabla^2 + 1)^2 u - u^3 \,, \tag{6.2}$$

where $u(x,y,t)$ is in general a real field, which describes the amplitude of the standing wave pattern. This equation is variational $\partial u/\partial t = -\delta F/\delta u$, that is, it drives the field $u(x,y,t)$ towards a minimum of the Lyapunov function $F$. The Lyapunov function $F(y)$ is a scalar function defined on a region $D$ that is continuous, positive definite $F(y)>0$, for all $y \neq 0$, and has continuous first-order partial derivatives at every point of $D$. The derivative of $F$ with respect to the system $f(y)$, is defined as the dot product $F^*(y) = \nabla F(y) \cdot f(y)$ [25]. The existence of a Lyapunov function for which $F^*(y) < 0$ on some region $D$ containing the origin, guarantees the stability of the zero solution of $f(y)$, while the existence of a Lyapunov function for which $F^*(y)$ is negative definite on some region $D$ containing the origin guarantees the asymptotical stability of the zero solution of $f(y)$. Thus, the existence of Lyapunov function can be used to demonstrate the stability or instability of some states of a system. For conservative systems in physics, the total energy is always a Lyapunov function. Therefore the Swift-Hohenberg equation drives the system towards the minimum of an effective free energy. Depending on the frequency parameter $\varepsilon$, different solutions (wave patterns) of Eq. (6.2) are obtained. For modeling of wave patterns with quasiperiodic ordering the Swift-Hohenberg equation must be generalized to two frequencies [26]. The application of the Swift-Hohenberg model to different systems does not mean that all systems behave in the same way, but rather that certain properties are common to a class of systems – that is, they belong to the same universality class.

The following section provides several examples of parametric waves, which are not as well known as Rayleigh-Bénard convection, reaction–diffusion or surface wave patterns in liquids.

### 6.2.1
### Pattern Dynamics of Spin Waves

Spin waves are low-energy collective excitations that occur in magnets. The most complete collection of literature concerning this vivid area of basic research can be found in [27–30]. Here, only the aspect of parametrically excited spin waves near the instability threshold will be introduced.

Classically, in the ground state of a ferromagnet, attained at T = 0 K, all the atomic spins are aligned parallel to each other. If there is an applied field or some anisotropy, then the alignment occurs along a certain direction. As there is a strong correlation between the directions of the atomic spins due to exchange interaction, the deflection of one magnetic moment will affect the neighboring moments, and their deflection, in turn, will affect their neighboring moments and so on, so that the perturbation does not remain localized, but rather propagates through the ferromagnetic crystal in a wave-like fashion. Such propagating perturbations are called "spin waves". The mathematical representation of spin waves is the same as of regular waves; thus, a wave vector and frequency are assigned to them.

If a ferromagnetic sample is in a single domain state – that is, it is magnetized to saturation by an external bias magnetic field – then the dynamics of magnetization vector is described by the Landau–Lifshitz–Gilbert torque equation

$$\frac{d\mathbf{M}}{dt} = -\gamma(\mathbf{M} \times \mathbf{H}_{eff}) + \frac{\alpha}{M_s}\left(\mathbf{M}\times \frac{d\mathbf{M}}{dt}\right), \tag{6.3}$$

where $\mathbf{M}=\mathbf{M}_s+\mathbf{m}(\mathbf{R},t)$ is the total magnetization, $\mathbf{M}_s$ and $\mathbf{m}(\mathbf{R},t)$ are the vectors of the saturation and the variable magnetization correspondingly, $\gamma$ is the modulus of the gyromagnetic ratio for the electron spin, $\alpha$ is a phenomenological damping constant, and $\mathbf{H}_{eff}$ is the effective magnetic field. $\mathbf{H}_{eff}$ is calculated as a variational derivative of the energy function $\mathbf{H}_{eff}=-\delta W/\delta\mathbf{M}$, where all the relevant interactions in the magnetic substance have been taken into account [31]. Total energy $W$ belongs to the class of Lyapunov functionals. It can be shown that the solutions for the motion equation represent waves. Each solution (mode) corresponds to certain wave vector $\mathbf{k}$ and frequency $\omega$. Since in general $\mathbf{H}_{eff}$ depends on $\mathbf{M}$ and the product of these quantities appears in the right-hand part of Eq. (6.3), this equation is intrinsically non-linear. Therefore, parametric wave instabilities should exist in systems possessing spin wave excitations. Spin waves can be excited by a small microwave pumping field.

The pattern dynamics of parametrically excited spin-waves in a ferromagnet have been recently studied by the finding of analytical solutions of Eq. (6.3) [32]. In this investigation, only parallel pumping (a linearly polarized microwave pumping field is applied parallel to the stationary field) has been analyzed for the sake of simplicity. Stripe, square and more complicated periodic stationary patterns formed by one-, two-, or three-standing waves have been predicted (see Fig. 6.7). Dynamics of magnetization or spin dynamics in more complicated cases, for example for perpendicular pumping, can be in principle be visualized by means of another theoretical technique, the micromagnetic simulations. However, whilst the propagation of spin waves in nanomagnetic elements has been investigated by using a micromagnetic approach [33], the stationary patterns have not been implicitly addressed.

The experimental visualization of spin wave patterns is much more difficult than for other parametric waves. Most of the experiments on non-linear spin waves reported in the literature were conducted using either microwave spectroscopy or traditional ferromagnetic resonance techniques. In microwave experiments, spin waves in the GHz frequency range are excited by a microstrip

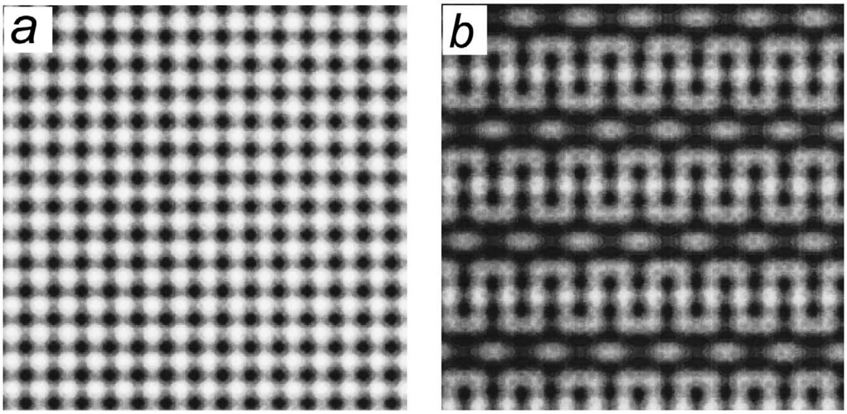

**Fig. 6.7** Simulated square two-wave (a) and periodic three-wave (b) spin wave patterns in uniformly magnetized sample. Reprinted with permission from [32].

antenna, and the propagating spin waves are detected by a second microstrip antenna that is connected to a microwave detector (see, e.g., [30]). By construction, the receiving antenna integrates the spin wave intensity along its length, and, therefore, all the information about the transverse distribution of the intensity in the propagating spin wave packet is lost. Thus, the processes of formation and propagation of temporal spin wave envelope solitons in all these studies were treated in the past as essentially being one-dimensional.

Ferromagnetic resonance techniques are unable to visualize the patterns which emerge above the instability threshold as they provide only spatially averaged information about spin wave patterns [27]. Among the very few experimental methods allowing spatially resolved measurements of two-dimensional radiation patterns is Brillouin Light Scattering Spectroscopy (BLS) [31] and Time-Resolved Scanning Kerr Microscopy (TRSKM) [34].

The BLS technique is based on the spectral analysis of laser light scattered by a magnetic sample. Due to photon-spin wave interaction, in addition to the photons at the laser frequency, the scattered light also contains photons at frequencies shifted by the frequencies of spin waves. Consequently, by analyzing these additional spectral components, conclusions can be drawn about the frequencies and intensities of spin waves existing at the point of the sample where the probing light is focused. A detailed and thorough description of the BLS method can be found in [31]. In recent BLS measurements [35, 36], the radiation of spin waves by rectangular multilayer magnetic elements into a surrounding magnetic film has been studied. The probing laser spot was positioned onto the CoFe film surrounding the magnetic element consisting of CoFe, Cu and NiFe layers, and the spectra of spin waves were measured at different distances from its edges. These measurements showed that the spectra demonstrate strong quantization, leading to an appearance of several well-pronounced peaks.

The very existence of these peaks is a prerequisite for the existence of a standing spin wave pattern. The visualization of patterns in real space, however, is difficult because of the inelastic character of the scattering.

In TRSKM, the difference of the polar Kerr signal with and without field pulse is measured. The detected signal is proportional to the change of magnetization due to the excitation. Hence, the spin wave patterns can, in principle, be visualized, although studies of quantized spin-waves were mostly focused on investigations of their frequency spectra and dynamic magnetization after a single excitation (see [37] and references therein).

Hence, in spite of theoretical evidence for existence of parametric spin wave instabilities, experimental visualization of the spatial structure of the non-linear state is still lacking, even in the simplest case of parallel pumping. A theoretical analysis of transverse pumping is much more complicated [38], and remains an interesting open question.

### 6.2.2
### Liquid Crystals in a Rotating Magnetic Field

Nematic liquid crystals are uniaxial materials (see Chapter 5; Section 5.1), their preferred axis perhaps varying from place to place, but in general being a continuous function of position. The axis of the order parameter (the so-called "director") coincides with the average orientation of the long axes of molecules. Nematics may consist of either polar or non-polar mesogens. In the non-polar case, a more or less uniform alignment of director (see Section 5.1) can usually be achieved by applying a magnetic field of a several hundred Oersteds, or greater. The preferred axis tends to align parallel to the field due to the anisotropy of the molecular diamagnetic susceptibility [39].

If the liquid crystal has been initially homeotropically aligned between two glass plates – that is, the director is perpendicular to the plates at the plate boundaries – the sample placed between crossed polarizers appears as a dark field. This situation changes when a homogeneous magnetic field *H*, parallel to

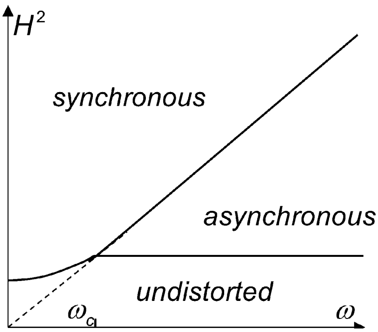

**Fig. 6.8** Schematic phase diagram of pattern formation in nematic liquid crystals in a rotating magnetic field.

the x-y plane (the plane of the galss plates), is rotated with angular frequency $\omega$ about the z-axis (the initial orientation of the director). Once the magnetic field starts to rotate, the director will follow the rotation with a phase lag because of viscosity, and the alignment of a nematic substance will be distorted. The boundary between distorted and undistorted phases becomes visible in polarized light, and the whole system reveals a rich variety of pattern-forming processes [40, 41].

The patterning depends on the strength and the frequency of field, as well as on viscosity $\gamma$ and diamagnetic susceptibility $\chi_a$ of the liquid crystal. However, all structures can be attributed to the class of solitons or their ensembles. Magnetically induced solitary waves or solitons (see Section 1.2.1) in nematics were first discovered by Helfrich [39]. In liquid crystals, a soliton separates two energetically equivalent but topologically distinct domains of the sample which differ in the spherical angle $\varphi$ by an amount $\pi$. This corresponds to a static discli-

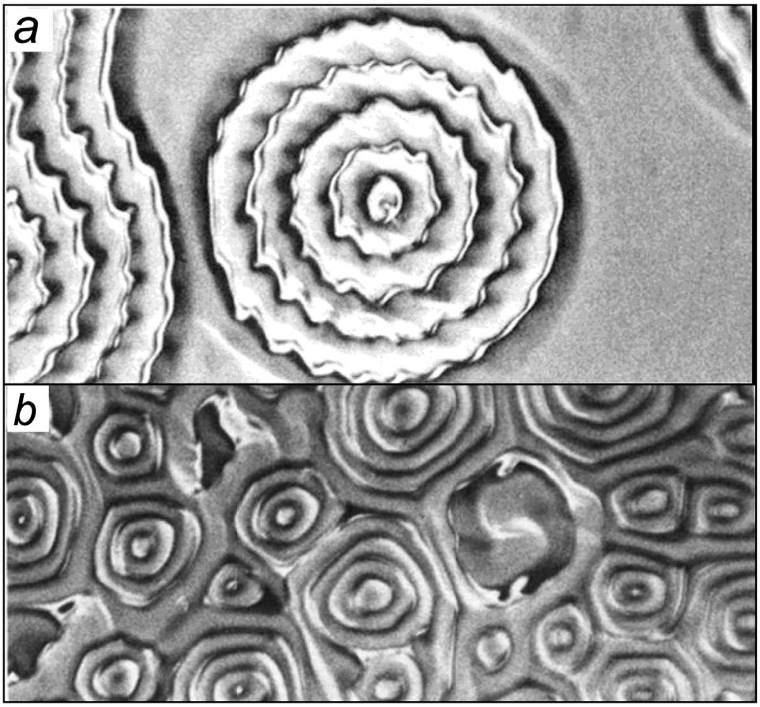

**Fig. 6.9** Photographs of the simplest asynchronous patterns. (a) Transverse instability (a ring-soliton with so-called viscosity reduction lattice boundary) nucleated from outer side boundary and dust particle. (b) Complex soliton lattice. Reprinted with permission from [40].

nation of strength $s = \pm 1$ (see Section 5.1). The director varies smoothly through the soliton. A dynamic soliton must be nucleated either by a dust particle or by the sidewall of the sample (see Fig. 6.9 a). After creation, the soliton propagates away and another soliton can be nucleated forming a soliton lattice (see Fig. 6.9 b). Similarly to vortex and antivortex pairs or two disclinations of opposite strength, two solitons can collide and annihilate.

The solitons appear due to competition between the elastic energy arising from the distortion of the orientation pattern and periodic potential due to rotating magnetic field. This type of competition can be analyzed in the framework of the Frenkel-Kontorova model introduced in Section 1.2. In the simplest case, a soliton is described by the one-dimensional overdamped sine-Gordon equation [40, 42] (see Section 1.2.1). One defines a local two-dimensional coordinate system, fixed in the sample. Axis $y$ is usually chosen to be parallel to the soliton, along which the structure is invariant, while $x$ is perpendicular to the soliton, parallel to its direction of propagation. It is assumed that splay, twist, and bend elastic constants are identical and equal to $K$. The fluid backflow and any variation of $\alpha$ in $z$ direction are neglected. The last assumption breaks in the so-called static soliton state [40]. Looking only at the phase lag angle $\alpha$ between $\mathbf{H}$ and $\mathbf{n}_\perp$, the projection of $\mathbf{n}$ in the $x$-$y$ plane, one can write down a one-dimensional torque equation about the $z$ axis

$$K\frac{\partial^2 \alpha}{\partial x^2} - \gamma\frac{\partial \alpha}{\partial t} + \gamma\omega - \frac{1}{2}\chi_a H^2 \sin 2\alpha = 0\,; \tag{6.4}$$

where $\gamma$ and $\chi_a$ are the rotational viscosity and the anisotropy of diamagnetic susceptibility respectively. Equation (6.4) has a soliton solution of the form $\alpha = \alpha(\mathrm{x{-}vt})$, where $v$ is the soliton's velocity. A velocity scale is usually given by $v_0 = l_c/\sqrt{2\tau}$ with $\tau = 2\gamma/\chi_a H^2$. The velocity of outward-growing isolated ring solitons is well predicted by Eq. (6.4). The one-dimensional model reproduces correctly three main regimes in the pattern responses: no distortion; synchronous; and asynchronous states. The undistorted region corresponds to weak fields (see Fig. 6.8). The synchronous state exists when $\omega\tau < 1$. This state is characterized by a constant-phase lag angle $\alpha = \omega t - \phi$. The condition for asynchronous state is $\omega\tau > 1$ and is characterized by continuously increasing phase lag angle [43].

In spite of the good reproduction of the experimental velocity of ring-solitons, the shape of theoretical and experimental $v = f(\omega\tau)$ curves differ [40]. The most significant discrepancy is that Eq. (6.4) predicts the speed of a soliton to proceed smoothly to 0 only as $\omega\tau$ approaches 0, while in experiments the transition of a dynamic soliton to a static one occurs abruptly at a finite $\omega\tau$. Later investigations [42] have shown that, for an accurate description of experimentally observed dynamics, the soliton must be described as a two-dimensional object with unconstrained director motion. Corresponding equations are much more complicated and cannot be solved analytically.

### 6.2.3
### Standing Waves in Two-Dimensional Electron Gas: Quantum Mirages

Two-dimensional electron gas was already earlier (see Section 2.6.1.4) in the context of the Wigner electron crystal. It has been pointed out that the electron crystal may be formed in two-dimensional systems at sufficiently high electron densities and low kinetic energy. This may be the case of an interface between GaAs and AlGaAs layers; above the surface of liquid helium, or in a microchannel capillary filled with liquid helium. In order to define a critical parameter of the formation of Wigner crystal, the quantity $\Gamma$ – that is, a measure of the ratio of Coulomb potential energy to kinetic energy per particle – has been defined. For the two-dimensional system this ratio is $\Gamma = \frac{\pi^{1/2} N_s^{1/2} e^2}{kT}$, with $N_s$ as the electron areal density, $e$ as the electron charge and $kT$ the thermal energy. The stable electron crystal is expected at $\Gamma > 100$, where the potential energy predominates.

**Inset 6.2** Surface states

Surface states are electronic states found at the surface of materials. They are formed due to the sharp transition from solid material that ends with a surface, and are found only at the atom layers closest to the surface. There are two types of surface states defined: Tamm, and Shockley states.

- The *Tamm states* appear when the surface-potential perturbation becomes sufficiently large. The Tamm states are usually split-off states of *d*- and *f*-valence band states.
- When the bulk bands are crossed, another type of surface state arises at the middle of the band gap even if there was no surface-potential perturbation. This state has been first postulated by *Shockley* and carries his name. The Shockley state is modeled by adding a weak potential to the free electron gas of a solid, and thus emerges from a formalism that is generally applied to the description of *sp*-bands in metals.

Apart from above-mentioned cases, the two-dimensional electron gas can be formed on the surface of certain metals due to the presence of Shockley surface states [44] (see Inset 6.2). Similar to the case of the electron gas at the interface of two semiconductors, electrons are free to move in the plane of the surface, but not in the direction normal to the surface, as Bloch states are forbidden in that direction at the Fermi energy. The wavelength of electrons in the surface states, $\lambda$, the effective mass of surface-state electrons, $m^*$, and the density of states $\rho_{\text{surf}}$ are related through the dispersion relationship

$$E_{\text{surf}}(k) - E_F = E_0 + \frac{\hbar k^2}{2m^*}\,, \tag{6.5}$$

where $\rho_{\text{surf}} = m^*/\pi\hbar^2$ (for $E > E_0$) includes both spin-up and spin-down electrons. In the cases of Cu(111), Au(111), and Ag(111), the surface-band minimum, $E_0$, is very close to the Fermi energy. Typical values are fractions of an eV below Fermi energy, while the Fermi energy itself is typically 5–10 eV. Small $E_0$ makes filling of the surface-state band rather small, and consequently the density of surface states – and hence electron areal density $N_s$ – are low. For example, the surface-state electron density derived from Eq. (6.5) for Cu(111) corresponds to approximately one electron per 1.2 nm$^2$ [45]. This, however, means that the electron gas at the close-packed surface of noble metals is in the regime $\Gamma < 1$ where the kinetic energy predominates and the system behaves like an electron gas.

An exciting peculiarity of this system is that, in contrast to all other discussed systems, the two-dimensional electron gas has not to be externally stimulated to obtain waves. The electrons themselves have the wave-like nature. Because of the high kinetic energy, the surface electrons are strongly delocalized – that is, they form so called "electron sea" or disordered superposition of electron waves. The simplest way to obtain correlated, standing waves is to allow the electrons to scatter from surface imperfections such as terrace edges, impurities, or adsorbates [46, 47]. As an electron is scattered from a step edge, the reflected wave interferes with the incident wave and the standing wave pattern emerges. The dispersion relation Eq. (6.5) of the electron gas in the plane of surface is, to a very good approximation, both quadratic and isotropic. An isotropic dispersion relationship is very convenient for the application of scattering theory because there is no need to know the orientation of the underlying crystal lattice, and therefore the standing wave patterns are highly predictable.

During recent years there has been a renaissance of interest in the physics of these electrons which, it is argued, play an important role in a variety of physical processes, including epitaxial growth, the determination of equilibrium crystal shapes, surface catalysis, molecular ordering, and atom sticking. This attention may be largely attributed to the advent of the scanning tunneling microscope (STM), which has enabled the direct imaging in real space of electrons in surface states, and their interactions with adsorbates [47], steps [46, 48], and other structures [48–50].

Similar to other types of surface wave, the symmetry of an electron standing pattern can be changed by variation of: (i) the wave frequency; and (ii) the interferential geometry. Here, the influence of frequency variation on pattern geometry will first be discussed. As can be seen from Eq. (6.5), the frequency of the wave vector can be changed by varying the energy of surface-state electrons $E_{\text{surf}}$. This energy, in turn, is easily tunable by the bias voltage in the STM measurements. Figure 6.10a shows experimentally visualized standing wave patterns in Co on Cu(111) [51]. Nanometer-scale Co islands on the Cu(111) substrate establish a particularly interesting system, because both substrate and islands exhibit their own standing wave patterns. The dispersion relationship for Cu is given in Figure 6.10b. The wave vector $\mathbf{k}$ rises parabolically with increasing bias voltage/surface state energy. Increase of the wave vector corresponds to the diminishing of the wave length $\lambda = \pi/k$. The $E_{\text{surf}}(k) - E_F$ curve is smooth, which means that distance between crests/troughs decreases continuously. The dispersion relationship for Co islands can also be fitted by a parabolic function,

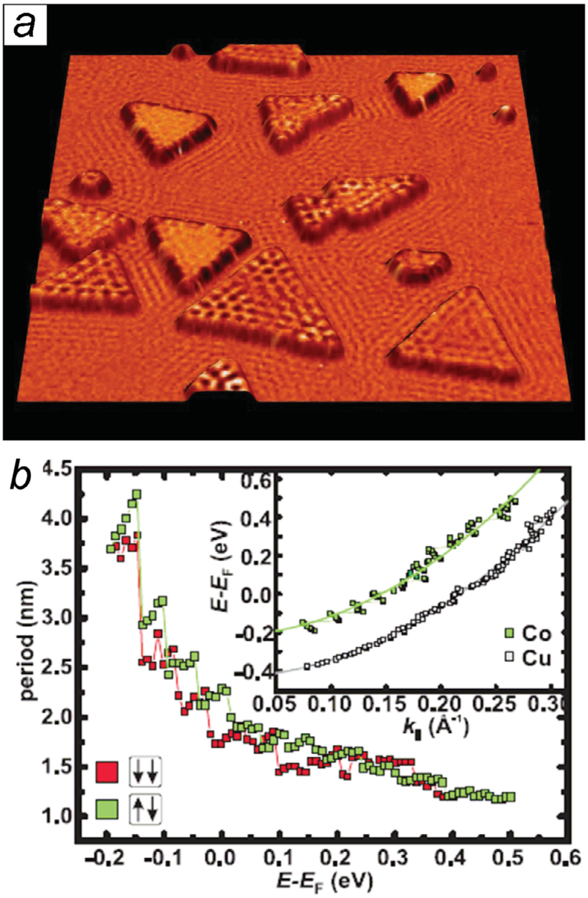

**Fig. 6.10** (a) STM image of standing wave pattern in Co islands on Cu(111). (b) Standing wave periods on Co islands as a function of bias voltage. The step-like structure results from electron confinement. Illustration courtesy of O. Pietzsch.

although the experimental data is step-like – that is, the **k** vector increases by discrete amounts. The step-like structure of the data manifests the effect of electron confinement, which reflects the occurrence of discrete resonance states.

From Figure 6.10 it can be seen clearly that the symmetry of the electron wave pattern reflects the symmetry of the island. This is in response to the question of how the pattern symmetry can be tuned. While the wave pattern has a hexagonal symmetry on triangular islands, parallelogram or even trapezoidal arrangements can be obtained, depending on the geometry of the particle [52]. Most complicated standing wave patterns can be obtained by artificially made nanoscale structures [49], geometrical arrays of Fe atoms positioned with

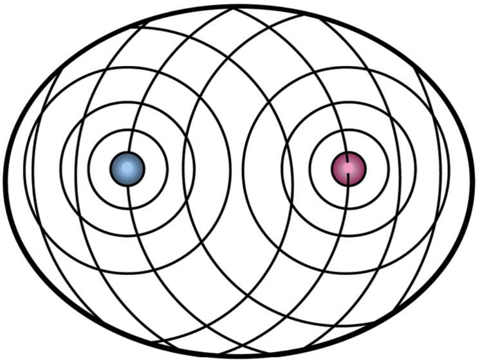

**Fig. 6.11** Schematic representation of the standing pattern of mercury waves when small amount of mercury are dropped in at one focus (red), while a mirage appears at another focus (blue).

atomic scale precision using the STM. These atomic constructions acquired the name of quantum corrals, which have also received theoretical attention [53, 54].

The most fascinating experiments on quantum corrals concern quantum mirage phenomena [47, 55]. In order to create a quantum mirage, several dozen cobalt atoms on a copper surface are first moved into an ellipse-shaped quantum corral. The size and shape of the elliptical corral determine its quantum states – that is, the energy and the wave pattern of the confined electrons. A quantum state which concentrated large electron densities at each focus point of the elliptical corral has been used. When an atom of magnetic cobalt was placed at one focus, a mirage of this atom appeared at the other focus. This means that the same electronic states in the surface electrons surrounding the cobalt atom were detected, even though no magnetic atom was actually present. The intensity of the mirage is about one-third of that around the cobalt atom. Only certain ellipses will produce a good mirage effect, normally those which have large surface-state amplitudes at the foci. This depends on the relative dimensions of the ellipse and on Fermi wave length $\lambda_F$.

The operation of the quantum mirage is similar to how light or sound waves are focused to a single spot by optical lenses, mirrors, parabolic reflectors or "whisper spots" in buildings. For example, faint sounds generated at either of the two "whisper spots" in the Old House of Representatives Chamber (now called Statuary Hall) in the U.S. Capitol Building in Washington, D.C., can be heard clearly far across the chamber at the other whisper spot. Another similar phenomenon stems from an experiment described by E. and W. Weber in the 18th [45]. Figure 6.11 illustrates a sketch of this experiment, which shows the surface waves of mercury in an elliptical container. The image corresponds to drops of mercury landing at one focus with the other focus empty. Nevertheless, the opposite foci appear identical, indicating that from the point of view of the wave, the two foci are excited equally.

## 6.3
## Summary

It was hoped to show in this introductory description of pattern formation in dissipative systems, that the notion of pattern formation does not attach itself exclusively to any particular area of science. Rather, it cuts across disciplines. The patterns seen in convecting fluids have much in common with those seen in two-dimensional electron systems, in magnets, in liquid crystals, or in granular materials. One can regard the patterns as independent objects, the behavior of which is governed by universal equations. The structure of these equations, however, can be interpreted in terms of the competing interactions, depending on the symmetry and microscopic properties of the original system.

## References

1 G. Nicolis, I. Prigogine, *Self-Organization in Nonequilibrium Systems, from Dissipative Structures to Order through Fluctuations*, Wiley, New York, **1977**.
2 H. Haken, *Synergetics, An Introduction. Nonequilibrium Phase Transitions and Self-Organization in Physics, Chemistry and Biology*, Springer, Berlin, **1983**.
3 V.I. Krinsky (Ed.), *Autowaves: Results, Problems, Outlook*s, Springer, Berlin, **1984**.
4 M.C. Cross, P.C. Hohenberg, *Rev. Mod. Phys.* **1993**, *65*, 852.
5 C. Kittel, *Introduction to Solid State Physics*, John Wiley & Sons, New York, **1971**.
6 P.Ball, *Designing the Molecular World: Chemistry at the Frontier*, Princeton University Press, London, **1994**.
7 T.C. Halsey, *Physics Today* **2000**, *53*, 36.
8 T.A. Witten, L.M. Sander, *Phys. Rev. Lett.* **1981**, *47*, 1400.
9 B.B. Mandelbrot, *The Fractal Geometry of Nature*, W. H. Freeman, New York, **1982**.
10 J. Feder, *Fractals*, Plenum Press, New York, **1988**.
11 L.M. Sander, *Contemporary Physics*, **2000**, *41*, 203.
12 E.Y. Vedmedenko, M. V. Kurik, I. N. Kuvichka, *Sov. Tech. Phys. Lett.* **1992**, *18*, 154.
13 E.Y. Vedmedenko, M.V. Kurik, I.N. Kuvichka, *Sov. Tech. Phys. Lett.* **1991**, *17*, 19.
14 N. Vandewalle, M. Ausloos, *Phys. Rev. E* **1995**, *51*, 597.
15 M. Ausloos, N. Vandewalle, R. Cloots, *J. Magn. Magn. Mater.* **1995**, *140–144*, 2185.
16 W.S. Edwards, S. Fauve, *Phys. Rev. E* **1993**, *47*, R788.
17 Y. Ding, P. Umbanhowar, *Phys. Rev. E* **2006**, *73*, 046305.
18 A. Kudrolli, B. Pier, J.P. Gollub, *Physica D* **1998**, *123*, 99.
19 P.B. Umbanhowar, F. Melo, H.L. Swinney, *Nature* **1996**, *382*, 793.
20 F. Melo, P.B. Umbanhowar, H.L. Swinney, *Phys. Rev. Lett.* **1995**, *75*, 3838.
21 E. Bodenschatz, W. Pesch, G. Ahlers, *Annu. Rev. Fluid Mech.* **2000**, *32*, 709.
22 R.C. DiPrima, H.L. Swinney. In: *Hydrodynamic Instabilities and the Transition to Turbulence*, 2nd edn., Topics in Applied Physics, *45*, Springer, Berlin, **1985**.
23 P. Grindrod, *The Theory and Applications of Reaction-Diffusion Equations: Patterns and Waves*, 2nd edn., Oxford Applied Mathematics and Computing Science Series, Clarendon Press, Oxford, **1996**.
24 J.B. Swift, P.C. Hohenberg, *Phys. Rev. A* **1977**, *15*, 319.
25 http://mathworld.wolfram.com
26 R. Lifshitz, D.M. Petrich, *Phys. Rev. Lett.* **1997**, *79*, 1261.
27 J.A.C. Bland, B. Heinrich (Eds.), *Ultrathin Magnetic Structures Vol. I and II*,

Springer, Heidelberg, Berlin, New York, Tokyo, **1992**.

**28** N. W. Ashcroft, N. D. Mermin, *Solid-State Physics*, Saunders, Philadelphia, **1976**.

**29** P. W. Anderson, *Basic Notions of Condensed Matter Physics*, Addison-Wesley, Reading, MA, **1984**.

**30** M. G. Gottam (Ed.), *Linear and Nonlinear Spin Waves in Magnetic Films and Superlattices*, World Scientific, Singapore, **1994**.

**31** S. O. Demokritov, B. Hillebrands, A. N. Slavin, *Phys. Rep.* **2001**, *348*, 441.

**32** F.-J. Elmer, *Phys. Rev. B* **1996**, *53*, 14323.

**33** R. Hertel, W. Wulfhekel, J. Kirschner, *Phys. Rev. Lett.* **2004**, *93*, 257202.

**34** M. Buess, R. Höllinger, T. Haug, K. Perzlmaier, U. Krey, D. Pescia, M. R. Scheinfein, D. Weiss, C. H. Back, *Phys. Rev. Lett.* **2004**, *93*, 077207.

**35** V. E. Demidov, S. O. Demokritov, B. Hillebrands, M. Laufenberg, P. Freitas, *Appl. Phys. Lett.* **2004**, *85*, 2866.

**36** V. E. Demidov, B. Hillebrands, S. O. Demokritov, M. Laufenberg, P. Freitas, *Appl. Phys. Lett.* **2005**, *97*, 10A717.

**37** K. Perzlmaier, M. Buess, C. H. Back, V. E. Demidov, B. Hillebrands, S. O. Demokritov, *Phys. Rev. Lett.* **2005**, *94*, 057202.

**38** H. Suhl, *J. Phys. Chem. Solids*, **1957**, *1*, 209.

**39** W. Helfrich, *Phys. Rev. Lett.* **1968**, *21*, 1518.

**40** K. B. Migler, R. B. Meyer, *Phys. Rev. Lett.* **1991**, *66*, 1485.

**41** C. Zheng, R. B. Meyer, *Phys. Rev. E* **1997**, *55*, 2882.

**42** C. Zheng, R. B. Meyer, *Phys. Rev. E* **1997**, *56*, 5553.

**43** F. Brochard, L. Léger, R. B. Meyer, *J. Phys. (Paris)* **1975**, *36*, C1-209.

**44** S. G. Davison, M. Stelicka, *Basic Theory of Surface States*, Oxford, New York, **1996**.

**45** G. A. Fiete, E. J. Heller, *Rev. Mod. Phys.* **2003**, *75*, 933.

**46** Y. Hasegawa, P. Avouris, *Phys. Rev. Lett.* **1993**, *71*, 1071.

**47** M. F. Crommie, C. P. Lutz, D. M. Eigler, *Nature* **1993**, *363*, 524.

**48** Ph. Avouris, I.-W. Lyo, *Science* **1994**, *264*, 942.

**49** M. F. Crommie, C. P. Lutz, D. M. Eigler, *Science* **1993**, *262*, 218.

**50** J. Li, W.-D. Schneider, R. Berndt, S. Crampin, *Phys. Rev. Lett.* **1998**, *80*, 3332.

**51** O. Pietzsch, A. Kubetzka, M. Bode, S. Heinze, S. Okatov, A. Lichtenstein, R. Wiesendanger, *Phys. Rev. Lett.* **2006**, *96*, 237303.

**52** S. L. Silva, M. F. Leibsle, *Surf. Sci.* **1999**, *441*, L904.

**53** E. J. Heller, et al., *Nature* **1994**, *369*, 464.

**54** S. Crampin, M. H. Boon, J. E. Inglesfield, *Phys. Rev. Lett.* **1994**, *73*, 1015.

**55** H. C. Manoharan, C. P. Lutz, D. M. Eigler, *Nature* **2000**, *403*, 512.

# Subject Index

# *Related Titles*

Waser, R. (ed.)

## Nanoelectronics and Information Technology

995 pages with 1148 figures and 47 tables

2005

Hardcover
ISBN-13: 978-3-527-40542-8

ISBN-10: 3-527-40542-9

Borisenko, V. E., Ossicini, S.

## What is What in the Nanoworld

### A Handbook on Nanoscience and Nanotechnology

347 pages with 120 figures and 28 tables

2004

Hardcover
ISBN-13: 978-3-527-40493-3

ISBN-10: 3-527-40493-7

Kelsall, R., Hamley, I. W., Geoghegan, M. (eds.)

## Nanoscale Science and Technology

448 pages

2005

Hardcover
ISBN-13: 978-0-470-85086-2

ISBN-10: 0-470-85086-8

Prasad, P. N.

## Nanophotonics

415 pages

2004

Hardcover
ISBN-13: 978-0-471-64988-5

ISBN-10: 0-471-64988-0